Complex Inkjets: Particles, Polymers and Non-Linear Driving

Claire McIlroy

Submitted in accordance with the requirements
for the degree of Doctor of Philosophy

The University of Leeds

Department of Applied Mathematics

October 2014

The candidate confirms that the work submitted is her own, except where work which has formed part of jointly authored publications has been included. The contribution of the candidate and the other authors to this work has been explicitly indicated below. The candidate confirms that appropriate credit has been given within the thesis where reference has been made to the work of others.

The work in Chapter 3, Section 2 of the thesis has appeared in publication as follows:
C. McIlroy and O. G. Harlen *Modelling Capillary Break-up of Particulate Suspensions* Physics of Fluids 26 (2014) 033101.
I am the principal author of this paper. I discussed the idea with my supervisor, Oliver Harlen, who provided guidance and comments on the drafts.

The work in Chapter 4 of the thesis has appeared in publication as follows:
C. McIlroy, O. G. Harlen and N. F. Morrison *Modelling the jetting of dilute polymer solution in drop-on-demand inkjet printing* Journal of Non-Newtonian Fluid Mechanics 201 (2013) 17-28.
I am the principal author of this paper. The model is based on previous publication: Hoath *et al.* *Jetting Behaviour of polymer solutions in drop-on-demand inkjet printing* Journal of Rheology 56 (2012) 1109. Neil Morrison provided the DoD axisymmetric jetting model. I discussed the idea with my supervisor, Oliver Harlen, who provided guidance and comments on the drafts.

For Mum and Dad.

‘Mathematicians are born not made.’ - Henri Poincaré

Acknowledgements

'If I have been able to see further, it was only because I stood on the shoulders of giants' -
Isaac Newton

Foremost, I would like to express my sincere gratitude to my supervisor Oliver Harlen for his continuous support throughout my studies. I could not imagine a better advisor and mentor for my PhD study. His motivation and enthusiasm have made my PhD experience truly enjoyable and I have been inspired to continue academic research.

I also thank my co-supervisor Mark Kelmanson. His insight gave a different perspective to my research and I have appreciated his advice and encouragement. In particular, I would like to thank Mark for his generous offer to implement his 'linked-list' numerical programme into my work.

This work was supported by the UK Engineering and Physical Sciences Research (EPSRC) through grant number EP/H018913/1 Innovation in Industrial Inkjet Technology (I4T). I found the collaboration with both academic and industrial partners within the I4T project highly motivational and their feedback invaluable. In particular, I would like to thank Neil Morrison, Steve Hoath and Rafa Casterjòn-Pita for many helpful discussions and contributions to my work.

I would also like to thank Christian Clasen and his PhD student Wouter Mathues from the University of Leuven for many inspiring conversations, insight and collaboration of their experimental data.

The School of Mathematics at the University of Leeds has provided years of first-class tutelage, as well as a social and friendly environment to work within. It has been a pleasure to study in the department and I have thoroughly enjoyed my time here. In particular, I would like to thank Laurence Hawke from the polymer group for helpful discussions.

Finally, I would like to thank my family for their love and unremitting support and my friends, who have made life in Leeds a truly amazing and unforgettable experience.

Thank you.

Publications

C. McIlroy and O. G. Harlen *Modelling Capillary Break-up of Particulate Suspensions* Physics of Fluids 26 (2014) 033101.

C. McIlroy, O. G. Harlen and N. F. Morrison *Modelling the jetting of dilute polymer solution in drop-on-demand inkjet printing* Journal of Non-Newtonian Fluid Mechanics 201 (2013) 17-28.

Publications that do not appear explicitly in the thesis are as follows:

S.D. Hoath, D.C.Vadillo, O.G. Harlen, **C. McIlroy**, N.F. Morrison W-K. Hsiao, T.R. Tuladhar S. Jung, G.D. Martin, I.M. Hutchings *Inkjet printing of weakly elastic polymer solutions* Journal of Non-Newtonian Fluid Mechanics 205 (2014) 1-10.

S.D. Hoath, J.R. Castrejon-Pita, W.K. Hsiao, S. Jung, G.D. Martin, I.M. Hutchings, T.R. Tuladhar, D.C. Vadillo, S.A. Butler, M.R. Mackley, **C. McIlroy**, N.F. Morrison, O.G. Harlen, H.N. Yow *Jetting of Complex Fluids* Journal of Imaging Science and Technology 57 (2013) 040403.

Research presented at NIP Conferences in Digital Printing Technology and Digital Fabrication include:

S.D. Hoath, T.R. Tuladhar, D.C. Vadillo, S.A. Butler, M.R. Mackley, **C. McIlroy**, O.G. Harlen, W. Hsiao, I.M. Hutchings *Jetting Complex Fluids containing Pigments and Resins* Proc. IS&T'2 NIP30: 30th Intl. Conf. in Digital Printing Technology and Digital Fabrication (IS&T, Philadelphia, PA, 2014) 30-33

S.D. Hoath, D.C. Vadillo, O.G. Harlen, **C. McIlroy**, N.F. Morrison, W. Hsiao, T.R. Tuladhar, S. Jung, G.D. Martin, I.M. Hutchings *DoD Inkjet Printing of Weakly Elastic Polymer Solutions* Proc. IS&T'2 NIP30: 30th Intl. Conf. in Digital Printing Technology and Digital Fabrication (IS&T, Philadelphia, PA, 2014) 152-156

S.D. Hoath, I.M. Hutchings, O.G. Harlen, **C. McIlroy**, N.F. Morrison *Regimes of Polymer Behaviour in Drop-on-Demand Ink-Jetting* Proc IS&T's NIP28: 28th Intl. Conf. in Digital Printing Technology and Digital Fabrication (IS&T, Spingfield, VA, 2012) 408-411

Abstract

Can inkjet technology revolutionise manufacturing processes as we know them?

By extending the existing benefits of inkjet methods to attain the speed, coverage and material diversity of conventional printing, we can transform inkjet from its present status as a niche technology into a mainstream process, with the UK as a major player. However, we require a better understanding of the science underlying the formation of small droplets and the effect of complex additives.

First, we highlight key inkjetting methods and discuss well-known effects that particles and polymers have on jet evolution. We describe how jetting and filament-thinning experiments can be used to measure key characterisation parameters and how these techniques can be modelled via an established simulation method. Second, we review the literature exploring jet stability and break-up, including the Rayleigh stability analysis and universal self-similar thinning laws.

In Chapter 3, we develop a simple one-dimensional model. First, we model particulate effects on the decay of a liquid bridge and identify three thinning regimes. In particular, we describe a mechanism for acceleration, which agrees quantitatively with experiments. In contrast, the addition of viscoelasticity retards thinning processes and delays break-up. Our viscoelastic jetting model demonstrates the theoretical exponential thinning law, 'beads-on-string' structures and is in quantitative agreement with axisymmetric simulations.

In Chapter 4, we develop a simplified drop-on-demand jetting model to predict the printability of polymer solutions. We demonstrate three known jetting regimes and the predicted 'jettable' concentration threshold is in quantitative agreement with experimental data. Using axisymmetric simulations, we identify a 'pre-stretch' mechanism that is able to fully extend polymers within the nozzle. Consequently, we show that molecules can undergo central scission due to high strain rates at the nozzle exit.

In Chapter 5, we simulate a one-dimensional continuous inkjet using an adaptive mesh technique. We explore non-linear behaviour caused by finite-amplitude modulations in the driving velocity profile, where jet stability deviates from Rayleigh behaviour. We identify a modulation range where pinching becomes 'inverted', occurring upstream of the filament connecting the main drops, rather than downstream. This behaviour can be controlled by the addition of a second harmonic to the initial driving signal. Our results are compared to full axisymmetric simulations in order to incorporate the effects of nozzle geometry.

Contents

Chapter 1

Inkjet Printing Complex Fluids

1.1 Inkjet Technology

'We are at the dawn of a digital age for printing.[1]*'*

Newspapers, books, photographs, the generic desktop printer - the print industry has existed for decades. However, the technology for drop generation and deposition has advanced dramatically over the last forty years [74]. With a combination of physics, chemistry, engineering and of course mathematics, jetting techniques are now more precise and flexible than ever, lending themselves to a diverse range of applications [41], [45].

Using inkjet technology to print conductive tracks is becoming common practice, particularly since nano-sized droplets are now possible [74]. As well as metals [87], we have the ability to print a range of materials, including ceramics [2] and polymers [73]. Advances at microscopic level means that we can print biological material, including DNA and even living cells [125], [115]. Whereas, at large scales, there is potential to build solid structures using 3D printing techniques [89]. Jetting is a new and powerful manufacturing tool; the possibilities seem endless in this new age of inkjet technology.

1.1.1 History and Development of Inkjet Printing

Traditionally, printing is the repeated reproduction of an image or text and German printer Johannes Gutenberg is credited with introducing the printing press to Europe in around 1439. This conventional technique involves transferring ink from a master pattern to a substrate via direct contact and changing the print requires changing the master pattern within the print head. As a relatively slow process with obvious restrictions, printing remained unchanged for hundreds of years.

Compared to traditional printing, inkjet technology implements a completely different principle in which small droplets of liquid are generated and deposited at precise locations on the substrate. The master pattern is controlled digitally and so any number of patterns can be reproduced without adapting the actual print head. The mathematical foundation

---

[1] Hutchings & Graham *et al.* [74]

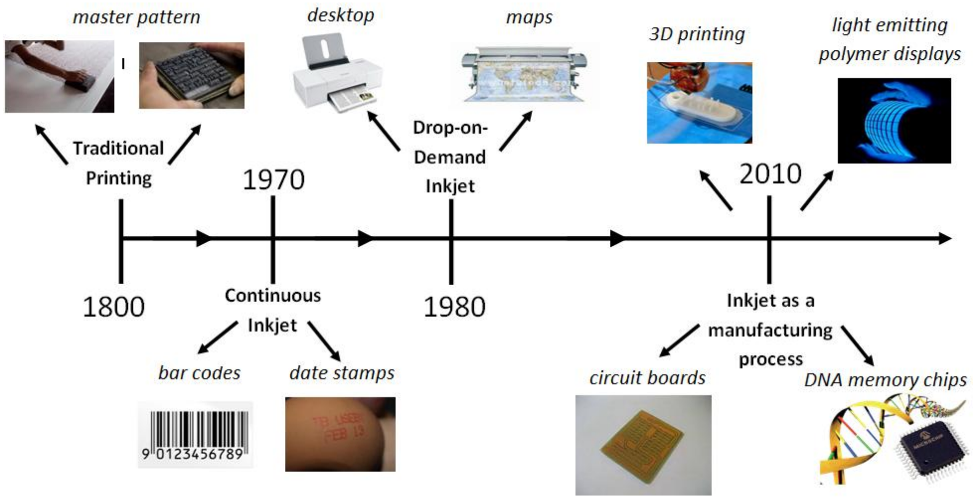

Figure 1.1: Time line illustrating the history and development of inkjet printing.

of this technology is attributed to Plateau and Rayleigh and their work on the stability of liquid jets [107], [109]. Rayleigh deduced that an infinitely long jet is linearly unstable to perturbations whose wavelengths exceeds the circumference of the jet and so will ultimately break up into droplets. Furthermore, Rayleigh identified the wavelength of the fastest growing disturbance and hence the separation distance between droplets.

Still, it took many decades before the applications of the physical properties of drop formation were used in inkjet devices. Inkjet printing as a distinct concept is attributed to Lord William Kelvin. A patent was granted to Lord Kelvin in 1867 for the direction of droplets through electrostatic forces and the device he invented was named the Siphon recorder. However, without the means to generate detailed instructions to steer the droplets, inkjet printing remained unused until the 1950's.

Kelvin's device was a direct forerunner of continuous inkjet (CIJ) technology, which is still used in production lines worldwide, mainly for labelling applications. CIJ provides high-speed printing with low resolution in the final printed text, thus it is ideal for printing dates and bar codes onto products. Although print quality is not a problem for these applications, for more precise printing high resolution is vital. Consequently, in the 1980's drop-on-demand (DoD) technology emerged, providing high-resolution printing at low costs. This new technology soon became readily available to the office and household environment in the form of your everyday desktop printer.

More recently, there has been a new wave of technological advances allowing inkjet printing to be used as a manufacturing process. Inkjets may be used as robotic pipettes to create micro arrays, fabricate three-dimensional structures and print electrical and optical devices. As a highly versatile tool, inkjet technology is ideal for a wide range of applications. For example, the pharmaceutical industry requires the accurate delivery of active ingredients at specific locations for which inkjets are ideal, the electronics industry uses printing techniques to produce conductive tracks and inkjet technology is also being developed for applications in tissue engineering.

In these new application areas the technology for drop generation and deposition remains essentially the same as in graphical printing. Several features of the existing technology are particularly attractive to the manufacturing industry. The digital process allows the location of the deposition to be pre-determined and changed in real time if necessary. Also, storing the master pattern as digital data is comparatively cheap compared to processes requiring a physical template. Since the method is non-contact, fragile materials can be printed that would not withstand conventional printing methods. As well as allowing a range of materials to be printed, the advanced technology is also modular and scalable; multiple print heads can be aligned to print simultaneously or jets may print a number of different materials in succession.

However, there are important limitations to the use of inkjet processes that must be considered, namely resolution, precision and material diversity. The achievable resolution not only depends upon the size of the printed drop after drying, but on the precision at which the drop can be deposited. Precision may be limited by the movement of the print head or the substrate, as well aerodynamic and electrostatic effects on the drop whilst in flight. Currently, drop placement accuracy is approximately several microns and $\sim 10\ \mu$m represents the lower size limit of features that can be printed by a DoD printer [74]. While this is adequate for graphical imaging, some manufacturing applications require higher resolutions. Furthermore, current inkjet printing technology can only be used to print a restricted range of fluids properties based upon established ‘good’ inks. To widen the range of complex materials available to inkjet technology, a systematic study of printability as a function of molecular structure, concentration and solvent characteristics is required.

1.1.2 Mechanisms for Drop Generation

Inkjet printing requires the generation and deposition of small ink drops onto a substrate. Many techniques for producing droplets have been devised, however continuous ink jetting (CIJ) and drop-on-demand (DoD) jetting remain the two most important technologies in the inkjet industry. The essential difference between the two methods is the nature of the flow through the nozzle.

In CIJ printing, as the name suggests, a continuous jet of liquid is ejected from a large reservoir through the nozzle orifice. The jet subsequently breaks up into droplets via the Rayleigh-Plateau instability of a liquid column. To control the break-up, the jet is modulated by imposing a pressure fluctuation on the nozzle close to the Rayleigh frequency to ensure that the size and spacing of every drop is uniform. Drop diameters are typically slightly larger than the nozzle diameter.

The droplets must then be directed and deposited on the substrate using electrostatic deflection. Selected droplets are charged as they pass through a set of charging electrodes. The stream of droplets then pass through a strong electric field generated by a deflector plate, which deflect selected droplets towards the substrate. All uncharged, and hence

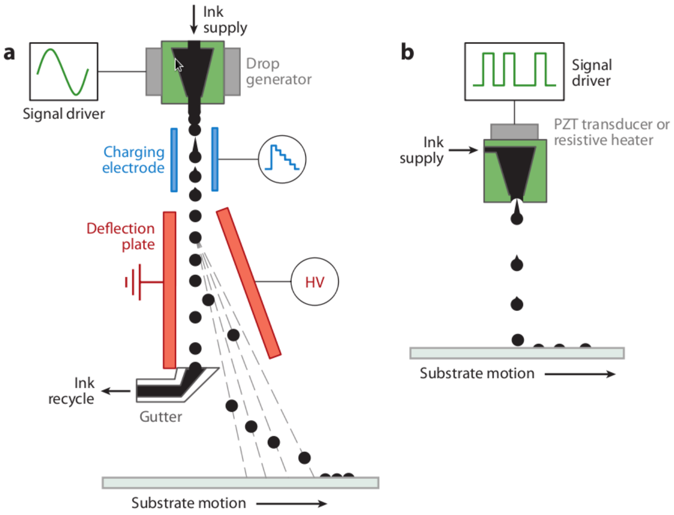

Figure 1.2: *(Left:)* The continuous inkjet; *(Right:)* The DoD inkjet. Diagram taken from Basaran's review paper [8].

undeflected droplets, collect in a gutter where they are then recycled and reused in the jetting process. This commonly used CIJ practice is known as the Sweet method [123] and allows an image of around 10 pixels in height in a single pass. An alternative method is to deflect the charged drops into the gutter and thus print with the uncharged drops. This provides higher accuracy but each nozzle can only print a single line with each pass.

In CIJ systems, drops are produced continuously and so key benefits include high-speed printing that keeps up with even the fastest production environments, as well as non-contact printing, which enables printing on virtually any surface. On the other hand, DoD printers produce droplets as and when required. Since DoD printing does not require a drop selection process, the nozzle can be located closer to the substrate, which increases precision in comparison to CIJ.

An industrial DoD print head consists of multiple nozzles, with each nozzle contributing to one line of printed drops that make up the complete image. Individual ink drops are ejected through a nozzle in response to a pressure pulse. The two most common actuation mechanisms used to generate this pressure pulse are thermal and piezoelectric actuation. In thermal DoD printing, a small film of fluid is heated so that it boils creating a small vapour bubble in the fluid reservoir. The bubble quickly expands creating the energy required to force a droplet through the nozzle. Alternatively, in piezoelectric DoD printing, the actuator is formed from a piezoelectric material that changes shape in response to an electric current creating a pressure pulse via direct mechanical actuation.

The shape of a single drop upon exit is that of a nearly spherical bead with a trailing ligament [91], [47]. The trailing ligament may either retract into the main drop or break up into a number of satellite drops. These smaller satellite drops are affected by aerodynamic drag and so do not precisely follow the pattern of the main drop. Thus, if these satellite drops are present at impact, then they can cause splash on the substrate and hence reduce print quality.

Usually the size of the main drop ejected in DoD printing is equivalent to the nozzle diameter. However, new experimental techniques have been developed to decrease the droplet radius in comparison to the nozzle size [29]. The use of a fixed drop size means that there is always a compromise between high performance and image quality to achieve production speed. Grey-scale technology, on the other hand, uses multiple pulses to provide drops of different sizes; small drops for high resolution images or text and large drops to cover large areas quickly.

While inkjet technology is highly flexible, it is currently slow compared with direct printing. If inkjet technology can be extended to attain the speed and coverage of conventional methods, then inkjet printing could revolutionise manufacturing processes. To achieve this transformation, we require a much better understanding of the science underlying the formation and behaviour of small liquid drops in both CIJ and DoD jetting techniques, particularly for more complex fluids.

1.1.3 Fluid Properties of Standard Inks

There are three significant fluid properties that dominate jet break-up and drop generation in inkjet printing of standard inks, that is, surface tension, viscosity and inertia. The cohesive forces in a liquid are responsible for the phenomenon known as surface tension and cause a liquid to form the shape with the lowest surface energy. This phenomenon is crucial to the process of inkjet printing; initially, fluid ejected though a nozzle is cylindrical in shape, however, surface tension drives the jet to neck inwards and ultimately break up into spherical drops that can be used for printing. This mechanism is know as the Rayleigh-Plateau or ‘capillary’ instability.

In contrast, the forces which resist the contraction of a liquid jet into droplets have two origins; the inertia of the liquid and its viscosity. Inertial forces are those associated with a body’s resistance to change in its state of motion or rest. In a liquid jet, this change in momentum is proportional to the density of the fluid times the rate of change of velocity.

Viscous forces arise from interactions between the molecules in the fluid. In particular, the viscosity is a measure of a fluid’s resistance to a gradual deformation of the fluid, for example in shear or extension. If the viscosity is independent of the deformation rate, then the fluid is classed as linear or Newtonian. But, even for these simple fluids, the measured viscosity varies depending on the type of deformation applied. For example, for Newtonian fluids, the extensional viscosity is three times that of the viscosity measured in simple shear flow. This key parameter is known as the Trouton ratio. On the other hand, for non-Newtonian fluids the stress-strain relationship is non-linear such that viscosity is a function of the deformation rate and the Trouton ratio grows much larger than three, particularly for polymeric fluids.

Standard inks commonly demonstrate shear-thinning properties, where a deformation reduces the local viscosity. This property can be beneficial to inkjetting; due to high shear

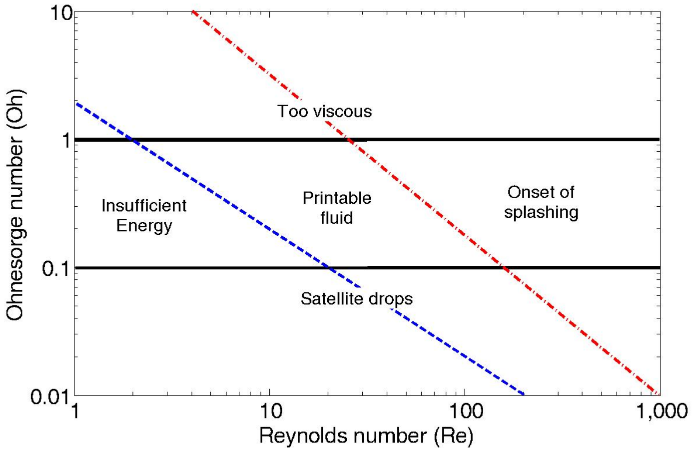

Figure 1.3: Phase diagram showing the range of stable DoD printing in terms of the Ohnesorge number and the Reynolds number taken from [74]

rates at the nozzle exit, the fluid viscosity is reduced allowing higher concentrations to be ejected. However, during flight the viscosity is recovered so that there is sufficient resistance for the trailing ligament retract and merge with the main drop. Thus, for Newtonian inks, the formation of unwanted satellite drops may be prohibited with the addition of shear-thinning additives.

The behaviour of liquid drops can be characterised by a number of dimensionless groupings of these fluid properties. The importance of surface tension γ, viscosity μ and inertia may be described using the Reynolds number and the Weber number. The Reynolds number describes the ratio between inertial and viscous forces in a jet and is defined as

$$Re = \frac{\rho L U}{\mu},$$

for fluid density ρ. The characteristic length L is often defined by the jet radius and U denotes the characteristic velocity. On the other hand, the Weber number represents the ratio between inertia and surface tension and is defined as

$$We = \frac{\rho L U^2}{\gamma}.$$

Drop formation is usually characterised by the Ohnesorge number,

$$Oh = \frac{\sqrt{We}}{Re} = \frac{\mu}{\sqrt{\rho \gamma L}},$$

which represents the ratio between viscosity and surface tension in the absence of a velocity scale.

It is useful to construct phase diagrams in order to determine the printability of a particular fluid; mapping out the parameter space demonstrates not only optimal fluid properties for drop generation, but also conditions to avoid. For Newtonian fluids, stable drop generation without satellites for DoD printing is limited to a narrow range of viscosities corresponding roughly to the Ohnesorge numbers in the range $0.1 < Oh < 1$ [45], [94].

If the Ohnesorge number is too high, then viscous forces prevent break off of the ligament from the nozzle. On the other hand, if the Ohnesorge number is too low, then surface tension causes the trailing ligament to break up into a number of unwanted satellites. Figure 1.3 shows that optimal printability in DoD printing depends on a combination of physical properties that depend on the nozzle size and velocity.

1.1.4 Jetting Complex Fluids

For many applications in materials science, the fluids to be printed are non-Newtonian. The rheology of particulate suspensions and polymer solutions, for example, is highly non-linear and simple rules such as those defined in Figure 1.3 do not apply.

Most graphical inks contain solid pigment particles rather than dyes and in many non-graphical applications, such as printed electronics, the functional components of the ink are solid particles. Solid-laden inks are also required in ceramic manufacture and textile printing. The existence of small particles in the ink can disturb the usual jetting process. However, there is relatively little known about particulate effects on the stability and break-up of liquid jets compared to Newtonian fluids or even other complex fluids such as polymer solutions.

It is known that the presence of particles in a solvent increases the bulk viscosity of a fluid [83]. Thus, particles are expected to retard the thinning process and consequently delay the time to break-up. However, experimental measurements using the pendant-drop technique [15], [60], [61] suggest that once the filament has thinned to approximately five particle diameters, the thinning no longer follows the behaviour predicted by the bulk viscosity. In fact, the thinning is 'accelerated' due to the effects of finite particle size. Even for small volume fractions $< 6\%$, van Deen *et al.* [133] show that even the presence of a single particle in the thinning filament modifies the detachment dynamics, again accelerating the thinning rate. Furthermore, the thinning dynamics of particulate fluids are found to be less predictable than those of continuous fluids.

A mathematical model [65] has also been developed to study the dynamics of filament evolution towards break-up in the presence of an embedded, solid, spherical particle. A

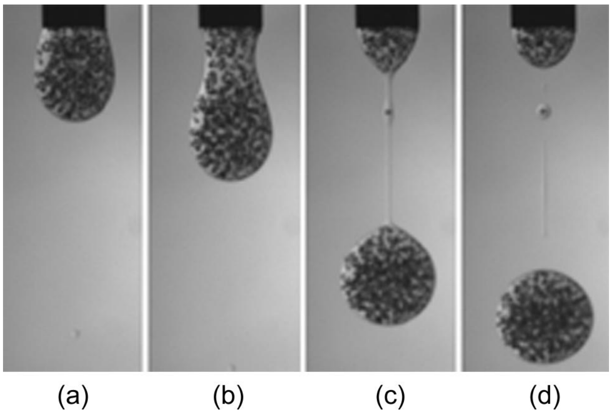

Figure 1.4: Furbank & Morris [60] pendant drop experiments of particulate suspensions.

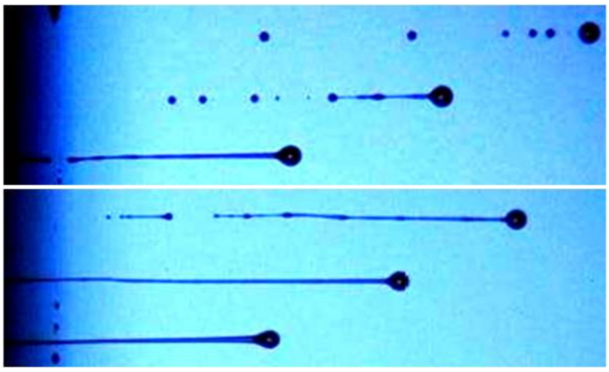

Figure 1.5: Hoath's images [132] of DoD jetting. *(Top:)* Newtonian fluid; *(Bottom:)* polymeric fluid.

single particle is modelled as a 'stresslet' and assumed to remain stationary at the jet midpoint. Initially the jet evolves much like a pure liquid jet, until stretching-induced stresslet flow begins to alter the dynamics. The particle-induced flow causes a strong local deformation of the free surface and their results demonstrate the formation of a liquid bulge around the particle, with the point of pinch off shifting from the centre to accommodate the particle. Their results explain the observations in experiments [60] that if a large enough number of particles become trapped in the filament region during the thinning process, then thinning is resisted rather than accelerated. However, this model does not explain the accelerated dynamics that is generally observed in experiments of particulate suspensions.

Alternatively, inks may exhibit viscoelastic properties, due to the presence of polymer molecules, for example. Polymers are long-chain macromolecules, which on average are randomly coiled like a scrunched up piece of string. However, when subjected to a flow the chains begin to unravel and are stretched out. Thermal fluctuations resist this action and try to restore the polymer to its equilibrium state. This gives the fluid an elasticity that enables polymeric fluids to be drawn out into extremely long thin filaments, which can have a significant effect on the jetting behaviour.

Figure 1.5 shows that the addition of polymer molecules can significantly affect the break-up of liquid filaments generated by flow through a DoD nozzle [9], [41], [43], [66], [120]. In particular, the addition of small amounts of high-molecular-weight polymer can inhibit the formation of unwanted satellite drops so that the ligament retracts into the main drop. On the other hand, polymer content affects the reliability of jetting; print speed may be compromised and, at high concentrations, the main drop may even fail to detach from the nozzle. Thus, there exists a critical polymer concentration threshold at which printing at the desired speed is possible, within the limit of the print head drive [71].

A fluid is formally defined to be viscoelastic if the rheological behaviour is dominated by an intrinsic timescale. In the case of polymeric fluids, this is the time taken for a polymer to return to its equilibrium state after a deformation, namely the relaxation time. In practice, inkjet inks often exhibit some degree of viscoelasticity over the timescales of jetting.

1.2 Theory of Polymeric Fluids

1.2.1 Modelling Polymer Molecules

Usually, small particles dissolved in a solvent diffuse through a liquid due to fluctuations of random collisions of particles. The mean-square displacement of a particle over time t in three-dimensional space is given simply by

$$< |\mathbf{r}(t) - \mathbf{r}(0)|^2 >= 6Dt,$$

where D is the diffusion coefficient that describes simple diffusive motion. If a constant force $\mathbf{F}$ is applied to a small isotropic particle suspended in a Newtonian fluid, then the particle will achieve a constant velocity $\mathbf{v}$ in the same direction as the applied force so that

$$\mathbf{F} = \xi \mathbf{v},$$

where ξ is the coefficient of friction. For a spherical particle of radius a moving through a Newtonian liquid of viscosity μ_s, the friction coefficient is found to be

$$\xi = 6\pi\mu_s a,$$

from the full Stokes-flow calculation of flow past an isolated sphere and is related to the friction coefficient ξ via the Einstein relation

$$D = \frac{k_B T}{\xi},$$

where k_B is the Boltzman constant and T is the absolute temperature.

Polymers, on the other hand, are very large molecules that do not move in simple diffusive motion. They are composed from a long chain or network of repeating units called monomers, which are typically joined by covalent bonds between the carbon atoms that make up the backbone of the polymer. The way in which these monomers are arranged, the polymer microstructure, significantly influences the material properties of the fluid and results in non-Newtonian phenomena.

Since the structure is highly flexible, polymer chains can exist in a large number of configurations. The carbon atoms are able to rotate about the covalent bonds in such a way that the orientation of a particular monomer is uncorrelated with others. Due to this rotational freedom, a polymer chain is modelled as a random walk of freely-jointed sections. Furthermore, the polymer shape is constantly changing as a result of random thermal fluctuations; if a polymer is stretched, then it will recoil due to the constant motion of the atoms in the chain. Since the configuration of the microstructure carries information about the flow history, polymers are said to have a deformation memory, which is represented by a relaxation time.

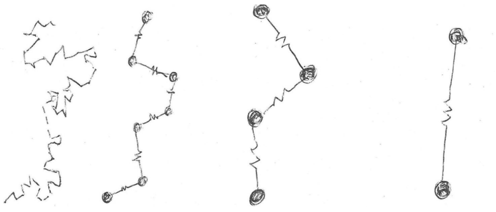

Figure 1.6: A sketch showing how a polymer chain can be modelled by a number of beads connected my springs.

In order to characterise the effect of a flow on the shape of a polymer chain, we require a model that changes its physical configuration in response to a deformation. A spring serves as the simplest form of a deformable object and captures the entropic tendency of a polymer chain to return to a relaxed random state after a deformation is applied. Consequently, a polymer chain is usually represented by a set of particles, or beads, connected by a number of springs. An illustration of these beads-springs models is shown in Figure 1.6.

Let $\mathbf{r}_0, \ldots, \mathbf{r}_N$ denote the position of $N+1$ beads connected by frictionless springs of length b. Therefore, we have N bond vectors given by

$$\mathbf{R}_i = \mathbf{r}_i - \mathbf{r}_{i-1}, \quad i = 1, \ldots, N,$$

with the end-to-end vector of the entire polymer chain

$$\mathbf{R} = \mathbf{r}_N - \mathbf{r}_0 = \sum_{i=1}^{N} \mathbf{R}_i.$$

If this end-to-end vector is measured for a large number of polymers suspended in a melt, then the distribution of the end-to-end vectors is always Gaussian, irrespective of the chemical properties of the polymer, and the root-mean-squared end-to-end distance scales with the number of bonds such that

$$< |\mathbf{R}|^2 > \propto Nb^2.$$

This is a consequence of the central limit theorem, which states that, provided the number of segments N is large enough, the end-to-end vector distribution will be Gaussianly distributed and the local structure of the polymer appears only through the statistical segment length b. Thus, a polymer molecule is represented by a Gaussian chain consisting of a collection of beads connected by harmonic springs of strength

$$k = \frac{3k_BT}{b^2}.$$

This spring constant captures the entropic restoring forces of the chain as a whole and is the origin of elastic behaviour.

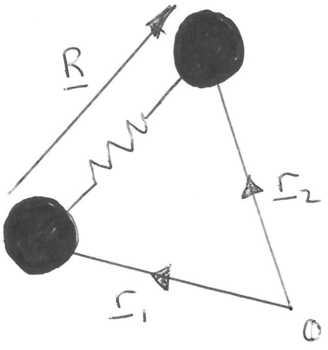

Figure 1.7: The dumbbell model for polymer molecules.

1.2.2 A Dumbbell Approximation

The simplest beads-springs model is known as the linear dumbbell model. For this simple approximation, the chain is represented by two beads connected by a single frictionless spring, as shown in Figure 1.7. In this way, the friction is concentrated at either end of the polymer chain. Let $\mathbf{r}_1$ and $\mathbf{r}_2$ denote the positions of the two beads so that the end-to-end distance $\mathbf{R} = \mathbf{r}_2 - \mathbf{r}_1$ is represented by the spring displacement. As long as the elongation remains smaller than the the maximum length of the chain, then the chain can be modelled by an elastic spring with spring constant

$$k = \frac{3k_BT}{R_g^2},$$

where R_g denotes the chain length at equilibrium. Thus, in this model the dumbbells are assumed to be infinitely extensible.

In total, there are three forces acting on each bead; the spring force, a frictional force and random thermal motion. The frictional force acting on each bead is proportional to the difference between the bead's velocity $d\mathbf{r}_i/dt$ and the fluid velocity at the bead $\mathbf{u}(\mathbf{r}_i)$. The thermal force, denoted $\mathbf{f}_i$, originates from individual collisions of separate polymer molecules. By equating these forces we can derive an equation of motion for the spring displacement $\mathbf{R}$.

For each bead, we have the equations

$$\xi\left(\frac{d\mathbf{r}_1}{dt} - \mathbf{u}(\mathbf{r}_1)\right) = k(\mathbf{r}_2 - \mathbf{r}_1) + \mathbf{f}_1,$$
$$\xi\left(\frac{d\mathbf{r}_2}{dt} - \mathbf{u}(\mathbf{r}_2)\right) = k(\mathbf{r}_1 - \mathbf{r}_2) + \mathbf{f}_2,$$

where ξ denotes the friction coefficient. Subtracting gives a differential equation for the end-to-end vector $\mathbf{R}$:

$$\xi\left(\frac{d\mathbf{R}}{dt} - \mathbf{u}(\mathbf{r}_2) + \mathbf{u}(\mathbf{r}_1)\right) = -2k\mathbf{R} + \mathbf{f},$$

where $\mathbf{f} = \mathbf{f}_2 - \mathbf{f}_1$

Since the length of the dumbbell is assumed to be much smaller than the length scale over which the fluid varies, the fluid velocity at the second bead can be expanded as a

Taylor series about the fluid velocity at the first. Thus, using index notation,

$$u_i(\mathbf{r}_2) = u_i(\mathbf{r}_1) + \frac{\partial u_i}{\partial x_j}|_{\mathbf{r}_1}(r_{2j} - r_{1j}) + \cdots .$$

The differential equation for the end-to-end vector $\mathbf{R}$ then becomes

$$\frac{d\mathbf{R}}{dt} - \mathbf{K} \cdot \mathbf{R} = -\frac{2k}{\xi}\mathbf{R} + \frac{\mathbf{f}}{\xi}, \tag{1.1}$$

where $\mathbf{K}$ is the velocity-gradient tensor defined as $K_{ij} = \frac{\partial u_i}{\partial x_j}$. Converting to index notation and multiplying equation (1.1) by R_j gives

$$R_j \frac{dR_i}{dt} - K_{ik} R_k R_j = -\frac{2k}{\xi} R_i R_j + \frac{f_i}{\xi} R_j. \tag{1.2}$$

The indices can be interchanged to give a second equation, which added to equation (1.2) and taking the ensemble average $< \cdots >$ yields

$$\begin{aligned} \frac{d}{dt} < R_i R_j > -K_{ik} < R_k R_j > - < R_i R_k > K_{jk} = \\ -\frac{4k}{\xi} < R_i R_j > + \frac{1}{\xi} < f_i R_j + f_j R_i > . \end{aligned} \tag{1.3}$$

In order to determine the last term, we employ the Ito-Stratonovich relationship from statistical mechanics [100] that is

$$< f_i R_i > = 2 k_B T \delta_{ij},$$

so that the evolution equation for the end-to-end vector becomes

$$\frac{d}{dt} < \mathbf{RR} > - \mathbf{K} \cdot < \mathbf{RR} > - < \mathbf{RR} > \cdot \mathbf{K}^T = -\frac{4k}{\xi} < \mathbf{RR} > + \frac{4 k_B T}{\xi}\mathbf{I},$$

where $\mathbf{I}$ denotes the unit tensor given by the Kronecker delta $I_{ij} = \delta_{ij}$.

At equilibrium, the steady-state solution determines the average

$$< \mathbf{RR} > = \frac{k_B T}{k}\mathbf{I} = \frac{R_g^2}{3}\mathbf{I}.$$

Hence, introducing the following structure tensor and relaxation time

$$\mathbf{A} = \frac{3}{R_g^2} < \mathbf{RR} > \quad \text{and} \quad \tau = \frac{\xi}{4k},$$

respectively, yields the evolution equation

$$\frac{d\mathbf{A}}{dt} = \mathbf{K} \cdot \mathbf{A} + \mathbf{A} \cdot \mathbf{K}^T - \frac{1}{\tau}(\mathbf{A} - \mathbf{I}).$$

This linear-dumbbell equation, also known as the Oldroyd-B model, describes the evolution of a polymer molecule provided that the chains are considered infinitely extensible.

The additional stress in a suspension due to the presence of these dumbbells is given by

$$\boldsymbol{\sigma}^P = \mathbb{C} k < \mathbf{RR} >,$$

where $\mathbb{C}$ is the number of chains per unit volume. By substituting for the spring constant and rescaling via the structure tensor $\mathbf{A}$ the polymer stress becomes

$$\boldsymbol{\sigma}^P = \mathbb{C} k_B T \mathbf{A} = G\mathbf{A},$$

where $G = \mathbb{C} k_B T$ is called the elastic modulus. Then, the total stress $\boldsymbol{\tau}$ is given by a combination of an isotropic term, the Newtonian stress and the additional polymer stress so that

$$\boldsymbol{\tau} = \beta\mathbf{I} + \mu_s(\mathbf{K} + \mathbf{K}^T) + G\mathbf{A},$$

where μ_s is the solvent viscosity. However, it is often useful to write the constitutive equation neglecting the isotropic term, such that $\boldsymbol{\tau} = \boldsymbol{\sigma} - p\mathbf{I}$, where $p = -(\beta + G)$ is the pressure. Then, the extra stress tensor $\boldsymbol{\sigma}$ is simply a combination of the Newtonian and polymeric stress, defined as

$$\boldsymbol{\sigma} = 2\mu_s \mathbf{E} + G(\mathbf{A} - \mathbf{I}),$$

where $\mathbf{E} = \frac{1}{2}(\mathbf{K} + \mathbf{K}^T)$ is the strain-rate tensor.

Strictly, the Oldroyd model is only applicable to configurations where the entropic spring force is linear. An alternative, more realistic constitutive model for describing dilute polymer solutions in extensional flow is the finitely extensible non-linear elastic (FENE) dumbbell model, which takes into account changes to the spring law as the end-to-end distance approaches the maximum length of the chain. The spring law is replaced by $kf(\mathbf{R})\mathbf{R}$ where $f(\mathbf{R})$ is a non-linear function called the FENE factor. However, when this term is incorporated into the bead equation (1.1) the resulting second moment equation (1.3) cannot be closed. Thus, this full FENE model involves a full solution of the probability density function, which requires a huge amount of computation time, even for simple flows. A simplified version, which employs the Chillcott-Rallison closure approximation [31], is known as the FENE-CR model and is defined as follows.

The FENE-CR constitutive equation is given by

$$\boldsymbol{\sigma} = 2\mu_s \mathbf{E} + Gf(\mathbf{A} - \mathbf{I}),$$

with the FENE factor f is defined as

$$f = \frac{L^2}{L^2 + 3 - \mathrm{tr}(\mathbf{A})},$$

where $\mathrm{tr}(\mathbf{A}) = A_{zz} + 2A_{rr}$ and the finite extensibility L represents a ratio of the length of a fully extended dumbbell to its equilibrium length. The conformation tensor $\mathbf{A}$ then satisfies

$$\frac{d\mathbf{A}}{dt} = \mathbf{K} \cdot \mathbf{A} + \mathbf{A} \cdot \mathbf{K}^T - \frac{f}{\tau}(\mathbf{A} - \mathbf{I}),$$

which is referred to as the FENE dumbbell equation.

An alternative model is the FENE-P model where the exact spring force for each dumbbell is replaced with an ensemble average. The net effect is that the term $-f(\mathbf{A}-\mathbf{I})/\tau$ is replaced by $-(f\mathbf{A} - \mathbf{I})/\tau$. In simple steady shear this gives a shear-thinning viscosity, as does the exact FENE equations, whereas the FENE-CR model gives a constant shear viscosity. However, in extensional flows the behaviour of the two approximations is similar.

1.2.3 General Beads-Springs Models

Although the dumbbell approximation can qualitatively predict the behaviour of polymers in solution, it provides a crude representation of the molecules, with a single mode of relaxation. A more accurate representation is to sub-divide the chain into a number of beads and springs, to distribute the friction throughout the chain.

Let $\mathbf{r}_0, \ldots, \mathbf{r}_N$ denote the position of $N+1$ beads connected by frictionless springs of length b. Assuming a Gaussian distribution, the equilibrium chain length scales like

$$R_g^2 \propto Nb^2.$$

In the absence of external forces, each bead moves randomly under Brownian motion and the general equation of motion can be derived from Langevin dynamics [46] to be

$$\frac{\partial \mathbf{r}_i}{\partial t} = \frac{1}{2} k_B T \sum_j \frac{\partial}{\partial \mathbf{r}_j} \cdot \mathbf{H}_{ij} + \sum_j \mathbf{H}_{ij} \cdot \left(-\frac{\partial U}{\partial \mathbf{r}_j} + \mathbf{f}_j \right). \tag{1.4}$$

Here U is the interaction potential given by

$$U = \frac{k}{2} \sum_{n=i}^{N} (\mathbf{r}_i - \mathbf{r}_{i-1})^2, \tag{1.5}$$

for spring force k, $\mathbf{f}_j$ is a stochastic variable representing random thermal forces and $\mathbf{H}_{ij}$ denotes a mobility matrix.

Let $\mathbf{F}_0, \ldots, \mathbf{F}_N$ be the forces acting on the respective beads that arise from the forces in the springs. Since spherical beads are independent of orientation, angular velocity is neglected and the velocity of each bead is given by

$$\mathbf{v}_i = \sum_j \mathbf{H}_{ij} \cdot \mathbf{F}_j.$$

If the velocity of the bead is determined only by the force acting on it, then the mobility matrix reduces simply to

$$\mathbf{H}_{ij} = \frac{\mathbf{I}}{\xi}. \tag{1.6}$$

That is, the mobility of the bead is affected only by the friction coefficient ξ. This is sometimes referred to as the Rouse approximation, which we consider in section 1.2.4.

However, in a fluid the velocity of a single bead also depends on the forces acting on surrounding beads; forces acting on one bead cause fluid motion and therefore affect the velocity of beads nearby. When these bead-bead interactions are included, the off-diagonal elements of the mobility matrix become non-zero and can be derived as follows [46].

In the absence of inertia, Stokes equation of motion for a fluid having velocity $\mathbf{u}$ and viscosity μ_s is

$$\mu_s \nabla^2 \mathbf{u} + \nabla p = \nabla \cdot \boldsymbol{\sigma},$$

where p denotes pressure and $\boldsymbol{\sigma}$ is the stress tensor that determines the external forces acting on a unit volume of fluid. To calculate the flow field $\mathbf{u}$ created by the external forces, the beads are assumed to be points so that the external forces are approximated as

$$\nabla \cdot \boldsymbol{\sigma} = -\sum_i \mathbf{F}_i \delta(\mathbf{r} - \mathbf{r}_i),$$

for some position $\mathbf{r}$ in the fluid. Thus, the momentum equation can be solved via Fourier transform, together with the incompressible condition $\nabla \cdot \mathbf{u} = 0$, to yield

$$\mathbf{u} = \sum_i \mathbf{H}(\mathbf{r} - \mathbf{r}_i) \cdot \mathbf{F}_i.$$

Here $\mathbf{H}$ is the Oseen tensor given by

$$\mathbf{H} = \frac{1}{8\pi\mu_s \mathbf{r}}(\mathbf{I} - \hat{\mathbf{r}}\hat{\mathbf{r}}),$$

where $\hat{\mathbf{r}}$ is the unit vector parallel to $\mathbf{r}$. Since the beads move at the same velocity as the fluid,

$$\mathbf{v}_i = \sum_j \mathbf{H}(\mathbf{r}_i - \mathbf{r}_j) \cdot \mathbf{F}_j,$$

and so the mobility tensor is given by

$$\mathbf{H}_{ij} = \begin{cases} \mathbf{H}(\mathbf{r}_i - \mathbf{r}_j), & \text{if } i \neq j, \\ \frac{\mathbf{I}}{\xi}, & \text{if } i = j. \end{cases} \tag{1.7}$$

The approximation given here for $i = j$ is commonly adopted in the theory of polymers, otherwise $\mathbf{H}_{ii} = \mathbf{H}(0)$ and the mobility tensor would become infinite. This failure arises from approximating that the beads are points.

As we have seen, this mobility matrix accounts for hydrodynamic interactions between individual beads. However, there are two more important interactions that can be incorporated into the interaction potential U. First, there is the hydrodynamic interaction between the beads and nearby solvent molecules, which causes the polymer chain to contract in a poor solvent. Second, there is an excluded volume effect that accounts for the finite volume of each chain segment; since segments of the chain cannot overlap, repulsive force cause the polymer to swell. Bead-solvent interactions and the excluded volume effect change the statistical properties of the chain so that the chain no longer has a Gaussian distribution. Thus, the equilibrium length R_g^2 is no longer proportional to Nb^2. Hydrodynamic interactions and the excluded volume effect are included in the Zimm model, which we discuss in section 1.2.5.

1.2.4 The Rouse Model for Relaxation Time

First we consider the Rouse model, which assumes an ideal chain with Gaussian distribution $R_g^2 \propto Nb^2$. The mobility matrix is given by equation (1.6), so that bead-bead interactions are neglected, and the interaction potential is given by equation (1.5), so that polymer-solvent interactions and the excluded volume effect are ignored. Thus, the Rouse model is ideal for modelling polymer melts, where hydrodynamic interactions are unimportant. Ultimately the Rouse model produces an equivalent bead-evolution equation as the dumbbell approximation. However, multiple modes are introduced to represent the relaxation times of each individual spring.

The time scale on which an individual bead diffuses distance b is determined from the diffusion coefficient to be

$$\tau_0 = \frac{b^2}{D} = \frac{\xi b^2}{k_B T},$$

where ξ is the bead friction coefficient. This is known as the Kuhn monomer relaxation time. Then, the total friction of the entire Rouse chain is found by summing the contributions from each of the N beads so that

$$\xi_R = N\xi.$$

Thus, the diffusion coefficient of the entire Rouse chain is obtained from the Einstein relation to be

$$D_R = \frac{k_B T}{N\xi}.$$

Over a characteristic time scale τ_R, a polymer chain will diffuse a distance the order of its size R_g^2 giving the Rouse time

$$\tau_R \approx \frac{Nb^2}{D_R} = \frac{\xi N^2 b^2}{k_B T},$$

or alternatively $\tau_R = \tau_0 N^2$.

This Rouse time has a special significance. On time scales less than the monomer relaxation time τ_0 the polymer will not move and exhibits an elastic response. For time scales longer than the Rouse time τ_R, the chain will simply diffuse through the solvent and the fluid behaviour is Newtonian. In the intermediate time scale $\tau_0 < t < \tau_R$, the chain demonstrates viscoelastic modes.

To derive the evolution equation for multiple modes, consider the Langevin equation (1.4) for the bead motion, which for the Rouse model reduces to

$$\xi \left(\frac{\partial \mathbf{r}_i}{\partial t} - \mathbf{u}(\mathbf{r}_i) \right) = k \frac{\partial^2 \mathbf{r}_i}{\partial i^2} + \mathbf{f}_i, \tag{1.8}$$

in the continuous limit. To derive the relaxation time, we ignore the thermal noise $\mathbf{f}_i$ and, treating relaxation in the absence of flow, we solve the simplified equation

$$\xi \frac{\partial \mathbf{r}_i}{\partial t} = k \frac{\partial^2 \mathbf{r}_i}{\partial i^2}, \tag{1.9}$$

with boundary conditions

$$\frac{\partial \mathbf{r}_0}{\partial t} = 0 \quad \text{and} \quad \frac{\partial \mathbf{r}_N}{\partial t} = 0.$$

We try specific solutions of the form

$$\mathbf{r}_i = \mathbf{X} \cos(Ai + B), \quad i = 0, \ldots, N$$

for constants A and B. The normal modes of the operator $\frac{\partial^2}{\partial i^2}$ are the sinusoidal functions. Considering the boundary conditions at the end beads, cosine modes are chosen for consistency and independent solutions are found from calculating constants A and B. Consequently, $\mathbf{r}_i$ can be represented as a sum of normal modes of the form

$$\mathbf{r}_i = \mathbf{X}_0 + 2 \sum_p \mathbf{X}_p \cos\left(\frac{p\pi i}{N} \right), \tag{1.10}$$

for integer p. The factor 2 in front of the summation is for reasons of convenience. The zero mode $\mathbf{X}_0$ gives the diffusion of the centre of mass and, since this does not contribute to the stress, it may be neglected. Taking $p = 1$ represents the stretching of the entire chain and therefore gives the longest relaxation time, or Rouse time τ_R. Modes such that $p > 1$ represents other changes to the configuration with shorter relaxation times.

Substituting this solution (1.10) into equation (1.9) for bead motion yields

$$\frac{\partial \mathbf{X}_p}{\partial t} = -\frac{\pi^2 k p^2}{\xi N^2}\mathbf{X}_p, \quad p = 1, \dots, N,$$

which has the relaxation time

$$2\tau_p = \frac{\xi N^2}{\pi^2 k p^2}, \quad p = 1, \dots, N.$$

Thus, substituting for the spring constant, the spectrum of Rouse relaxation times is given by

$$\tau_p = \frac{\xi N^2 b^2}{6\pi^2 k_B T p^2} = \frac{\tau_R}{p^2}, \quad p = 1, \dots, N.$$

Notice that the relaxation time derived in the dumbbell model $\tau = \xi/4k$ has the same form as the longest Rouse time τ_R but differs by a numerical factor of $\pi^2/4 \approx 2.5$. Both models predict that the longest relaxation time increases as N^2 so that for the same chemistry, the relaxation time should increase with the square of the molecular mass of the polymer.

Each normal mode has a different relaxation time but contributes the same to the elastic modulus. Thus, the additional polymer stress is simply

$$\boldsymbol{\sigma}^P = G\sum_{p=1}^{N}\mathbf{A}_p, \quad p = 1, \dots, N,$$

and the equivalent evolution equation is derived from the full dynamical equation (1.8) to be

$$\frac{d\mathbf{A}_p}{dt} = \mathbf{K}\cdot\mathbf{A}_p + \mathbf{A}_p\cdot\mathbf{K}^T - \frac{1}{\tau_p}(\mathbf{A}_p - \mathbf{I}), \quad p = 1, \dots, N,$$

which has a relaxation time for each mode.

This modal spectrum for relaxation times was first derived by Paul Rouse in 1953. Although an improvement on the dumbbell approximation, important physics remain to be considered. In particular, inkjet printing of polymer solutions is restricted to dilute solutions, where hydrodynamic interactions are significant. Hydrodynamic interactions were first treated by Zimm in 1956. For this level of molecular detail, the off-diagonal entries of the mobility matrix $\mathbf{H}_{ij}$ are non-zero to account for bead-bead interactions and the interaction potential U is adapted to include solvent effects and interactions between segments of the chain.

1.2.5 The Zimm Model for Dilute Solutions

A dilute solution is defined to be a solution of sufficiently low concentration such that the polymers are separated enough from each other that polymer-polymer interactions are negligible. As the weight-fraction concentration ϕ increases, the polymer coils become closer together and begin to overlap each other. The critical concentration at which this occurs is called the overlap concentration ϕ^*. For $\phi/\phi^* < O(1)$, the frictional interactions between neighbouring polymer molecules are considered negligible and the rheological response of the fluid is determined solely by the deformation of the polymer coupled with the hydrodynamic interactions.

In the Zimm model, the polymer is again represented by $N+1$ beads connected by springs of length b. However, the friction is not distributed throughout the beads like in the Rouse model; alternatively, the resistance is a function of the solvent viscosity μ_s acting on the whole chain. For an ideal Gaussian chain with equilibrium length $R_g^2 \propto Nb^2$, the friction coefficient is predicted by Stokes' law to be

$$\xi_Z = 6\pi\mu_s R_g,$$

where the prefactor 6π is usually neglected. Thus, from the Einstein relation, the diffusion coefficient for the Zimm model is

$$D_Z = \frac{k_B T}{\xi_Z} = \frac{k_B T}{\mu_s \sqrt{N} b}.$$

The polymer molecule will diffuse like a particle with a volume proportional to the pervaded volume of the chain in solution, which for an ideal chain is equivalent to its size R_g^2. Hence, the characteristic time scale for the entire chain is

$$\tau_Z \approx \frac{Nb^2}{D_Z} = \frac{\mu_s N^{3/2} b^3}{k_B T},$$

the longest Zimm relaxation time.

Since the modes are of the same form as the Rouse model, the constitutive equation and the polymer evolution equation remain the same:

$$\begin{aligned}
\boldsymbol{\sigma}^P &= G \sum_{p=1}^{N} \mathbf{A}_p \\
\frac{d\mathbf{A}_p}{dt} &= \mathbf{K} \cdot \mathbf{A}_p + \mathbf{A}_p \cdot \mathbf{K}^T - \frac{1}{\tau_p}(\mathbf{A}_p - \mathbf{I}), \quad p = 1, \ldots, N.
\end{aligned}$$

However, the relaxation spectrum τ_p is changed.

For an ideal Gaussian chain, the interaction potential is equivalent to that used in the Rouse model (1.7). To incorporate bead-bead interactions, the full mobility tensor given by equation (1.7) is included and a similar normal-mode analysis yields the Zimm relaxation spectrum [46]

$$\tau_p = \frac{\mu_s N^{3/2} b^3}{\sqrt{3\pi} k_B T p^{3/2}} = \frac{\tau_Z}{p^{3/2}}.$$

So far we have neglected the effects of excluded volume and bead-solvent interactions. This effect can be modelled by modifying the bead interaction potential to

$$U = \frac{1}{2} \nu k_B T \sum_{ij} \delta(\mathbf{r}_i - \mathbf{r}_j),$$

for excluded volume exponent ν. The equilibrium chain length is now proportional to

$$R_g^2 \propto N^{2\nu} b^2,$$

rather than Nb^2, so that the chain is no longer assumed to have a Gaussian distribution. The exponent includes both excluded volume effects, which cause the chain to swell, and polymer solubility effects that cause the chain to contract in a poor solvent. A solvent in which these effects balance is called a Θ-solvent. In this way, the spectrum of Zimm relaxation times becomes

$$\tau_p \approx \frac{\mu_s N^{3\nu} b^3}{k_B T p^{3\nu}} \approx \frac{\tau_Z}{p^{3\nu}},$$

full details of which are given in reference [46]. Taking $\nu = 1/2$ gives Θ conditions, whereas in a good solvent, the excluded volume exponent is approximately $\nu \approx 3/5$.

The dynamics of polymers in a dilute solution can be studied by measuring their viscoelastic properties. The total viscosity μ of a fluid is the sum of the solvent viscosity μ_s and the polymer contribution to viscosity, so that

$$\mu = \mu_s + G \sum_{p=1}^{N} \tau_p.$$

In both Rouse and Zimm theory, the contribution G to the elastic modulus is invariant of each mode and depends only on the concentration by weight, denoted ϕ, and the molecular weight M_w of the polymer [57] such that

$$G = \frac{\phi k_B T N_A}{M_w}.$$

Here N_A is the Avogadro number, which defines the number of constituent particles in one mole of a given solution.

On the other hand, the reduced viscosity for polymer concentration ϕ is defined to be

$$\frac{\mu - \mu_s}{\phi \mu_s}.$$

In the limit of very low concentrations, the reduced viscosity becomes linear in concentration so can be represented by an intrinsic viscosity defined as [46]

$$[\mu] = \lim_{\phi \to 0} \frac{\mu - \mu_s}{\phi \mu_s}.$$

Since the polymer contribution to viscosity is proportional to $G\tau$, we have

$$\mu - \mu_s = G\tau = \frac{\phi k_B T N_A}{M_w} \tau,$$

and for the longest Zimm relaxation time τ_Z, the intrinsic viscosity is defined as

$$[\mu] \sim \frac{N_A}{M_w} N^{3\nu} b^3 \approx \Phi \frac{R_g^3}{M_w},$$

for coil size $R_g = N^\nu b$. This is known as the Flory-Fox relation and the prefactor is found to be $\Phi = 0.45 N_A \approx 2.56 \times 10^{23} \mathrm{mol}^{-1}$. Thus, the intrinsic viscosity increases as a power law in molecular weight, known as the Mark-Houwink relation

$$[\mu] = K M_w^a.$$

The constant K depends upon the polymer system and the exponent is given by $a = 3\nu - 1$, which describes the molecular weight dependence on coil size in a particular solvent with excluded volume exponent ν.

Since the number of polymers in a unit volume if given by $\phi N_A/M_w$, the overlap concentration ϕ^* is estimated as

$$\frac{\phi^* N_A}{M_w}\frac{4}{3}\pi R^3 \sim 1.$$

Hence, in terms of the intrinsic viscosity, the widely accepted definition of the overlap concentration [36] is

$$\phi^* = \frac{0.77}{[\mu]}.$$

Near to this overlap concentration such that $\phi/\phi^* \sim 1$, the Zimm model is no longer valid. In fact, the Rouse model is more appropriate for concentrated polymer solutions in which the hydrodynamic interactions are screened by neighbouring molecules. However, fluids used in inkjet printing are limited to the dilute regime, where the Zimm model is more appropriate.

1.3 Measuring Rheological Properties

1.3.1 The Capillary-Thinning Rheometer

The progressive thinning of a fluid filament is driven by surface tension and retarded by inertia, viscosity and additional stresses arising from the extensional deformation of the fluid microstructure. For non-Newtonian fluids that contain polymers or suspended particles, the way that fluids stretch, thin and eventually break into droplets is dominated by these additional stresses. Thus, many studies of capillary-driven break-up concentrate on determining the transient extensional viscosity of the fluids, a review of which is given by McKinley [93]. Viscoelastic fluids have been of particular interest both experimentally [5] and numerically [35]. Overall, extensional flows have dramatic effects on polymeric fluids since the flow is able to stretch out the coiled up polymer molecules more effectively than shear flow.

There are many possible free-surface conformations that may be realised during the thinning and break-up of a fluid. Common experimental methods to induce surface-tension driven flow on a thin filament of fluid involve stretching a sample of fluid between two vertically-orientated end-plates. A predominantly extensional flow is generated, however in the early stages shear forces are important due to the non-slip boundary condition at the fluid-plate interface. The role of pre-shear on extensional flow is not well understood and has only been considered by few authors [4].

In particular, capillary-thinning rheometers have long been used to study the thinning dynamics of both Newtonian and polymeric fluids [143],[21],[126]. This method imposes a rapid step strain of given magnitude on a fluid sample. Subsequently, an unstable liquid bridge is generated between the two end-plates and proceeds to thin, under the action

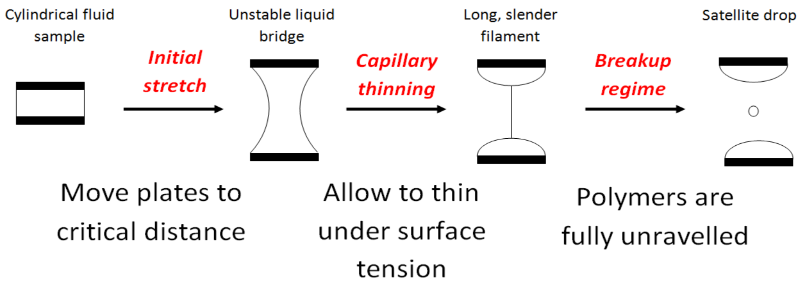

Figure 1.8: The slow-retraction method for capillary thinning.

of capillary forces, into a slender filament shape, before eventually pinching. The rate at which the filament radius decreases is controlled by a balance between surface tension, viscosity, inertia and elasticity. In the absence of external forcing, the dynamics of the necking process are often self-similar and observations of the minimum filament radius can be used to extract qualitative, or even quantitative measures of the extensional viscosity of a fluid.

Compared to filament-stretching devices, which separate end plates exponentially in time, capillary-thinning rheometers are considered superior for low-viscosity fluids, since surface tension can be used to measure the force acting on the liquid filament. However, there is no active control over the extension rate. For very low-viscosity fluids it can be difficult to create an unstable liquid bridge fast enough to observe a fully developed capillary-thinning regime; the bridge may collapse before the plates have finished moving. Also, the rapid separation of the plates may produce inertia-induced oscillations in the filament free surface, which may obscure measurements of the thinning dynamics.

The slow-retraction method [21] is a revised protocol for measuring extensional rheology using a capillary-thinning rheometer and is illustrated in Figure 1.8. The end-plates are separated at a moderate velocity, slower than the axial step-strain of traditional capillary-thinning rheometers. This velocity is prescribed to be sufficiently fast such that the fluid sample does not sag due to gravity, but slow compared to the intrinsic timescale of the fluid. For example, for polymeric fluids this separation velocity is determined by the polymer relaxation time so that the molecules remain at equilibrium during the initial stretching stage. The plates are separated to a distance just below the critical aspect ratio at which the liquid bridge is on the verge of stability. After this stable separation distance is reached, the plates are extended at a much slower velocity to induce capillary thinning. The main benefit of this revised technique is that the initial conditions are well defined and can be easily controlled. Since the plates are extended through the critical separation distance at a much slower velocity, the oscillation effects due to fluid inertia are minimised and consequently the minimum filament radius can be measured more accurately.

1.3.2 Rheometry using Inkjet Technology

Although rheometers have long been employed to measure fluid response and extract rheological properties, the speed at which traditional rheometers operate is slow compared to the jetting speed of a DoD printer. For example the Cambridge Trimaster [131] operates at around 0.15 m/s, corresponding to a filament extension rate of 250 s^{-1}. On the other hand, the optimum print speed for DoD printer is usually around $\sim 2-6$ m/s, generating much higher extension rates in the region $\sim 10^4$ s^{-1} depending on the nozzle size. Although current filament-thinning experiments cannot reach the extension rates achieved in inkjet printing processes, they do enable the measurement of very short extensional relaxation times with time scales comparable with inkjet drop formation [132].

Recent developments of the Trimaster rheometer have lead to a revised model, which can extend fluids at a speed of 2 m/s, giving extension rates of $\sim 10^3$ s^{-1}, much closer to real jetting conditions. However, at such a fast stretching speed, shock waves are induced when the pistons stop moving, which may be problematic when measuring the minimum filament radius. Furthermore, it has recently been suggested that filament-stretching devices alone may be insufficient to predict inkjet behaviour due to effects that occur within the nozzle[2]. Hoath *et al.* [70] find that DoD jetting behaviour is not consistent with the extensional relaxation time measurements obtained from a fast filament-stretching rheometer [130]. Rather, it is suggested that the predicted slowing of the main drop and the delay in the break-off time are caused by the polymer molecules becoming fully extended during the jetting process, which produces an enhanced extensional viscosity. Full extension of the molecules arises from the high speed jets with small nozzle diameters, in combination with the relatively high solvent viscosity and small molecular weights. Consequently, inkjet fluid assessment methods need to provide a full characterisation including both linear and non-linear viscoelastic properties.

The least developed, but potentially high-impact method to characterise extensional properties of complex fluids is to use real inkjets as rheometers. The use of jet break-up to measure the extensional viscosity of a material was first proposed by Schummer & Tebel [119]. In both DoD and CIJ printing, the generation of an ink drop involves a thinning liquid filament, either between the droplet and the nozzle in the case if DoD printing or between two adjacent droplets in a continuous jet. This filament is analogous to that generated in a capillary-thinning rheometer and so the thinning data could be used to extract extensional properties at jetting strain rates.

1.3.3 Polymer Behaviour in Extensional Flow

Consider the uniaxial deformation of a polymeric fluid. For extension rate $\dot{\epsilon}$, the axial velocity is given by $u_z = \dot{\epsilon} z$ and mass conservation of an incompressible fluid determines

---

[2] Published: S. D Hoath, D. C. Vadillo O. G. Harlen, **C. McIlroy**, N. F. Morrison, W. Hsiao, T. R. Tuladhar, S. Jung, G. D. Martin, I. M. Hutchings *Inkjet printing of weakly elastic polymer solutions* J. Non-Newt. Fluid Mech. 205 (2014) 1-10

the radial velocity u_r to be

$$\begin{aligned} \nabla \cdot \mathbf{u} = \frac{1}{r}\frac{\partial}{\partial r}(ru_r) + \frac{\partial u_z}{\partial z} &= 0, \\ \frac{\partial}{\partial r}(ru_r) &= -r\dot{\epsilon}, \\ u_r &= -\frac{1}{2}\dot{\epsilon}r. \end{aligned}$$

Thus the velocity profile for uniaxial extension is given by

$$(u_r, 0, u_z) = (-\frac{1}{2}\dot{\epsilon}r, 0, \dot{\epsilon}z),$$

and the velocity gradient tensor is

$$K_{ij} = \frac{\partial u_i}{\partial x_j} = \begin{pmatrix} \frac{\partial u_r}{\partial r} & 0 & 0 \\ 0 & \frac{u_r}{r} & 0 \\ 0 & 0 & \frac{\partial u_z}{\partial z} \end{pmatrix} = \begin{pmatrix} -\frac{1}{2}\dot{\epsilon} & 0 & 0 \\ 0 & -\frac{1}{2}\dot{\epsilon} & 0 \\ 0 & 0 & \dot{\epsilon} \end{pmatrix}$$

The extensional viscosity describes the fluid's resistance to uniaxial stretching and is calculated from the thinning data via

$$\mu_E = \frac{F}{\dot{\epsilon}\pi h_{min}^2},$$

where the force F is the tension on the filament and h_{min} is the minimum filament radius. Furthermore, the total stress in a liquid cylinder consists of an isotropic pressure plus the extra stress tensor, so that at the free surface $r = h$ the radial stress is given by

$$\tau_{rr} = -p + \sigma_{rr} = -p_{atm}.$$

Thus, the axial force required to stretch the fluid in the z-direction is

$$F = 2\pi \int_0^h r(\tau_{zz} + p_{atm})dr = \pi h^2(\sigma_{zz} - p + p_{atm}) = \pi h^2(\sigma_{zz} - \sigma_{rr}),$$

and the extensional viscosity is reduced to

$$\mu_E = \frac{\sigma_{zz} - \sigma_{rr}}{\dot{\epsilon}},$$

at the minimum filament radius $h = h_{min}$.

For a Newtonian fluid, stress is a linear function of shear viscosity μ and the stress tensor is defined by the constitutive equation

$$\boldsymbol{\sigma} = \mu(\mathbf{K} + \mathbf{K}^T),$$

so that the extra stress components are given by

$$\sigma_{zz} = 2\mu\dot{\epsilon} \quad ; \quad \sigma_{rr} = -\mu\dot{\epsilon}.$$

Hence, the force in the filament is given by

$$F = 3\pi h^2 \mu\dot{\epsilon},$$

and the extensional viscosity is simply

$$\mu_E = 3\mu.$$

This is the Trouton ratio, which states that the extensional viscosity is three times the shear viscosity in Newtonian fluids.

For polymeric fluids, we consider only the polymeric stress defined by the constitutive equation

$$\boldsymbol{\sigma} = Gf(\mathbf{A} - \mathbf{I}),$$

for elastic modulus G and FENE factor

$$f = \frac{L^2}{L^2 + 3 - \mathrm{tr}(\mathbf{A})},$$

that accounts for the finite extensibility L of the polymer molecules. The evolution equations of the polymer configuration tensor $\mathbf{A}$ are given by

$$\begin{aligned} \frac{dA_{rr}}{dt} &= -\dot{\epsilon}A_{rr} - \frac{f}{\tau}(A_{rr} - 1), \\ \frac{dA_{zz}}{dt} &= 2\dot{\epsilon}A_{zz} - \frac{f}{\tau}(A_{zz} - 1), \end{aligned}$$

in extensional flow.

In the Oldroyd limit of infinitely extensible dumbbells, $f = 1$ and the dumbbell evolution equations are solved simply by the integration factor method to give

$$\begin{aligned} A_{rr} &= \frac{1}{1 + \dot{\epsilon}\tau}\left(1 + \dot{\epsilon}\tau \exp\left(-\frac{(1 + \dot{\epsilon}\tau)}{\tau}t\right)\right), \\ A_{zz} &= \frac{1}{1 - 2\dot{\epsilon}\tau}\left(1 - 2\dot{\epsilon}\tau \exp\left(-\frac{(1 - 2\dot{\epsilon}\tau)}{\tau}t\right)\right). \end{aligned}$$

Hence, in the limit $t \to \infty$, the extensional viscosity is given by

$$\mu_E = \frac{G(A_{zz} - A_{rr})}{\dot{\epsilon}} = \frac{3G\tau}{(1 + \dot{\epsilon}\tau)(1 - 2\dot{\epsilon}\tau)}.$$

Thus, as $\dot{\epsilon}\tau \to 1/2$, the extensional viscosity becomes singular. This value $\dot{\epsilon}\tau = 1/2$ defines the boundary between viscous and elastic-solid like behaviour. For $\dot{\epsilon} < 1/2$, fluid behaviour is viscous and for $\dot{\epsilon} \ll 1$ the Newtonian Trouton ratio is recovered.

On the other hand, for $\dot{\epsilon}\tau > 1/2$, A_{zz} grows exponentially, indicating the unravelling of the polymer chains. In this limit of large deformations, $A_{rr} \ll A_{zz}$ and the FENE factor is approximated as

$$f \approx \frac{L^2}{L^2 - A_{zz}}.$$

For steady state $\frac{d\mathbf{A}}{dt} = 0$, the evolution equation of the axial configuration tensor reduces to

$$\left(2\dot{\epsilon} - \frac{f}{\tau}\right)A_{zz} = 0,$$

giving a second approximation to the FENE factor, $f = 2\dot{\epsilon}\tau$. Thus, equating the two approximations, we find that for long deformation times

$$A_{zz} = L^2\left(1 - \frac{1}{2\dot{\epsilon}\tau}\right);$$

as breakup time approaches, $\dot{\epsilon} \to \infty$ so that $A_{zz} \to L^2$. Thus, at finite extension, the polymers behave like a suspension of rigid rods with extensional viscosity

$$\mu_E = \frac{GfA_{zz}}{\dot{\epsilon}} = 2G\tau L^2,$$

as recognised by Entov & Hinch [54].

The above derivation of extensional viscosity assumes that the filament thins uniformly as a liquid cylinder. A more detailed model is required to obtain an expression for tension, particularly for complex fluids, so that the extensional viscosity can be accurately measured solely from the actual necking shape of the thinning filament.

1.4 Modelling and Simulating Jets

1.4.1 Long-Wavelength Approximation for Newtonian Jets

In the study of Newtonian jets, the biggest challenge both theoretically and numerically is to solve the full Navier-Stokes equation,

$$\rho\left(\frac{\partial \mathbf{u}}{\partial t} + \mathbf{u}(\nabla \cdot \mathbf{u})\right) = -\nabla p + \nabla \cdot \boldsymbol{\sigma} + \rho \mathbf{g},$$

for an incompressible fluid such that

$$\nabla \cdot \mathbf{u} = 0,$$

in a domain with an evolving boundary, where the forcing depends critically on the shape of this boundary. Here we denote density ρ, pressure p, jet velocity $\mathbf{u}$ and stress $\boldsymbol{\sigma}$. In inkjet applications, the gravitational force $\mathbf{g}$ is negligible since the jet dimensions are small and we consider motions driven by capillarity alone. For complex fluids, there is an additional constitutive equation to solve for the stress.

In capillary thinning, the driving force is the Laplace pressure

$$\Delta p = \gamma \kappa,$$

for surface tension γ and mean curvature κ. If $\mathbf{n}$ is the outward normal, then the mean curvature is given by

$$\kappa = -\nabla|_{\delta\Omega} \cdot \mathbf{n},$$

where ∇ is restricted to the surface $\delta\Omega$. The Laplace pressure describes the pressure jump across a curved interface, which produces an increased pressure inside a convex surface.

It is known that the free surface moves with the local fluid velocity. Thus, to derive an equation for this motion we define a function $S(\mathbf{r}, t)$ that is constant at the jet surface [53]. Thus, for jet velocity $\mathbf{u} = (u_r, u_\theta, u_z)$, the evolution of the free surface is described by the kinematic equation

$$\frac{\partial S}{\partial t} + (\mathbf{u} \cdot \nabla)S = 0.$$

For an axisymmetric jet that is not folded on itself, the free surface is defined by a height function $S = h(z,t) - r$, which gives the local radius of the jet at some axial position z. Thus, the kinematic equation reduces to

$$\frac{\partial h}{\partial t} + u_z \frac{\partial h}{\partial z} = u_r|_{r=h}, \tag{1.11}$$

which specifies that the jet surface moves with the velocity of the neighbouring liquid. Furthermore, the strength of the forcing on the free surface is proportional to the mean curvature, which for an axisymmetric jet is defined to be

$$\kappa = \frac{1}{h(1+h_z^2)^{1/2}} - \frac{h_{zz}}{(1+h_z^2)^{3/2}}, \tag{1.12}$$

where the subscript here indicates differentiation with respect to z. Thus, as the jet radius decreases to zero, the mean curvature becomes infinite, so that jet break-up is a singularity. At the liquid-air interface, the pressure and the viscous forces are balanced by the surface tension. Thus, for a known velocity, the motion of the interface is described by the kinematic equation (1.11) and the shape of the interface couples back into the flow via the boundary condition

$$\boldsymbol{\sigma} \cdot \mathbf{n} = -\gamma\kappa\mathbf{n}|_{\delta\Omega}.$$

However, solving the full Navier-Stokes equations in this way can be computationally expensive. In order to simplify the problem, the slender-jet approximation is often used for modelling jet break-up. In this case, perturbations are assumed to have a wavelength much longer than the radial extension so that

$$L_r = \epsilon L_z, \quad \epsilon \ll 1,$$

where ϵ is a small number and the hydrodynamic fields are expanded in the radial direction such that

$$\begin{aligned} u_z(r,z,t) &= u_0(z,t) + u_2(z,t)(\epsilon r)^2 + \cdots, \\ u_r(r,z,t) &= -u_0'(z,t)\frac{\epsilon r}{2} - u_2'(z,t)\frac{(\epsilon r)^3}{4} - \cdots, \\ p(r,z,t) &= p_0(z,t) + p_2(z,t)(\epsilon r)^2 + \cdots, \end{aligned}$$

where the ‘prime’ denotes differentiation with respect to z. The leading-order axial velocity is denoted $v(z,t) \equiv u_0$. This long-wavelength description, based on Reynolds’ lubrication theory, is surprisingly accurate, even if the long-wavelength assumption is not strictly valid [52], [3]. Results under this approximation are found to be highly quantitative and often represent the exact solution near to break-up.

A unique long-wavelength description requires choosing a length scale L, as well as a time scale T, which correspond to a balance of terms in the Navier-Stokes equation. A convenient choice is the balance in which surface tension, inertia and viscosity all enter the governing equation at leading order [53] so that

$$L = \frac{\mu^2}{\gamma\rho} \quad ; \quad T = \frac{\mu^3}{\gamma^2\rho},$$

Quantities are made dimensionless using the above scaling and the radial expansion is inserted into the full Navier-Stokes equation for incompressible flow so that the z-component reduces to

$$\rho\left(\frac{\partial v}{\partial t}+v\frac{\partial v}{\partial z}\right)=-\gamma\frac{\partial \kappa}{\partial z}+\frac{1}{h^2}\frac{\partial}{\partial z}\left(h^2\left(\sigma_{zz}-\sigma_{rr}\right)\right).$$

The full derivation of this leading-order equation is detailed by Eggers [50].

For a Newtonian fluid, the stress tensor $\boldsymbol{\sigma}$ is defined by the constitutive equation

$$\boldsymbol{\sigma}=\mu(\mathbf{K}+\mathbf{K}^T),$$

for fluid viscosity μ and velocity gradient tensor $K_{ij}=\frac{\partial u_i}{\partial x_j}$. Thus, the axial and radial stress components are

$$\sigma_{zz}=2\mu\frac{\partial v}{\partial z}\quad;\quad\sigma_{rr}=-\mu\frac{\partial v}{\partial z},$$

and Navier-Stokes reduces to

$$\rho\left(\frac{\partial v}{\partial t}+v\frac{\partial v}{\partial z}\right)=-\gamma\frac{\partial \kappa}{\partial z}+3\mu\frac{1}{h^2}\frac{\partial}{\partial z}\left(h^2\frac{\partial v}{\partial z}\right).$$

This equation describes the force acting on a cross-section of fluid that has momentum h^2v per unit length; the right hand side consists of a combination of capillary and viscous forcing, and the left-hand side corresponds to inertia. Additionally, in the long-wavelength approximation, the kinetic boundary condition (1.11) is reduced to

$$\frac{\partial h^2}{\partial t}+\frac{\partial}{\partial z}(h^2v)=0,$$

which explicitly describes the motion of the free surface and is the conservation law for the volume h^2dz contained in a small cross-section of the jet of length dz.

Although mean curvature κ is given by

$$\kappa=\frac{1}{h},$$

at leading order, in order to include the effects of longitudinal curvature and retain accuracy of the curvature beyond the limit where $|h_z|\ll 1$, the full expression of the curvature (1.12) is kept. A detailed comparison with the full Navier-Stokes simulations has been carried out by Ambravaneswaran *et al.* [3], with excellent agreement for a wide range of parameters. This method can be pursued to higher order in ϵ by continuing the radial expansion to higher powers in r. In principle, this could lead to a better description of non-linear jet dynamics. However, due to the increasing order of spatial derivatives, which are difficult to compute, this has not generally been pursued.

Since the equations of fluid dynamics are based upon conservation laws, it is convenient to express the governing equations in flux-conservative form. The conservation of mass equation is already in this form, while the left-hand side of conservation of momentum can be re-written as

$$\frac{\partial v}{\partial t}+v\frac{\partial v}{\partial z}=\frac{1}{h^2}\left(\frac{\partial}{\partial t}(h^2v)+\frac{\partial}{\partial z}(h^2v^2)\right),$$

using conservation of mass and the gradient of curvature is rewritten as [55]

$$-\frac{\partial \kappa}{\partial z} \equiv \frac{1}{h^2}\frac{\partial}{\partial z}(h^2 K(h)),$$

where K is defined to be

$$K \equiv \frac{1}{h(1+h_z^2)^{1/2}} + \frac{h_{zz}}{(1+h_z^2)^{3/2}}.$$

Note that K has almost the same form as the mean curvature κ, but both the axial and radial contribution to this curvature term are positive. Hence, the Newtonian slender-jet equations may be written in flux-conservative form:

$$\begin{aligned} \frac{\partial h^2}{\partial t} + \frac{\partial}{\partial z}(h^2 v) &= 0, \\ \rho\left(\frac{\partial}{\partial t}(h^2 v) + \frac{\partial}{\partial z}(h^2 v^2)\right) &= \frac{\partial}{\partial z}\left(h^2\left(\gamma K + 3\mu\frac{\partial v}{\partial z}\right)\right). \end{aligned} \tag{1.13}$$

Models based on these one-dimensional equations have been developed for their simplicity and computational efficiency, with much success in modelling the thinning of liquid jets [35], [90], [131] and the formation of droplets [3], [6]. These equations will form the foundation of our one-dimensional jetting models developed in Chapters 3 and 5.

1.4.2 Full Numerical Simulations

There has been a vast improvement in computational speed and resources over the last decade. Over the last ten years, powerful and accurate computational tools have been developed to simulate flow through a nozzle, liquid jet dynamics and the subsequent formation of drops. Consequently numerical simulation of inkjet printing using computational fluid dynamics (CFD) is now as equally important as experimental data in analysing the jetting process. Much research has focused on axisymmetric models that employ finite-difference or finite-element methods in order to solve the Navier-Stokes equations [142], [66], [30]. Often, for simplicity, the full flow inside the nozzle is neglected, with boundary conditions imposed at the nozzle exit.

In this thesis, the simulation method of Morrison & Harlen [66] is used for comparison with simpler models. This axisymmetric simulation uses a Eulerian-Lagrangian finite-element method to capture the evolving free-surface shape and has previously been used to study jet breakup in drop-on-demand printing for both Newtonian [24] and viscoelastic fluids [66] and continuous inkjet printing of Newtonian fluids [23]. Here we give a short overview of the numerical techniques used for this particular simulation method.

The velocity $\mathbf{u}$ of a general fluid with density ρ and pressure p is described by the usual conservation of momentum equation

$$\rho\left(\frac{\partial \mathbf{u}}{\partial t} + \mathbf{u}(\nabla \cdot \mathbf{u})\right) = -\nabla p + \nabla \cdot \boldsymbol{\sigma}, \tag{1.14}$$

along with the incompressible condition.

$$\nabla \cdot \mathbf{u} = 0, \tag{1.15}$$

and a constitutive equation for the stress tensor $\boldsymbol{\sigma}$. The software uses a moving-mesh, finite-element method to solve these governing equations. By allowing the finite elements to deform with the fluid velocity, the constitutive equation is solved in the co-deforming frame. For free-surface problems such as inkjet printing, this method naturally captures the free-surface shape. Further details of the numerical scheme can be found in references [66], [67] and [139].

Since the mesh deforms with the fluid, it is distorted by velocity gradients, which reduces the accuracy of the finite-element solution. Thus, it is necessary to limit the mesh distortion by introducing a re-meshing algorithm to maintain element-shape quality and resolution. To reconnect the mesh after each time step, nodes are retained as material points and reconnected is such a way to produce best triangulation via the process of Delaunay triangulation. There is a simple algorithm for reconnecting an existing mesh to obtain a Delaunay triangulation given in [67].

In addition to controlling mesh distortion, an adaptive mesh resolution is also employed. A greater resolution is needed in regions of high stress or velocity gradient, such as the neck regions that precede break-up, and, for polymeric fluids, in regions of high polymer extension. Due to the nature of a Lagrangian mesh, it is necessary to continually add and remove nodes to control mesh resolution. A quantitative measure of the need for extra resolution is certain areas of the mesh is given in [67].

At the fluid-air interface the boundary condition is defined to be

$$[\boldsymbol{\sigma}\cdot\hat{\mathbf{n}}]_{air}^{ink} = -\gamma\left(\frac{1}{R_1}+\frac{1}{R_2}\right)\hat{\mathbf{n}},$$

where $\hat{\mathbf{n}}$ is the unit vector normal to the interface, γ denotes surface tension and R_1, R_2 are the principle radii of curvature. The boundary conditions imposed in the axial direction determine the jetting conditions of the desired simulation. For example, periodic boundary conditions are specified to model an infinite jet, whereas Dirichlet boundary conditions are imposed to correspond to the fixed end plates of a capillary-thinning rheometer. Furthermore, certain nozzle geometries and initial velocity profiles can be implemented to simulate both DOD and CIJ jetting.

1.4.3 A Drop-on-Demand Inkjet Simulation

The nozzle geometry used for the axisymmetric simulation of a DoD inkjet is detailed in Figure 1.9. The jet is assumed to be axisymmetric such that a 2D coordinate system may be employed to fully describe the jet dynamics and nozzle geometry, with the axis of symmetry at the centre of the outlet nozzle. The nozzle shape and dimensions considered here are based on the Xaar XJ126-200 print head used by Hoath *et al.* [71]. The simulations only consider the contraction flow into the nozzle and do not model the details of the print head itself, which is non-axisymmetric.

The fluid is driven by imposing a time-dependent velocity profile on the curved inlet boundary upstream of the nozzle. The driving signal uses the profile of Morrison & Harlen

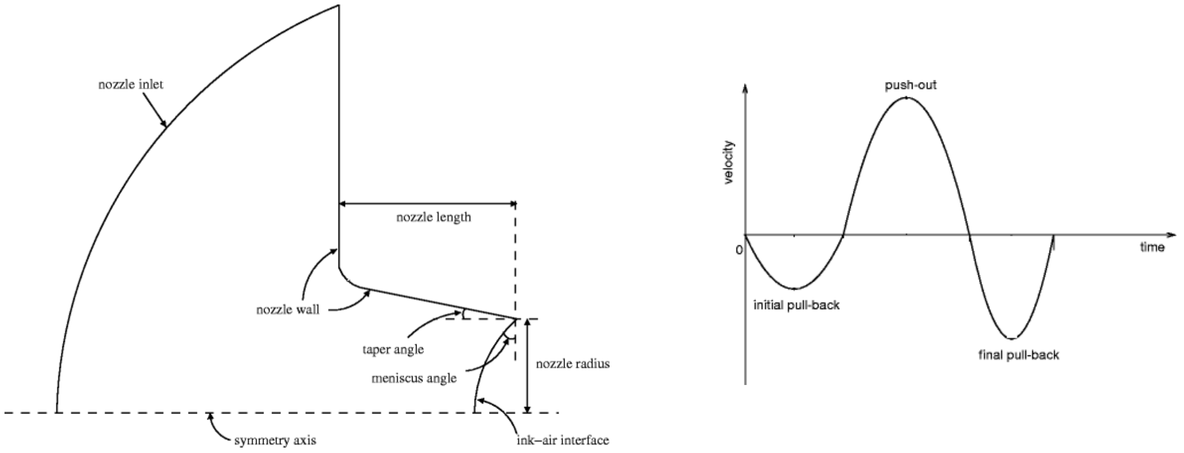

(a) Nozzle Geometry

(b) Driving Wave Form

Figure 1.9: (a) Nozzle geometry used in axisymmetric simulations; (b) Initial velocity profile/driving signal applied to the curved nozzle inlet.

[66] and consists of three stages known as the ‘pull-push-pull’ curve, shown in Figure 1.9. This profile is chosen to match the flow conditions of the Xaar print head near to the nozzle outlet, although some other DoD printers use a push only profile. The initial ‘pull’ phase draws fluid into the print head from the nozzle outlet, the following ‘push’ phase ejects the fluid from the nozzle and the final ‘pull’ phase draws back the trailing ligament to ensure that it breaks primarily at the nozzle.

Figure 1.10 shows a time series from a simulation of Newtonian jet generation and breakup from a DOD inkjet. The initial pull phase of the driving signal is shown in Figure 1.10(a). The velocity U_0 corresponds to the tip velocity when the ligament length and diameter are equal (and equal to the nozzle diameter). This occurs at the beginning of the final ‘pull’ stage of the simulated driving signal and can be seen in Figure 1.10(b). The ligament is then seen to break off from the nozzle at the end of this ‘pull’ phase in Figure 1.10(c). The final velocity U_f is the speed that the front of the main drop reduces to. This is usually measured at 1 mm from the nozzle exit and corresponds to Figure 1.10(d). However, the velocity after break off from the nozzle is approximately constant across Figures 1.10(c-e).

After break off from the nozzle, the trailing ligament may merge with the main drop or break up due to the capillary instability. The front drop, which is the drop of greatest volume, is referred to as the main drop and any subsequent droplets generated by ligament breakup are called satellite drops. The generation of satellite drops is dependent on a number of factors, notably the Ohnesorge number, and for polymeric fluids the concentration and the molecular weight significantly affect both the number and the size of the satellite drops produced [66]. In counting the satellite drop volume in our simulations, no post-breakup coalescence is considered, whereas in reality drops may merge into one another. The ligament is seen to breakup into numerous satellite drops in Figure 1.10(e).

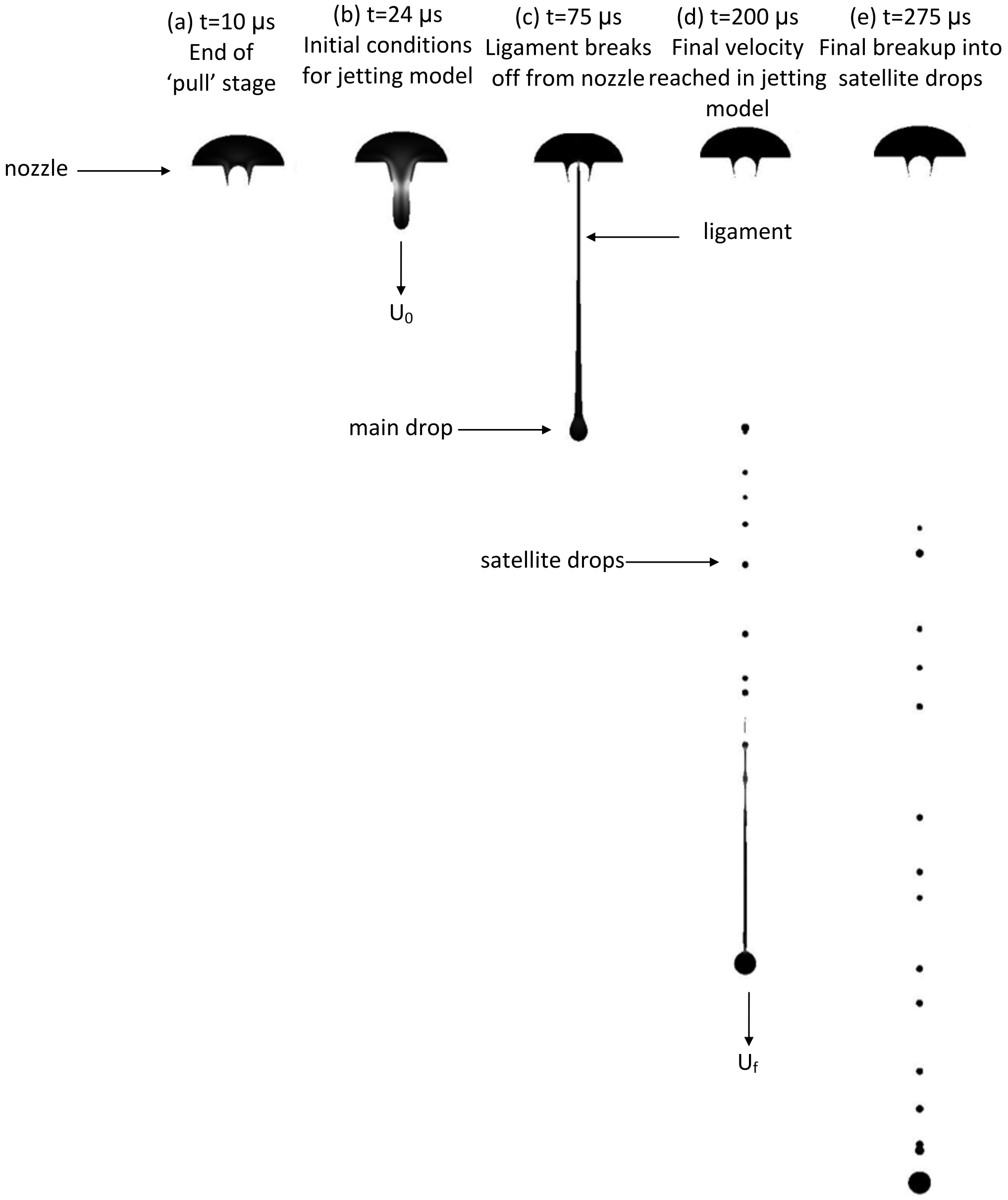

Figure 1.10: Simulation of the different phases of DoD jet generation for a Newtonian fluid.

1.4.4 A Continuous Inkjet Simulation

The shape of the print head used in our axisymmetric CIJ simulations is chosen to replicate the dimensions of CIJ nozzles used in experiments, while simplifying the interior of the print head above the nozzle. The initial finite-element grid, with a nozzle aspect ratio 1, is shown in Figure 1.11. A slight fillet is applied to the sharp corner where the conical and straight nozzle sections meet. The print head inlet is located at the top boundary of the grid. Here a time-dependent-velocity boundary condition is imposed to represent the drive modulation. The bottom boundary condition represents the nozzle outlet and the initial

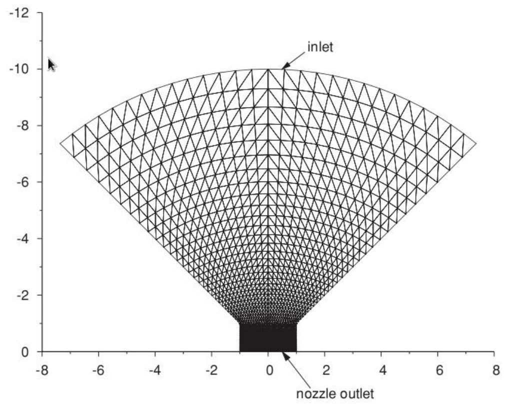

Figure 1.11: Initial grid used in CIJ simulations for nozzle aspect ratio 1.

meniscus is assumed to be flat as observed in experiments. The remaining boundaries correspond to the rigid interior walls of the print head, thus a no slip boundary condition is imposed.

To simulate a jet with modulation of frequency f and amplitude ϵ, the inlet velocity is prescribed in terms of time t as

$$u_{in}(t) = u_0(1 + \epsilon \sin(2\pi f t)),$$

where

$$u_0 = \frac{\pi R^2 U}{A_{in}},$$

for nozzle radius R, mean jet velocity U and the inlet surface area A_{in}. While this is not expected to fully represent the experimental flow throughout the entire print head, it is designed to produce sufficiently similar flow conditions in the vicinity of the nozzle. The possible presence of higher harmonics in the jet actuation is neglected. Again, no method of coalescence was implemented in the simulations.

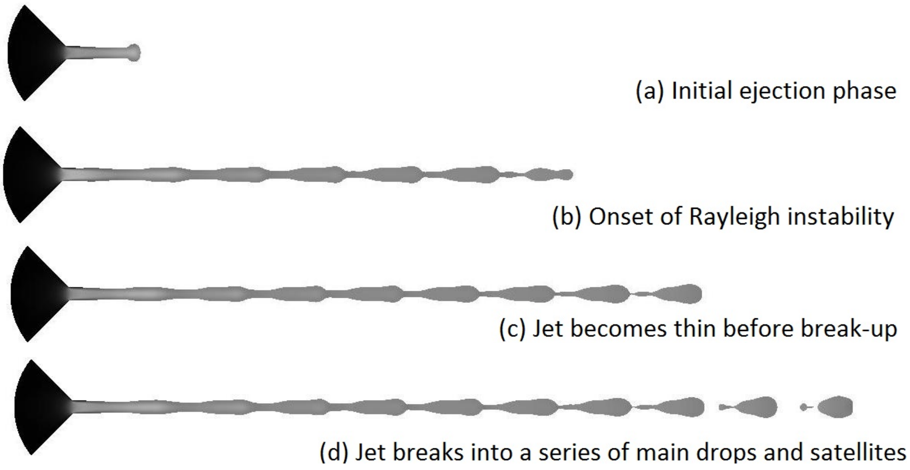

Figure 1.12: Simulation of the different phases of CIJ drop generation for a Newtonian fluid.

Figure 1.12 shows a time series from a simulation of Newtonian jet generation and break-up from a continuous inkjet nozzle. Figure 1.12(a) shows the initial ejection phase. Figure 1.12(b) shows the onset of the Rayleigh capillary instability downstream of the nozzle exit and the jet becomes increasingly thin downstream, as seen in Figure 1.12(c). The jet subsequently breaks up into a series of main drops and smaller satellite droplets as shown in Figure 1.12(d). At break-up the droplets are slightly elongated due to the shape of the nozzle and eventually evolve into a spherical shape.

1.5 Thesis Outline

The research surrounding inkjet printing and its applications is vast. However, the foundation of this advancing technology lies simply in the stability and break-up of liquid jets. In Chapter 2, we review the literature detailing key mathematical advances in understanding the formation of liquid drops.

In the following chapters, we discuss three distinct problems related to the development of inkjet technology. In particular, we use simple numerical modelling to examine the effect that particles, polymers and non-linear driving have on certain jetting techniques, including DoD and CIJ. We compare our results with full numerical simulations and, for some cases, experimental data. A brief outline of these chapters is given here.

In Chapter 3, we develop a simple one-dimensional model, based on the long-wavelength approximation. First, we simulate particle effects on the capillary-thinning of a liquid bridge and establish the mechanism responsible for accelerating the thinning process. Second, we examine viscoelastic effects on infinite-jet dynamics and validate our one-dimensional model against the results of the full axisymmetric simulation.

In Chapter 4, we develop a simple DoD jetting model in order to determine the maximum polymer concentration that can be jetted at a desired print speed. Furthermore, we discuss a prestretch mechanism, driven by an abrupt contraction in the nozzle geometry, and the jetting conditions for which polymer degradation is possible.

In Chapter 5, we use an adaptive mesh alongside our one-dimensional model developed in Chapter 3 to simulate CIJ printing of Newtonian fluids. In particular, we examine how break-up behaviour is affected by non-linear modulations in the velocity profile. We compare our results with full axisymmetric simulations in order to incorporate nozzle effects into our one-dimensional model.

Chapter 2

Stability and Break-up of Liquid Jets

2.1 History of Studying Liquid Jets

A jet is defined to be a stream of matter that is cylindrical in shape. With such an extensive definition, jets appear in a huge number of circumstances and the study of their stability is often motivated by practical questions and applications: will the jet break, and if so, how long will it take? How does viscosity affect the ultimate break-up regime into spherical droplets? After break-up, what is the size distribution of droplets?

Jet dynamics probe a wide range of physical properties such as surface tension, viscosity, and both bulk and surface rheology. It is the interaction of these properties that is key to understanding, and therefore characterising, jet thinning and break-up processes. Moreover, optimising jet propulsion for a wide range of complex fluids is important to the future development of inkjet technology.

The earliest study of liquid jets is attributed to Leonardo da Vinci in his collection of largely scientific writings known as the Codex Leicester. He correctly noted that the detachment of falling drop is governed by the balance between gravity and surface tension [39]. However, he mistakenly assumes that the same mechanism is responsible for the separation of the drop itself. This problem was solved one hundred years later by Laplace [84] and Young [144], who demonstrated the crucial role of mean curvature in the form of the Laplace pressure

$$\Delta p = \gamma \left(\frac{1}{R_r} + \frac{1}{R_z} \right) \equiv \gamma \kappa,$$

where γ is the surface tension and κ is the mean curvature. The axial R_z and radial R_r contributions are known as the principle radii of curvature.

The work of Laplace and Young demonstrates the fact that surface tension can act in two different ways. For a hanging drop, the surface tension acts like an elastic membrane and is therefore stabilising, resisting the gravitational force. On the other hand, once a cylindrical shape is reached, the radial curvature acts as the driving force to destabilise the free surface and leads to the detachment of the drop. In the absence of viscosity, the

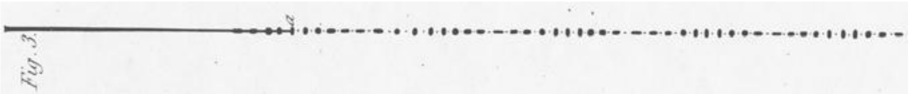

Figure 2.1: A figure from Savart's original paper [118] showing the break-up of a liquid jet. The production of smaller satellite droplets is clearly visible.

characteristic time scale on which this break-up occurs is given by

$$t_b = \sqrt{\frac{\rho R^3}{\gamma}},$$

where ρ denotes the fluid density and R is the initial radius of the cylinder.

This mathematical break through was followed by Savart's pioneering experimental work in the study of jet break-up [118], as shown in Figure 2.1. He observed that the break-up of a jet into droplets occurs spontaneously and is governed by laws independent of the circumstance under which the jet is produced, concluding that the thinning and break-up behaviour is a feature intrinsic to the jet properties. Savart also noted the appearance of smaller satellite drops in between the main drops of fluid, a non-linear characteristic of jet break-up, which can be observed in Figure 2.1.

A fully developed mathematical theory describing the break-up of liquid jets, in which the role of surface tension was truly recognised, came fifty years later with the work of Plateau and Rayleigh. Plateau [107] was first to recognise that a jet is unstable to small perturbations that reduce the surface area and proposed that that there exists a critical wavelength below which jets are always stable. Rayleigh then introduced the method of linear stability analysis to quantify this critical wavelength, first for inviscid fluids in a vacuum [109] and then a few years later he discussed the case of a viscous cylinder [110]. However, as perturbations become large, non-linear effects become increasingly important and ultimately dominate near to break up, where Rayleigh's linear stability analysis is no longer valid.

With the development of high-speed photography, intricate features of drop break-up, such as the formation of secondary and even tertiary droplets, could be documented. In particular, early jetting experiments showed that satellite drops originate from an elongated neck joining two main drops of fluid. Also, the shape of the neck region close to break-up was observed to be independent of initial conditions such as nozzle size, jet speed and the amplitude of the initial perturbation. In the absence of viscosity, a dimensional analysis of the characteristic break-up time t_b shows that the minimum neck radius can be described by a simple power law

$$h_{min} \sim \left(\frac{\gamma}{\rho}\right)^{1/3} (t - t_b)^{2/3}.$$

However, this early research lacked a theoretical framework for fully describing non-linear features of the free-surface flow. Significant progress occurred after the suggestion that self-similarity could provide the foundation for a theoretical description [104],[127].

In this chapter, we first consider the stability of a liquid jet subject to small perturbations and derive the dispersion relation for an inviscid jet via the classic Rayleigh linear stability analysis [109]. This inviscid result is compared to the viscous case in order to highlight the increased break-up length due to the influence of viscosity, which reduces the growth rate of small disturbances. In light of the Newtonian theory, we derive the viscoelastic dispersion relation, as given by Goldin *et al.* [62], and comment on the failure of this linear analysis to predict the change in break-up length for viscoelastic fluids. Second, we consider the subsequent dynamics of an unstable liquid jet, for which non-linearity dominates the flow. We detail the universal self-similar solutions that describe Newtonian thinning and derive the exponential thinning law unique to viscoelastic fluids. Finally, we consider the ultimate break-up of Newtonian and viscoelastic filaments.

2.2 The Initial Capillary Instability

2.2.1 The Classic Rayleigh Stability Analysis

From the work of Young and Laplace it is known that the surface tension, or capillary force, drives a cylindrical jet to minimise its surface area and consequently break up into a number of spherical droplets. Pioneered by Rayleigh, a mathematical description of this instability is provided by the powerful tool that is known as linear stability analysis. By this method, the characteristic time and length scales associated with this free-surface transition can be predicted. Furthermore, Rayleigh established that an inviscid cylinder of liquid will only destabilise provided that the wavelength λ exceeds the circumference. That is, a cylindrical liquid jet will break up into droplets if and only if

$$\lambda > 2\pi R,$$

for jet radius R. Here we derive this well-known result.

For a Newtonian liquid jet of viscosity μ, density ρ, and pressure p the Navier-Stokes equation is given by

$$\rho\left(\frac{\partial \mathbf{u}}{\partial t} + (\mathbf{u}\cdot\nabla)\mathbf{u}\right) = -\nabla p + \mu\nabla^2\mathbf{u},$$

for jet velocity $\mathbf{u}$, together with the incompressibility condition

$$\nabla\cdot\mathbf{u} = 0.$$

As described earlier, the Laplace pressure at the jet free surface Δp is written in terms the mean curvature κ. For an axisymmetric jet with free surface $h(z,t)$, the mean curvature is defined as

$$\kappa = \frac{1}{h(1+h_z^2)^{1/2}} - \frac{h_{zz}}{(1+h_z^2)^{3/2}}, \tag{2.1}$$

where the subscript z denotes the spatial derivative.

For a linear stability analysis, a base state is defined by a solution to the governing equations; for example, it is typical to take the base state $\mathbf{u}_0 = 0$. Instability of a liquid jet arises due to the existence of small perturbations from the base state. Perturbations can be thought of as small disturbances in the jet radius and velocity and are usually written in the form

$$\tilde{\delta} = \delta' \exp(i(kz + m\phi) + \alpha t),$$

for some parameter δ. Here δ' is the amplitude of the disturbance, α is the growth rate of the disturbance and ϕ is the azimuthal angle. The longitudinal wave number k is defined in terms of the jet wavelength λ to be

$$k = \frac{2\pi}{\lambda}.$$

In this way, growing and decaying disturbances can be easily identified; growing perturbations are unstable modes acting to destabilise the jet whereas decaying perturbations are stable, returning the jet to the base state. Azimuthal perturbations $m > 0$ correspond to corrugation of the free surface and so always increase the surface area of the jet. Consequently, all azimuthal modes corresponding to non-axisymmetric perturbations are stable. Thus, we restrict ourselves to axisymmetric perturbations where $m = 0$.

For a perturbed base state, linearisation leads to a simple set of governing equations, which can be solved to yield a dispersion relation. The dispersion relation determines the rate at which the perturbations grow and depends on both the wave number k and the jet radius R:

$$\alpha \equiv \alpha(k, R).$$

The fastest growing disturbance, with the maximum growth rate α^* and corresponding critical wave number k^*, will eventually dominate the dynamics and cause the jet to pinch off into droplets. Solutions of the dispersion relation determine jet stability, as well as the rate at which the jet will destabilise. It is also possible to derive conditions for the critical wavelength λ^* and therefore the ultimate break-up length of the jet.

For an inviscid jet $\mu = 0$, conservation of momentum and incompressibility can be combined to give the Laplace equation

$$\nabla^2 p = 0, \tag{2.2}$$

for pressure p under a linear approximation. We seek axisymmetric perturbations about the base state $\mathbf{u}_0 = 0$ of the form

$$\mathbf{u}(r, z) = \mathbf{u}_0 + \tilde{\mathbf{u}}(r, z) \quad ; \quad p(r, z) = p_0 + \tilde{p}(r, z),$$

in the radial r and axial z directions. The pressure perturbation takes the form

$$\tilde{p}(r, z) = F(r)\cos(kz),$$

where the function $F(r)$ is found from the Laplace equation (2.2) to satisfy

$$\frac{\partial^2 F}{\partial r} + \frac{1}{r}\frac{\partial F}{\partial r} - k^2 F = 0,$$

the non-singular solution of which is the modified Bessel function $F(r) = p' I_0(kr)$ for disturbance amplitude p'.

We now seek a boundary condition for the liquid-air interface, where the Laplace pressure is $\Delta p = \gamma\kappa$. The perturbation about the free surface takes the form

$$\tilde{h}(z,t) = R + \epsilon(t)\cos(kz),$$

where R is the radius of the base state. Then, by the definition of the mean curvature given by equation (2.1), the linearised pressure perturbation at the free surface is given by

$$\tilde{p}(r = R, z) = -\frac{\gamma}{R^2}\left(1 - k^2R^2\right)\epsilon\cos(kz),$$

and

$$\tilde{p}(r,z) = -\frac{\gamma}{R^2}(1 - k^2R^2)\frac{I_0(kr)}{I_0(kR)}\epsilon\cos(kz). \tag{2.3}$$

The problem is closed by relating the amplitude of the pressure perturbation p' to the interface displacement $\epsilon(t)$.

We assume that the time dependence of the perturbation is given by

$$\epsilon(t) = h'\exp(-\alpha t),$$

for the disturbance growth rate α and amplitude h'. In a linear approximation, the motion of the free surface is determined by the kinematic equation to be

$$\frac{\partial\tilde{h}}{\partial t} = \tilde{u}_r(r = R, z).$$

Furthermore, the radial velocity $\tilde{u}_r$ is related to the pressure by the linearised conservation of momentum equation

$$\frac{\partial\tilde{u}_r}{\partial t} = -\frac{1}{\rho}\frac{\partial\tilde{p}}{\partial r}.$$

Thus, the free-surface evolution is described by the equation

$$\frac{\partial^2\tilde{h}}{\partial t^2} = -\frac{1}{\rho}\frac{\partial\tilde{p}}{\partial r}(r = R, z).$$

Seeking the time-dependent perturbation $\epsilon(t) = h'e^{-\alpha t}$, along with the pressure perturbation given by equation (2.3), yields the dispersion relation

$$\alpha^2 = \frac{\gamma k}{\rho R^2}(1 - k^2R^2)\frac{I_1(kR)}{I_0(kR)}, \tag{2.4}$$

first derived by Rayleigh [109], where I_0 and I_1 denote the modified Bessel functions.

The growth rate α depends on the ratio of the driving surface tension to the initial jet radius; the larger the surface tension, the faster the growth rate of disturbance wave. Furthermore, for α to have real positive roots requires

$$kR < 1 \Rightarrow \lambda > 2\pi R.$$

Thus, jets are stable and will not break up into droplets provided that the wavelength is less than the jet circumference.

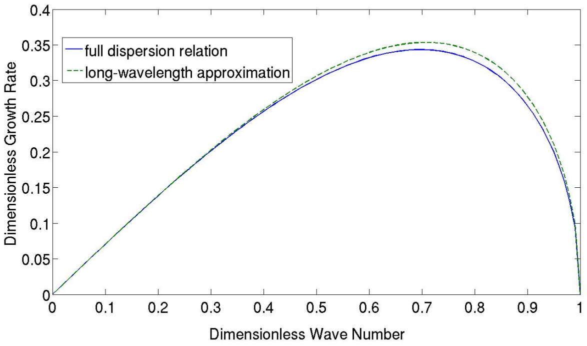

Figure 2.2: The dimensionless growth rate αT determined by the dimensionless wave number kR for an inviscid jet given by dispersion relation (2.4) and the long-wavelength approximation (2.5).

Solving the dispersion relation (2.4) yields the maximum growth rate

$$\alpha^* = \frac{1}{3}\sqrt{\frac{\gamma}{\rho R^3}},$$

with the characteristic time scale for the instability determined by a balance of inertia and surface tension

$$T = \sqrt{\frac{\rho R^3}{\gamma}}.$$

The corresponding critical wave number

$$k^* R \approx 0.7,$$

is the most amplified wave number, known as the Rayleigh mode, and corresponds to wavelength

$$\lambda^* \approx 9R.$$

Since the most unstable wavelength is given by approximately 9 times the jet radius, a long wavelength model describes the linear stability of a jet well, provided that the full curvature (2.1) is kept to describe the cut off at short wavelengths.

Hence, assuming that the wavelength of the disturbance is large compared to the initial jet radius so that $kR \ll 1$, the modified Bessel functions appearing in equation (2.4) can be approximated by the leading-order term in the expansions such that

$$I_0 = 1 \quad ; \quad I_1 = \frac{kR}{2}.$$

Thus, for a long-wavelength approximation of an inviscid jet, the dispersion relation (2.4) is simplified to

$$\alpha^2 = \frac{\gamma k^2}{2\rho R}(1 - k^2 R^2), \tag{2.5}$$

which has maximum growth rate

$$\alpha^* T = \frac{1}{2\sqrt{2}}.$$

Figure 2.2 compares the dimensionless growth rate αT predicted by the long-wavelength approximation given by equation (2.5) to that calculated from the full dispersion relation (2.4).

2.2.2 A Dispersion Relation for Viscous Jets

It is also possible to perform the linear stability analysis for the viscous case by solving perturbations to the full Navier-Stokes equations. However, the resulting analytic formulae involve Bessel functions and the effects of viscosity are more easily seen by considering the simplification of Rayleigh's analysis that assumes the long-wavelength approximation.

Recall that the Newtonian slender-jet equations (1.13) for the free-surface height $h(z,t)$ and velocity $v(z,t)$ are given by

$$\begin{gathered}\frac{\partial h^2}{\partial t}+\frac{\partial}{\partial z}(h^2 v)=0,\\ \rho\left(\frac{\partial}{\partial t}(h^2 v)+\frac{\partial}{\partial z}(h^2 v^2)\right)=\frac{\partial}{\partial z}\left(h^2\left(\gamma K+3\mu\frac{\partial v}{\partial z}\right)\right),\end{gathered}$$

where the curvature term is defined as

$$K\equiv\frac{1}{h(1+h_z^2)^{1/2}}+\frac{h_{zz}}{(1+h_z^2)^{3/2}}.$$

By taking this long-wavelength approximation, we implicitly assume that the jet radius is much smaller than the perturbation wavelength so that $kR \ll 1$. Note that the stability of modes with $kR > 1$ is not affected by viscosity since the stability arises from the curvature term.

We consider small perturbations about the base state

$$h_0 = R \quad ; \quad v_0 = 0,$$

which take the form

$$h = R(1+\tilde{h}(z,t)) \quad ; \quad v = \tilde{v}(z,t).$$

We then seek solutions

$$\begin{aligned}\tilde{h}(z,t)&=h'\exp(ikz+\alpha t),\\ \tilde{v}(z,t)&=v'\exp(ikz+\alpha t),\end{aligned}\tag{2.6}$$

where the prime $'$ denotes the amplitude of the perturbation, k is the wave number and α is the growth rate of the disturbance.

Applying the perturbation to conservation of mass and linearising yields

$$2\frac{\partial\tilde{h}}{\partial t}+R\frac{\partial\tilde{v}}{\partial z}=0.$$

Then, substituting solution (2.6), we find the amplitude of the free-surface perturbation to be

$$h'=-\frac{1}{2}\frac{ik}{\alpha}v'.$$

Similarly, applying the perturbed state to conservation of momentum and linearising yields

$$\rho R^2\frac{\partial\tilde{v}}{\partial t}=\gamma\left(R^2\frac{\partial^3\tilde{h}}{\partial z^3}+\frac{\partial\tilde{h}}{\partial z}\right)+3\mu R^2\frac{\partial^2\tilde{v}}{\partial z^2}.$$

and substituting solution (2.6) gives

$$\left(\alpha + \frac{3\mu k^2}{\rho}\right) v' = \frac{\gamma}{\rho R}(1 - R^2k^2)ikh'.$$

Finally, eliminating h', we arrive at the dispersion relation

$$\alpha^2 + \frac{3\mu k^2}{\rho}\alpha - \frac{\gamma k^2}{2\rho R}(1 - k^2R^2) = 0, \tag{2.7}$$

as first derived by Rayleigh [109] for a viscous cylinder of fluid.

In this case, the growth rate of the disturbance depends on the balance between the driving surface tension and the resisting viscosity and fluid inertia. Solving the dispersion relation via implicit differentiation yields the maximum growth rate

$$\alpha^* T = \frac{1}{2\sqrt{2} + 6Oh},$$

for Ohnesorge number

$$Oh = \frac{\mu}{\sqrt{\rho\gamma R}},$$

and corresponding wave number

$$k^* R = \frac{1}{\sqrt{2 + 3\sqrt{2}Oh}}.$$

Thus, viscous forces are predicted to dampen the growth rate of disturbances so that the lifetime of the jet is increased, as expected.

In this case, the critical wavelength λ^* depends on the viscosity of the jet as well as the jet radius. Consider the surface displacement of the form

$$\tilde{h} = h' \exp(ik^*z + \alpha^*t),$$

where h' is the amplitude of the most rapidly growing disturbance. Then, the time taken for the perturbation at $z = 0$ to become comparable to the initial jet radius R is

$$t^* = \frac{1}{\alpha^*} \ln\left(\frac{R}{h'}\right).$$

Defining the break-up length as $\lambda^* = Ut^*$, for a characteristic jet velocity U, yields

$$\lambda^* = C\frac{U}{\alpha^*},$$

for some constant C that can be determined experimentally. Thus, for maximum growth rate α^*, the break-up length is determined by

$$\frac{\lambda^*}{R} \approx \sqrt{We}\left(2\sqrt{2} + 6Oh\right),$$

for Weber number

$$We = \frac{\rho U^2 R}{\gamma}.$$

Hence, the critical break-up length is seen to increase with viscosity.

Figure 2.3 shows the dimensionless growth rate αT for a range of Ohnesorge numbers. An inviscid jet is the most unstable and the maximum growth rate of disturbance occurs at

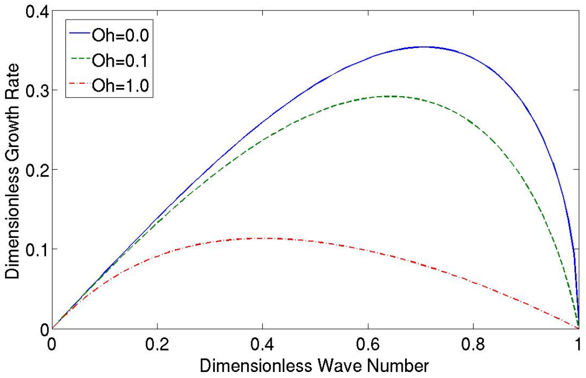

Figure 2.3: The dimensionless growth rate αT determined by the dimensionless wave number kR for an inviscid jet and viscous jets having Ohnesorge numbers $Oh = 0.1$ and $Oh = 1.0$.

$k^*R \approx 0.7$, the critical Rayleigh wave number. As the Ohnesorge number is increased, the maximum growth rate is reduced due to viscosity retarding the disturbance. Furthermore, the critical wave number corresponding to the maximum growth rate is shifted to smaller values highlighting the fact that the length of the most unstable wave increases for higher viscosity jets.

2.2.3 The Stability of Polymeric Jets

The study of non-Newtonian effects on the stability of a liquid jet is comparatively recent compared to Rayleigh's work. Since the linear stability analysis proved very successful in predicting the behaviour of Newtonian fluids, a similar analysis was desired for viscoelastic jets.

In 1965, Middleman [96] was first to publish a viscoelastic dispersion relation, based on the Oldroyd fluid model, by extending the stability analysis of the slender-jet model described in the previous section to include viscoelasticity. The solution of this simple approach predicts that viscoelastic jets are less stable compared to the corresponding Newtonian case having the same viscosity. This surprising result contradicts much experimental evidence demonstrating that viscoelasticity prolongs the lifetime of a jet.

Later Goldin *et al.* [62] extend the full stability analysis of an axisymmetric jet to a generalised viscoelastic material and compare their results to experimental data. They also conclude that a liquid column of viscoelastic fluid exhibits a faster growth rate of axisymmetric disturbance waves than a Newtonian fluid and show that this result is independent of the constitutive equation chosen. Experiments in weakly elastic fluids confirm their expectation. However, for jets having more pronounced elastic properties, the break-up observed does not occur by the growth of clearly defined disturbance waves. In this case, non-linear phenomena dominate and so the linear stability analysis is not valid. Goldin *et al.* also note that the analysis assumes a relaxed initial profile; if stress relaxation occurs along a significant proportion of the jet, then this assumption ceases to be valid.

Brenn *et al.* [20] further extend the full analysis to include the effects of an inviscid gaseous environment. Again a linear theory predicts that a non-Newtonian liquid breaks up faster than a corresponding Newtonian liquid but is inapplicable for calculating the break-up lengths of viscoelastic jets due to the strong influence of nonlinear dynamics in the final stages of thinning. They conclude that a high-density environment enhances the instability of viscoelastic jets.

In this section, we extend the stability analysis of the slender-jet model given by equation (1.13) to incorporate the effects of viscoelasticity using the Oldroyd-B model. We derive the viscoelastic dispersion relation and demonstrate the effect that viscoelasticity has on the initial growth rate of disturbance waves, which contradicts the stabilising effect observed in experiments.

Consider the general slender-jet equations for radius $h(z,t)$ and velocity $v(z,t)$ given by

$$\begin{aligned} &\frac{\partial h^2}{\partial t} + \frac{\partial}{\partial z}(h^2 v) = 0, \\ &\rho\left(\frac{\partial}{\partial t}(h^2 v) + \frac{\partial}{\partial z}(h^2 v^2)\right) = \frac{\partial}{\partial z}\left(h^2(\gamma K + \sigma_{zz} - \sigma_{rr})\right), \end{aligned} \tag{2.8}$$

where the axial and radial stress components, σ_{zz} and σ_{rr} respectively, are determined by a choice of constitutive equation. For a general linear viscoelastic model, as used by Goldin *et al.* [62], the stress tensor satisfies

$$\sigma_{ij} = 2\int_{-\infty}^{t} G(t-t')E_{ij}(t')dt',$$

where $G(t)$ is the relaxation modulus and E_{ij} is the strain rate tensor. For the case where E_{ij} is of the form

$$E_{ij} = E'_{ij}\exp(ikz + \alpha t),$$

we can write the stress perturbation as

$$\tilde{\sigma}_{ij} = 2E'_{ij}\eta(\alpha)\exp(ikz + \alpha t),$$

where the viscosity is defined as

$$\eta(\alpha) = \int_0^{\infty} G(s)e^{-\alpha s}ds.$$

Note that the base state of the stress tensor is assumed to be zero.

For simplicity, we take the Oldroyd-B approximation, where this viscosity is written as a sum of the solvent viscosity μ_s and the polymer contribution to viscosity such that

$$\eta(\alpha) = \mu_s + \frac{G\tau}{1+\alpha\tau}, \tag{2.9}$$

for relaxation time τ. In this way, the long-wavelength approximation for conservation of momentum (2.8) reduces simply to

$$\rho\left(\frac{\partial}{\partial t}(h^2 v) + \frac{\partial}{\partial z}(h^2 v^2)\right) = \frac{\partial}{\partial z}\left(h^2\left(\gamma K + 3\eta(\alpha)\frac{\partial v}{\partial z}\right)\right),$$

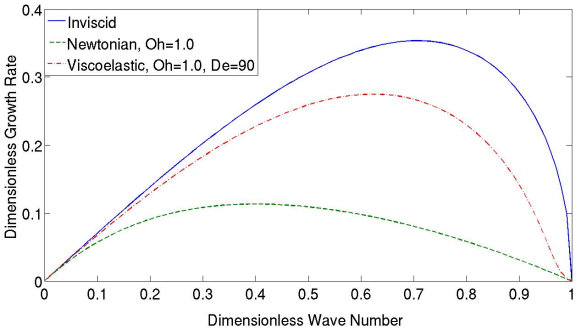

Figure 2.4: The dimensionless growth rate αT determined by the dimensionless wave number kR for a viscoelastic jet with $Oh = 1.0$ and $De = 90$ compared to an inviscid jet and the corresponding Newtonian jet with $Oh = 1.0$.

and the stability analysis is equivalent to the Newtonian case with $\eta(\alpha) = \mu_s$.

Hence, the dispersion relation is deduced directly from the Newtonian case (2.7) to be

$$\alpha^2 + \frac{3\eta(\alpha)k^2}{\rho}\alpha - \frac{\gamma k^2}{2\rho R}(1 - k^2R^2) = 0, \tag{2.10}$$

with maximum growth rate

$$\alpha^* T = \frac{1}{2\sqrt{2} + 6Oh_{\eta^*}},$$

for the modified Ohnesorge number

$$Oh_{\eta^*} = \frac{\eta(\alpha^*)}{\sqrt{\rho\gamma R}}.$$

Comparing this viscoelastic growth rate α^* to that of the Newtonian fluid α_0^* yields

$$\frac{\alpha_0^*}{\alpha^*} = \frac{2\sqrt{2} + 6Oh_{\eta^*}}{2\sqrt{2} + 6Oh},$$

which indicates that the ratio α_0^*/α^* depends only on the magnitude of the viscosity at the maximum growth rate α^*. Furthermore, we have

$$\frac{\eta(\alpha)}{\mu_s + G\tau} < 1, \qquad \text{for } \alpha > 0,$$

demonstrating that the viscosity is a monotonically decreasing function of the growth rate, with μ_s as the lower limit. Thus, we can conclude that

$$\eta(\alpha^*) > \eta(\alpha_0^*) \Rightarrow \alpha^* > \alpha_0^*,$$

revealing that the growth rate of a viscoelastic jet is faster than that of the corresponding Newtonian jet. This result is consistent with the full stability analysis for a linear generalised viscoelastic fluid, as given by Goldin *et al.* [62].

Thus, contrary to experimental observations of the break-up length of viscoelastic jets, the linear stability analysis shows that a viscoelastic jet is less stable than a Newtonian jet of the same zero-shear-rate viscosity. Confirming this result, Figure 2.4 compares the dispersion relation for an inviscid jet (2.5), the Newtonian dispersion relation with

Ohnesorge number $Oh = 1$ given by equation (2.7) and the equivalent viscoelastic case given by equation (2.10) with the Deborah number

$$De = \frac{\tau}{T},$$

set to $De = 90$.

2.2.4 Unrelaxed Viscoelastic Tension

Goren & Gottlieb [63] were first to recognise that a liquid jet may be subject to an unrelaxed axial tension due to the deformation history, and consequently, the initial growth of small perturbations may be affected. The idea is that, although the jet radius and velocity approach asymptotic values some distance several jet diameters downstream of the nozzle exit, as a result of shear stresses within the nozzle, the axial tension may not have decayed to zero. In this section, we consider a simple case of the theory presented by Goren & Gottlieb [63], where we assume the long-wavelength approximation of a viscoelastic jet described by the Oldroyd-B model. The analysis predicts that a non-zero elastic tension in the axial direction can be a stabilising influence.

Suppose that the axial tension decays exponentially according to

$$T(z) = T_0 \exp(-z/\tau U),$$

for jet velocity U, relaxation time τ and initial axial tension T_0. Thus, the base state of the axial stress σ_{zz} is no longer zero and a small disturbance is imposed such that

$$\sigma_{ij}(z,t) = T\hat{\mathbf{z}}\hat{\mathbf{z}} + \tilde{\sigma}_{ij}(z,t),$$

for unrelaxed tension T in the $\hat{\mathbf{z}}\hat{\mathbf{z}}$-direction.

Again, applying the linear stability analysis to the long-wavelength approximation for a viscoelastic fluid described by the Oldroyd-B constitutive model with viscosity (2.9), the following dispersion relation is derived:

$$\alpha^2 + \frac{3k^2\eta(\alpha)}{\rho}\alpha - \frac{\gamma k^2}{2\rho R}(1 - k^2R^2) - \frac{Tk^2}{\rho}\left(\frac{1-\alpha\tau}{1+\alpha\tau}\right) = 0.$$

If the axial tension $T = 0$, then the relation reduces to the earlier viscoelastic case (2.10). However, an unrelaxed axial tension $T > 0$ is stabilising provided that $\alpha\tau > 1$. Thus, in the high Deborah number limit, unrelaxed tension acts to resist the driving surface tension and reduces the maximum growth rate of the disturbance wave, as shown in Figure 2.5 for $T = 0.5$, $De = 90$, $Oh = 1.0$.

Goren & Gottlieb claim that the addition of an unrelaxed axial tension to the linear stability analysis accounts for the increased stability of viscoelastic jets observed in experiments. However, a quantitative comparison of the full theory with experimentally measured breakage patterns requires measurement of rheological responses from which time restraints can be inferred, as well as a measure of the initial elastic tension T_0.

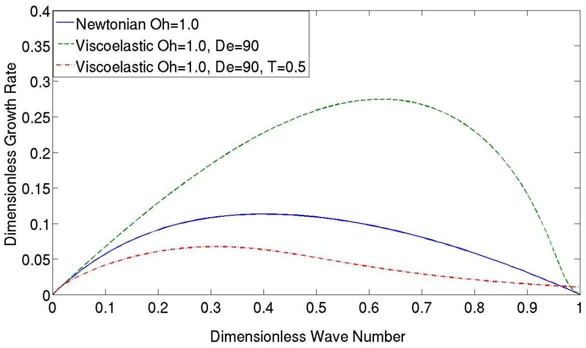

Figure 2.5: The dimensionless growth rate αT determined by the dimensionless wave number kR for a viscoelastic jet with unrelaxed axial tension $T = 0.5$, compared to the usual viscoelastic (2.10) and Newtonian (2.7) dispersion relations for $Oh = 1.0$ and $De = 90$.

Following this proposal, Bousfield *et al.* [18] present a full non-linear analysis of surface-tension driven break-up, which numerically predicts the entire evolution of a viscoelastic filament in the small Deborah number limit. They claim that, although large initial stresses originating from the nozzle flow will delay the initial growth rate of the disturbance wave, they are unlikely to be relevant to the ultimate break-up mechanism.

Their finite-element solution of the Navier-Stokes and Oldroyd-B constitutive equations for an infinite jet shows that the initial capillary instability grows more rapidly on viscoelastic filaments than Newtonian filaments of the same zero-shear-rate viscosity, in agreement with the linear stability analysis. However, as the amplitude of the disturbances grow, non-linear extensional stresses stabilise the filament and delay break-up time, such that the minimum radius ultimately decays exponentially at a rate $1/3\tau$. Furthermore, their one-dimensional approximation is consistent with the full numerical result and the predicted profile evolution is in agreement with experimental data for the break-up of Newtonian and polymeric jets. Thus, Bousfield *et al.* conclude that, although a residual tensile stress from the nozzle flow will retard the initial disturbance growth rate, ultimately it is non-linear extensional stresses that control the final break-up length of a viscoelastic jet.

2.3 Asymptotic Scaling Laws and Break-up

2.3.1 Newtonian Thinning Near to Pinch Off

As we have seen, the initial stages of Newtonian thinning are governed by linear theory. The growth rate of a disturbance wave is exponential so that the break-up time and the break-up length can be estimated. However, this linear theory does not explain features of break-up, such as satellite drops, due to the exclusion of non-linear effects. A theory for drop formation, based on flow close to break-up, has been developed by Eggers [49].

As a jet thins and approaches break-up, the minimum radius of the jet approaches zero creating a singularity in the curvature term. Thus, solutions to the governing equations do not posses a characteristic time scale. However, the behaviour of this singular solution is expected to be governed by a universal scaling law, independent of initial or boundary conditions. The physical reasoning for this assumption is that singularities involve the production of infinitesimally small scales and ultimately, the governing equations evolve on scales widely separate from those set by the boundary conditions. It is therefore appropriate to seek solutions that are invariant under a suitable scale formation; a universal solution, which, in the absence of a time scale, is self-similar near to the singularity.

Asymptotically, break-up always proceeds according to a solution that balances surface tension γ, viscosity μ and inertial forces. Thus, the natural length and time scales for an invariant self-similar solution are chosen to be

$$L = \frac{\mu^2}{\gamma\rho} \quad ; \quad T = \frac{\mu^3}{\gamma^2\rho},$$

for fluid density ρ. Choosing z_b and t_b as the origin of the singularity, the dimensionless distance and time from break-up are given by

$$z' = \frac{z - z_b}{L} \quad ; \quad t' = \frac{t_b - t}{T}.$$

A crucial simplification to the asymptotic analysis of break-up comes in by taking a long-wavelength description of the jet as given by equation (1.13) in Chapter 1. Close to the singularity, higher-order radial terms appearing in the long-wavelength expansion become arbitrarily small and this slender-jet description gives the exact asymptotic representation of the full governing equations.

In the pinch region such that $|z'| \ll 1$ and $|t'| \ll 1$, the radius and velocity are expected to obey the power laws

$$h(z,t) = Lt'^{\alpha_1}\phi(\xi) \quad ; \quad v(z,t) = \left(\frac{L}{T}\right) t'^{\alpha_2}\psi(\xi),$$

for some similarity functions $\phi(\xi), \psi(\xi)$, where the similarity variable is

$$\xi = \frac{z'}{t'^{\beta}}.$$

The power law exponents are found by balancing the terms of the original equation or the one-dimensional counter-part. It is easy to confirm that with the choice $\alpha_1 = 1, \alpha_2 = -1/2$ and $\beta = 1/2$, this self-similar profile satisfies the slender-jet equations (1.13) for $t' \to 0$. The slender-jet equations (1.13) are then transformed to similarity equations for the scaling functions ϕ, ψ:

$$\phi' = \phi \frac{1 - \psi'/2}{\psi + \xi/2},$$

$$\frac{\psi}{2} + \xi\frac{\psi'}{2} + \psi\psi' = \frac{\phi'}{\phi^2} + 3\psi'' + 6\frac{\psi'\phi'}{\phi},$$

where the prime $'$ denotes differentiation with respect to the similarity variable ξ.

This system has many solutions, which correspond to a discrete sequence of self-similar profiles for increasingly small radii. A unique physical solution can be obtained by applying

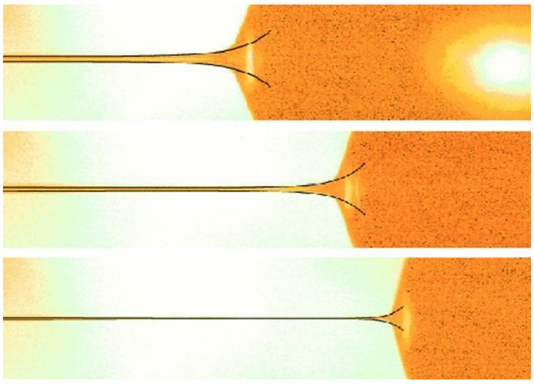

Figure 2.6: A sequence of free surface profiles of a jet of glycerol close to the point of break-up compared to the self-similar solution (2.11), taken from reference [53].

matching conditions to the flow away from the singularity. Numerical evidence suggests that only the first solution in the sequence, the solution which gives the thickest minimum radius, is stable and therefore gives a physically realistic solution. The minimum of this stable similarity solution is found to be $\phi_{min} \approx 0.030426\cdots$, which predicts a minimum jet radius of

$$h_{min} = 0.0304 \left(\frac{\gamma}{\mu}\right)(t_b - t). \tag{2.11}$$

This equation (2.11) is fully derived by Eggers [49] for the universal pinching of 3D axisymmetric free-surface flow. Figure 2.6 shows that this similarity solution (2.11) appears increasingly elongated, leading to a thin filament connected to the main drop. Thus, the solution is highly asymmetric; the steep side merges onto the drop whereas the other takes the form of a thin thread. The neck connecting the two regions is where break-up occurs, causing the filament to contract and create a small spherical satellite drop [51].

For extreme values of Ohnesorge number, other self-similar thinning regimes are also possible. If the initial jet radius R is much greater than the length scale L, then the dynamics are characterised by a balance between inertia and surface tension. So for low Ohnesorge numbers ($Oh \ll 1$), the fluid viscosity can be neglected and the thinning is described solely by inviscid dynamics. Inviscid pinch-off is particularly important in inkjet printing, both during ejection from the nozzle and the subsequent break up of airborne drops. The pinch-off region of an inviscid flow takes the form of a double cone due to an overturning profile. Since such a shape is strictly two-dimensional, pinch-off cannot be examined by the slender-jet equations; instead the full inviscid equations must be solved. From the balance of surface tension and inertia, a dimensional analysis shows that the only non-dimensional grouping of the fluid parameters is $\gamma t^2/R^3\rho$. Thus, the natural length scale for break-up in this case is

$$\left(\frac{\gamma t^2}{\rho}\right)^{1/3}.$$

The similarity solution derived by Day *et al.* [40] is found to have a double-cone shape with angles 18.1° and 112.8° and the minimum jet radius is given by

$$h_{min} = 0.64 \left(\frac{\gamma}{\rho}\right)^{1/3} (t_b - t)^{2/3},$$

which is again independent of initial conditions. In this case, pinching is also asymmetric, occurring near to the end-drops so that a satellite drop is produced at break-up.

On the other hand, if initially the jet radius R is much smaller than the viscous length scale L, then inertia cannot play a significant role. So for large Ohnesorge numbers ($Oh \gg 1$), inertial forces can be neglected and the dynamics are characterised by a balance between viscosity and surface tension. Papageorgiou [103] was first to examine the thinning properties of a viscous thread and the model is based on Stokes equations for viscous flow under the slender-jet approximation. The equations are solved numerically and the jet radius found to vanish after a finite time, with the minimum radius behaving like

$$h_{min} = 0.0709 \left(\frac{\gamma}{\mu}\right) (t_b - t).$$

The model admits self-similar solutions that, unlike Eggers solution (2.11), give symmetric shapes at break-up; the jet ruptures at the mid-filament position and no satellite drops are produced at break-up. It is also verified that the terminal state of the simplified model is identical to that predicted without invoking the slender-jet assumption.

The dominant parameter controlling thinning dynamics can be understood by considering the local Ohnesorge number

$$Oh = \frac{\mu}{\sqrt{\rho\gamma h}},$$

for jet radius h. In order to determine the critical Ohnesorge number defining the boundary between viscous and inertia dominated regimes, we consider the thinning velocity of each regime, as proposed by Campo-Deano *et al.* [21]. The velocity of a thinning liquid filament can be calculated by differentiating the radius with respect to time:

$$u_z = -\frac{\partial h}{\partial t}.$$

Thus, the thinning velocities of the viscous regime and the inertial regime are given respectively by

$$U_\mu = 0.0709\frac{\gamma}{\mu} \quad ; \quad U_\rho = 0.3414\sqrt{\frac{\gamma}{\rho h}}.$$

Formulating the Ohnesorge number from the ratio of these thinning velocities yields

$$\frac{U_\mu}{U_\rho} = \frac{Oh}{0.2077},$$

and the critical Ohnesorge number identifying the boundary between regimes is defined when the thinning velocities are equal $U_\mu = U_\rho$. Thus, the critical Ohnesorge number is

$$Oh^* = 0.2077,$$

with excellent agreement to the experimental results of Campo-Deano *et al.* [21]. Hence, for fluids with $Oh < Oh^*$ behaviour is initially governed by inertial forces, whereas a viscosity dominated regime is observed for fluids such that $Oh > Oh^*$. However, both the inertial and viscous regimes eventually cross over to the universal Eggers solution (2.11) for some critical radius.

In the case of inertial flow, as the filament radius becomes thinner, the local Ohnesorge number increases so that eventually viscous effects are significant. Somewhat surprisingly in the viscous regime, inertia eventually becomes important. This is because as the minimum radius shrinks to zero, the extension rate becomes infinite, leading to a divergence of axial velocity and hence a growth of the local Reynolds' number. In each case, the local balance induces a transition to the Eggers regime (2.11) in which all three forces become significant. However, the critical radius at which this transition occurs may not be within the limits of observation or the continuum approximation.

2.3.2 Satellite Drop Formation

Savart [118] was one of the first experimentalists to note the appearance of smaller satellite drops interspersed between the main drops of fluid in the break-up of a continuous jet. Since then, the understanding of satellite drop formation has been the motivation behind much research on drop formation.

Qualitatively, satellites appear through two properties of the pinching singularity. First, the singularity is localised and causes break-up at a specific point on the jet free surface. Second, for low-viscosity fluids, self-similar thinning is highly asymmetric, with a thin filament of fluid joining the main drop and break-up occurring in the connecting neck region. Consequently, at break-up the filament separates from the main drop and contracts to form a smaller satellite drop in a symmetric flow.

Since linear theories based on the Rayleigh stability analysis do not predict the formation of satellite drops, the development of weakly non-linear theories is required. In particular, Yeun [145] and Lee [86] use the method of strained coordinates to develop a solution for an inviscid jet, up to third order, for a temporal disturbance of the free surface. Yeun's theory predicts the formation of satellite drops for all wave numbers and that the detachment of the satellite drop from the two adjacent main drops occurs at both necks simultaneously, due to the symmetry of the flow.

However, as shown in Figure 2.7, satellites can form in several different ways depending on the nature of the applied initial disturbance. In most liquid jet applications it is necessary to excite the jet via a velocity perturbation creating a disturbance wave that grows with distance from the nozzle exit. Keller *et al.* [77] show that this disturbance is only equivalent to a temporally growing Rayleigh wave in the limit of infinite Weber number. Consequently, Pimbley & Lee [106] conduct a non-linear analysis of the drop formation problem, through to second-order, via a spatial instability analysis.

Pimbley & Lee [106] find that the two most relevant parameters that control satellite formation are the amplitude and wavelength of the initial perturbation. For certain values of these parameters satellite detachment can occur on the fore side of the droplet first,

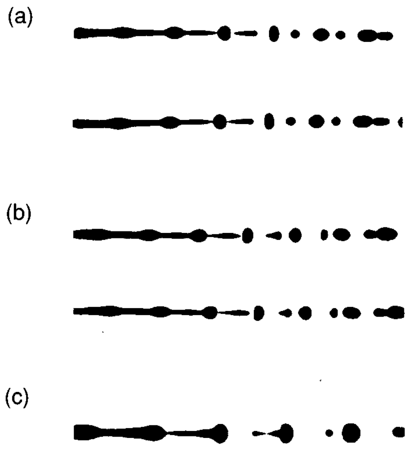

Figure 2.7: Satellite formation at three different initial perturbation amplitudes, increasing from (a) to (c) taken from reference [26].

the aft side first, or on both sides simultaneously. This transition is characterised by a ‘satellite interaction’ time, which is defined by the time period between the two breaks and signifies a transfer of momentum. If there is a strong backward pull, then this causes rear-merging as in Figure 2.7(a), whereas forward momentum causes the drop to merge with the leading drop as in Figure 2.7(c). Zero satellite interaction time marks an infinity condition, where the two breaks occur simultaneously, as shown in Figure 2.7(b).

Pimbley & Lee’s theory agrees qualitatively with the experimental findings of Chaudhary & Maxwell [26] in that there is a transition from rear to forward-merging behaviour for increasing perturbation amplitude and the critical amplitude corresponding to the infinity condition increases with wave number. Furthermore, Chaudhary & Maxwell [27] show that this break-up behaviour can be controlled by forcing the jet with a suitable harmonic component added to the initial velocity profile. However, left out of these studies is the effect of changing Weber number, which has been shown by Vasallo & Ashgriz [135] to have a significant effect.

2.3.3 Exponential Thinning of Polymeric Fluids

Simple Newtonian fluids thin relatively rapidly and break up into droplets. However, the addition of small amounts of polymer to a Newtonian solvent significantly delays this surface-tension-driven thinning due to the presence of resistive elastic forces. Consequently, the formation of satellite drops can be eliminated.

For small deformations, polymer molecules remain coiled in an equilibrium state. So, for the temporal instability on an infinite jet, the early stages of polymeric thinning follow the behaviour predicted by the instability theory for linear viscoelastic fluids described in section 2.2.3. However, capillary forces induce a strong extensional flow, which acts to unravel the polymer molecules from their equilibrium state. This mechanism causes elastic stresses to build up in the fluid. Consequently, thinning deviates from linear viscoelastic behaviour and enters an elasto-capillary regime in which non-linear viscoelasticity balances surface tension [54].

During this elasticity-dominated regime, viscoelastic jets thin exponentially in time. To prevent the molecules from relaxing, the jet radius must decay continuously in time at a rate proportional to the relaxation time of the fluid. Thus, the extension rate in the thinning filament is constant and the radius decreases exponentially in time at an inverse rate that is three times the relaxation time of the fluid [35]. Thus, measurement of the elasto-capillary thinning rate enables a direct determination of the relaxation time.

The polymeric resistance to stretching causes long, thin filaments to form between the main drops of fluid, as shown in Figure 2.8. Thus, a one-dimensional model provides a sensible approximation in order to derive the exponential thinning regime [54], [35]. In this section we derive the exponential thinning law for a thin filament of viscoelastic fluid described by the Oldroyd-B constitutive model, based on the slender-jet equations for free-surface height $h(z,t)$ and velocity $v(z,t)$ given by

$$\frac{\partial h^2}{\partial t} + \frac{\partial}{\partial z}(h^2 v) = 0,$$
$$\rho\left(\frac{\partial}{\partial t}(h^2 v) + \frac{\partial}{\partial z}(h^2 v^2)\right) = \frac{\partial}{\partial z}\left(h^2\left(\gamma K + 3\mu\frac{\partial v}{\partial z} + \sigma_{zz} - \sigma_{rr}\right)\right).$$

where curvature term K is defined as

$$K \equiv \frac{1}{h(1+h_z^2)^{1/2}} + \frac{h_{zz}}{(1+h_z^2)^{3/2}}. \tag{2.12}$$

In the Oldroyd-B framework, the polymeric stress is defined as

$$\boldsymbol{\sigma} = G(\mathbf{A} - \mathbf{I}),$$

for elastic modulus G and conformation tensor $\mathbf{A}$, which describes the deformation of infinitely extensible dumbbells. The evolution of the stress is then given by

$$\frac{D\boldsymbol{\sigma}}{Dt} = G\frac{D\mathbf{A}}{Dt},$$

where substituting for the linear dumbbell evolution equation yields

$$\frac{D\boldsymbol{\sigma}}{Dt} = \mathbf{K}\cdot\boldsymbol{\sigma} + \boldsymbol{\sigma}\cdot\mathbf{K}^T + G(\mathbf{K}+\mathbf{K}^T) - \frac{\boldsymbol{\sigma}}{\tau},$$

Thus, the axial stress evolution is given by

$$\frac{\partial \sigma_{zz}}{\partial t} + v\frac{\partial \sigma_{zz}}{\partial z} = 2\frac{\partial v}{\partial z}\sigma_{zz} + 2\frac{\mu_p}{\tau}\frac{\partial v}{\partial z} - \frac{\sigma_{zz}}{\tau},$$

for polymer contribution to viscosity $\mu_p = G\tau$.

We assume that the jet radius decays exponentially such that

$$h = R_0 \exp(-\alpha t),$$

where R_0 denotes the initial radius of the uniform filament region, shown in Figure 2.8, and α denotes the growth rate. Inserting this solution into conservation of mass gives

$$\frac{\partial v}{\partial z} = 2\alpha,$$

indicating that the extension rate is constant in the filament region. Thus, assuming that the axial stress σ_{zz} is spatially constant, the stress evolution equation reduces to

$$\frac{\partial \sigma_{zz}}{\partial t} = 4\alpha\sigma_{zz} - \frac{\sigma_{zz}}{\tau}.$$

Hence, the axial stress is found by integration to be

$$\sigma_{zz} = \sigma_0 \exp\left(\left(4\alpha - \frac{1}{\tau}\right)t\right),$$

for an initial stress σ_0.

During elasto-capillary thinning, the capillary force, governed by the curvature term K, balances the axial elastic stress σ_{zz}. Thus, inertia is neglected from conservation of momentum and, since $\frac{\partial v}{\partial z}$ is constant, the elasto-capillary balance is determined by

$$\frac{\partial}{\partial z}(h^2(\gamma K + \sigma_{zz})) = 0,$$

where the radial stress σ_{rr} is assumed to be small. Thus, in the uniform filament region, $K \approx 1/h$ and integrating yields

$$\gamma h + h^2\sigma_{zz} = T,$$

where T denotes the tension in the filament, which is assumed to be non-zero [35]. For consistency, σ_{zz} must grow like $1/h$, thus

$$\exp\left(\left(4\alpha - \frac{1}{\tau}\right)t\right) = \exp(\alpha t),$$

giving a growth rate of $\alpha = 1/3\tau$. Thus, the filament radius decays like

$$h(z,t) = R_0 \exp\left(-\frac{t}{3\tau}\right).$$

The initial radius R_0 of the uniform filament can then be calculated by matching the filament region to the end drop, as shown in Figure 2.8.

For uniaxial extension, the extension rate is given by

$$\dot{\epsilon} = -\frac{2}{h}\frac{\partial h}{\partial t}.$$

Thus, assuming that $t \gg \tau$, the dumbbell evolution equations

$$\frac{dA_{zz}}{dt} = \left(2\dot{\epsilon} - \frac{1}{\tau}\right)A_{zz},$$
$$\frac{dA_{rr}}{dt} = -\left(\dot{\epsilon} + \frac{1}{\tau}\right)A_{rr},$$

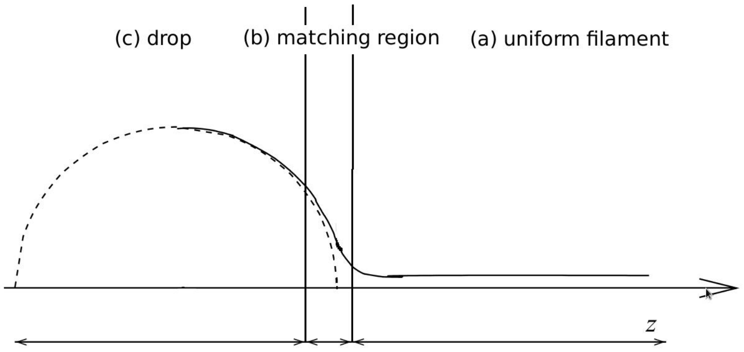

Figure 2.8: (a) Uniform filament region. (b) Matching region. (c) Drop region.

can be integrated to give the axial and radial components of the configuration tensor

$$A_{zz} = \left(\frac{h_0}{h}\right)^4 \quad ; \quad A_{rr} = \left(\frac{h}{h_0}\right)^2,$$

respectively. The radius at which the polymers begin to uncoil is denoted h_0 and corresponds to extension rate $\dot{\epsilon}\tau = 1/2$. Hence, the elastic stress appearing in the momentum equation takes the form

$$h^2 G(A_{zz} - A_{rr}) = G\left(\frac{h_0^4}{h^2} - \frac{h^4}{h_0^2}\right),$$

and assuming that elasticity balances the capillary forces yields

$$\gamma h^2 K + G\left(\frac{h_0^4}{h^2} - \frac{h^4}{h_0^2}\right) = T. \tag{2.13}$$

We now seek two solutions to this elasto-capillary balance (2.13); the first solution corresponds to the uniform filament region so that curvature can be approximated to leading order and the second solution corresponds the matching region shown in Figure 2.8.

In the uniform region, the filament is assumed to be thin so that $h \ll 1$ and the curvature term (2.12) is approximated as $K \approx 1/h$. Thus, the uniform filament solution at $h = R_0$ is

$$\gamma R_0 + \frac{G h_0^4}{R_0^2} = T. \tag{2.14}$$

On the other hand, in the matching region, the full curvature term (2.12) must be kept. In this case, the elasto-capillary balance (2.13) is multiplied by integration factor h_z/h^3 to give

$$\gamma K \frac{h_z}{h} + G\frac{h_z}{h^3}\left(\frac{h_0^4}{h^2} - \frac{h^4}{h_0^2}\right) = T\frac{h_z}{h^3},$$

which can then be integrated to yield

$$\frac{2\gamma h}{(1 + h_z^2)^{1/2}} + G\left(\frac{h_0^4}{2h^2} + \frac{h^4}{h_0^2}\right) - \frac{2h^2}{C} = T,$$

for some constant of integration C. Thus, at $h = R_0$, the solution is

$$2\gamma R_0 + \frac{G h_0^4}{2R_0^2} = T, \tag{2.15}$$

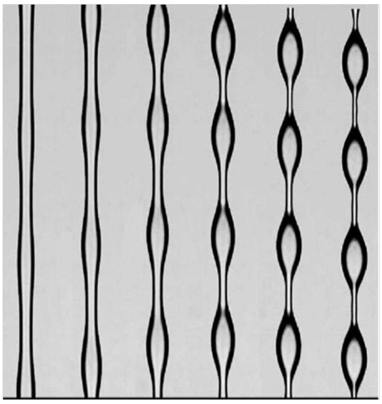

Figure 2.9: Beads-on-string structures generated during the exponential thinning phase, taken from reference [117].

where we assume $h \ll 1$ and h_z vanishes.

Eliminating tension T from our two solutions (2.14) and (2.15), we find the initial filament radius to be

$$R_0 = h_0 \left(\frac{G h_0}{2\gamma} \right)^{1/3} .$$

Hence, in the elasto-capillary thinning regime, the filament radius decay is described by

$$h_{min} = h_0 \left(\frac{G h_0}{2\gamma} \right)^{1/3} \exp\left(-\frac{t}{3\tau} \right),$$

for polymer relaxation time τ. Under the assumption of infinitely long dumbbells, the filament will never break [111].

Christianti & Walker [32] study the droplet size distribution and jet break-up length for a series of polymer solutions. As the molecular weight and concentration increases, elastic stresses in the fluid become increasingly important and the jet break-up evolves from the classical Rayleigh mode towards the classic ‘beads-on-string’ morphology, where the main drops are connected by thin long-lived filaments of fluid, as shown in Figure 2.9. Furthermore, they find that the formation of satellite drops can be completely eliminated for a range of elasticities.

Clasen *et al.* [35] give a qualitative description of the shape and the flow inside the filament of these beads-on-string structures for a one-dimensional approximation. By matching the spherical end drops to the uniform filament region, they introduce a similarity description of the neck region, which they compare to experimental observations. Although the experimental data converges onto a single curve, in much the same way as the computed profiles, the experimental profiles are sharper than the theory predicts. This discrepancy is attributed to the validity of the one-dimensional approximation for increasingly steep gradients.

Exponentially thinning filaments are generated in capillary-thinning rheometers and so the relaxation time can be extracted from the thinning data. However, the relaxation time measured in rheometers is often found to differ from the longest Zimm relaxation time τ_Z, described in Chapter 1. In particular, both Vadillo *et al.* [130] and Clasen *et al.*

[36] find that the relaxation measured by capillary thinning does not agree with the linear viscoelastic relaxation time measured by oscillatory shear.

2.3.4 The Break-up of Polymeric Filaments

During the final thinning stages before break-up, highly-extended viscoelastic filaments are observed to become unstable to further instability and a complex flow pattern develops. This phenomenon is known as iterated beading and is shown in Figure 2.10. Bhatt *at al.* [11] present a phase diagram in order to determine the fluid parameters responsible for a number of different beads-on-string morphologies.

Yet, the mechanism for this secondary instability is not fully understood. The elasto-capillary balance and resulting exponential stress growth obtained from the Oldroyd-B model excludes the possibility of filament break-up [111]. However, Chang [25] gives a stability analysis that shows the neck region connecting the main drop to the uniform filament is unstable to small perturbations. This leads to elastic recoil and the formation of smaller satellite drops on the main filament, which are connected to the main drops by finer filaments. Under the assumption of infinitely extensible dumbbells, the process repeats indefinitely in a self-similar way. Although the evaluation of the exponential thinning regime is also possible from the finer filaments that connect the satellite drops to the main drops, the induced oscillations caused by the appearance of higher-order satellites restricts a quantitative evaluation of the minimum filament radius [21].

Ultimately there are two effects that modify the thinning dynamics; inertia and the finite extensibility of the molecule. Since finite extensibility bounds the maximum stress that can be exerted by the chain [54], the iterating process is restricted and the thinning dynamics depart from the exponential law, an effect which has been observed experimentally [10], [5].

When polymers reach full extension, rather than behaving like elastic springs, the solution is similar to a suspension of rigid rods. Consequently, the polymer stress is thought of as viscous and the dynamics adopt a linear thinning regime, rather than exponential decay. In order to predict this final regime, and thus the break-up time of a viscoelastic filament, the finite extensibility L of the polymers must be incorporated into the constitutive model.

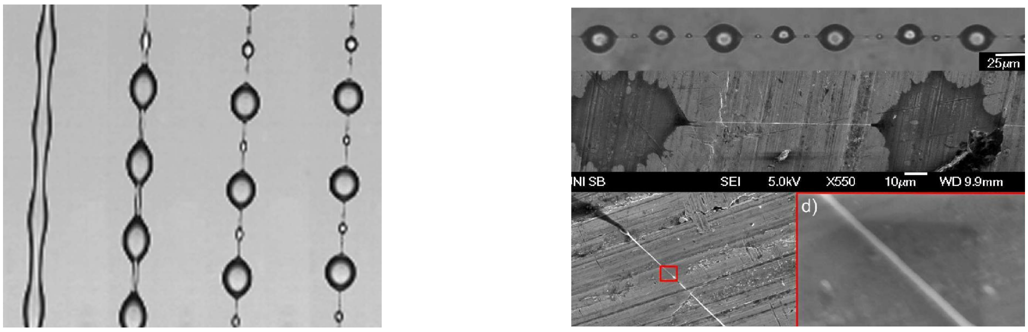

Figure 2.10: Iterated beads-on-string structures and the generation of a solid fibre. Images taken from reference [117].

Entov and Hinch [54] estimate the time to break-up by patching together the exponential law derived from the FENE model with Newtonian viscous thinning. They find the break-up time to be approximately $t_b \approx t_c + 3\tau$, where t_c is the cross over time between elastic and viscous behaviour. This result gives a good approximation to experimental data for long polymers with finite extensibility $L \geq 150$.

However, for sufficiently high polymer concentrations, a viscoelastic filament is found not to break [117]. Instead the filament is observed to form a solid fibre less than a micron across, as shown in Figure 2.10. Since evaporation does not play a significant role, the formation of the solid fibre is claimed to be the result of a slow induced phase separation. This phenomenon is observed for a range of polymer-solvent systems.

Chapter 3

A One-Dimensional Model

3.1 The Slender-Jet Approximation

3.1.1 Governing Equations

As discussed in Chapter 1, a simplification of the full Navier-Stokes equations is to assume the slender-jet approximation for long wavelengths [53], which for the Newtonian case is defined by equation (1.13). To non-dimensionalise equation (1.13), the initial jet radius R is chosen as a typical length scale and the Rayleigh capillary time $T = \sqrt{\rho R^3/\gamma}$ as a typical time scale to give the non-dimensionalised equations

$$\begin{aligned} \frac{\partial h^2}{\partial t} + \frac{\partial}{\partial z}(h^2 v) &= 0, \\ \frac{\partial}{\partial t}(h^2 v) + \frac{\partial}{\partial z}(h^2 v^2) &= \frac{\partial}{\partial z}\left(h^2\left(K + 3Oh\frac{\partial v}{\partial z}\right)\right). \end{aligned} \tag{3.1}$$

for Ohnesorge number

$$Oh = \frac{\mu_s}{\sqrt{\rho\gamma R}}.$$

For a polymer solution, there is an additional stress difference arising from the state of deformation of the polymer chains.

In the Oldroyd-B constitutive model, as derived in Chapter 1 for linear dumbbells, the zz and rr stress components satisfy the evolution equations

$$\begin{aligned} \frac{\partial \sigma_{zz}}{\partial t} + \frac{\partial}{\partial z}(v\sigma_{zz}) &= 3\sigma_{zz}\frac{\partial v}{\partial z} + 2\frac{\mu_p}{\tau}\frac{\partial v}{\partial z} - \frac{\sigma_{zz}}{\tau}, \\ \frac{\partial \sigma_{rr}}{\partial z} + \frac{\partial}{\partial z}(v\sigma_{zz}) &= -\frac{\mu_p}{\tau}\frac{\partial v}{\partial z} - \frac{\sigma_{rr}}{\tau}, \end{aligned}$$

Here τ denotes the relaxation time of the polymer and $\mu_p = G\tau$ is the polymer contribution to viscosity for elastic modulus G. We non-dimensionalise these governing equations using the characteristic length scale R and time scale T, so that the unit of stress is γ/R. This introduces two additional non-dimensional variables. The Deborah number is defined to be

$$De = \frac{\tau}{T}.$$

The Deborah is intrinsic to the fluid since it is defined only in terms of material and geometric parameters and is independent of the imposed fluid velocity. For capillary-driven

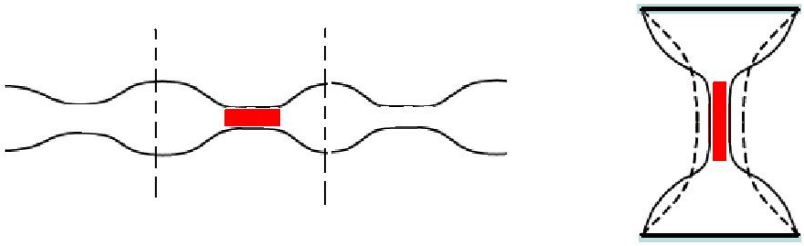

Figure 3.1: Simulating experimental conditions: The infinite jet compared to a liquid bridge suspended between two end-plates, taken from reference [93].

flows, where the stretching rate is determined by surface tension, the Deborah number determines the extent to which the polymers are deformed during capillary thinning. The dimensionless polymer concentration is defined as

$$c = \frac{\mu_p}{\mu_s} = \frac{G\tau}{\mu_s},$$

which determines the relative contribution of the polymer contribution to the shear viscosity. Thus, the non-dimensional polymeric slender-jet equations are defined as

$$\begin{aligned} \frac{\partial h^2}{\partial t} + \frac{\partial}{\partial z}(h^2 v) &= 0, \\ \frac{\partial}{\partial t}(h^2 v) + \frac{\partial}{\partial z}(h^2 v^2) &= \frac{\partial}{\partial z}\left(h^2\left(K + 3Oh\frac{\partial v}{\partial z} + \sigma_{zz} - \sigma_{rr}\right)\right), \\ \frac{\partial \sigma_{zz}}{\partial t} + \frac{\partial}{\partial z}(v\sigma_{zz}) &= 3\sigma_{zz}\frac{\partial v}{\partial z} + \frac{2c}{De}\frac{\partial v}{\partial z} - \frac{\sigma_{zz}}{De}, \\ \frac{\partial \sigma_{rr}}{\partial t} + \frac{\partial}{\partial z}(v\sigma_{rr}) &= -\frac{c}{De}\frac{\partial v}{\partial z} - \frac{\sigma_{rr}}{De}, \end{aligned} \tag{3.2}$$

where σ_{zz} and σ_{rr} are now dimensionless quantities, as derived by Forest & Wang [59]. By applying appropriate boundary conditions, we are able to simulate experimental conditions. Figure 3.1 shows examples of capillary-driven flows in a continuous jet and a liquid bridge held between two end plates.

The conditions of an infinite jet are created by applying periodic boundary conditions as in references [6] and [90]. This infinite-jet model can be thought of as section of a free jet containing a single wavelength and the configuration is analogous to a downstream section of a continuous inkjet, driven at the Rayleigh wavelength in the limit of infinite Weber number. We choose the frame of the moving jet so that the jet is assumed to be initially at rest and a small sinusoidal perturbation is applied to the free surface at time zero, such that

$$h(z,0) = R + \epsilon\cos\left(\frac{2\pi z}{L}\right),$$

where R is the initial jet radius and L is the length of one wavelength. Since there is no external forcing, the jet is subject only to the capillary instability.

Alternatively, to simulate a capillary-thinning rheometer, where a liquid bridge is held between two end plates, we impose Dirichlet boundary conditions to account for the end plates used in experiments; the free surface height is fixed at each plate and there is zero axial velocity. To induce instability in this case, the free surface profile is initially modelled as an arc of a circle for some initial mid-filament radius R. Thus, the initial condition assumes a liquid bridge on the verge of stability, like that generated by the slow-retraction method [21]. Under the action of surface tension the liquid bridge develops into two hemispherical drops connected by a thin filament. Apart from this difference in boundary conditions, this set up is equivalent to the break-up of an infinite jet and so the local thinning behaviour is expected to be the same in the thin-filament region. This one-dimensional approximation for the thinning of a liquid bridge is surprisingly accurate, even though the long-wavelength assumption is not strictly valid [3], [52].

3.1.2 The Lax-Wendroff Scheme

The slender-jet equations (3.1) and (3.2) are solved using the explicit Lax-Wendroff scheme [108]. This numerical scheme is appropriate for problems of flux-conservative form, which are in general given by

$$\frac{\partial a}{\partial t} = -\frac{\partial F}{\partial z},$$

for some flux variable F and provides solutions that are second-order accurate in both time and space. Lax was first to introduce a finite-difference approximation for equations in conservative form that adheres to the physical principle of flux conservation more appropriately than non-conservative schemes [85].

In this chapter, the slender-jet equations are solved on a uniform mesh for equally spaced mesh nodes z_j and times steps t_n given by

$$\begin{aligned} z_j &= z_0 + jdz, \quad j = 0, 1, \ldots J, \\ t_n &= t_0 + ndt, \quad n = 0, 1, \ldots, N, \end{aligned}$$

for mesh size dz and time step dt. In general, the notation a_j^n will be used to denote the value $a(z_j, t_n)$ at a particular time and spatial position.

To solve the general flux-conservative equation, the Lax-Wendroff scheme is based on forward differencing in time

$$\left.\frac{\partial a}{\partial t}\right|_j^n = \frac{a_j^{n+1} - a_j^n}{dt} + O(dt).$$

and central differencing in space

$$\left.\frac{\partial F}{\partial z}\right|_j^n = \frac{F_{j+1}^n - F_{j-1}^n}{dz} + O(dz^2),$$

where O denotes the order of the approximation. Central differencing in this way ensures second-order spatial accuracy. However, applying this forward-time, central-space method directly to a general flux-conservative equation yields an unconditionally unstable scheme [108]. This numerical instability may be cured by a simple change due to Lax; at each node, the value a_j^n is replaced by the average value

$$a_j^n = \frac{1}{2}(a_{j+1}^n + a_{j-1}^n). \tag{3.3}$$

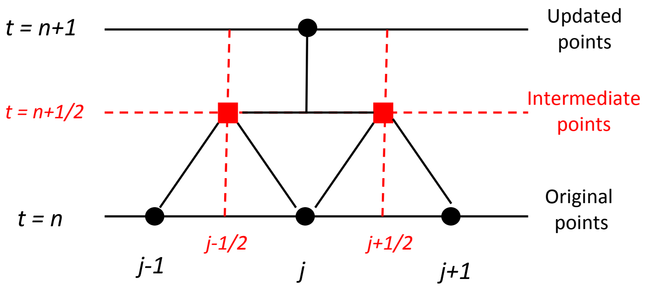

Figure 3.2: Representation of the two-step Lax-Wendroff differencing scheme. Two intermediate points are calculated by the Lax averaging approximation. The intermediate points plus one of the original points produce the updated value via a staggered leap frog method.

Furthermore, to increase temporal accuracy from first to second order, the Lax-Wendroff scheme employs a two-step method for which a half-time step $t_{n+1/2}$ is introduced. The Lax-Wendroff scheme is defined as follows and a diagram of the two steps is given in Figure 3.2.

The first step of the algorithm introduces intermediate values defined at half-time steps $t_{n+1/2}$ and half-mesh nodes $z_{j+1/2}$. Central differencing in space across the half-mesh node $z_{j+1/2}$ and projecting forward in time to the half-time step $t_{n+1/2}$ yields

$$\begin{aligned} \left.\frac{\partial a}{\partial t}\right|_{j+1/2}^{n} &= -\left.\frac{\partial F}{\partial z}\right|_{j+1/2}^{n} + O(dt, dx^2), \\ \Rightarrow \frac{2}{dt}(a_{j+1/2}^{n+1/2} - a_{j+1/2}^{n}) &= -\frac{1}{dz}(F_{j+1}^{n} - F_{j}^{n}) + O(dt, dx^2). \end{aligned}$$

Then, using the Lax averaging approximation (3.3) the intermediate values are found to be

$$\begin{aligned} \frac{2}{dt}\left(a_{j+1/2}^{n+1/2} - \frac{1}{2}(a_{j+1}^{n} - a_{j}^{n})\right) &= -\frac{1}{dz}(F_{j+1}^{n} - F_{j}^{n}) + O(dt, dx^2), \\ \Rightarrow a_{j+1/2}^{n+1/2} &= \frac{1}{2}(a_{j+1}^{n} + a_{j}^{n}) - \frac{dt}{2dz}(F_{j+1}^{n} - F_{j}^{n}) + O(dt, dx^2), \end{aligned}$$

Using this information, the intermediate flux values $F_{j+1/2}^{n+1/2}$ can be evaluated, which are required for the second step of the scheme.

The second step of the algorithm calculates the updated nodal values a_j^{n+1} using a staggered leap frog method [108]. Staggering enables forward-time differences to be used in conjunction with central spacing without developing instability. The forward-time difference is now centred about the half-time step $t_{n+1/2}$ so that second-order temporal accuracy is achieved:

$$\begin{aligned} \left.\frac{\partial a}{\partial t}\right|_{j}^{n+1/2} &= -\left.\frac{\partial F}{\partial z}\right|_{j}^{n+1/2} + O(dt^2, dz^2), \\ \Rightarrow \frac{1}{dt}(a_j^{n+1} - a_j^{n}) &= -\frac{1}{dz}(F_{j+1/2}^{n+1/2} - F_{j-1/2}^{n+1/2}) + O(dt^2, dz^2). \end{aligned}$$

Hence, the properly centred expression for the updated values is given by

$$a_j^{n+1} = a_j^n - \frac{dt}{dx}(F_{j+1/2}^{n+1/2} - F_{j-1/2}^{n+1/2}) + O(dt^2, dx^2),$$

where the intermediate flux values are determined during the first step. Once the updated values have been computed, the intermediate values can be discarded.

The Newtonian slender-jet equations (3.1) consist of a coupled pair of flux-conservative equations, which can in general be written as

$$\frac{\partial a}{\partial t} = -\frac{\partial F}{\partial z},$$
$$\frac{\partial F}{\partial t} = -\frac{\partial G}{\partial z},$$

so that $a = h^2$, $F = h^2 v$ and $G = h^2(v^2 - K - 3Oh\frac{\partial v}{\partial z})$. The first and second derivatives contained in flux term G are calculated separately by the usual central-difference formulae. For example, the first and second derivatives of the free surface height $h(z,t)$ are given by

$$\left.\frac{\partial h}{\partial z}\right|_j^n = \frac{h_{j+1}^n - h_{j-1}^n}{2dz} + O(dz^2) \quad \text{and} \quad \left.\frac{\partial^2 h}{\partial z^2}\right|_j^n = \frac{h_{j+1}^n - 2h_j^n + h_{j-1}^n}{dz^2} + O(dz^2).$$

Derivatives at the intermediate step can also be found by central differencing and for the case of Dirichlet boundary conditions, one-sided second-order difference formulae are used.

In the case of a polymeric fluid, there are two additional equations

$$\frac{\partial \sigma_{zz}}{\partial t} + \frac{\partial}{\partial z}(v\sigma_{zz}) = 3\sigma_{zz}\frac{\partial v}{\partial z} + \frac{2c}{De}\frac{\partial v}{\partial z} - \frac{\sigma_{zz}}{De},$$
$$\frac{\partial \sigma_{rr}}{\partial t} + \frac{\partial}{\partial z}(v\sigma_{rr}) = -\frac{c}{De}\frac{\partial v}{\partial z} - \frac{\sigma_{rr}}{De},$$

which can also be solved using the Lax-Wendroff scheme. Terms appearing on the right-hand side are treated as source terms, as opposed to the flux terms appearing on the left. These source terms are calculated separately during both steps of the algorithm and added to the final solution. For example, in general the stress evolution may be written as

$$\frac{\partial a}{\partial t} = -\frac{\partial F}{\partial z} + S,$$

for some flux term F and source term S. The Lax average (3.3) is used to calculate the source terms at the half mesh nodes to ensure stability

$$S_{j+1/2}^n = \frac{1}{2}(S_{j+1}^n + S_j^n).$$

Then, the intermediate values are given by

$$a_{j+1/2}^{n+1/2} = \frac{1}{2}(a_{j+1}^n + a_j^n) - \frac{dt}{2dz}(F_{j+1}^n - F_j^n) + \frac{dt}{4}(S_{j+1}^n + S_j^n) + O(dt, dz^2).$$

On the right-hand side, the first term comes from the Lax averaging approximation, the second from central differencing the flux term and the third from averaging the source term. Similarly, the updated values are given by

$$a_j^{n+1} = a_j^n - \frac{dt}{dz}(F_{j+1/2}^{n+1/2} - F_{j-1/2}^{n+1/2}) + \frac{dt}{2}(S_{j+1/2}^{n+1/2} + S_{j-1/2}^{n+1/2}) + O(dt^2, dz^2).$$

Again, the intermediate flux and source terms are calculated using information found in the first step and then discarded.

3.1.3 Stability of Solutions

Von Neumann stability analysis is a simple method to determine the local stability of numerical solutions. It is restricted to constant-coefficient, partial differential equations, where the difference scheme implemented consists of no more than two time steps [108]. This stability analysis does not rigorously treat the effects of boundary conditions, but despite its lack of rigour, the von Neumann analysis gives a good indication of the restrictions required on the time stepping dt in relation to the mesh size dz.

Let mesh nodes be denoted z_j for $j = 0, 1, \dots, J$ with uniform mesh size dz where $x_0 = 0$ and $x_J = L$ is the length of the domain. Let time steps be denoted t_n for $n = 0, 1, \dots, N$. For linear problems, the stability of a difference scheme can be analysed in terms of the initial error E^0 at time $t = 0$. Since the error at a particular mesh node z_j is defined over the finite interval $z_j \in [0, L]$, the error can be expressed by a finite Fourier series, which is then reflected in the domain $[0, L]$ to obtain a complex Fourier representation

$$E^0(z_j) = \sum_{m=-J}^{J} C_m \exp\left(\frac{im\pi z_j}{L}\right).$$

In the domain $[-L, L]$, the maximum possible wavelength is $\lambda_{max} = 2L$ and the minimum possible wavelength is $\lambda_{min} = 2dz$, such that the nodes are resolvable on the mesh. The corresponding wave numbers are thus

$$k_{min} = \frac{2\pi}{\lambda_{min}} = \frac{\pi}{L} \quad ; \quad k_{max} = \frac{2\pi}{\lambda_{max}} = \frac{\pi}{dz}.$$

In the Fourier series we have

$$k_{min} = \frac{m\pi}{L}, \text{ for } m = 1 \quad ; \quad k_{max} = \frac{m\pi}{L}, \text{ for } m = J,$$

hence, in general the wave number is expressed as

$$k_m = \frac{m\pi}{L}, \quad m = 1, \dots, J.$$

We assume that the solution has a standard linear waveform

$$a(x, t) = \exp(i(k_m z - \omega t)),$$

where ω is a complex number defining the wave frequency. Thus, the error at time step t_n can be written as

$$E(z_j, t_n) = \sum_{m=-J}^{J} C_m \exp(-i\omega t_n) \exp(ik_m z_j).$$

By the principle of superposition, it is sufficient to consider just one harmonic and so the subscript m is dropped. Thus, for mesh node $z_j = jdz$ and time step $t_n = ndt$, we consider the single error component

$$E_j^n = \exp(-i\omega ndt) \exp(ikjdz).$$

Since $|e^{i\theta}| = 1, \quad \forall \theta \in \mathbb{R}$, the magnitude of the error is

$$|E_j^n| = |e^{-i\omega dt}|^n,$$

and so the error is bounded provided that $|e^{-i\omega dt}| \leq 1$.

The amplification factor ξ is defined to be the error ratio between successive time steps

$$\xi = \frac{E_j^{n+1}}{E_j^n} = e^{-i\omega dt}.$$

Thus, a numerical scheme is considered to be stable provided $|\xi| \leq 1$. By linearity the error E_j^n satisfies the difference scheme, so we can assume that independent solutions of the difference scheme take the form

$$a_j^n = \xi^n e^{ikjdz}.$$

We seek the local stability of the Newtonian slender-jet equations (3.1). The first governing equation

$$\frac{\partial h^2}{\partial t} + \frac{\partial}{\partial z}(h^2 v) = 0,$$

corresponds to conservation of mass for the jet area h^2, advected with jet velocity v. For simplicity, the equation is linearised by assuming that velocity is constant in a local analysis. Conservation of mass is coupled with conservation of momentum and solved via the Lax-Wendroff algorithm, which, for a general flux-conservative equation

$$\frac{\partial a}{\partial t} = -\frac{\partial F}{\partial z},$$

is given by the two-step scheme:

$$\begin{aligned} a_{j+1/2}^{n+1/2} &= \frac{1}{2}(a_{j+1}^n + a_j^n) - \frac{dt}{2dz}(F_{j+1}^n + F_j^n) + O(dt, dz^2), \\ a_j^{n+1} &= a_j^n - \frac{dt}{dz}(F_{j+1/2}^{n+1/2} - F_{j-1/2}^{n+1/2}) + O(dt^2, dz^2). \end{aligned}$$

The first step calculates intermediate variables and the second updates variables at the next time step.

For conservation of mass, we have $a = h^2$ and $F = av$, where v is considered constant in the linear approximation. Thus, the Lax-Wendroff scheme can be reduced to a single step by writing the intermediate flux variables as

$$F_{j+1/2}^{n+1/2} = v a_{j+1/2}^{n+1/2} = v\left(\frac{1}{2}(a_{j+1}^n + a_j^n) - v\frac{dt}{2dz}(a_{j+1}^n - a_j^n)\right),$$

and substituting them into the second step to give

$$a_j^{n+1} = a_j^n - \frac{vdt}{dz}\left(\frac{1}{2}(a_{j+1}^n + a_j^n) - \frac{vdt}{2dz}(a_{j+1}^n - a_j^n) - \frac{1}{2}(a_j^n + a_{j-1}^n) + \frac{vdt}{2dz}(a_j^n - a_{j-1}^n)\right).$$

Assuming the independent solution takes the form $a_j^n = \xi^n e^{ikjdz}$ and simplifying yields an equation for the amplification factor

$$\xi = 1 - i\alpha \sin kdz - \alpha^2(1 - \cos kdz).$$

where α is defined to be

$$\alpha \equiv \frac{vdt}{dz}$$

Thus, the magnitude of the amplification factor is

$$|\xi|^2 = 1 - \alpha^2(1-\alpha^2)(1-\cos kdz)^2.$$

and the stability criterion $|\xi|^2 \leq 1$ therefore reduces to

$$\alpha^2 \leq 1 \quad \Rightarrow \quad vdt \leq dz.$$

This is the famous Courant-Friedrichs-Lewis stability criterion, often called simply the Courant condition. Consider a wave travelling across a discrete spatial grid and the amplitude of the wave is required at discrete time steps of equal length. The length of the time step must be less than the time taken for the wave to travel to adjacent mesh nodes. Thus, when the mesh size is reduced, the upper limit of the time step must decrease. The numerical domain must contain the analytical domain to ensure that the scheme can access the information required to form the solution.

In the momentum equation $a = h^2 v$, which is also advected with velocity v. Consequently, the stability of this equation also requires that the Courant condition is met. Furthermore, the stability of this explicit method is also subject to the condition that the time step dt must be less than the diffusion time h^2/Oh, thus is restricted at high viscosities [35]. Hence for $Oh > 3$, we find that an implicit numerical scheme is more suitable, the details of which are given in Chapter 5.

3.1.4 Capillary Thinning of a Newtonian Liquid Bridge

To simulate the capillary thinning of a Newtonian liquid bridge, the slender-jet equations (3.1) are solved via the Lax-Wendroff scheme described in the previous section. We implement a uniform mesh for nodes $j = 1, \ldots, J$, where the mesh size dz satisfies the Courant stability condition $vdt \leq dz$ for time step dt. The initial shape of the free surface is modelled as an arc of a circle, with mid-filament radius set to $R = 1$, to induce capillary thinning. We assume Dirichlet boundary conditions, where the free surface h is fixed and there is zero axial velocity v at the end-plates. The end-plates have radius 2 and are held at fixed separation distance 6.

As discussed in Chapter 2, the thinning dynamics of a liquid bridge are governed by a balance of surface tension, viscosity and inertia, characterised by the Ohnesorge number. Under the action of surface tension the liquid bridge develops into two hemispherical drops connected by a thin filament. In Figure 3.3 we compare the evolution of the minimum filament radius predicted by our model for two Newtonian fluids of differing viscosities.

In Figure 3.3(a) we show the results for a fluid with $Oh = 0.2$ (typical of inkjet printing fluids for which $0.1 < Oh < 1$), where the origin of time is shifted to the break-up time. Since $Oh < Oh^*$, the thinning is initially dominated by inertia and is seen to follow the

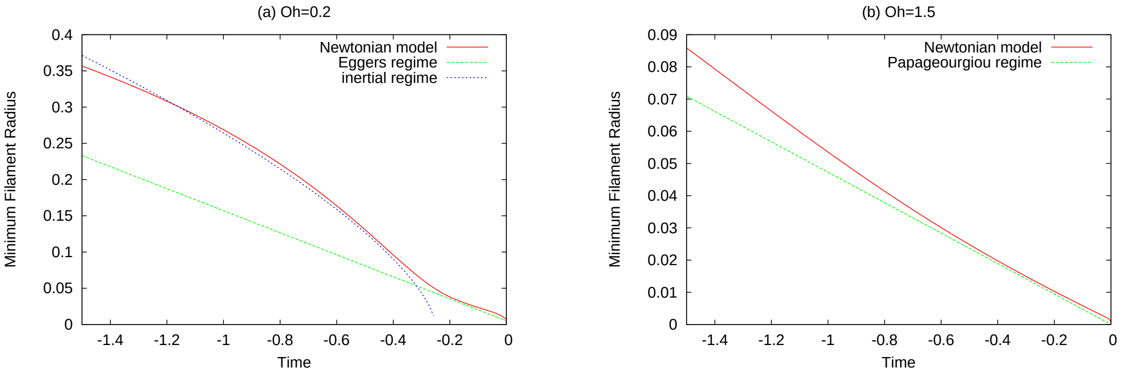

Figure 3.3: (a) Newtonian model $Oh = 0.2$ for filament thinning compared to the inertial regime (3.4) and the Eggers regime (3.5). (b) Newtonian model $Oh = 1.5$ compared to the Papageorgiou viscous regime (3.6).

inertial regime given by

$$h_{min} = 0.64 \left(\frac{\gamma}{\rho}\right)^{1/3} (t - t_b)^{2/3}. \tag{3.4}$$

However, since the Ohnesorge number is close to the critical value $Oh^* = 0.2077$, we observe the transition to the universal Eggers regime, where viscosity enters the force balance. Thus, once the filament radius has thinned to approximately $h_{min} \sim 0.05$, we observe a transition from inertia-dominated thinning to a inertial-viscous regime , where the minimum filament radius is given the equation

$$h_{min} = 0.0304 \frac{\gamma}{\mu} (t - t_b). \tag{3.5}$$

In contrast, a fully developed viscous regime is seen for $Oh = 1.5$ in Figure 3.3(b), where the radial decay follows Papageorgiou's linear thinning regime

$$h_{min} = 0.0709 \frac{\gamma}{\mu} (t - t_b), \tag{3.6}$$

These results are in agreement with the experimental observations of Campo Deano *et al.* [21].

3.2 Modelling Capillary Break-up of Particulate Suspensions

3.2.1 Problem Outline[1]

A diverse range of materials can be manipulated using inkjet technology, the most common being particulate suspensions. Particles appear in most graphical inks, as well as in inks used for printed electronics and ceramic manufacture. However, compared to the Newtonian and viscoelastic cases, there is little known about particulate effects on jet stability and break-up.

The existence of universal thinning laws (3.4), (3.5) and (3.6) initiated the use of capillary break-up as a rheological technique and recent studies have demonstrated that extensional rheometry can be successfully performed on particulate suspensions [140], [28], [121]. In particular, large-scale pendant-drop experiments have observed that the presence of particles in a solution accelerates the thinning process compared to that predicted for the equivalent Newtonian fluid [15], [60], [61]. However, the detachment dynamics of particle-laden fluids are not yet fully understood.

The hypothesis is that the accelerated thinning arises from variations in the local particle density. As the filament thins, the variations are amplified leading ultimately to sections of the filament containing no particles at all. Sections of the filament that have a low particle density consequently have a lower viscosity and can therefore thin more easily. Similar fluctuations in particle density have been observed by Roche *et al.* [114] during the thinning of a liquid bridge; close to break-up, certain regions within the bridge become jammed whilst particles experience a significant flow in other areas.

To test this hypothesis, we construct a simple one-dimensional model for capillary break-up of a liquid bridge, in which the viscosity is determined from the local particle density, found by tracking individual particles within the suspension. The particles are assumed to be non-Brownian so that they are simply advected with the fluid velocity. Since the particles only contribute to the dynamics through the local viscosity, the direct effects of hydrodynamic interactions between the particles and the effects of the individual particles on the shape of the free surface are not included. Nevertheless, this model is able to reproduce the accelerated thinning found in experiments.

3.2.2 A Simple Particle Model

In their study of falling particle plumes, Crosby & Lister [38] conclude that the effect of particle density modes in the r and θ directions are unimportant. Thus, we shall assume that particle density varies only in the axial coordinate z and adopt a one-dimensional approximation for the particle distribution.

As in section 3.1.4 for a Newtonian liquid bridge, we solve the slender-jet equations

---

[1] Published: **C. McIlroy** & O. G. Harlen *Modelling Capillary Break-up of Particulate Suspensions* Phys. Fluids 26 (2014) 033101

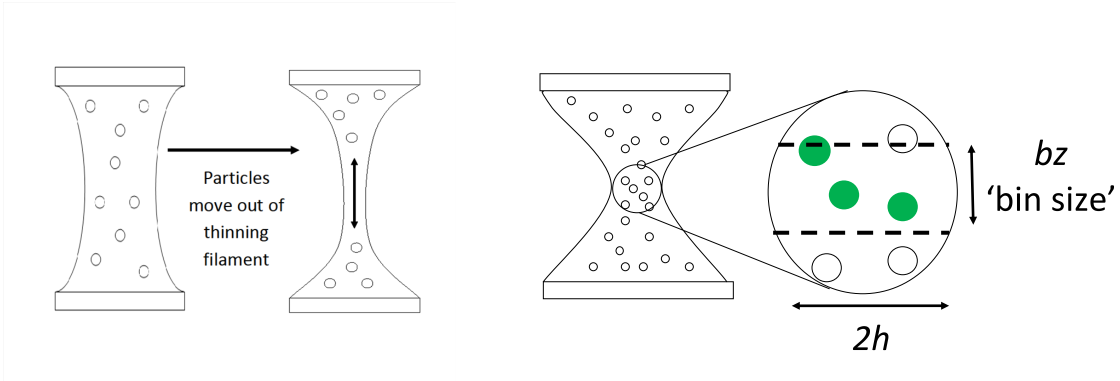

Figure 3.4: A one-dimensional model to represent the capillary thinning of a particulate suspension. Particles are sorted into 'bins' of length bz. Shaded particles are allocated to a bin according to their position.

(3.1) via the Lax-Wendroff scheme. The initial shape of the free surface is modelled as an arc of a circle, with mid filament radius set to $R = 1$, to induce capillary thinning. We assume Dirichlet boundary conditions such that the free surface h is fixed and there is zero axial velocity v at the end-plates. The end-plates have radius 2 and are held at fixed separation distance 6.

Initially, particles are uniformly distributed at random locations throughout the fluid. We assume that the number of particles N is much larger than the number of mesh nodes J. The initial particle positions z_p for $p = 1, \ldots, N$ are assigned as follows. We define the accumulated volume $V(z)$ as

$$V(z) = \pi \int_0^z h^2(z')dz'. \tag{3.7}$$

A corresponding V position is chosen for each particle from a uniform distribution on the interval $[0, V_{tot}]$, where V_{tot} is the volume of the entire liquid bridge. Then, the corresponding value of z_p is found by inverting equation (3.7). In subsequent motion, we assume that each particle moves with the axial velocity $v(z_p, t)$ obtained by linear interpolation between grid points. The distribution of particles is then determined from particle position. A diagram of particle motion within the liquid bridge is shown in Figure 3.4.

Brownian motion opposes the creation of particle-density gradients, however, in our model, we assume that the particles are sufficiently large that Brownian motion is negligible. The importance of particle diffusion on the length scale of the particle radius r is measured by the Peclet number,

$$Pe = \frac{6\pi\mu_s\dot{\epsilon}r^3}{k_BT},$$

for the Boltzman constant k_B and absolute temperature T. The characteristic stretching rate $\dot{\epsilon}$ is defined by the time scale of the flow, which is taken to be the smaller of the inverse Rayleigh time scale $\sqrt{\gamma/\rho R_0^3}$ or the inverse viscous time scale $\gamma/\mu R_0$. For an extension rate of $\dot{\epsilon} \sim 10$ s^{-1}, which is typical of capillary-thinning experiments, the Peclet number for 1 μm particles is of the order $Pe \sim 10^4$ for solvent viscosity 389 mPa.s and filament

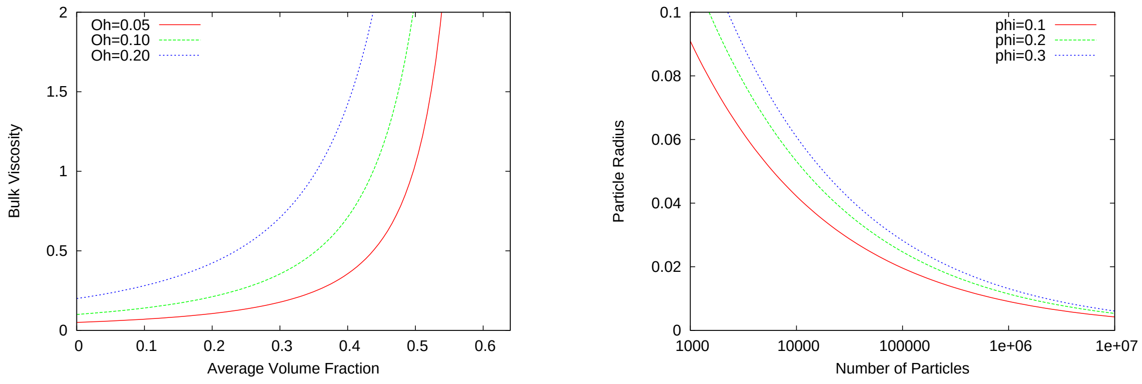

Figure 3.5: (a) Plot showing the bulk viscosity Oh_{av} obtained from the Krieger-Dougherty model as a function of particulate volume fraction for various values of solvent viscosity Oh_s. (b) Effective particle radius r as a function of the total number of particles N for various volume fractions ϕ_{av}.

radius 1 mm. Thus, the large Peclet number assumption is valid for the pendant drop experiments [15], [60], where the particle sizes are around $\sim 40 - 250$ μm. For inkjet printing applications, where inks are much less viscous ($\sim$ 11 mPa.s) and typical nozzle length scales are around $R_0 \sim 50$ μm, the extension rates are around $\dot{\epsilon} \sim 10^4$ s^{-1} and the limiting particle size is approximately $\sim$ 10 nm.

The average volume fraction of particles in a suspension is given by

$$\phi_{av} = \frac{N}{V_{tot}} V^p,$$

where V^p is the particle volume, which for spherical particles is

$$V^p = \frac{4}{3}\pi r^3.$$

Thus, particle size can be varied by changing the total number of particles N for a given average volume fraction ϕ_{av}. We determine the local particle volume fraction by dividing the filament into a number of 'bins', as shown in Figure 3.4. The length of each bin bz is set to $\sim 2r$ so that the length scale for volume fraction perturbations is set equal to the particle diameter. This bin size is typically larger than the grid resolution used in the velocity calculation.

The local viscosity is determined by the Krieger-Dougherty model [83] so that the local Ohnesorge number in the governing equation (3.1) is given by

$$Oh_i = Oh_s \left(1 - \frac{\phi_i}{\phi_{max}}\right)^{-2}, \quad i = 1, \dots J, \tag{3.8}$$

for local volume fraction ϕ_i and solvent Ohnesorge number Oh_s. Here ϕ_{max} is the maximum packing coefficient, which is found from numerical simulations to be $\phi_{max} = 0.64$ for random close-packing of monodisperse spheres [113]. This maximum packing condition implicitly constrains the number of particles that can occupy a particular axial position.

For a uniform distribution of particles, the average or bulk viscosity Oh_{av} can be calculated by evaluating the Krieger-Dougherty model at the average volume fraction ϕ_{av}.

The concentration dependence of the bulk viscosity predicted by the Krieger-Dougherty model is plotted in Figure 3.5 for a range of solvent viscosities Oh_s. Also shown in Figure 3.5 is the dependence of particle size on the total number of particles for a range of average volume fractions. For example, a suspension of $\phi_{av} = 20\%$ particles will increase a solvent viscosity of $Oh_s = 0.1$ to the bulk value $Oh_{av} = 0.22$ and for $N = 100000$ particles the effective particle radius is $r = 0.024$.

3.2.3 The Effect of Particles on Thinning Behaviour

The addition of particles to a Newtonian solvent increases the bulk viscosity of the fluid, as predicted by the Krieger-Dougherty equation (3.8). For solvent viscosity $Oh_s = 0.1$, the addition of $\phi_{av} = 20\%$ particles to the Newtonian solvent increases the viscosity to the bulk value $Oh_{av} = 0.22$. The increased resistance acts to retard the thinning process and Figure 3.6 shows that the time to break-up for a Newtonian fluid with the bulk viscosity is nearly twice as long as that of the solvent viscosity.

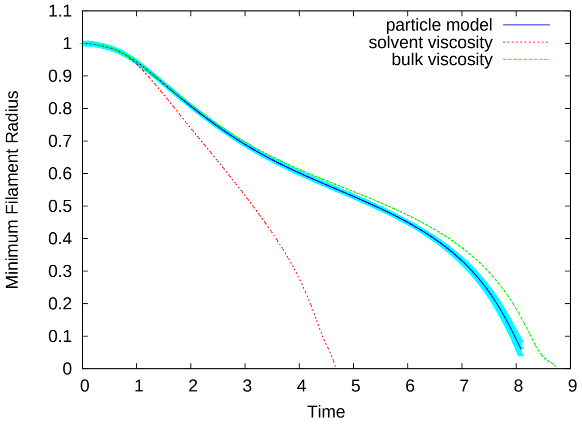

Figure 3.6: Radial decay profiles of pure solvent $Oh_s = 0.1$, bulk viscosity $Oh_{av} = 0.22$ and the corresponding particulate suspension of volume fraction $\phi_{av} = 20\%$ and particle size $r = 0.024$. The shaded area shows that standard deviation from the mean for ten realisations.

Figure 3.6 also shows the mean radial decay profile of ten realisations predicted by our particle model, where the effective particle size is $r = 0.024$ relative to the initial mid-filament radius; the shaded region indicates the standard deviation from the mean. The particulate suspension is seen initially to follow the behaviour of the bulk viscosity. However, as the filament radius decays we observe accelerated thinning and the time to break-up is consequently reduced. The results of choosing different bin sizes are shown in Figure 3.7 and compared to the bulk viscosity model. The difference in the radial decay

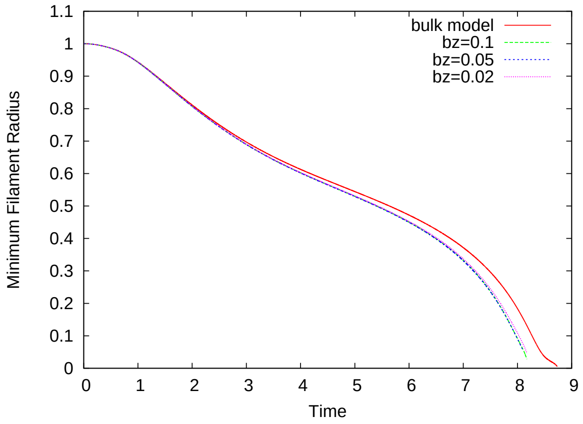

Figure 3.7: Radial decay profile of a particle suspension for varying bin size bz compared to the bulk viscosity model for suspension properties $Oh_s = 0.1$, $\phi_{av} = 20\%$, $r = 0.024$

profile for different bin lengths is small compared to the effect of particles on the bulk behaviour. Furthermore, the difference due to changing bin size is within the standard deviation measured for the suspension shown in Figure 3.6. Consequently, the specific bin size does not significantly affect the dynamics provided $b_z > 2r$, but remains small compared to the filament length.

To understand particle effects on the thinning behaviour, we study the evolution of the local particle density. Since the particles move with the fluid velocity, they are transported out of the thinning filament and into the end drops as the filament radius decays. Thus, although the average particle density in the filament remains constant, large fluctuations in the local particle density appear, as shown in Figure 3.8(a). Near to break-up, there are regions depleted of particles as well as regions of high density.

Figure 3.8(b) shows that the particle fluctuations are mirrored in the fluid viscosity so that there are regions of both high and low viscosity in the filament compared to the bulk viscosity $Oh_{av} = 0.22$. The viscosity is reduced to that of the solvent $Oh_s = 0.1$ in areas devoid of particles. It is these areas of low viscosity that allow the filament to neck and thin faster than a Newtonian fluid of the bulk viscosity.

The free surface evolution profile of the particulate suspension is shown in Figure 3.9(a). Although our model is unable to predict individual particle effects on the free surface, close to break-up the profile appears ‘lumpy’ with variations in filament thickness that reflect variations in particle concentration. Particle-rich regions appear as bulges that correspond to clusters of particles. In the region containing no particles, the free surface is able to thin down and form a uniform filament, as observed in the corresponding Newtonian case shown in Figure 3.9(b).

A plot of particle evolution with time is shown in Figure 3.10, which provides a spatio-temporal diagram of the variation in volume fraction with radial decay and axial position.

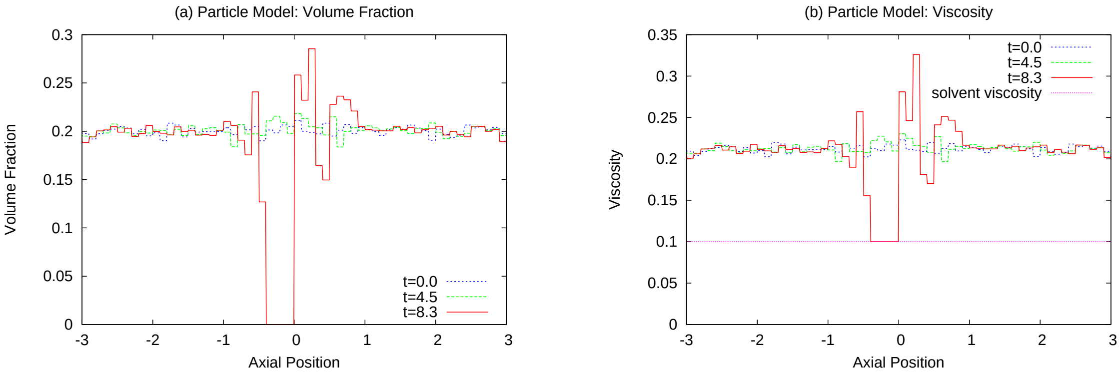

Figure 3.8: (a) Volume fraction evolution profile, (b) viscosity evolution profile for suspension properties $Oh_s = 0.1$, $\phi_{av} = 20\%$, $r = 0.024$.

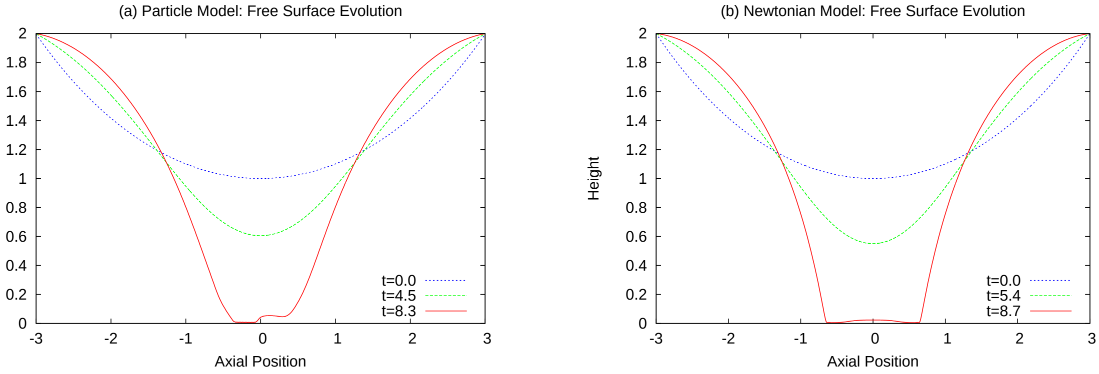

Figure 3.9: Free surface evolution profile of (a) suspension with properties $Oh_s = 0.1$, $\phi_{av} = 20\%$, $r = 0.024$, (b) bulk viscosity Newtonian fluid $Oh_{av} = 0.22$.

We illustrate two different scenarios in Figures 3.10(a) and 3.10(b); first, we show the full particle model, where the onset of particle fluctuations is fed back into the fluid viscosity and therefore affects the local thinning dynamics; second, we show a hypothetical case in which viscous feedback is neglected and we consider only the motion of the particles in a fluid of uniform viscosity. The latter case is referred to as the average viscosity model. By comparing Figures 3.10(a) and 3.10(b), we can examine how the dynamics affect fluctuations in particle density.

In particular, Figure 3.10(a) shows how the volume fraction variations grow with time for one particular realisation of a suspension with $Oh_s = 0.1$, $\phi_{av} = 20\%$ and $r = 0.024$, whereas Figure 3.10(b) shows how the fluctuations would have evolved if we hypothetically impose a uniform viscosity $Oh = 0.22$, which corresponds to the average volume fraction used in the full particle simulation. We continue by highlighting the differences between these two plots and describing how particle fluctuations develop as a consequence of variations in the local viscosity.

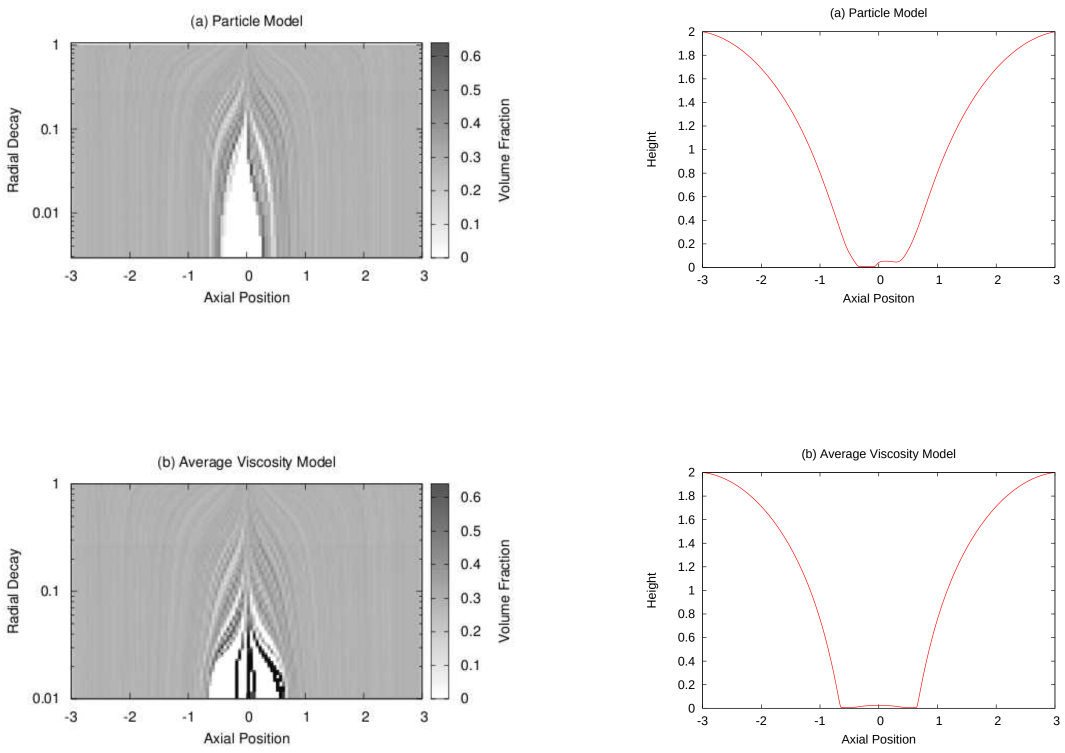

Figure 3.10: (a) Evolution of volume fraction variations for one realisation in the case $Oh_s = 0.1$, $\phi_{av} = 20\%$, $r = 0.024$ predicted by the particle model. (b) Evolution of particle fluctuations for the same suspension properties, but for a hypothetically imposed uniform viscosity $Oh = 0.22$ (see text for details). Each are compared to the free surface profile at the point of break-up.

In each case, the initial statistically uniform state corresponding to $h_{min} = 1$ shows little variation in the particle density. It is evident that fluctuations are amplified as the volume of fluid in the filament is reduced, which can be observed in the development of light and dark areas in Figure 3.10. For the average viscosity model shown in case (b), random clusters of particles form during radial decay, whereas the fluctuations in density develop much more smoothly for the full particle simulation shown in case (a).

In the latter case, the particle density feeds back into the fluid viscosity. The higher viscosity of particle-rich regions means that these tend not to thin further, but are advected along the filament. On the other hand, in the light areas that contain a lower particle density, the viscosity is reduced and consequently the region is able to thin more rapidly than the rest of the fluid. The reduction in volume drives more particles out of the filament into the end drops so that the low-viscosity region is able to develop into a uniform filament. We observe that, in most realisations, the viscous feedback of the particle model allows a single, uniform, low-viscosity filament to form between the two end drops. This is in contrast to the average viscosity model, which neglects dynamic feedback, where we see

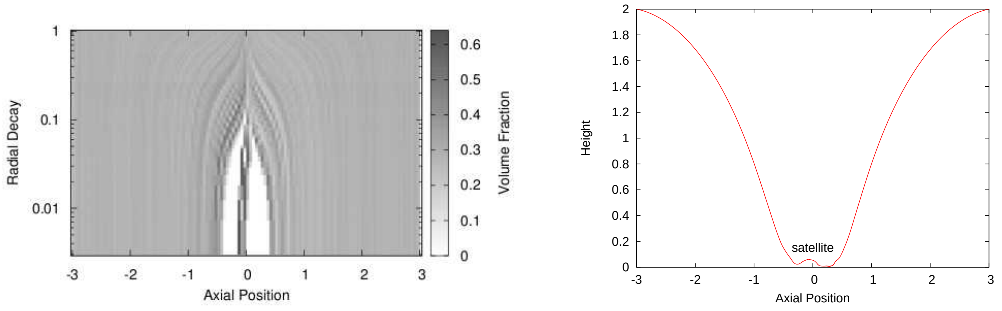

Figure 3.11: Evolution of volume fraction fluctuations for one realisation predicted by the particle model compared to the free surface profile at the point of break-up for $Oh_s = 0.1$, $\phi_{av} = 20\%$, $r = 0.024$.

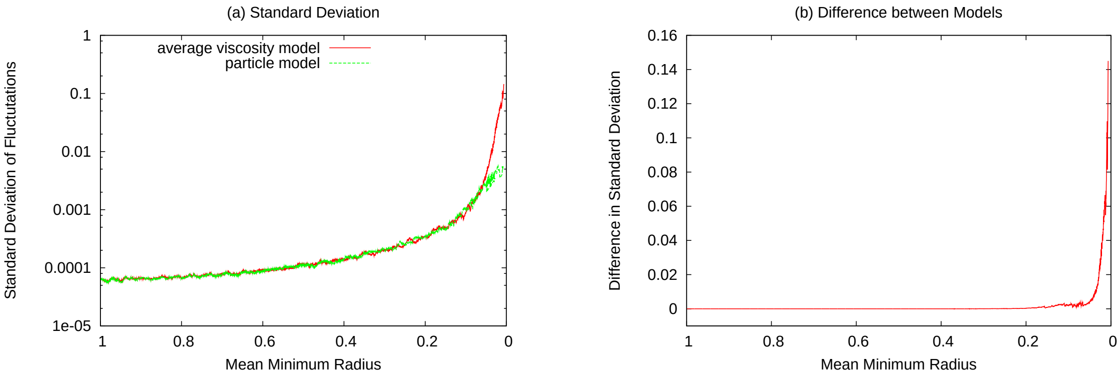

Figure 3.12: (a) Standard deviation of particle density from the average volume fraction $\phi_{av} = 20\%$ averaged over six realisations for suspension properties $Oh_s = 0.1$, $r = 0.024$. (b) Difference between the particle model and average viscosity model.

alternating regions of low and high volume fraction over the length of the filament. In our model, we neglect the effects of individual particles on the free surface. These effects are expected to become important only when the filament diameter is of the order of the particle diameter. However, at this point we observe that the filament contains no particles at all and consequently the local thinning dynamics at the minimum filament radius are unlikely to be affected by these interactions.

Other structures are possible depending on the initial distribution of particles, as shown in Figure 3.11. Instead of a single uniform filament, we observe an area of high particle density located at the centre of the axis, with regions depleted of particles surrounding it. This corresponds to the generation of a small satellite drop at the mid-filament point, which is connected to the end drops by threads of liquid. Instead of being advected into the end drops, particles remain trapped in the satellite indicated by the darker central

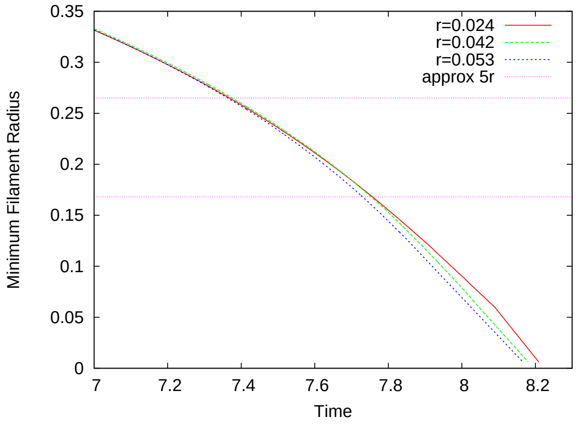

Figure 3.13: Radial decay profile of a particulate suspension $Oh_s = 0.1$, $\phi_{av} = 20\%$ for varying particle size.

region, which does not thin down due to its high local viscosity. The surrounding areas have a lower viscosity and are therefore able to thin more rapidly than the central droplet. This creates two shorter, uniform filaments that suspend the particle dense satellite drop between the end drops. Similar 'beads-on-string' morphologies have been observed by Zimoch & McKinley [147] and also compared to a one-dimensional model. For this 'beads-on-string' case, the particle interactions with the free surface are more important and our model assumptions do not hold in the region of the bead. However, our model will still capture the differential thinning of the connecting filaments that contain no particles.

We have calculated the standard deviation of particle density from the average volume fraction $\phi_{av} = 20\%$ and taken the mean over six realisations. Figure 3.12(a) compares the particle model to the average viscosity model without dynamics and Figure 3.12(b) highlights the difference between the two cases. The variation in particle fluctuations is equivalent in the initial stages of thinning. The effect of viscosity variation on the distribution becomes evident at approximately $h_{min} \sim 0.1$, where the fluctuations observed in the particle model grow more slowly than in the case without viscosity feedback. In this example the dimensionless particle radius is $r = 0.024$. Thus, the point at which finite size affects the dynamics occurs when the filament radius has reduced to around four to five times the particle radius. This observation is not affected by the bin discretisation, as we have shown in Figure 3.7. This change in dynamics agrees with experimental observations that the dynamics follow that of the bulk viscosity up to the point where the filament diameter has thinned to approximately five particle diameters [61].

Figure 3.13 shows the effect of increasing particle size on the mean minimum filament radius and the time to break-up. As particle size increases, the total number of particles in the simulation decreases and, as a consequence, the statistical variability between realisations increases. Therefore more realisations are required in order to determine the

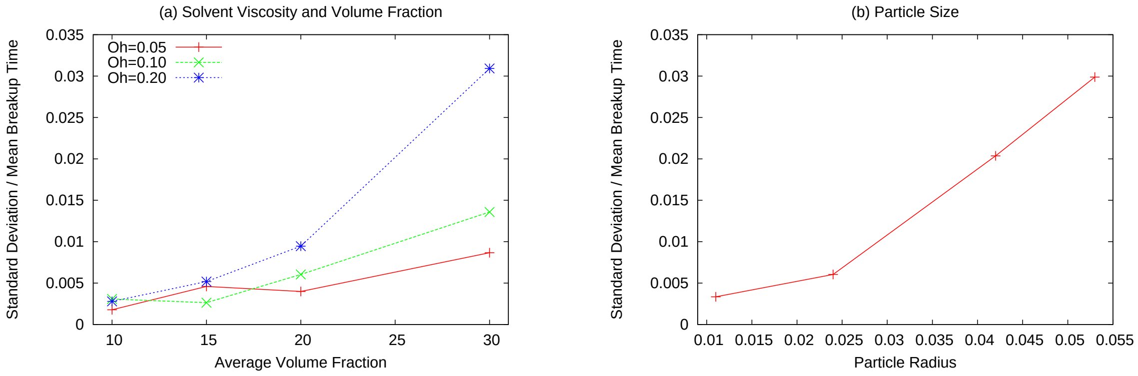

Figure 3.14: Standard deviation divided by mean break-up time averaged over ten realisations. (a) Increasing solvent viscosity Oh_s and volume fraction ϕ_{av}. (b) Increasing particle size.

mean break-up time. We observe that the thinning behaviour is equivalent for each of the particle radii until finite size affects the dynamics at approximately $h_{min} \sim 5r$. For larger particles, fluctuations in volume fraction are amplified and these variations occur earlier in the thinning process. Thus, increasing particle size further reduces the average time to break up. For very small particles $r \ll 0.01$, Newtonian behaviour will be recovered.

For a range of Ohnesorge numbers, volume fractions and particle sizes, we find that the mean time to break-up of a particulate suspension is reduced in each case, in comparison with the break-up time of the corresponding Newtonian fluid of the bulk viscosity. However, variation from the mean break-up time is found to increase with each of these properties. The values of the standard deviation normalised by the mean break-up time, averaged over ten realisations, are shown in Figure 3.14. Hence, as seen in experiments, the behaviour of particulate suspensions is less predictable than that of the equivalent continuum fluid.

Although on average the time to break-up for a particulate suspension is decreased compared to that of the continuous fluid, this may not necessarily be the case for a single realisation. Our model demonstrates that as particle size and volume fraction are increased, the standard deviation from the mean break-up time is increased. The spread of break-up times depends upon the distribution of particles as break up approaches. In general a particle-free filament, having a lower viscosity than the bulk, is generated and we observe accelerated thinning due to particle effects. However, in some cases particles become trapped in the filament region creating areas of high viscosity compared to the bulk. These structures may change the whole pinch off dynamics depending on the number of particles that are trapped in the filament.

Experiments have shown that, for small numbers of particles in the filament, finite size effects induce accelerated thinning as discussed above. On the other hand, if a sufficiently large number of particles become trapped in the filament region, then the effect tends to be stabilising; the individual motions of the particles are restricted and the necking of the filament is slowed [60]. Hammeed & Morris [65] study this mechanism further by modelling the local deformation of the fluid interface due to particle-induced flow. They show that for a single particle located at the centre of a thinning filament, the thinning rate is decreased for larger particle sizes. Consequently, the larger the particle trapped in the filament, the more stable the filament is and break-up time is consequently delayed.

Our model does not include this stabilisation mechanism, which occurs at a later stage in the development when the minimum filament radius is less than the particle radius. However, our model does predict that thinning becomes more varied as particle size and volume fraction are increased. Fluctuations in the particle density become more random and so it is more likely that more particles become trapped in the filament for highly concentrated suspensions containing larger particles. Thus, the stabilising effect of increasing particle size or volume fraction may decrease the number of satellite drops produced during jetting.

3.2.4 Three Distinct Thinning Regimes

We have already observed that the initial thinning behaviour of a particulate suspension follows that of the corresponding Newtonian fluid of bulk viscosity. As the filament radius is reduced, the thinning enters an accelerated thinning regime due to finite size effects. For solvent viscosity $Oh_s = 0.2$ we have tested a range of average volume fractions $\phi_{av} = 0.15, 0.20, 0.25$. The thinning profiles for each fraction collapse onto a single curve near the break-up point, as shown in Figure 3.15, where the origin of time has been shifted to the break-up time. This suggests that the thinning behaviour near to break-up is independent of the initial volume fraction ϕ_{av}. The accelerated regime we observe is not only faster than the rate of corresponding Newtonian fluid of bulk viscosity, it is faster than the

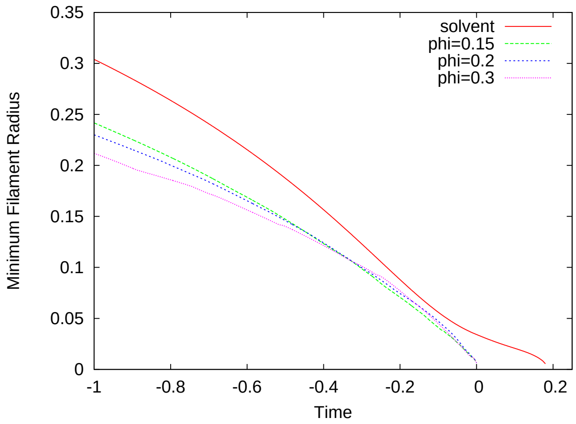

Figure 3.15: Radial decay profiles near to the point of break-up for a range of average volume fractions $\phi_{av} = 0.15, 0.20, 0.25$ compared to that of the solvent $Oh_s = 0.2$.

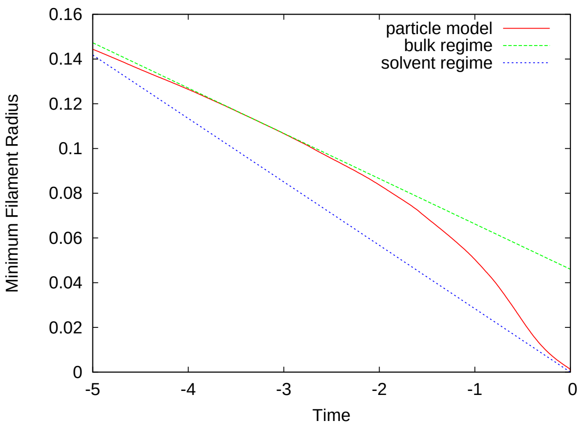

Figure 3.16: Radial decay profile near to break-up for volume fraction $\phi_{av} = 10\%$ and particle size $r = 0.02$ compared to the Papageorgiou regime (3.6) for the solvent $Oh_s = 2.5$ and the bulk viscosity $Oh_{av} = 3.5$.

thinning rate of the pure solvent, which is also shown in Figure 3.15.

We have seen that as the filament becomes devoid of particles, the viscosity is reduced to that of the solvent. Thus, we would expect to observe a transition from the acceleration phase to a final regime in which the thinning follows the behaviour of the solvent. However, in these cases, it is difficult to determine a final thinning regime adopted by the suspension in comparison to the solvent behaviour, since $Oh_s \approx Oh^*$. In section 3.1.4 for Newtonian fluids, we observe changes in the thinning behaviour at this solvent Ohnesorge number due to inertia; Figure 3.3 shows that there is a transition from inertial regime (3.4) to the universal Eggers regime (3.5), which occurs at around the same radius that finite size affects the dynamics. Thus, at this low Ohnesorge number, inertia still plays a significant role in the thinning process and may obscure dynamics due to particle effects.

In order to avoid this, we consider a larger Ohnesorge number for which a fully developed Papageorgiou regime (3.6) is observed. Figure 3.16 illustrates the thinning profile of a particulate suspension with solvent viscosity equivalent to $Oh_s = 2.5$. For volume fraction $\phi_{av} = 10\%$, the bulk viscosity increases to $Oh_{av} = 3.5$ and for this suspension, the effective particle size is given by $r = 0.02$.

The thinning profile of the suspension initially follows the bulk behaviour and Figure 3.16 shows that the radial decay obeys Papageorgiou's thinning law (3.6) for the bulk viscosity. We then observe a transition to the accelerated thinning regime due to finite size effects at approximately $h_{min} \sim 5r$; particles are forced into the end drops and particle-free regions develop. Again, the rate of the accelerated regime is seen to be faster than the thinning rate of the pure solvent given by Papageorgiou's law (3.6), which is valid for long, uniform filaments. Acceleration is attributed to the fact that a depleted filament is not yet slender, thus has a relatively high curvature and therefore must thin faster than a uniform filament in order to conserve volume [21]. When the filament becomes sufficiently long and thin, the thinning dynamics enter a final regime. Figure 3.16 shows that the transition into this regime occurs at around $h_{min} \sim r$ and the thinning behaviour can be described solely by the solvent properties, characterised by Papageorgiou's law (3.6) for the solvent viscosity.

If large numbers of particles become trapped within the filament, then the generation of a slender filament may be restricted. Our model predicts this is more likely to occur for higher volume fractions. For these cases, we propose that the solvent regime will be observed once the filament has thinned to less than the particle radius. A liquid bridge of solvent is suspended between two individual particles, which subsequently forms a slender filament following Papageorgiou's law for the solvent viscosity. However, our model is valid only for $h_{min} > r$, since we neglect individual particle effects on the free surface.

3.2.5 Comparison to Experimental Data

In Figure 3.17 we compare our numerical results with experimental data; polystyrene particles of radius 20 μm are suspended in silicon oil (PDMA) and the minimum filament radius is measured using a capillary-thinning rheometry [92]. The end plates have radius 2 mm and are held at fixed separation distance 6 mm. The initial shape is modelled as an arc of a circle with mid-filament radius $R = 1$ mm. The Ohnesorge number of the solvent alone is $Oh_s = 2.5$. For a 10% solution the bulk Ohnesorge number is increased to $Oh_{av} = 3.5$ and the suspension does not demonstrate shear-thinning properties. Despite the simplicity of our model, the numerical results are in excellent agreement with the experiment.

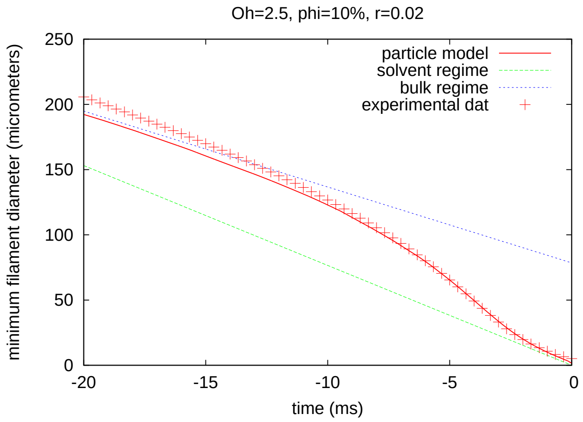

Figure 3.17: Radial decay profile near to break-up for $\phi_{av} = 10\%$ polystyrene particles with $r = 20$ μm suspended in silicon oil compared to the Papageorgiou regime (3.6) for the solvent $Oh_s = 2.5$ and the bulk viscosity $Oh_{av} = 3.5$. Experimental data given by crosses.

Initially, we observe the bulk regime in which there is a uniform distribution of particles and the suspension behaves like a Newtonian fluid having the bulk viscosity. As the filament thins, fluctuations in the particle density are amplified and development of low-viscosity regions induces a faster thinning rate. Thus, the dynamics enter the accelerated regime. The filament eventually becomes devoid of particles and so the thinning behaviour is governed by the properties of the solvent only. Thus, we observe the final solvent regime.

3.3 Modelling the Jetting of Polymer Solutions

3.3.1 Problem Outline

In contrast to the addition of particles, the addition of small amounts of long-chain polymers delays surface-tension-driven thinning and break-up. This mechanism may be exploited to prevent the formation of unwanted satellite drops in inkjet printing applications [66], [73], [120].

During the thinning of a viscoelastic jet, a stable uniform filament develops between the main drops of fluid. This polymeric phenomenon is known as the 'beads-on-string' structure and is examined in detail by Clasen *et al.* [35]. The long-lived filament is highly stable due the elastic forces and, as detailed in Chapter 2, exhibits classic exponential thinning at the inverse rate of three times the polymer relaxation time τ [21], [54], [130]. As fluid is expelled from the thinning filament, the main drops become increasingly spherical and, under the assumption of infinitely extensible dumbbells, the filament will never break [111]. For sufficiently low polymer concentrations, the filament may become unstable to the formation of smaller beads that develop on the uniform filament. These secondary satellites form an iterated beads-on-string structure, which has been observed in many experiments [32], [11], [117]. Furthermore, it has been suggested that this structure is self-similar [25].

In this section, we use our one-dimensional model, together with the Oldroyd-B constitutive equation, to explore the effects of viscoelasticity on an infinite jet. In particular, we demonstrate the exponential thinning law during the development of the beads-on-string structure and show a case where a secondary bead forms on the filament between the two main drops. For the latter case, we propose that the secondary satellite grows exponentially in time and compare the satellite drop shape to a Gaussian distribution, as in Sattler *et al.* [117]. We compare the results of our one-dimensional model to full axisymmetric simulations, the details of which are given in Chapter 1. We do not consider the final stages of break-up where the finite extensibility of the polymer affects the dynamics.

3.3.2 An Infinite-Jet Model

To simulate an infinite jet of polymeric fluid described by the Oldroyd-B constitutive equation, we solve the polymeric slender-jet equations (3.2) with periodic boundary conditions via the Lax Wendroff scheme. For the Oldroyd-B constitutive model, the polymers are assumed to be infinitely extensible dumbbells, so that we neglect the effects of finite extensibility.

The jet is assumed to be initially at rest so that $v = 0$ and $\sigma_{zz} = \sigma_{rr} = 0$. In order to provoke instability, we introduce a small sinusoidal perturbation to the free-surface profile

$$h(z, 0) = R + \epsilon \cos\left(\frac{2\pi z}{\lambda}\right),$$

for initial radius $R = 1$, where $\lambda = 20$ is the disturbance wavelength and the amplitude is set to $\epsilon = 0.01$. These initial parameters are chosen for direct comparison with the one-dimensional model results of Li & Fontelos [90].

3.3.3 Exponential Thinning of Polymeric Jets

To observe the typical beads-on-string structure the Ohnesorge number, polymer concentration and Deborah number for this simulation are chosen to be $Oh = 0.79$, $c = 2.37$ and $De = 94.9$, respectively, for direct comparison with Li & Fontelos [90]. For comparison to a Newtonian solvent, we also solve the Newtonian slender-jet case (3.1) for $Oh = 0.79$, which follows Papageorgiou's thinning regime (3.6).

The profiles given in Figure 3.19 are shown for a length of two periods for clear visualisation. Figure 3.19(a) shows that the initial perturbations to the jet radius remain small. Since the associated strains are small, the polymers remain close to their equilibrium configuration. Thus, the elastic stresses are small and the stress originates mainly from the solvent viscosity. Consequently the jet is Newtonian in character and, at this time $t = 20$, Figure 3.18 shows that the radial decay profile of the minimum filament radius is close to that of the Newtonian solvent.

Figure 3.19(b) shows the point at which elastic stresses become comparable to the capillary and viscous forces. This force balance is called the elasto-capillary balance.

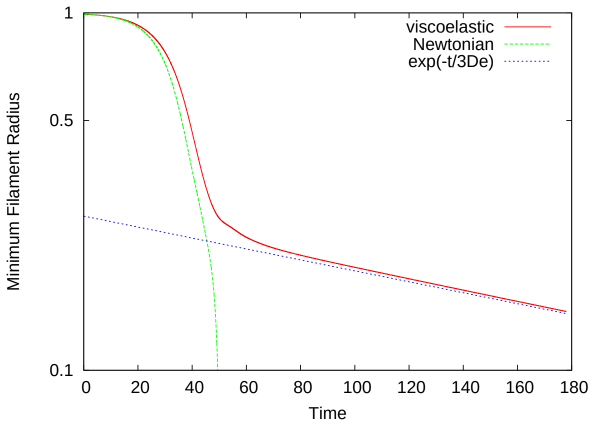

Figure 3.18: Radial-decay profile predicted by our one-dimensional model for fluid parameters $Oh = 0.79$, $c = 2.37$ and $De = 94.5$ compared to the exponential thinning law (3.9) and the corresponding Newtonian case.

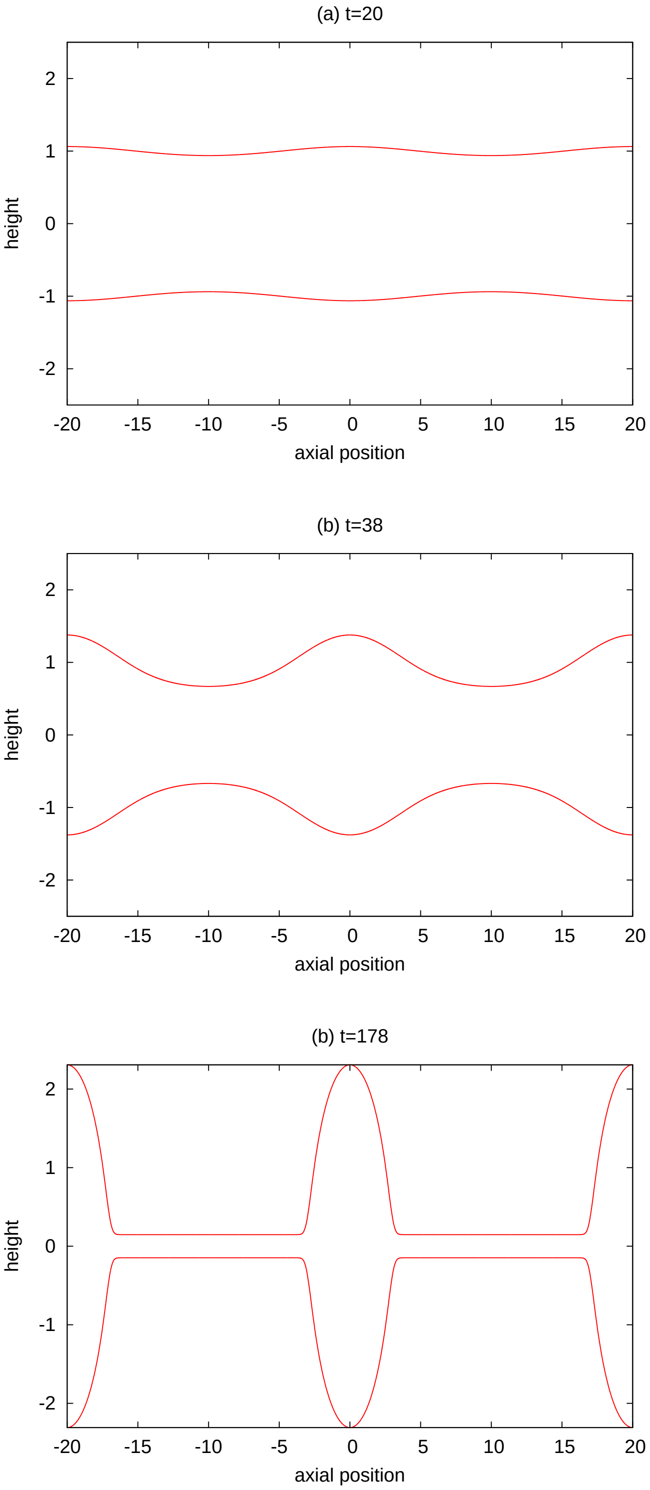

Figure 3.19: Free-surface evolution profiles predicted by our one-dimensional model for fluid parameters $Oh = 0.79$, $c = 2.37$ and $De = 94.5$ at time (a) $t = 20$, (b) $t = 38$, (c) $t = 178$

Stretching is evident at the centre of the jet, where the free surface begins to adopt a uniform shape. Since the viscous forces are large compared to the driving surface tension in this case, any necking action near to the main drops is dampened and the free surface continues to develop symmetrically. At this time $t = 38$, the radial decay profile shown in Figure 3.18 is seen to deviate from the Newtonian prediction and enter a new regime, which is dominated by elasticity. In this elastic phase, the thinning behaviour adopts the classic exponential thinning regime in which the minimum filament radius decays according to

$$h_{min} \sim \exp(-\frac{t}{3De}), \tag{3.9}$$

that is three times the relaxation time of the fluid, as shown in Figure 3.18.

As elastic stresses continue to grow, the jet evolves into a fully developed uniform filament connecting the main drops of fluid. Figure 3.19(c) shows this typical beads-on-string structure; the end drops are almost spherical and the thin filament is an order of magnitude smaller than the drop radius. These results agree with those of Li & Fontelos [90] and show that, for the Oldroyd-B model, a stable viscoelastic filament is formed that does not break in finite time. Ultimately, the effects of finite extensibility will cause the filament to break, but this will be at a later time compared to the Newtonian fluid.

3.3.4 Secondary Beads-on-String Structures

At lower Ohnesorge numbers, surface tension drives a necking instability causing the free surface to evolve into an asymmetric shape before entering the elastic phase. Consequently, secondary beads appear between the main drops in the beads-on-string structure. For this scenario, we simulate fluid parameters $Oh = 0.25$, $c = 0.75$ and $De = 300$, again for direct comparison with Li & Fontelos [90]. We compare to the Newtonian model (3.1) for solvent viscosity $Oh = 0.25$, which is close to the critical Ohnesorge number $Oh^* = 0.2077$ and breaks asymmetrically creating a satellite drop.

Figure 3.20(a) shows that, as in the elastic case shown in Figure 3.19, the jet is not very stretched and so the stress originates from the solvent viscosity. However, in contrast to the elastic case, the elastic stresses build up much more slowly and the solvent viscosity is too small to dampen the capillary-driven flow. Thus, in Figure 3.20(b) we observe a necking instability for which the free surface pinches in near to the end drops before a uniform filament is able to develop. This pinching behaviour and the development of neck regions is typical of the Newtonian behaviour predicted by Egger's self-similar solution described in Chapter 2.

In these neck regions, the jet stretches and so elastic stresses build and eventually dominate the flow. Any further necking is resisted by this elasticity and a smaller satellite drop develops. This smaller drop is connected to each main drop by a smaller uniform filament and Figure 3.21 shows that the thinning behaviour adopts the exponential decay law (3.9). Consequently, a two-level beading structure is created where smaller droplets appear in between the main drops.

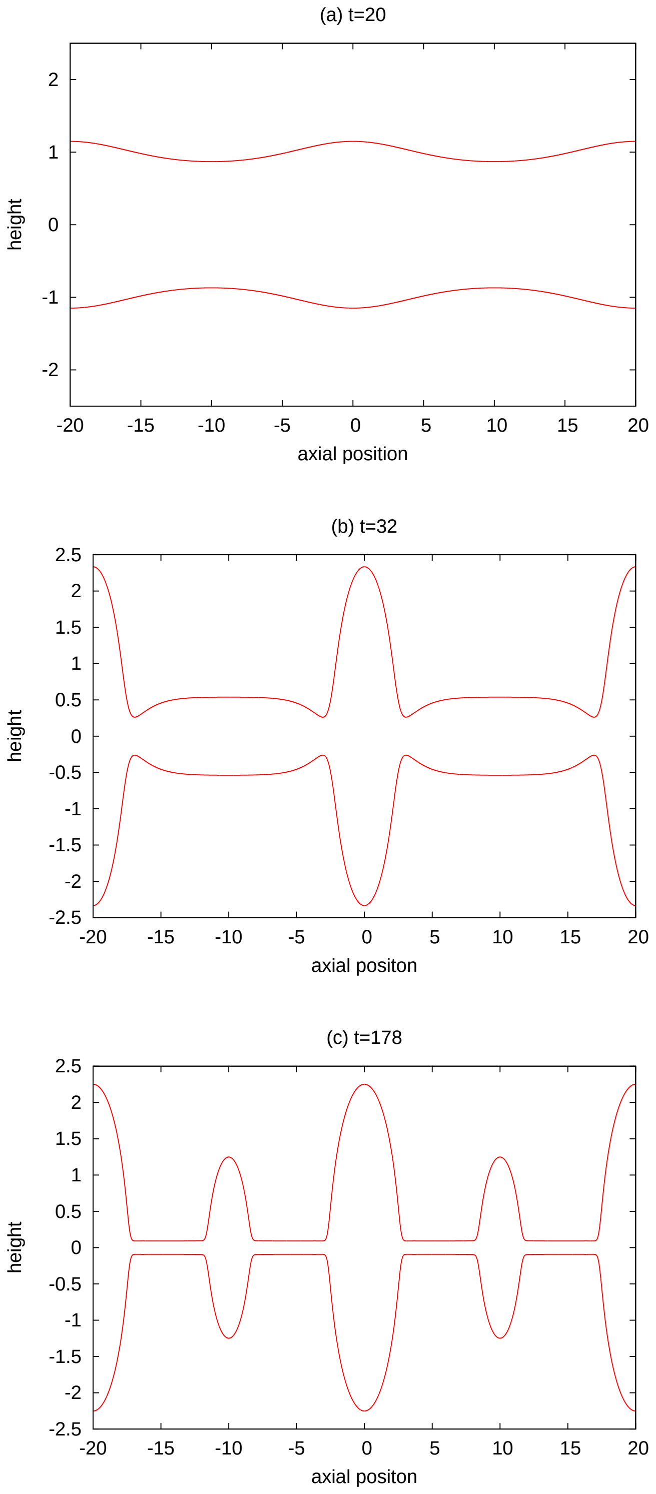

Figure 3.20: Free-surface evolution profiles predicted by our one-dimensional model for fluid parameters $Oh = 0.25$, $c = 0.75$ and $De = 300$ at time (a) $t = 20$, (b) $t = 32$, (c) $t = 178$

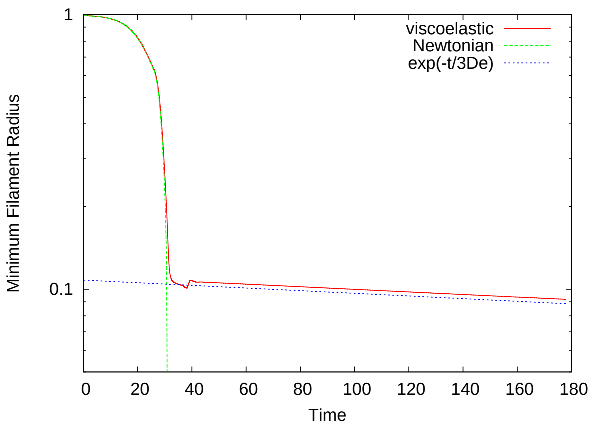

Figure 3.21: Radial-decay profile predicted by our one-dimensional model for fluid parameters $Oh = 0.25$, $c = 0.75$ and $De = 300$ compared to the exponential thinning law (3.9) and the corresponding Newtonian case.

In Figure 3.22, the secondary drop shape is compared to the Gaussian distribution

$$d(z,t) \approx h_0(t) + A(t)\exp\left(\frac{z - z_d(t)}{w(t)}\right)^2, \tag{3.10}$$

for comparison with the isolated drops observed experimentally by Sattler *et al.* [117], which are well approximated by equation (3.10). Here $h_0(t)$ is the radius of the filament outside the drop and $A(t)$, $w(t)$ and $z_d(t)$ are the amplitude, width and position of the drop, respectively. The drop shape of the simulation is much sharper than the Gaussian approximation observed by Sattler *et al.* and may be a consequence of the long-wavelength approximation. Figure 3.22(b) shows that these secondary drops initially grow exponentially, demonstrating a linear instability on the polymeric filament. The droplet size then

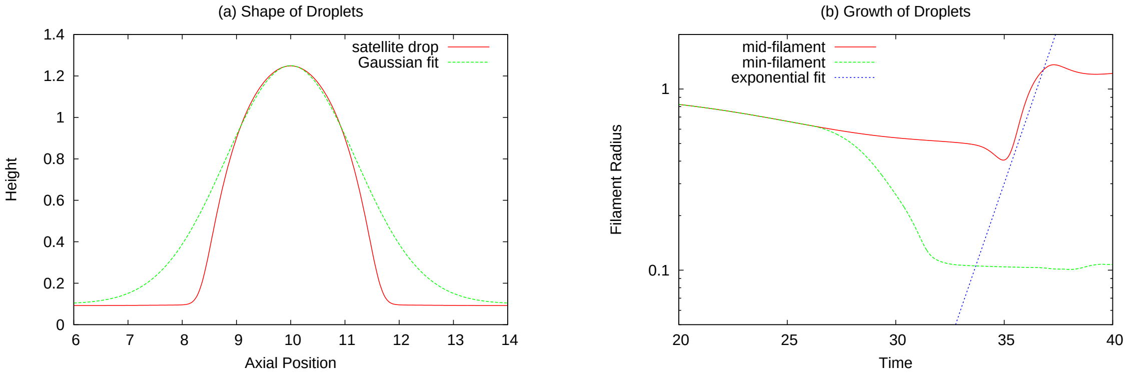

Figure 3.22: (a) Droplet free surface compared to the Gaussian distribution (3.10). (b) Exponential growth of droplet height for fluid parameters $Oh = 0.25$, $c = 0.75$ and $De = 300$.

reaches a constant radius.

It should be noted, however, that at this Ohnesorge number $Oh = 0.25$, the corresponding Newtonian fluid develops satellites between its main drops and therefore this two-level bead-on-string structure is the result of elasticity frustrating the formation of satellites. This is quite different from the iterated mechanism given by Chang *et al.* [25] that is caused by an instability at the junction between the bead and the filament. This instability not observed in this model or in previous studies using a one-dimensional model [6],[90], which may be a result of the long-wavelength approximation.

Experimentally, iterated beading originating from a highly-stretched state has been investigated by Oliveira *et al.* [101], [102] and is termed 'blistering'. Due to the effects of finite extensibility, the Oldroyd-B constitutive model is not sufficient to capture this effect. Oliveira *et al.* suggest that the hierarchy of beads and connecting filaments is self-similar. However, further investigation by Sattler *et al.* [117] show that blistering is not necessarily a self-similar process and the sequence of instabilities suffered by polymeric filaments is considerably more complicated than previously reported.

3.3.5 Comparison to Axisymmetric Simulations

In this section, we compare the results predicted by our one-dimensional model to full axisymmetric simulations [66] described in Chapter 1. Again, we assume an infinite jet of viscoelastic fluid described by the Oldroyd-B constitutive model for fluid parameters $Oh = 0.79$, $c = 2.37$ and $De = 94.9$.

Figure 3.23 shows that the one-dimensional approximation for the free-surface height is in quantitative agreement with the axisymmetric simulation. For this elastic case, a uniform filament is generated creating the typical beads-on-string structure described earlier. The axisymmetric simulation gives a clear visualisation of the axial stress that is generated

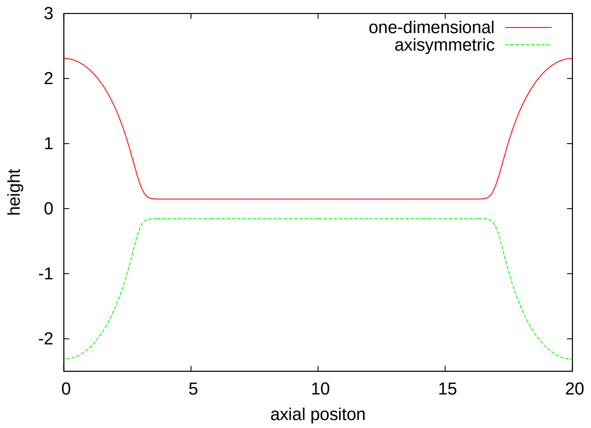

Figure 3.23: Free-surface profile predicted by the one-dimensional model compared to the axisymmetric model for fluid parameters $Oh = 0.79$, $c = 2.37$ and $De = 94.9$.

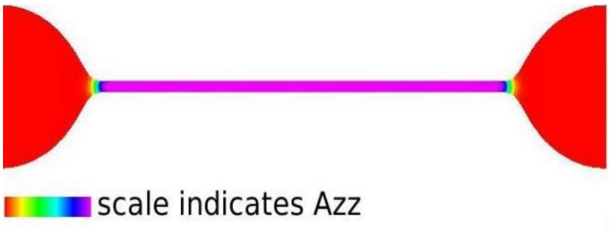

Figure 3.24: Jet profile predicted by the axisymmetric model for fluid parameters $Oh = 0.79$, $c = 2.37$ and $De = 94.9$. The colour scale corresponds to the axial component of the structure tensor $\mathbf{A}$ describing dumbbell stretch.

throughout the filament region compared to the relaxed end-drops; the colour scale shown in Figure 3.24 indicates the increase in the axial component of the conformation tensor $\mathbf{A}$, which describes the structure of the dumbbells, and is related to the polymer stress via

$$\boldsymbol{\sigma} = G(\mathbf{A} - \mathbf{I}).$$

The high extension rate in the filament region causes the infinitely-extensible dumbbells to uncoil indefinitely and consequently the axial stress becomes large in this area. In contrast, the dynamics are slow in the drops of fluid and so the polymers remain relaxed. Furthermore, the stress appears uniform across the filament radius. This is in contrast to numerical simulations of the filament-stretching technique, which report a high stress boundary layer near to the free surface of the filament [12], [143].

Figure 3.25 compares the evolution of the minimum filament radius predicted by our one-dimensional model to the full axisymmetric simulation. The profiles have been shifted so that the initial Newtonian regime collapses onto approximately the same curve. The filament radius is seen to decay exponentially according to equation (3.9) and the results

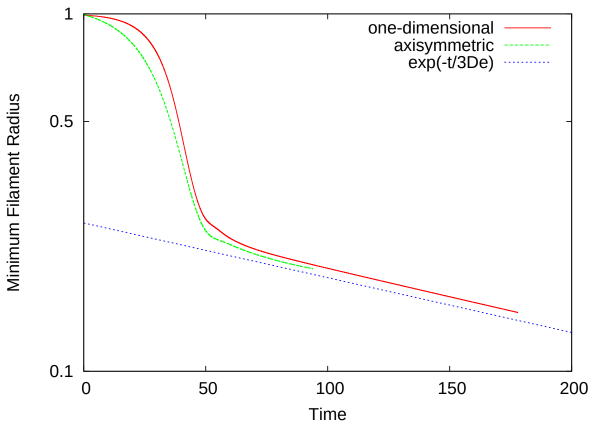

Figure 3.25: Evolution of the minimum filament radius predicted by the one-dimensional model compared to the axisymmetric model for fluid parameters $Oh = 0.79$, $c = 2.37$ and $De = 94.9$. The exponential thinning law is also plotted.

of the two models are in agreement once a slender filament is generated. Discrepancies during the early stages of thinning are probably due to discrepancies in the initial growth rate of radial perturbations of the free surface between the full solution and the long-wavelength approximation in the one-dimensional model. Similar differences have been observed when comparing this axisymmetric model to a one-dimensional approximation for fast filament stretching [130]. Vadillo *at al.* [130] also found it necessary to use a multi-mode FENE approach in order to obtain realistic agreement between experiments and the full axisymmetric simulation.

3.4 Concluding Remarks

In this chapter, we have developed a simple one-dimensional model under the long-wavelength approximation in order to simulate surface-tension-driven thinning. In particular we have considered two cases; a liquid bridge held between two end-plates and the case of an infinite jet of fluid. This model has proved successful in predicting the thinning dynamics observed for Newtonian fluids, particulate suspensions and viscoelastic solutions. Here we summarise the results presented in this chapter.

First, we developed the model to demonstrate experimental observations of drop formation in the case of particulate suspensions. A two-stage thinning model has previously been suggested [60] based on the idea that the initial and final thinning dynamics involve a transition from a regime where particle effects are governed by bulk properties, to one where finite size effects dominate the behaviour.

For an initially uniform distribution of particles, our model predicts that as a liquid filament thins, fluctuations in the local particle density are amplified resulting in areas of both high and low particle density. These fluctuations are reflected in the fluid viscosity. Initially, the particulate suspension behaves like a Newtonian fluid with the corresponding bulk viscosity, however, the development of low-viscosity regions allows the filament to thin more easily. We therefore observe an accelerated thinning regime in which the thinning rate is faster than that of the bulk and the solvent behaviour. Furthermore, our model is able to quantify that finite-size effects dominate when the filament radius has thinned to approximately five times the radius of the particle, as seen in large scale pendant drop experiments [15], [60], [61].

For high-viscosity suspensions, we observe a transition from the accelerated regime to an ultimate thinning regime, once the filament has become sufficiently long and thin. Since the filament is particle-free, the thinning is no longer governed by finite-size effects, but follows the behaviour of the pure solvent, which is characterised by Papageorgiou's thinning law. For low-viscosity suspensions, a slender filament is not generated at this final stage and the solvent regime is not observed.

Second, we developed the model to simulate the evolution of a viscoelastic infinite jet under the action of surface-tension-driven thinning. In contrast to the acceleration effect particles have on a Newtonian fluid, the addition of polymer to a Newtonian solvent significantly delays to time to break-up. As the polymers are unravelled by the extensional flow, elasticity becomes increasingly important and the elasto-capillary balance is achieved. Our model shows that the thinning then enters the well-established elasto-capillary regime, unique to polymeric fluids, in which the minimum filament radius decays exponentially; the radius decays at an inverse rate that is three times the relaxation time of the fluid, as predicted by the theory [35]. Consequently, the time to break-up is increased in comparison with the corresponding Newtonian fluid. Our model is able to predict the classic 'beads-on-string' structures seen in experiments, including two-level beading [117], and is in quantitative agreement with other one-dimensional modelling [90] and full axisymmetric simulations [66].

Chapter 4

The DoD Inkjet

4.1 Problem Outline[1]

As we have observed, the addition of polymer molecules to a Newtonian solvent can significantly affect the break-up of liquid filaments. This increased stability due to viscoelasticity has also been observed in liquid ligaments generated by flow through a nozzle [9], [43], [120]. In particular, the addition of small amounts of high-molecular-weight polymer can cause the ligament to retract into the main drop, so that the formation of unwanted satellites can be inhibited. On the other hand, polymer content affects the reliability of jetting; print speed may be compromised and, at high concentrations, the main drop may even fail to detach from the nozzle. Thus, there exists a critical polymer concentration threshold at which printing at the desired speed is possible, within the limit of the print head [71].

Hoath *et al.* [71] have recently analysed experimental results for the drop-on-demand jetting behaviour of two polystyrene solutions. These solutions consist of mono-disperse, linear polystyrene dissolved in two solvents of disparate viscosity and are jetted through different nozzle diameters at different print speeds. They introduce a simple model (based on one originally proposed by Bazilevskii *et al.* [9]), in which the fluid is modelled as a solution of finitely-extensible dumbbells (FENE model) and the parameters are chosen to fit the Zimm model [36]. Although the polymers present in ink formulations are rarely linear [141], the model system was chosen to determine how the polymer-concentration threshold, at which jetting at the desired speed is possible, varies with molecular weight.

Three regimes of jetting behaviour are defined by the dominant mechanism that limits jet speed; regime 1 is restricted by (zero-shear) viscosity, regime 2 by viscoelasticity and regime 3 by high-strain-rate extensional viscosity. The transitions between these regimes are determined by the initial Weissenberg number $Wi_0 = U_0\tau/D$, where U_0 is the jet velocity at the nozzle exit, τ is the fluid relaxation time and D is the nozzle diameter. The first transition from regime 1 to 2 occurs at $Wi_0 = 1/2$, at which point polymers can become significantly extended from their equilibrium configuration. The second transition from regime 2 to 3 occurs at $Wi_0 = L$, when polymers reach their finite-extensibility limit

---

[1] Published: **C. McIlroy**, O. G. Harlen, N. F. Morrison *Modelling the jetting of dilute polymer solutions in drop-on-demand inkjet printing* J. Non-Newt. Fluid Mech. 201 (2013) 17-28

L.

In their paper, Hoath *et al.* [71] demonstrate that the scaling of the maximum jettable polymer concentration with molecular weight, predicted by these jetting regimes, agree with experimental data. However, they do not perform a quantitative comparison. The aim of this chapter is to explore these jetting regimes, and the transitions between them, numerically and attempt a quantitative comparison with the experimental measurements for the two polymer systems.

Furthermore, flow-induced deformations can lead to irreversible changes in the structure of a polymeric fluid; if the rate of extension far exceeds the rate of relaxation, then the polymer chain can be broken. Mechanical degradation of polymers in extensional flow has long been recognised [99] and leads to a reduction in the average molecular weight. A-Alamry *et al.* [1] have recently reported evidence of flow-induced polymer degradation in DoD jetting; central scission of high-molecular weight polystyrene is observed in a number of good solvents under certain jetting conditions. Since only those molecules that are fully extended can be fractured at the centre of the polymer chain [97], in this chapter we investigate if the strain rates in the ligament are large enough for central scission to occur in DoD jetting.

4.2 Modelling Drop-on-Demand Jetting

4.2.1 Constitutive Model

A simple constitutive model for describing dilute polymer solutions in extensional flow is the finitely-extensible non-linear elastic dumbbell model with the Chilcott-Rallison closure approximation [31], also known as the FENE-CR model. Recall from Chapter 1 that the total stress is given by

$$\boldsymbol{\sigma} = 2\mu_s \mathbf{E} + Gf(\mathbf{A} - \mathbf{I}),$$

where μ_s is the solvent viscosity, $\mathbf{E}$ is the strain-rate tensor and the polymer stress consists of the elastic modulus G, the conformation tensor $\mathbf{A}$ and the FENE factor

$$f = \frac{L^2}{L^2 + 3 - \mathrm{tr}(\mathbf{A})}, \tag{4.1}$$

that accounts for the finite extensibility L of the polymer chain. The conformation tensor $\mathbf{A}$ satisfies the evolution equation

$$\frac{D\mathbf{A}}{Dt} = \mathbf{K} \cdot \mathbf{A} + \mathbf{A} \cdot \mathbf{K}^T - \frac{f}{\tau}(\mathbf{A} - \mathbf{I}), \tag{4.2}$$

where τ is the relaxation time of the polymer and $K_{ij} = \frac{\partial u_i}{\partial x_j}$ is the velocity-gradient tensor.

For a dilute, monodisperse polymer solution the parameters in the FENE-CR model, namely elastic modulus G, relaxation time τ and finite extensibility L, can be determined as functions of the molecular weight M_w, concentration by weight ϕ and solvent quality factor ν using Zimm theory [36]. The elastic modulus is governed by the number density of polymer chains and so is proportional to concentration and inversely proportional to molecular weight such that

$$G = \frac{\phi R T}{M_w}. \tag{4.3}$$

Here R is the universal gas constant and T is the absolute temperature. The relaxation time τ of the dumbbell is chosen to be the longest Zimm time and is defined as

$$\tau = \frac{1}{\Lambda} \frac{[\mu]\mu_s M_w}{RT}, \tag{4.4}$$

where $\Lambda = \hat{\tau}/\tau = \sum_i i^{-3\nu}$ is the universal ratio of the characteristic relaxation time $\hat{\tau}$ to the longest relaxation time τ. The intrinsic viscosity $[\mu]$ is described by the Mark-Houwink relation

$$[\mu] = K M_w^{3\nu - 1}, \tag{4.5}$$

where K is a constant dependent upon the polymer system. The finite extensibility L can be determined from the ratio of the equilibrium coil to the fully-extended length of the polymer so that

$$L^2 = 3 \left(\frac{j \sin^2(\theta/2) M_w}{C_\infty M_u} \right)^{2(1-\nu)}, \tag{4.6}$$

where θ is the carbon-carbon bond angle, j is the number of bonds of a monomer unit with molar mass M_u and C_∞ is the characteristic ratio. It should be noted that there is experimental evidence [124] suggesting that this equation over-predicts the finite extensibility of a molecule. For Zimm theory to be valid we require that

$$\phi/\phi^* \ll 1, \tag{4.7}$$

where ϕ^* is the critical overlap concentration.

Hence, for a dilute mono-disperse polymer solution, the FENE-CR model parameters scale with molecular weight as

$$G \sim M_w^{-1} \quad ; \quad \tau \sim M_w^{3\nu} \quad ; \quad L \sim M_w^{(1-\nu)}, \tag{4.8}$$

derived from the equations (4.3)-(4.6). As an example, polystyrene dissolved in acetophenone (ATP), a good solvent with a quality factor of $\nu = 0.59$, has relaxation time

$$\tau = \frac{M_w^{1.77}}{3.24 \times 10^8} \ \mu\text{s}, \tag{4.9}$$

and finite extensibility

$$L^2 = \frac{M_w^{0.82}}{9.2 \times 10^3}, \tag{4.10}$$

for a molecular weight M_w measured in Daltons (Da).

4.2.2 A Simple Jetting Model

In their recent paper, Hoath *et al.* [71] describe a simple model for predicting the printability of polymeric fluids, as illustrated in Figure 4.1. After ejection from the nozzle, the main drop is slowed down by the extensional flow in the connecting fluid ligament. We

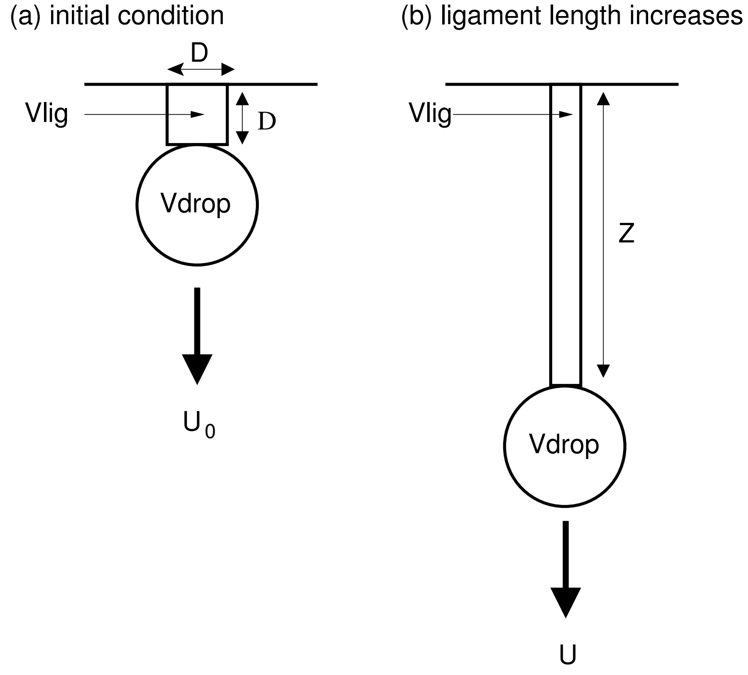

Figure 4.1: Simplified model of drop-on-demand printing. The main drop slows down from velocity U_0 in (a) to velocity U in (b). The ligament increases from initial length D in (a) to length Z in (b).

assume that a drop of density ρ and volume V_{drop} is ejected from a nozzle of diameter D, at speed U_0, which we define as the speed of the main drop when it is a distance D from the nozzle exit. The main drop is connected to the nozzle by a ligament of volume V_{lig} and initial length D. The volume of fluid in the drop and the ligament is assumed to remain constant and the ligament is assumed to deform uniformly as its length Z increases. The main drop slows down to final velocity U_f, due to resistive forces in the ligament.

The initial conditions defined for the simplified jetting model, as shown in Figure 4.1, correspond to the time at which the fluid leaves the nozzle orifice in both experimental applications and the full axisymmetric simulations. Thus, for comparison, we assume that the model velocity U_0 is equivalent to the velocity at which the drop exits the nozzle. This velocity is greater than the final jet velocity U_f, which is the drop speed measured at a distance of 1 mm from the nozzle exit, by a factor of 1.5 to 3 times (see Hoath *et al.* [72]).

For our simplified jetting model, we have the following governing equations [71]. The speed of the drop at some time t is given by

$$U = \frac{dZ}{dt},$$

and the strain rate is $\dot{\epsilon} = U/Z$. Assuming that the only forces acting on the drop are from the stress difference in the ligament, the drop velocity satisfies the force balance

$$\rho V_{drop} \frac{dU}{dt} = -\frac{V_{lig}}{Z} \left(\frac{3\mu_s U}{Z} + Gf(A_{zz} - A_{rr}) \right).$$

The force consists of a viscous and polymer contribution multiplied by the cross-sectional area of the jet. From the dumbbell evolution equation (4.2), the configuration tensor components A_{zz} and A_{rr} satisfy the evolution equations

$$\begin{aligned}\frac{dA_{zz}}{dt} &= \left(\frac{2U}{Z} - \frac{f}{\tau}\right) A_{zz} + \frac{f}{\tau},\\ \frac{dA_{rr}}{dt} &= -\left(\frac{U}{Z} + \frac{f}{\tau}\right) A_{rr} + \frac{f}{\tau}.\end{aligned} \tag{4.11}$$

These equations are non-dimensionalised using relaxation time τ as the unit of time and nozzle diameter D as the length scale. Hence, for dimensionless velocity u and dimensionless length z we have the following set of non-dimensional governing equations:

$$\begin{aligned}u &= \frac{dz}{dt},\\ \frac{du}{dt} &= -\frac{El^*}{z}\left(\frac{3u}{z} + cf(A_{zz} - A_{rr})\right),\\ \frac{dA_{zz}}{dt} &= \left(\frac{2u}{z} - f\right) A_{zz} + f,\\ \frac{dA_{rr}}{dt} &= -\left(\frac{u}{z} + f\right) A_{rr} + f,\end{aligned} \tag{4.12}$$

together with the initial conditions,

$$\begin{aligned}&u = Wi_0 = \frac{U_0 \tau}{D}, \quad \text{at } t = 0,\\ &z = A_{zz} = A_{rr} = 1, \quad \text{at } t = 0.\end{aligned}$$

In our dimensionless units, the velocity at time zero is equal to the initial Weissenberg number Wi_0. However, the Weissenberg number at time t is given by $Wi = U\tau/Z = u/z$ and is a decreasing function of time, as the length of the ligament z increases. Thus, even if the initial Weissenberg number is large, the extension rate in the ligament will drop below the coil-stretch transition by the time that the ligament has grown to a dimensionless length of $2Wi_0$.

The dimensionless number that determines the deceleration of the drop is the modified elasticity number El^*, defined as

$$El^* = \frac{V_{lig}}{V_{drop}} \frac{Wi_0}{Re} = \frac{V_{lig}}{V_{drop}} \frac{\mu_s \tau}{\rho D^2}.$$

This is a combination of the initial Weissenberg number, Wi_0, defined as above and the Reynolds' number

$$Re = \frac{\rho U_0 D}{\mu_s},$$

which gives a measure of the viscous forces compared to the inertial forces. The pre-factor V_{lig}/V_{drop} appearing in the modified elasticity number is assumed to be 1/4 based on observations in both simulations and experiments that approximately 80% of the fluid ejected from the nozzle ends up in the main drop. The dimensionless polymer concentration c is given by

$$c = \frac{G\tau}{\mu_s},$$

and is equivalent to the dimensionless grouping ϕ/ϕ^*.

The governing equations (4.12) are solved numerically to calculate the 'maximum jettable concentration' as a function of molecular weight. In experiments, this concentration is considered to be the maximum polymer content that can be jetted from the nozzle at a desired jetting velocity U_f, using the range of drive voltages available. For our simplified model, we define this maximum to be the polymer concentration at which the specified ratio U_0/U_f is achieved.

This simple model has a number of limitations. First, the model neglects the nozzle geometry and any subsequent effects due to the flow though the nozzle. Consequently, the model assumes that the polymers are initially at equilibrium i.e. $\mathbf{A}^0 = \mathbf{I}$. Second, the model does not take into account the break-off of the ligament from the nozzle.

4.2.3 Asymptotic Predictions of the Simple Jetting Model

To determine the three jetting regimes, as derived by Hoath *et al.* [71], we consider the asymptotic limits of the force balance equation

$$\frac{1}{Wi_0}\frac{du}{dt} = -\frac{1}{4Re}\left(\frac{3u}{z^2} + \frac{cf}{z}(A_{zz} - A_{rr})\right), \tag{4.13}$$

as given in the governing equations (4.12). For reference, the molecular-weight scalings of the initial Weissenberg number Wi_0, the dimensionless concentration c and extensibility L are

$$Wi_0 \sim M_w^{3\nu} \quad ; \quad c \sim M_w^{3\nu-1} \quad ; \quad L \sim M_w^{1-\nu}, \tag{4.14}$$

which can be derived from the scalings given by equation (4.8).

In jetting regime 1, the initial Weissenberg number Wi_0 is small such that the extension rate in the ligament $u/z \ll 1$. So in this limit,

$$A_{zz} \sim 1 + 2u/z, \quad A_{rr} \sim 1 - u/z, \quad f = 1,$$

and the force balance equation (4.13) reduces to

$$\frac{1}{Wi_0}\frac{du}{dt} = -\frac{1}{4Re}\left(\frac{3u}{z^2}(1+c)\right).$$

The fluid behaviour is Newtonian with a viscosity given by

$$\mu_0 = \mu_s(1+c).$$

Thus, the maximum polymer concentration that can be jetted at a particular molecular weight is limited by the increase in the zero-shear-rate viscosity and the reduction in drop velocity scales with molecular weight via (4.14) such that

$$-\Delta u \sim \frac{c}{Re} \sim M_w^{3\nu-1}.$$

Jetting regime 2 is defined to be the regime in which the initial Weissenberg number satisfies $1/2 < Wi_0 < L$. In this case, the initial extension rate is strong enough to stretch the polymer molecules and fluid behaviour is viscoelastic. However, as the strain increases, the strain rate decreases so that the polymers ultimately relax. Thus, in this regime the polymers relax before becoming fully extended and so the FENE factor can again be approximated by $f \approx 1$. Assuming that $1 \ll A_{zz} \ll L^2$, the dumbbell evolution equation (4.12) can be integrated to give

$$A_{zz} \approx z^2 e^{-t},$$

and so the force balance equation (4.13) reduces to

$$\frac{1}{Wi_0}\frac{du}{dt} = -\frac{1}{4Re}\left(\frac{3u}{z^2} + c(ze^{-t})\right).$$

Integrating along the ligament length from 1 to z, the reduction in drop velocity is given by

$$\frac{\Delta u}{Wi_0} = -\frac{1}{4Re}\left(3\left(1-\frac{1}{z}\right) + c\int_0^t z(t)e^{-t}dt\right).$$

Recalling that the initial Weissenberg number is equivalent to the dimensionless velocity, the integral can be approximated by taking $z = 1 + Wi_0 t$ and the limit $z \to \infty$

$$\int_0^\infty ze^{-t}dt = 1 + Wi_0.$$

The reduction in drop velocity is thus given by

$$\frac{\Delta u}{Wi_0} = -\frac{1}{4Re}\left(3 + c(1 + Wi_0)\right),$$

which for $cWi_0 \gg 1$ has the molecular-weight scaling

$$-\Delta u \sim \frac{cWi_0}{Re} \sim M_w^{6\nu-1},$$

using equation (4.14) .

In jetting regime 3, defined by $Wi_0 > L$, the polymer chains reach their finite-extension limit and the fluid then behaves like a suspension of rigid rods. Assuming that $A_{zz} \to L^2$, the dumbbell evolution equation (4.12) is approximated as

$$fA_{zz} \approx \frac{u}{z}L^2,$$

and so the force-balance equation (4.13) reduces to

$$\frac{1}{Wi_0}\frac{du}{dt} = \frac{1}{4Re}\left(3 + 2cL^2\right)\frac{u}{z^2} \sim \left(\frac{u}{z^2}\right)cL^2.$$

Integrating along the fully extended ligament length from L to $z \to \infty$ finds the reduction in drop velocity to be

$$-\Delta u \sim \frac{cL}{Re} \sim M_w^{2\nu},$$

using the molecular-weight scalings (4.14).

Thus, by using the Zimm model to determine the molecular-weight dependence of the relaxation time we can determine how the maximum jettable polymer concentration scales with molecular weight during each of the three jetting regimes. These scalings

Concentration	Regime 1	Regime 2	Regime 3
wt%	$M_w^{1-3\nu}$	$M_w^{1-6\nu}$	$M_w^{-2\nu}$
c	1	$1/Wi_0$	$1/L$

Table 4.1: Regime scalings in terms of wt% concentration and dimensionless concentration c.

laws are summarised in Table 4.1, where the concentration by weight ϕ is related to the dimensionless concentration via $c = \phi/\phi^*$.

The transition from regime 1 to regime 2 occurs at $Wi_0 = 1/2$ and corresponds to the molecular weight at which coil-stretch transition will occur during the jetting process. The transition from regime 2 to regime 3 occurs at $Wi_0 = L$, at which polymers of this molecular weight reach their finite extension limit during jetting. The transitions depend upon jetting conditions such as drop speed and nozzle diameter, as well as polymer characteristics and the solvent viscosity.

4.3 Jettable Concentration Thresholds

In order to test whether these asymptotic regimes exist in practice, we have calculated numerical solutions to the governing equations (4.12) for parameter values chosen to match the experimental systems studied by de Gans *et al.* [42] and Hoath *et al.* [73]. These calculations were performed using `MATLAB`.

4.3.1 Polystyrene/ATP Solution jetted using the AutoDrop System

The fluids studied by de Gans *et al.* [42] are solutions of polystyrene dissolved in acetophenone (ATP) jetted at $U_f = 2$ m/s from a 70 μm diameter nozzle using an AutoDrop system. The AutoDrop system, manufactured by microdrop technologies, uses a standard micropipette for the nozzle. The speed of the jet on exiting the nozzle is unknown for this case. We estimate that the ratio between final jet speed and the speed at which the ink

Nozzle	Micropipette	**Solvent**	ATP
nozzle diameter, D	70 μm	solvent viscosity, μ_s	0.0017 Pa.s
initial speed, U_0	3 m/s	quality factor, ν	0.59
print speed, U_f	2 m/s	fluid density, ρ	1028 kg/m^3

Table 4.2: Jetting conditions and fluid parameters for polystyrene dissolved in ATP jetted from an AutoDrop system chosen to correspond with experimental data [42].

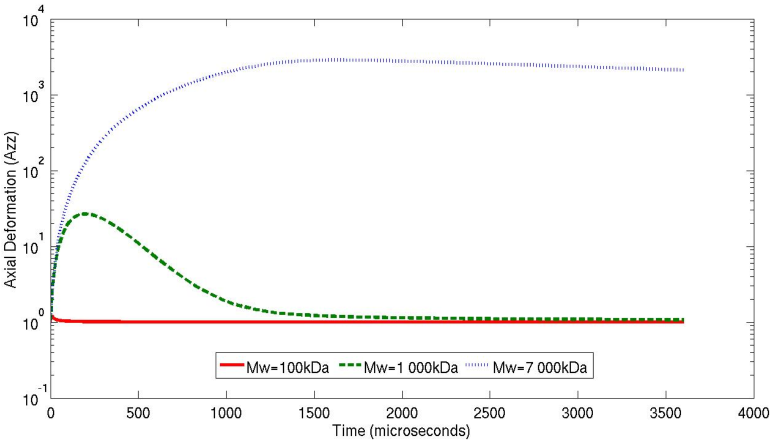

Figure 4.2: A_{zz} profiles for molecular weights $M_w = 100$ kDa (solid), $M_w = 1000$ kDa (dash) and $M_w = 7000$ kDa (dot) for polystyrene in ATP jetted from an AutoDrop system.

exits the nozzle for a micropipette to be 1.5 by fitting the jetting model to the experimental data at low molecular weight, where the fluid behaviour is Newtonian. Thus, we shall take $U_0 = 3$ m/s. The solvent ATP is of low-viscosity ($\mu_s = 0.0017$ Pa.s) and is classed as 'good', with solvent quality factor $\nu = 0.59$. The jetting conditions and fluid parameters are listed in Table 4.2.

Figure 4.2 demonstrates the change in zz-component of the configuration tensor $\mathbf{A}$ as molecular weight is increased. For low molecular weights ($M_w = 100$ kDa), A_{zz} remains small indicating that the flow is not strong enough to deform the polymer molecules. Thus, the axial stress is proportional to the strain rate and jettability depends on the fluid viscosity. For intermediate molecular weights ($M_w = 1000$ kDa), A_{zz} initially grows but then relaxes before reaching its finite extensibility limit $L^2 = 762$. Thus, the deformation remains within the Oldroyd limit where $A_{zz} \ll L^2$ and jettability is limited by viscoelasticity. For large molecular weights ($M_w = 7000$ kDa), A_{zz} approaches the finite extensibility limit $L^2 = 3783$ indicating that polymer molecules reach their finite extension limit.

In the steady state equilibrium $dA_{zz}/dt = 0$, the FENE factor given by equation (4.1) balances the stretching induced by the velocity gradient. So, in the limit $A_{zz} \gg 1$, the dumbbell evolution equation (4.11) reduces to

$$0 = \left(2\dot{\epsilon} - \frac{f}{\tau}\right) A_{zz},$$

and the FENE factor can be approximated as $f = 2\dot{\epsilon}\tau$. In this limit, the FENE factor is also approximated as

$$f = \frac{L^2}{L^2 - A_{zz}}.$$

Thus, equating the two approximations, the axial stress component can be written as

$$\frac{A_{zz}}{L^2} = 1 - \frac{1}{2Wi}.$$

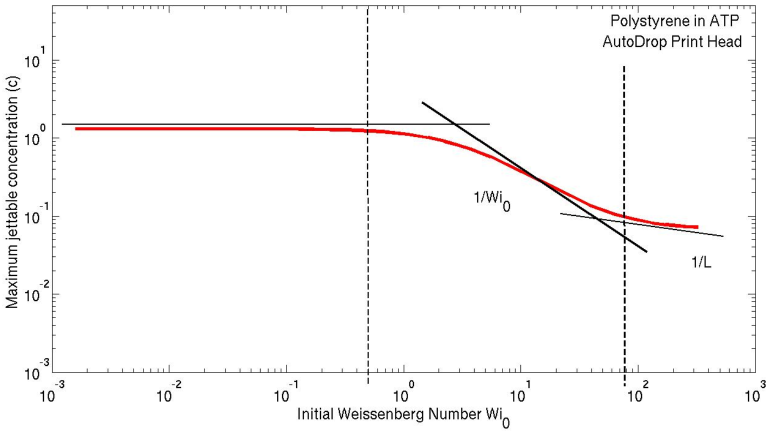

Figure 4.3: Maximum jettable concentration (c) of polystyrene in ATP jetted using an AutoDrop system predicted by the jetting model (solid curve). Predicted asymptotic scaling laws for each regime (solid lines). Transitions between regimes (dashed lines) calculated from Zimm theory.

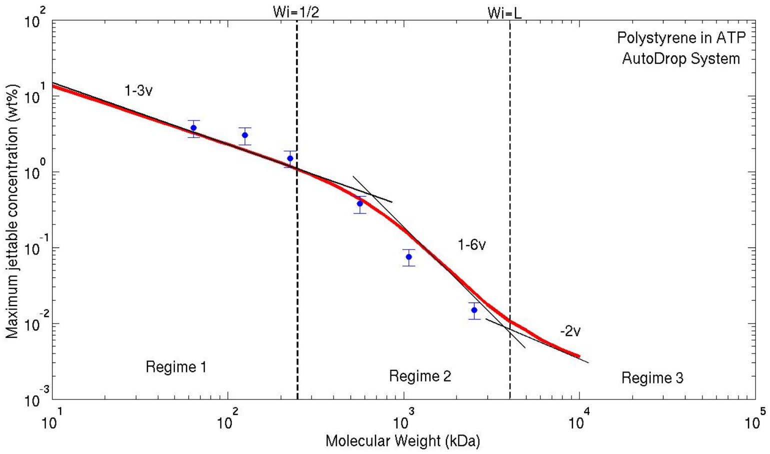

Figure 4.4: Maximum jettable concentration (wt%) of polystyrene in ATP jetted using an AutoDrop system predicted by the jetting model (solid curve). Experimental results [71] (circles) assuming a 25% error bar. Transitions between regimes (dashed lines) calculated from Zimm theory.

Provided that $Wi > 1/2$, it is the non-linear spring that is responsible for the relaxation of the axial stress. The molecules do not recoil, but remain in a fully-extended equilibrium. Consequently, jettability is limited by high-strain-rate extensional viscosity rather than molecule elasticity.

Figure 4.3 shows the maximum jettable concentration predicted by the jetting model in terms of the dimensionless concentration, c, compared to the initial Weissenberg number, Wi_0. In this case, the maximum jettable concentration is considered to be the ejected concentration at which the ratio $U_0/U_f = 1.5$ is achieved. The numerical calculations demonstrate three distinct jetting regimes. The scaling of jetting regimes 1 and 3 are in quantitative agreement with the asymptotic scaling laws Wi_0^0 and L^{-1}, respectively. However the asymptotic scaling of regime 2, namely Wi_0^{-1}, is not quite achieved for reasons which we now discuss.

Hoath *et al.* [71] define the transition from the Newtonian regime to the viscoelastic regime to be at $Wi_0 = 1/2$. The corresponding molecular weight at which this transition occurs is calculated using the Zimm relaxation time (4.9) to be

$$M_w = \left(\frac{1}{2}\frac{D}{U_0}3.24 \times 10^8\right)^{1/3\nu} \approx 258 \text{ kDa.}$$

At this molecular weight, although the initial strain rate exceeds the coil-stretch transition ($\dot{\epsilon}_0\tau = 1/2$), the strain rate then drops below critical so that the polymers have not uncoiled for a sufficient amount of time to allow viscoelasticity to fully dominate. Thus, the transition from regime 1 to regime 2 predicted by our model occurs at a higher molecular weight than the theoretical criterion $Wi_0 = 1/2$. On the other hand, the second transition from regime 2 to 3 at $Wi_0 = L$ is calculated using the Zimm relaxation time (4.9) and finite extensibility (4.10) to be

$$M_w = \left(\sqrt{9.2 \times 10^{-3}}\frac{D}{U_0}3.24 \times 10^8\right)^{1/(4\nu-1)} \approx 3273 \text{ kDa,}$$

and is in agreement with our observations. Since $Wi_0 = 1/2$ is too early as a criterion for the beginning of regime 2, the viscoelastic regime does not fully develop and we do not fully achieve the asymptotic scaling law in our model.

Figure 4.4 compares the maximum jettable concentration (wt%) that can be jetted experimentally [71] with that predicted by the jetting model. The experimental results agree well with the model predictions, however, the data does not extend into regime 3.

4.3.2 Polystyrene/DEP Solution jetted using the Xaar Print head

We now consider the system studied by Hoath *et al.* [73] in which polystyrene dissolved in diethlyphthalate (DEP) is jetted at $U_f = 6$ m/s from a 50 μm diameter nozzle using a Xaar XJ126-200 print head. Hoath *et al.* [72] show that the actuation pulse used in the Xaar print head typically produces a ratio of 2-3 between the drop speed upon exiting the nozzle and the final drop speed measured at a distance of 1 mm from the nozzle exit. Here we will take the ratio as 3 and assume $U_0 = 18$ m/s in the jetting model. The solvent

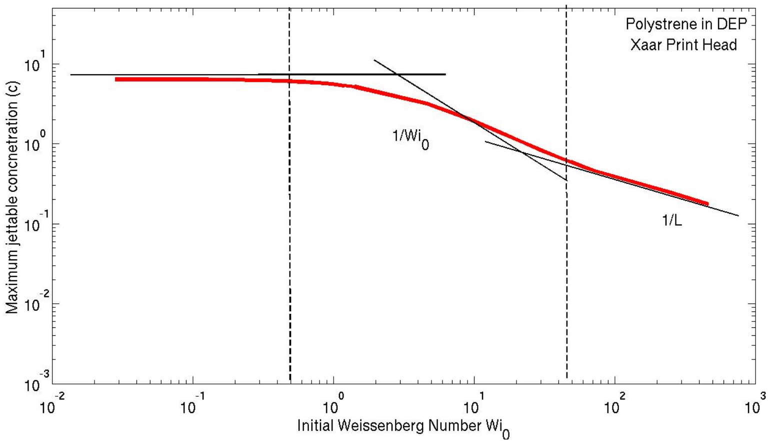

Figure 4.5: Maximum jettable concentration of polystyrene (c) in DEP from the Xaar print head predicted by the jetting model (solid curve). Predicted scaling laws for each regime (solid lines). Transitions between regimes (dashed lines) calculated from Zimm theory.

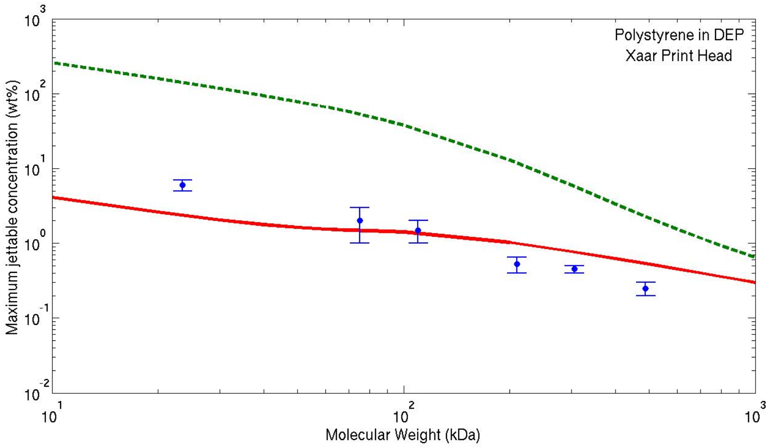

Figure 4.6: Maximum jettable concentration of polystyrene (wt%) in DEP from the Xaar print head predicted by the jetting model (dashed curve) compared to the corrected jetting model (solid curve). See text for details. Experimental results [71] with error bars (circles).

Nozzle	Xaar	**Solvent**	DEP
nozzle diameter, D	50 μm	solvent viscosity, μ_s	0.01 Pa.s
initial speed, U_0	18 m/s	quality factor, ν	0.567
print speed, U_f	6 m/s	fluid density, ρ	1117 kg/m^3

Table 4.3: Jetting conditions and fluid parameters for polystyrene dissolved in DEP jetted from a Xaar XJ126-200 print head chosen to correspond with experimental data [73].

DEP has a higher viscosity than ATP ($\mu_s = 0.01$ Pa.s) and is also classed as 'good', with a similar solvent quality factor $\nu = 0.567$. The jetting conditions and fluid parameters are listed in Table 4.3.

Figure 4.5 shows the maximum jettable concentration, c, on the assumption that the ratio $U_0/U_f = 3$ is achieved. The results follow the predicted asymptotic scaling laws Wi_0^0 and L^{-1} for jetting regimes 1 and 3, respectively, however, as in the previous case, the middle regime asymptote of Wi_0^{-1} is not achieved. Again using Zimm values for relaxation time and finite extensibility, the first transition from regime 1 to 2 is predicted to occur at approximately $M_w = 54$ kDa, again a lower value than predicted by our model for reasons discussed earlier, and the second transition from regime 2 to 3 is predicted to occur at $M_w = 608$ kDa.

In this case, the Weissenberg numbers for a particular molecular weight are larger due to the higher solvent viscosity of DEP and faster jetting speed of the Xaar print head. Consequently, the second transition occurs at a lower molecular weight than in the previous case. Thus, the development of viscoelastic regime is further restricted by the range of Weissenberg numbers and we observe a greater discrepancy from the asymptotic scaling law. Furthermore, Figure 4.6 shows the maximum jettable concentration (wt%) predicted by the jetting model (dashed line) significantly overestimates the experimental data [71]. There are two partial explanations for this discrepancy.

First, we have assumed that the relaxation time given by equation (4.4) is independent of concentration. However, Vadillo *et al.* [130] measure the relaxation time for polystyrene in DEP from oscillatory shear and find that it increases with concentration for ϕ close to the overlap concentration ϕ^*. This data is shown in Figure 4.7 for molecular-weight range $M_w = 70 - 488$ kDa, where the experimentally measured relaxation time τ_E is compared to the Zimm relaxation time τ_Z given by equation (4.4); the relaxation time measured at a dimensionless concentration $c = 1$ is about a factor of 3 larger than the Zimm time. To compensate for this concentration dependence, the relaxation time τ defined in the jetting model is adjusted according to the line of the best fit shown in Figure 4.7, which is given by a second-order polynomial. In making this correction, the predicted concentration threshold is reduced and is now much closer to the experimental data, as shown by the solid line in Figure 4.6.

However, even with this correction, at high molecular weights ($M_w > 100$ kDa) the

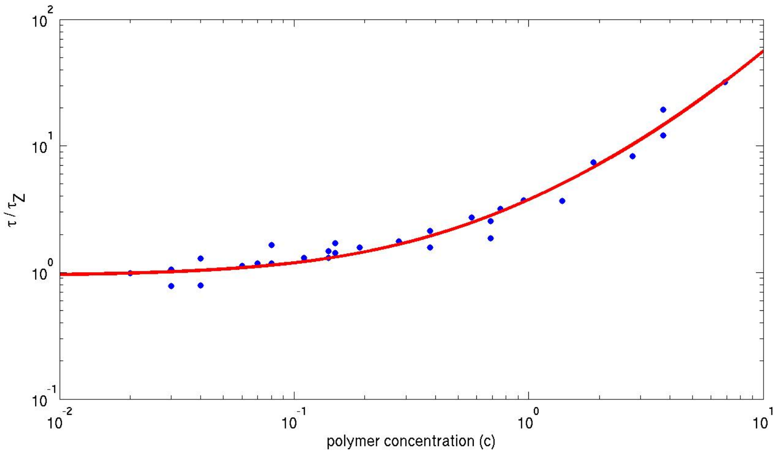

Figure 4.7: The measured relaxation time τ_E compared to the Zimm relaxation time τ_Z is shown as a function of concentration $c = \phi/\phi^*$ for a range of molecular weights $M_w = 70 - 488$ kDa, as given in reference [130]. Line of best fit is a second-order polynomial.

jetting model continues to overestimate the experimental data. This is in contrast to the ATP/micropipette system where we find quantitative agreement. A possible explanation for this discrepancy is pre-stretch of the polymers due to the print-head geometry. The AutoDrop system uses a micropipette nozzle, which tapers gently to the nozzle exit, whereas the Xaar print head has a sudden contraction. Consequently, the contraction flow into the nozzle may extend the polymers before they are subjected to the extensional flow in the ligament. Similar issues were suspected for the Dimatix DMP print head used by A-Alamry *et al.* [1], which we will discuss in section 4.5.

Evidence of polymers subjected to pre-stretch in a nozzle has previously been observed experimentally by Clasen *et al.* [34] in the study of the dripping to jetting transition. This transition has also been studied numerically using a simplified jetting model [33]. Pre-stretch was seen to prevent the occurrence of first-stage inertio-capillary thinning of a liquid jet and, for very small nozzles, even prohibit the establishment of the viscoelastic thinning regime. To investigate the effect of pre-stretch requires full simulations of the flow within the nozzle.

4.4 Full Axisymmetric Simulations

4.4.1 Comparison to Axisymmetric Simulations

In order to explain the discrepancies between the jetting model and the experimental data discussed in section 4.3.2, we have performed full axisymmetric simulations of a polystyrene/DEP system jetted from a Xaar print head. The axisymmetric model [66] has been fully described in Chapter 1. Simulations of each jetting regime are shown in Figure 4.8. The molecular weights chosen to represent each regime are listed in Table 4.4 along with the maximum jettable concentration predicted by the simulations. The solvent

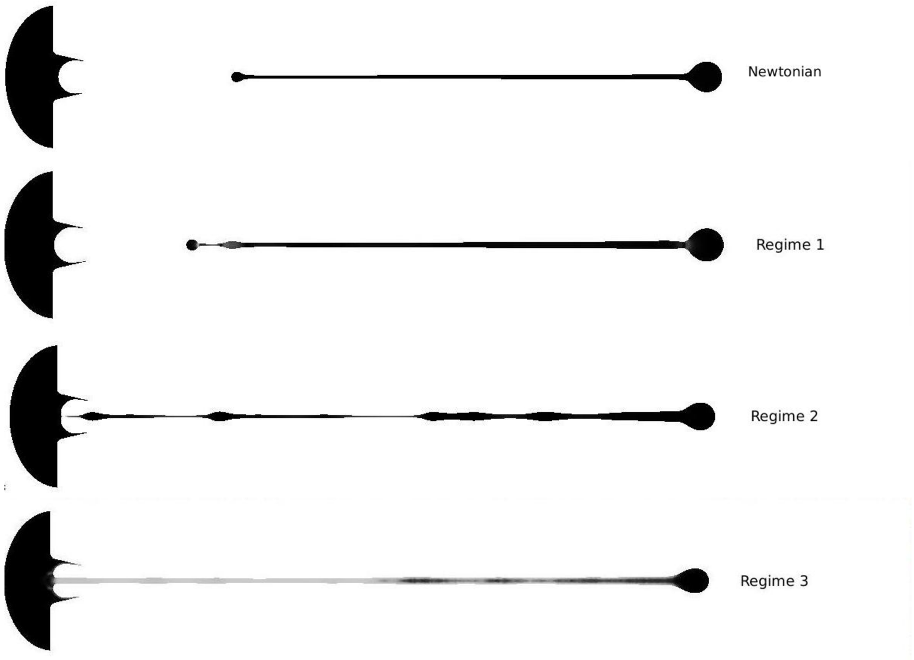

Figure 4.8: Newtonian simulation with fluid viscosity 0.02 Pa.s. Simulations of polystyrene in DEP jetted from a Xaar print head; regime 1 (3% M_w = 50 kDa), regime 2 (0.095% M_w = 200 kDa) and regime 3 (0.003% M_w = 2000 kDa) shown when the main drop is 1 mm from the nozzle exit.

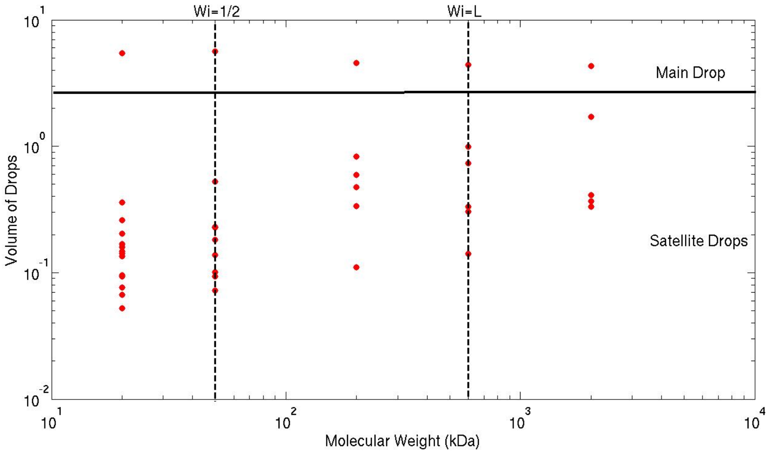

Figure 4.9: Volume distribution of drops produced in simulations of jetting polystyrene in DEP through a Xaar print head for molecular weights spanning the three jetting regimes.

	M_w (kDa)	Wi_0	**Max conc.** (wt%)	**Max conc.** (c)
Regime 1	50	0.4	3%	0.47
Regime 2	200	4.6	0.095%	0.04
Regime 3	2000	232	0.003%	0.005

Table 4.4: Molecular weights chosen to represent each jetting regime and maximum jettable concentrations predicted by the axisymmetric simulations.

parameters and jetting conditions used for these simulations correspond to those detailed in Table 4.3.

Figure 4.8 demonstrates the distinct jetting behaviours of each regime. In regime 1, the breaking behaviour is similar to that of a Newtonian fluid. Break-off from the nozzle occurs earlier than in the other regimes, as expected, and the ligament undergoes capillary thinning before subsequently breaking up into a number of satellite drops. In the second jetting regime, the ligament becomes unstable and develops the beads-on-string structure [11], where the droplets are held together by thin filaments of fluid in which the polymers are highly extended. In regime 3, an extremely long ligament is generated that is still attached to the nozzle when the main drop is 1 mm away. The polymers in the ligament are close to their extension limit, indicating that extensional viscosity dominates the fluid behaviour in this regime. The fluid acts like a suspension of rigid rods and this high extensional viscosity limits the capillary instability.

Figure 4.9 shows the satellite-drop-volume distribution for a range of molecular weights, which span each of the jetting regimes. At this Ohnesorge number, the low molecular

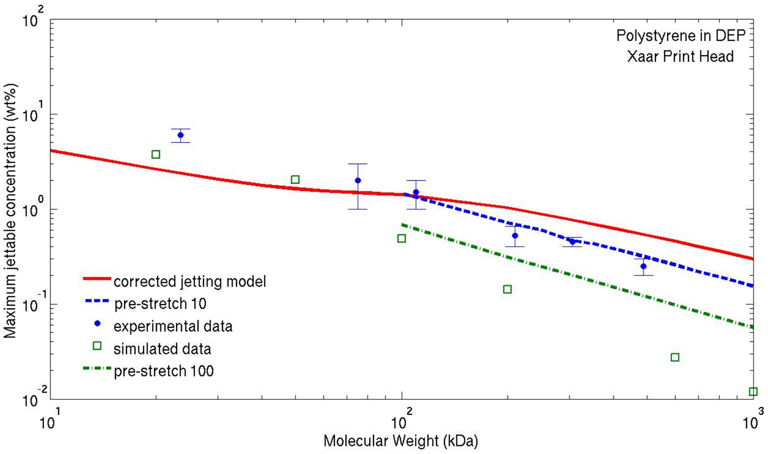

Figure 4.10: Maximum jettable concentration (wt%) of polystyrene in DEP from a Xaar print head predicted by the corrected jetting model (solid line), the corrected jetting model with pre-stretch factor 10 (dash line) and with pre-stretch factor 100 (dot-dash line) axisymmetric simulations (squares) and experimental data (circles).

weight solution breaks up into numerous, small satellite droplets, whereas, at high molecular weights fewer, but larger, satellite drops are generated. For example, Figure 4.9 shows that the number of satellite drops is reduced from 16 relatively small drops in jetting regime 1 (with nearly half having volume < 0.1) to 4 larger drops in jetting regime 3.

Figure 4.10 shows the maximum jettable concentration (wt%) predicted by the axisymmetric simulations compared to the corrected jetting model results. Again, we see that the jetting model overestimates the jettable concentration predicted by these axisymmetric simulations, as well as the experimental data. As discussed earlier, one cause may be due to the pre-stretching of the polymer molecules in the print head prior to exiting the nozzle.

4.4.2 Pre-Stretch due to Nozzle Geometry

We define the average initial value of A_{zz} for a cross-section radius a to be

$$\widehat{A^0_{zz}} = \frac{2}{a^2}\int_0^a rA^0_{zz}dr, \tag{4.15}$$

where A^0_{zz} is the value of A_{zz} at the positions along the nozzle exit. This pre-stretch factor is calculated from our simulations for a range of molecular weights spanning each jetting regime.

The A^0_{zz} profile is not uniform across the jet radius, but is shown in Figure 4.11 to increase steeply in a thin boundary layer close to the outer edge of the jet. Figure 4.12 demonstrates that there is a large difference in the pre-stretch factor calculated for the entire jet radius compared to that calculated for a central section of the jet that excludes

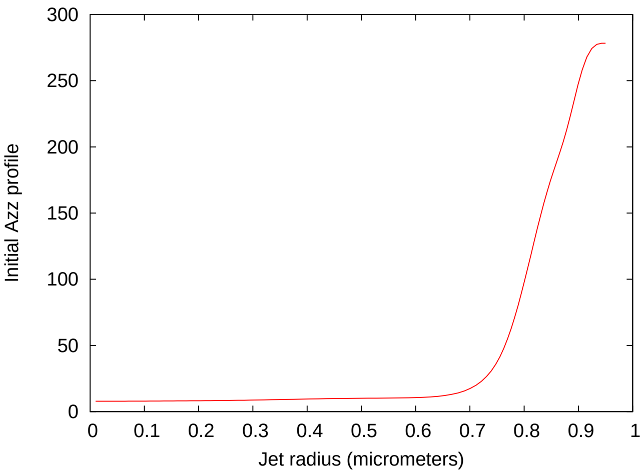

Figure 4.11: Simulation of initial A^0_{zz} profile across the nozzle exit generated by jetting a polymer of molecular weight $M_w = 2000$ kDa through a Xaar nozzle $D = 50$ μm at initial speed $U_0 = 12$ m/s.

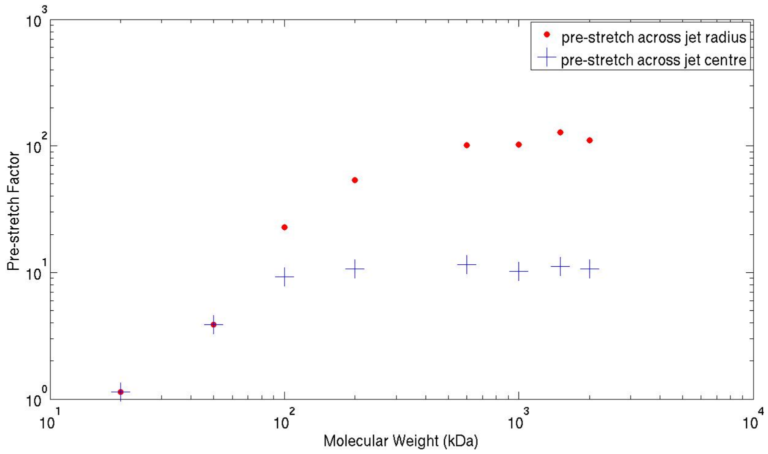

Figure 4.12: Pre-stretch factor from simulations of jetting polystyrene in DEP through a Xaar print head calculated by equation (4.15) across the entire jet radius (dot) and across the jet centre (plus).

the high-stress boundary. Stretching in this central section of the jet is attributed to the contraction flow into the nozzle, whereas the high stress region at the outer edge of the jet is due to the stretching of the free surface. In both cases the pre-stretch factor increases with molecular weight indicating that polymers are indeed stretched out to some degree inside the print head. As molecular weight increases, the degree to which the polymers can uncoil via the pre-stretch mechanism is limited. For example, the pre-stretch factor calculated across the centre of the jet reaches a maximum value of $\sim$ 10 as molecular weight increases, due to the limited strain available through the contraction. Including the high-stress boundary, the pre-stretch factor reaches a maximum value of $\sim$ 100.

The presence of a high-stress boundary layer has been observed in simulations of a filament stretching device [12], [143], in which a polymeric liquid filament is extended between two end plates. An area of concentrated stress develops in a thin layer near to the fluid-air interface at the mid-point of the filament and remains even when a homogeneous extensional strain is reached. This is due to the viscoelastic memory of the fluid to its deformation history.

Excluding the high-stress boundary by choosing the initial condition $A^0_{zz} = 10$ gives a quantitative agreement between the corrected jetting model results and the experimental data, as seen by the dashed line in Figure 4.10. However, the axisymmetric simulations significantly underestimate the jettable concentration predicted by the experiments. This discrepancy is probably the result of differences in the print head geometry between the axisymmetric simulations and the actual highly non-axisymmetric print head. However, a second possible explanation is that the polymers are being fractured due to the high stresses.

4.5 Polymer Scission during Jetting

4.5.1 Fracturing Polymer Molecules

Evidence of polymer scission occurring in inkjet printing was recently reported by A-Alamry *et al.* [1], in jetting experiments where approximately monodisperse polystyrene solutions are jetted through two different print heads. They examined the molecular-weight distributions of the polymer before and after jetting. In the faster Dimatix print head, they found a change in the molecular-weight distribution corresponding to an increase in the fraction of polymers of half the mean molecular weight. However, the distribution remained unchanged when using the Microfab printer, which is much slower and has a wider nozzle diameter. Full details of the two print heads are given later.

Halving of the molecular-weight distribution indicates that the polymer is broken into two equally sized chains during the jetting process. This mechanism is known as central scission. Although there may be some circumstances where reducing the molecular weight during printing may be advantageous, flow-induced degradation is a serious problem in jetting applications involving functional organic materials, where damage to the molecular structure will prevent the molecules from functioning correctly.

Odell & Keller [99] show that flow-induced central scission of high molecular weight polymers can occur in the high-strain extensional flow produced by an opposed jet. A polymer molecule will fracture if the tension force at the centre of a fully extended polymer molecule exceeds the carbon-carbon bond force. For polystyrene in ATP this gives a critical fracture strain rate [99] of

$$\dot{\epsilon}_f = \frac{7.24 \times 10^{17}}{M_w^2}\ \mathrm{s}^{-1}, \tag{4.16}$$

for molecular weight measured in Daltons (Da). This is a decreasing function of molecular weight indicating that higher molecular weight polymers are easier to fracture. For a molecule to undergo central scission, the polymer must be both fully extended (i.e. in jetting regime 3) and the the strain rate of the flow must overcome this fracture condition (4.16).

In order to investigate whether the conditions for central scission exist within inkjet

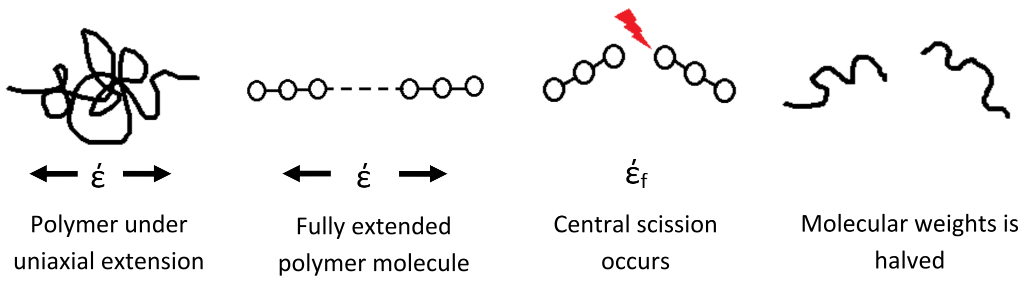

Figure 4.13: Central scission of a fully extended polymer molecule when the strain rate $\dot{\epsilon}$ of the flow exceeds the fracture strain rate $\dot{\epsilon}_f$ given by equation (4.16).

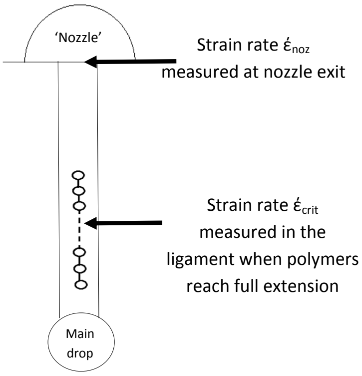

Figure 4.14: Critical strain rate $\dot{\epsilon}_{crit}$ given by equation (4.17) compared to the strain rate measured at the nozzle $\dot{\epsilon}_{noz}$ given by equation (4.18) in the jetting model.

printing, we consider the strain rate of the flow at two locations; in the ligament when the polymers become fully extended and at the nozzle exit. These strain rates are illustrated in Figure 4.14. The critical strain rate at which the polymers are at full extension in the ligament is defined to be

$$\dot{\epsilon}_{crit} = \frac{U_{crit}}{Z_{crit}} \text{ s}^{-1}, \tag{4.17}$$

where critical values are defined at maximum axial stress. The strain rate at the nozzle exit is defined as

$$\dot{\epsilon}_{noz} = 8\frac{U_0}{D} \text{ s}^{-1}, \tag{4.18}$$

on the assumption of fully developed Poiseuille flow in the nozzle.

4.5.2 Polystyrene/ATP Solution jetted using the Dimatix Print head

A-Alamry *et al.* [1] examine the changes to the molecular-weight distribution of polystyrene dissolved in ATP for two different print systems. First, the solution is jetted at $U_f = 10$ m/s from a 23 μm diameter nozzle using a Dimatix DMP-2800 10Pl print head. We assume that the ratio between the final print speed and the speed at which the ink exits the nozzle is 3. Thus, the speed used in the jetting model is $U_0 = 30$ m/s. The jetting conditions

Solvent	ATP	**Nozzle**	Dimatix
solvent viscosity, μ_s	0.0017Pa.s	nozzle diameter, D	23 μm
solvent quality, ν	0.59	initial speed, U_0	30 m/s
fluid density, ρ	1028 kg/m^3	print speed, U_f	10 m/s

Table 4.5: Fluid parameters and jetting conditions for polystyrene in ATP jetted from a Dimatix DMP-2800 10pl print head.

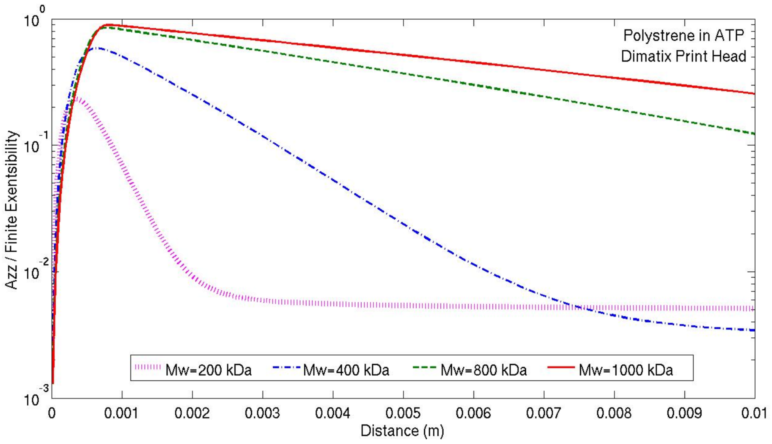

Figure 4.15: A_{zz}/L^2 profiles for molecular weight range $M_w = 200 - 1000$ kDa for polystyrene in ATP jetted from a Dimatix print head.

and fluid parameters are listed in Table 4.5. A-Alamry *et al.* find that central scission occurs for the molecular weight range $290 < M_w < 770$ kDa under these conditions.

Figure 4.15 shows the evolution of the axial configuration component A_{zz}, predicted by our simple jetting model, compared to the finite extensibility limit L^2 as ligament length increases for a number of molecular weights. The change in behaviour from the viscoelastic regime to the fully extended regime, in which the non-linear spring dominates, is evident as molecular weight is increased. In particular, for $M_w = 1000$ kDa, $A_{zz} \sim L^2$ indicating that the polymer has reached full extension. For a sufficient strain rate, the tension force may exceed the strength of the chain bond leading to fracture of the polymer backbone. The jetting model can be used to determine whether the strain rate is large enough for this degradation to occur.

We calculate that the transition from regime 2 to regime 3 occurs at $M_w = 256$ kDa and this transition is plotted in Figure 4.16. Thus, there exists a range of molecular weights used by Alamry *et al.* within jetting regime 3, where polymers will become fully extended under these jetting conditions. However, the strain rate at full extension given by equation (4.17) is not large enough to fracture the polymer molecules, as shown in Figure 4.16. Hence, we can conclude that the extensional flow in the ligament of the DoD jet is not strong enough to cause central scission.

On the other hand Figure 4.16 also suggests that the nozzle strain rate given by equation (4.18) is sufficient to exceed the fracture condition. Thus, polymers will undergo central scission at the nozzle exit, provided that the molecules have become fully extended within the nozzle. Our axisymmetric simulations in section 4.4 have demonstrated that significant stretching occurs within a print head with a sudden contraction and Figure 4.17 demonstrates the high stress boundary layer near to the free surface generated at the nozzle exit for Dimatix jetting parameters. In this region, the initial axial configuration A^0_{zz} is near to the upper limit L^2, suggesting that the polymers are near to their finite extension limit as the fluid exits the nozzle.

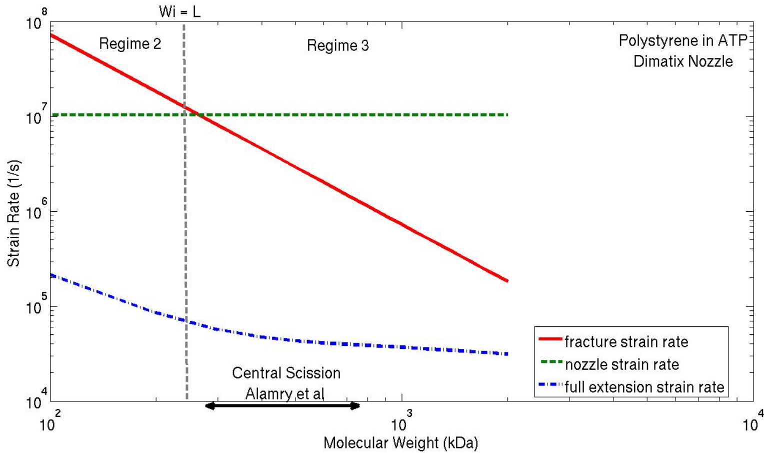

Figure 4.16: Fracture strain rate (4.16) (solid), nozzle strain rate (4.18) (dashed) and critical strain rate (4.17) (dash-dot) for the Dimatix nozzle with the transition from regime 2 to 3 (dashed). The arrow indicates the range of M_w for which central scission is reported [1].

In conclusion, our modelling suggests that, under the conditions present in the Dimatix print head used in the experiments of A-Alamry *et al.* [1], a proportion of the molecules will become both fully extended and subjected to a sufficient strain rate at the nozzle exit such that central scission is possible. Hence, we can conclude that the mechanism responsible for central scission under DoD jetting conditions is likely to be the high strain rate at the nozzle exit rather than the extensional flow in the jet. A-Alamry *et al.* observe central scission occurs in the molecular weight range $290 < M_w < 770$ kDa. The lower boundary

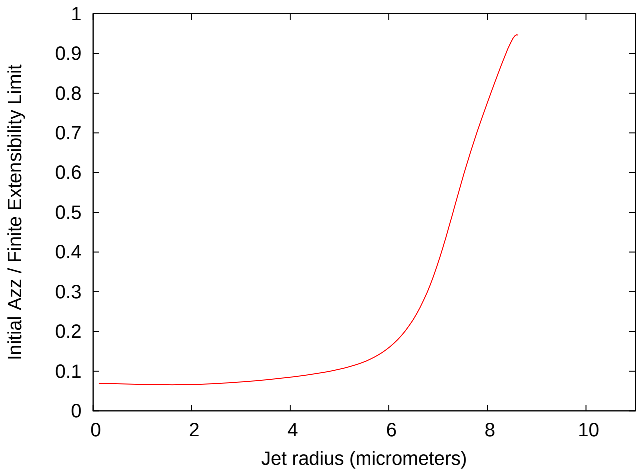

Figure 4.17: Simulation of A^0_{zz}/L^2 across the nozzle exit generated by jetting a polymer of molecular weight $M_w = 500$ kDa through a Dimatix nozzle $D = 23$ μm at reduced speed $U_0 = 10$m/s.

coincides with the transition to regime 3, as well as the nozzle strain rate overcoming the fracture condition. The upper boundary is possibly due to these very large molecules being unable to uncoil to their full extension within the nozzle.

4.5.3 Polystyrene/ATP Solution jetted using the Microfab Print head

A-Alamry *et al.* [1] also jet the polystyrene/ATP solution at $U_f = 5$ m/s through a 50 μm diameter nozzle using a Microfab micropipette system. Recall that the micropipette nozzle is smooth and tapered compared to the sudden contraction of the Dimatix nozzle and so are unlikely to cause pre-stretch in the nozzle. In contrast to the Dimatix print head, A-Alamry *et al* do not observe central scission with this system.

Solvent	ATP	**Nozzle**	Microfab
solvent viscosity, μ_s	0.0017Pa.s	nozzle diameter, D	50 μm
solvent quality, ν	0.59	initial speed, U_0	15 m/s
fluid density, ρ	1028 kg/m^3	print speed, U_f	5 m/s

Table 4.6: Fluid parameters and jetting conditions for polystyrene in ATP jetted from a Microfab micropipette system.

In Figure 4.18, we show that the strain rate at the nozzle exit and the strain rate at full extension, on the assumption that the fluid velocity at the exit is 3 times the final velocity i.e. $U_0 = 15$ m/s. Details of the jetting conditions and fluid parameters are given in Table 4.6. Again we see that the strain rate in the ligament is too small to cause fracture. On the other hand, although the strain rate at the nozzle is lower than the Dimatix system, it

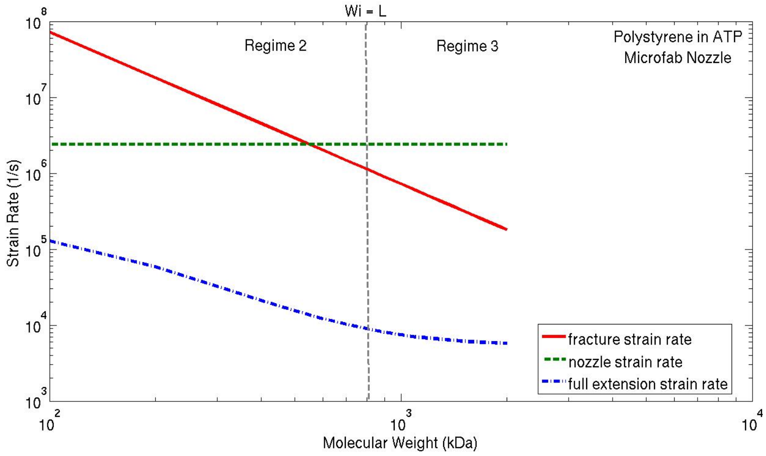

Figure 4.18: Fracture strain rate (4.16) (solid), nozzle strain rate (4.18) (dashed) and critical strain rate (4.17) (dash-dot) the Microfab nozzle with the transition from regime 2 to 3 (dashed).

is still sufficient to induce central scission for molecular weights $M_w > 500$ kDa. However, unlike the Dimatix head, the Microfab print head does not have a sudden contraction and therefore it is unlikely that the polymers will become fully extended in the nozzle. Indeed, A-Alamry *et al.* do not observe central scission in this case.

4.6 Concluding Remarks

In this chapter, we have tested the predictions of the simple model of jetting given by Hoath *et al.* against both experimental observations and full numerical simulations. For a low viscosity solvent (ATP), where the molecular weight corresponding to a relaxation rate equal to the initial strain rate is large, we have identified all three of the asymptotic regimes defined by Hoath *et al.* Furthermore, the predictions of the model agree quantitatively with the experiments of de Gans *et al.* [42] using a micropipette system. However, for the higher-viscosity DEP system jetted through an industrial print head, the middle scaling regime is restricted and there is a significant discrepancy from the experimental results.

We have identified three factors that contribute to these discrepancies. First, for the DEP system of Hoath *et al.* [72], where jetting of low molecular weight polymers is possible at concentrations above ϕ^*, the Zimm model underestimates the relaxation time and therefore both the polymer contribution to viscosity and the Weissenberg number. Second, the abrupt contraction of the industrial print head compared to the gently tapering micropipette nozzle produces a significant pre-stretch of the polymers that is not accounted for in the model. When these effects are included, the model produces predictions similar to the full numerical simulations and the experimental data. Finally, there is possibility, already identified by A-Alamry *et al.* [1], that polymers are degraded due to flow-induced scission. Our modelling suggests that this does not occur as a result of the extensional flow in the ligament, but rather as a consequence of the high strains and strain rates in the nozzle and so could be avoided by changing the nozzle geometry.

Chapter 5

The Continuous Inkjet

5.1 Problem Outline

Many studies have contributed to understanding droplet creation and evolution during the continuous inkjet (CIJ) process [64], [68], [134], [23], the first attempts dating back to the nineteenth century and the studies of Rayleigh [109] and Savart [118]. However, although the inks used in CIJ printing are predominantly Newtonian, there remain unsolved problems surrounding the break-up regime.

Theoretical and numerical predictions of jet break-up prove challenging due to the pinch-off singularity that occurs in free-surface flows. Several approaches have been followed in recent years, of which a comprehensive review can be found in reference [50]. The first quantitative comparison of drop formation with experimental data was carried out by Eggers & Dupont [52], who use a second-order, finite-difference scheme on a highly non-uniform mesh that is adapted to the solution. They find that fully implicit time integration is essential in order to control numerical instabilities.

Since the continuous jetting technique can achieve much faster print speeds than DoD printing, applications based on continuous inkjet technology continue to be developed. However, pushing the boundaries of print resolution and complex material properties requires a fast and accurate numerical simulation of the jet break-up and drop formation. The Lagrangian axisymmetric jetting model [66], described in Chapter 1, has previously been applied to the CIJ problem, with quantitative agreement to experimental data [23]. However, the implementation of this fully axisymmetric simulation is computationally expensive.

In this chapter, we apply the one-dimensional slender-jet model, described in Chapter 3, to a continuous inkjet of Newtonian fluid. In addition, we implement the adaptive-mesh technique previously developed by Kelmanson [79], [80], [81], [82]. In this way, the computation time is dramatically reduced compared with the full axisymmetric model. Using this adaptive model, we explore the stability and break-up of a continuous jet, for two different driving techniques.

As detailed in Chapter 2, jetting through a nozzle creates a stream of liquid that is rendered unstable by surface tension. For a continuous free jet, this instability creates a succession of main drops connected by thin filaments, with drop separation determined by the fastest growing mode. However, in order to control break-up and increase printing speed, CIJ printing exploits the effects of finite-amplitude modulations in the jet velocity profile, giving rise to conditions in which jet stability deviates from linear Rayleigh behaviour.

It is the growth of non-linear interactions, caused by large modulations in the driving velocity, that significantly influence the break-up behaviour. In particular, we identify a modulation range for which pinching occurs upstream of the connecting filament, rather than downstream - a phenomenon we call 'inverted' break-up. Furthermore, this behaviour can be controlled by the addition of a second harmonic to the initial driving signal. Our results are compared to the full axisymmetric simulations in order to incorporate the effects of nozzle geometry in our one-dimensional model.

5.2 An Adaptive Mesh Technique

5.2.1 Linked Lists for Adaption

Adaptive meshing is an efficient modelling technique that allows multi-spatial-scale contemporaneous resolution. That is, the solution may be computed on a low-resolution mesh that adapts to allow refinement only in regions where high resolution is required, within the context of the problem. In this way an accurate solution can be achieved for a reduced computation time.

As observed in previous chapters, capillary thinning of a low-viscosity Newtonian jet induces a necking instability, which ultimately causes the production of small satellite drops. These neck regions, where pinching of the free surface occurs, require a sufficiently fine mesh size in order to obtain a more accurately resolved solution. On the other hand, dynamics within the main drops of fluid are slow and therefore can be computed on a coarser mesh. Consequently, the use of an adaptive mesh scheme, which, by construction, automatically refines areas of high curvature, is beneficial to this problem. A computational mesh that adapts in this way may be implemented using a linked-list data structure, as used in references [79], [80], [81], [82].

The linked-list data structure is an elegant way to implement the dynamically adaptive storage requirements associated with an irregular evolving mesh. Since this structure facilitates the addition of information to an existing set of data, it is convenient for the development of an adaptive mesh scheme, where new nodes are added to the original mesh in order to increase resolution. The addition of new nodes to a mesh is analogous to adding new information to the linked-list data structure. Moreover, information can be readily deleted from the list in the event that mesh coarsening occurs.

A linked list contains an ordered collection of elements, each of which corresponds to a node on a mesh. When allocated in memory, each list element is assigned an address, as

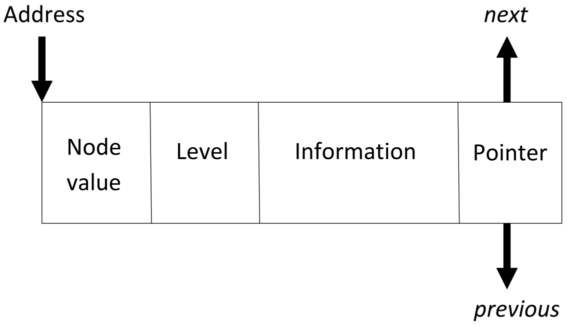

Figure 5.1: An element of a linked list.

well as information relating the element to the global mesh structure and to the variables of the problem. Typically, each element consists of

- address,
- node value,
- level of refinement,
- information field,
- pointer field.

Figure 5.1 shows a representation of a single element of a linked list, the details of which are now explained.

First, the nodal value locates the element in relation to the global mesh in physical space. For example, for mesh nodes denoted

$$z_j = z_0 + jdz, \quad j = 0, 1, \ldots, J,$$

for some mesh size dz, the nodal value j is stored in the list element and determines the location of the element in relation to the boundaries, which are defined to be at $j = 0$ and $j = J$. Second, the level of refinement implicitly defines the local mesh size. For example, level 0 corresponds to the coarsest mesh size dz; after one refinement, the level increases to 1 and the mesh size is halved to $dz/2$, and so forth. Next, the information field of an element contains the physical variables at the mesh location marked by the particular nodal value. For the CIJ problem, the free-surface height $h(z_j, t)$ and the velocity $v(z_j, t)$ are stored in the information field at time t. Finally, the pointer field, shown graphically as arrows, contains a reference to the next element in the list i.e. the memory address of the adjacent element. In this way, the next element in the list can be found in memory, wherever it is dynamically allocated as the mesh evolves. The overall structure of the list is built by using pointers to connect all the elements sequentially. Figure 5.2 illustrates the linked-list structure in relation to a uniform mesh structure.

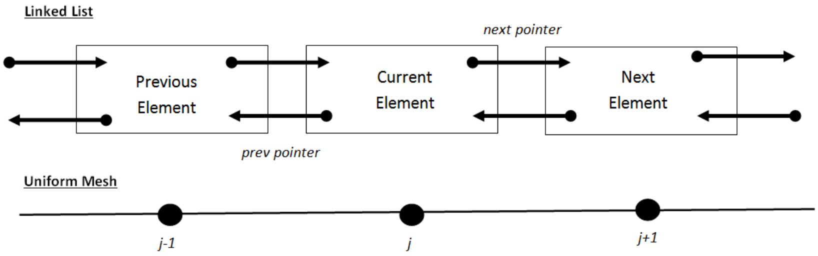

Figure 5.2: The structure of a doubly-linked list compared to a uniform mesh.

The order in which a list is traversed is naturally ‘left to right’ for a one-dimensional problem. However, for higher dimensions this process must be more clearly defined [79], [80], [81], [82]. For a singly-linked list, the data may only be traversed in one direction, whereas doubly-linked lists allow traversal in both directions. In the latter case, an additional pointer is defined for each element, which points to the previous element in the list. Thus, for a doubly-linked list, the pointer field contains the addresses for the adjacent elements in both the forward and backward directions. Although more space is required per element for a doubly-linked list, computing time associated with the list traversal (an essential part of the adaption process) can be significantly reduced.

For the last element in the list, the next pointer contains a special value known as `NULL`. This is not a valid address but signifies the end of the list and usually admits a physical correspondence with the ‘earth’ in an electrical circuit. Similarly, for a doubly-linked list the previous pointer of the first element is also set to `NULL`. Using the `NULL` points, the terminal elements corresponding to the boundary nodes of the problem can be easily identified within the linked-list structure.

5.2.2 Mesh Refinement and Smoothing Algorithms

First, an ‘adaption criterion’ for identifying nodes at which higher resolution is required must be decided in order to trigger the refinement process. For the CIJ problem, the dynamics near to the nozzle boundary are assumed to be simple under our one-dimensional approximation (as expanded upon later) and therefore do not require high resolution. On the other hand, downstream of the nozzle the jet is subject to the Rayleigh instability and becomes thin before breaking into droplets. The dynamics in this spatial region are much more complicated due to the steepening gradient of the free surface; the curvature becomes large in the neck regions, where the jet pinches inwards, compared to the curvature of the free surface near the nozzle. Thus, we choose an adaption criterion based on an increase in the free-surface curvature. An upper-bound is decided such that, if the curvature exceeds this limit at a particular mesh node, then the node is marked for refinement. Furthermore, if the curvature drops below this limit after refinement has occurred, then a coarser mesh can be recovered with a corresponding release of resources back into the memory.

The original mesh is made finer by adding a new node in between two existing nodes.

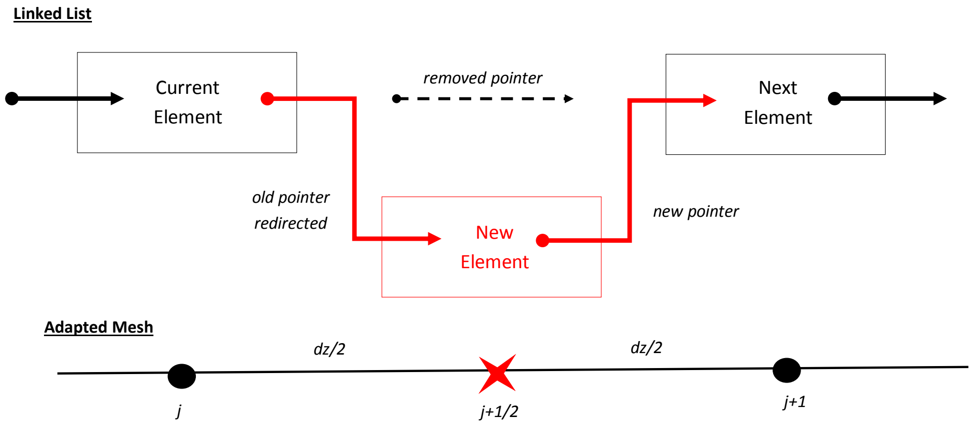

Figure 5.3: Adding a new element to a linked list during mesh refinement.

In particular, for our adaptive scheme, new nodes are inserted at the mid-point so that the mesh size is halved during the refinement process. In the linked-list format, this corresponds to adding a new element to the list, at the corresponding level of refinement. Introducing a new element to the linked-list data structure is done in two steps. First, the information field of the flagged element, identified by the adaption criterion, is updated; since the mesh size is halved, the level of adaption stored in the flagged element is increased by one. Second, a new element is inserted into the list:

- memory is allocated for the new element;
- the pointer of this new element is set to point to the next element in the list;
- the pointer of the flagged current element is set to point to the new element;
- the new element is then filled with data, using interpolation of the old data.

The process of adding a new element to a linked list is illustrated schematically in Figure 5.3. For the CIJ problem, cubic Lagrange interpolation is used to calculate the free-surface height and the velocity at the new node, giving $h(z_{j+1/2}, t)$ and $v(z_{j+1/2}, t)$ to be stored in the information field of the new element.

There are two possible modes of adaption; 'level-by-level' and 'coarse-to-fine'. In level-by-level adaption, the entire mesh is refined by one level where necessary during one transversal of the list. Refinement to the next finer level requires a second transversal of the list and so forth. In this way each element of the list is tested by the adaption criterion during each transversal of the list. On the other hand, in coarse-to-fine mode, if an element is marked by the adaption criterion, then the mesh is refined to the finest level required before moving on to the next element. Since each element is visited only once in a single transversal of the list, coarse-to-fine adaption is more efficient than level-by-level.

Since we use finite-difference approximations to calculate derivatives in our one-dimensional model, we limit the number of local mesh structures that arise during the refinement process. This is done using a mesh-smoothing algorithm, which ensures the difference in level between adjacent elements is no more than one: if this scenario is ever violated, then extra elements are added to smooth the mesh. This smoothing algorithm ensures that only two local mesh structures can occur:

- parent-parent structure in which adjacent elements are at the same level of adaption and so the mesh size is the same for each node;
- parent-child structure in which the child element is at one level of adaption higher than the parent element. In this case, the mesh size of the child node is half that of the parent node.

Thus, the smoothing algorithm eliminates the possibility of a parent-grandchild structure in which the mesh size of adjacent nodes differs by a factor of $2^2 = 4$.

For the parent-parent structure, the mesh size is uniform across the local mesh and so the usual second-order, central-difference approximation may be used to calculate the first derivative of the free-surface height

$$\left.\frac{\partial h}{\partial z}\right|_j = \frac{h_{j+1} - h_{j-1}}{2dz} + O(dz^2),$$

for mesh size dz. In the linked list, the free-surface height h_j is stored in the information field of the current element; h_{j+1} is the height stored in the next element of the list and h_{j-1} is stored in the previous element. Thus, in linked-list notation, this central-difference equation can be written as

$$\left.\frac{\partial h}{\partial z}\right|_{cur} = \frac{h_{next} - h_{prev}}{2dz} + O(dz^2).$$

Similar central-difference formula can be used for higher orders of differentiation and one-sided formulae are used at the boundaries. However, for asymmetric structures such as the parent-child, the local mesh is non-uniform and the difference approximation must be adapted accordingly. A systematic method for determining finite-difference approximations on a non-uniform mesh is discussed later.

5.2.3 Error Analysis for Mesh Refinement

As stated above, the central-difference approximation for the first, spatial derivative is given by

$$h'_j = \frac{h_{j+1} - h_{j-1}}{2dz} + O(dz^2), \quad j = 1, \dots, J,$$

where we use 'prime' to denote differentiation with respect to z. This approximation is accurate to second order in space. For a periodic data set with period J, this central-difference approximation can be used at all nodes $j = 1, \dots, J$. Assembly of central differences in this way yields a matrix-vector system such that

$$\mathbf{h}' = \begin{pmatrix} h'_1 \\ h'_2 \\ \dots \\ h'_J \end{pmatrix} = \frac{1}{dz} \begin{pmatrix} 0 & 1/2 & \dots & \dots & 0 \\ -1/2 & 0 & 1/2 & \dots & \dots \\ \dots & \dots & \dots & \dots & \dots \\ 1/2 & \dots & \dots & -1/2 & 0 \end{pmatrix} \begin{pmatrix} h_1 \\ h_2 \\ \dots \\ h_J \end{pmatrix} \equiv \mathbb{D}_2\mathbf{h},$$

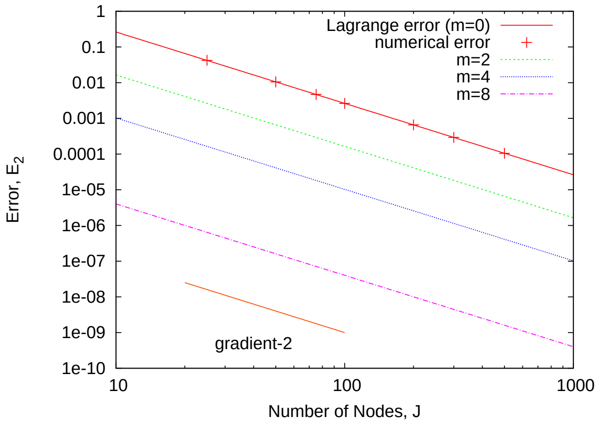

Figure 5.4: Log-log plot of the error E_2 for the second-order finite-difference approximation compared to number of nodes J for a unrefined mesh (m=0) and for a refined mesh with levels increasing from $m = 2$ to $m = 8$. The error gradients are all -2 in keeping with the theoretical prediction (5.1).

where $\mathbb{D}_2$ is the polynomial differentiation matrix that differentiates to first order with second-order spatial accuracy. Differentiation matrices are circulant, in that the rows 'wrap' round when they are displaced and they also demonstrate skew-symmetry such that $\mathbb{D}^T = -\mathbb{D}$.

The maximum error of differentiation at the nodes is of order $O(dz^2)$ and is determined by

$$E_2 \equiv ||\mathbf{h}' - \mathbb{D}_2\mathbf{h}||_\infty,$$

where $\mathbf{h}'$ is a vector of the exact first derivative for some prescribed function $\mathbf{h}$, defined at nodal values z_j. In the following example, $h(z) = \exp(\sin(z))$ is used to generate the nodal data h_j. Using the Lagrange error formula [78], it is possible to make the theoretical prediction

$$E_2^* = \frac{26.319}{J^2}, \tag{5.1}$$

for the error incurred using the approximation $\mathbb{D}_2$. Figure 5.4 demonstrates how this error is reduced by increasing the number of mesh nodes J and that the gradient of the numerically obtained E_2, is in agreement with this theoretical prediction E_2^*.

The equivalent error for m-levels of refinement in our scheme is of the order

$$O((dz/2^m)^2)) = O(4^{-m}dz^2),$$

since the mesh size is halved at each level of refinement. Thus, the theoretical error for m-levels of adaption is

$$E_2^* = 26.319\frac{4^{-m}}{J^2},$$

and is also plotted in Figure 5.4 for increasing m. We see that the error incurred on a refined mesh is simply a factor 4^{-m} of the error incurred for $m = 0$. Thus, a significant reduction in the error is achieved for increasing levels of refinement. In our example $h(z) = \exp(\sin(z))$, the implementation of two levels decreases the error E_2^* incurred by a factor of 10 compared to the unrefined case and this error may be reduced to as little as 10^{-8} for eight levels of refinement.

5.3 Numerical Schemes for Non-Uniform Meshes

5.3.1 Finite-Difference Approximations

Refining a global mesh via a locally determined adaption criterion leads to a highly non-uniform mesh structure. Since we intend to solve our one-dimensional jetting model using a second-order finite-difference scheme, the asymmetry resulting from non-uniform adapted mesh structures leads to node-specific discrete approximations of derivatives. The derivation of these asymmetric equations requires knowledge of only the local mesh structure surrounding the nodes required for a particular approximation.

For a regularly spaced mesh with initial nodes $z_1, \ldots, z_J$, the original mesh size is given by

$$dz = \frac{z_J - z_1}{J},$$

and nodal data can be determined using Taylor's theorem. For example,

$$h_{j+1} \equiv h(z_{j+1}) \equiv h(z_j + dz) = h_j + dz h_j' + \frac{dz^2}{2!} h_j'' + O(dz^3),$$
$$h_{j-1} \equiv h(z_{j-1}) \equiv h(z_j - dz) = h_j - dz h_j' + \frac{dz^2}{2!} h_j'' - O(dz^3),$$

where a 'prime' denotes differentiation with respect to z. By manipulating Taylor expansions, finite-difference approximations for certain derivatives of the nodal data may be derived. For example, the second-order, central-difference approximation to the first derivative is found by subtracting the two expansions given above to yield

$$h_j' = \frac{h_{j+1} - h_{j-1}}{2dz} + O(dz^2).$$

This equation can be interpreted of as a molecule containing the atomic weights $\{-1/2, 0, 1/2\}$ acting on the three nodes $\{z_{j-1}, z_j, z_{j+1}\}$ in the global mesh, to obtain an approximation of h_j' at the base node z_j. Figure 5.5 illustrates this difference equation in molecular form, which is said to be central since it is symmetric about the base node. The base node corresponds to the current element in the linked-list data structure. The arrows point away from the base node and the weights appear inside the circles. At the boundaries, one-sided molecules are required, which use only information ahead of, or behind, the base node. In the linked-list data structure, information to the right of the current element can be accessed via the next pointers for forward-difference approximations. Similarly, for backward-difference equations, information to the left of the current element can be accessed via the previous pointers.

In order to obtain both higher derivatives and higher-order errors, more terms are required in the Taylor expansion, thereby increasing the number of nodes required in

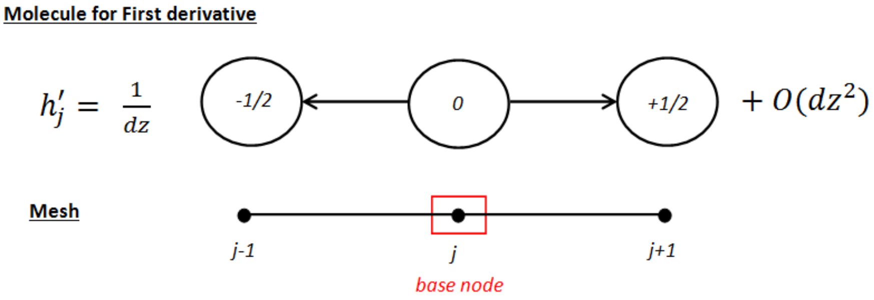

Figure 5.5: Second-order finite-difference approximations to the first derivative in molecular form.

the molecule to eliminate the higher derivatives. In fact, adding the order of the error and the order of derivative sought gives the maximum number of nodes required for the approximation. For the CIJ problem, we require second-order spatial accuracy and so approximations of the first derivative require a maximum of three nodes and approximations of the second derivative require a maximum of four nodes. Note that central-difference approximations are special symmetric cases and so require one less node.

In general, the second-order, central-difference approximation to the first derivative at the base node z_j may be postulated as

$$\frac{w_{j-1}h_{j-1} + w_j h_j + w_{j+1}h_{j+1}}{dz} = h'_j + Cdz^2 + O(dz^3),$$

for which the weights $\{w_{j-1}, w_j, w_{j+1}\}$ and the error coefficient C are to be found. For this example, the weights can be calculated by rewriting h_{j-1} and h_{j+1} using Taylor expansions about h_j. Comparing coefficients then gives a set of simultaneous equations to solve for weights $\{w_{j-1}, w_j, w_{j+1}\}$ and the error coefficient C.

This well-known method can be generalised further to incorporate varying mesh size, which arises in our adaptive scheme, by considering this method in the matrix-vector form

$$\mathbf{M} \cdot \mathbf{w} = \mathbf{b}, \tag{5.2}$$

for the vector $\mathbf{w}$ of the unknown weights. The order of differentiation plus the order of the error defines the size of vector $\mathbf{b}$ and therefore the number of unknown weights. In the CIJ problem, the $\mathbf{b}$ vectors are

$$\mathbf{b} = \begin{cases} (0, 1!, 0)^T, & \text{for second-order, first derivative,} \\ (0, 0, 2!, 0)^T, & \text{for second-order, second derivative.} \end{cases} \tag{5.3}$$

The square matrix $\mathbf{M}$ corresponds to the distance of the local nodes used in the approximation from the base node z_j and can be generated via the simple formula

$$M_{ij} = d_j^{(i-1)} \tag{5.4}$$

where d_j is $1/dz$ times the distance of node j from the base node. Essentially, d_j is a structure vector defining a local mesh labelling about the base node. A specific example is given below.

For known d_j, the unknown weights can readily be found by solving equation (5.2). Since we require only second-order approximations to the first and second derivatives, the size of matrix $\mathbf{M}$ does not exceed 4×4 and it is convenient to use usual Gaussian elimination to solve the system.

Example: Second-order, forward-difference approximation for h'_j on the parent-child local mesh structure

Consider the second-order, forward-difference approximation to the first derivative given by

$$\frac{w_j h_j + w_{j+1} h_{j+1} + w_{j+3/2} h_{j+3/2}}{dz} = h'_j + C dz^2 + O(dz^3),$$

at the base node z_j. For the global nodes $\{z_j, z_{j+1}, z_{j+3/2}\}$ required in the approximation, the base node is relabelled z_0, so that the local labelling is given by $\{0, 1, 3/2\}$. Since the mesh spacing between z_0 and z_1 is twice that between z_1 and $z_{3/2}$, the local mesh has the parent-child structure, which is reflected in the structure vector

$$d_j = (0, 1, 3/2)^T.$$

By choosing vector $\mathbf{b}$ from equation (5.3) and using equation (5.4) to generate the matrix $\mathbf{M}$, we have

$$\mathbf{M} = \begin{pmatrix} 1 & 1 & 1 \\ 0 & 1 & 3/2 \\ 0 & 1 & 9/4 \end{pmatrix}, \quad \mathbf{w} = \begin{pmatrix} w_j \\ w_{j+1} \\ w_{j+3/2} \end{pmatrix}, \quad \mathbf{b} = \begin{pmatrix} 0 \\ 1! \\ 0 \end{pmatrix}.$$

In general, the vector $\mathbf{b}$ has one non-zero entry appearing in the position corresponding to the derivative sought. The value of the entry arises from the factorial dividing the corresponding derivative in the Taylor expansion i.e. 1! for the first derivative. By viewing the matrix $\mathbf{M}$ as

$$\mathbf{M} = \begin{pmatrix} 1 & 1^0 & (3/2)^0 \\ 0 & 1^1 & (3/2)^1 \\ 0 & 1^2 & (3/2)^2 \end{pmatrix},$$

we see that equation (5.4) captures in one formula all Taylor coefficients of the atomic nodes relative to the base node.

The matrix-vector system

$$\mathbf{M} \cdot \mathbf{w} = \mathbf{b},$$

is solved via Gaussian elimination to yield the weights

$$\mathbf{w} = (-5/3, 3, -4/3)^T.$$

Thus, the second-order, forward-difference approximation to the first derivative is given by

$$h'_j = \frac{-5h_j + 9h_{j+1} - 4h_{j+3/2}}{3dz} + O(dz^2),$$

Local Labelling	**Forward**	**Central**	**Backward**
parent-parent	$\{0,1,2\}$	$\{-1,0,1\}$	$\{-2,-1,0\}$
parent-child	$\{0,1,3/2\}$	$\{-1,0,1/2\}$	$\{-3/2,-1/2,0\}$
child-parent	$\{0,1/2,3/2\}$	$\{-1/2,0,1\}$	$\{-3/2,-1,0\}$

Table 5.1: Local mesh labelling for a second-order approximation to the first derivative.

at global base node z_j. The parent-child mesh structure is incorporated via the atomic weights; for comparison the weight vector calculated for this forward approximation to the first derivative in the parent-parent case is $\mathbf{w} = (-3/2, 2, -1/2)^T$

By using d_j dictated by the appropriate Taylor expansion, any second-order difference approximation to the first or second derivative can be readily derived. Table 5.1 summarises the local mesh labelling required for the first derivative, for each possible structure. It is clear to see that the local labelling for the child-parent structure is a reflection about the base label 0 of the parent-child case. Similar labelling can be derived for the second derivative approximation, however, more structures are possible since more nodes are required.

5.3.2 An Implicit Numerical Scheme

Implicit time-marching algorithms involve solving a boundary-value problem at each time step in order to advance the solution forward in time. The reward for this costly process is that implicit methods are stable for much longer time steps by comparison with explicit schemes. For non-linear equations, a fully-implicit algorithm is highly computationally expensive. Thus, for the Navier-Stokes equations, it is more common to use a semi-implicit algorithm in which some terms are approximated by an explicit scheme, while others are approximated implicitly. Since the thinning is driven by surface tension, we use an implicit treatment of the terms determining the jet shape, but treat the velocity terms explicitly. For the CIJ problem, we use the following semi-implicit algorithm, which we found to be stable for non-uniform mesh structures.

Consider the Newtonian slender-jet equations (3.1) given by

$$\begin{aligned} \frac{\partial h^2}{\partial t} + \frac{\partial}{\partial z}(h^2 v) &= 0, \\ \frac{\partial}{\partial t}(h^2 v) + \frac{\partial}{\partial z}(h^2 v^2) &= \frac{\partial}{\partial z}\left(h^2\left(K + 3Oh\frac{\partial v}{\partial z}\right)\right), \end{aligned}$$

for the free-surface height $h(z,t)$ and jet velocity $v(z,t)$. The curvature term is denoted by K and the Ohnesorge number by Oh.

Discretising conservation of mass such that $a_j^n = h^2(z_j, t_n)$ and $v_j^n = v(z_j, t_n)$, for mesh node z_j and time step t_n, yields

$$\left.\frac{\partial a}{\partial t}\right|_j^n = -\left(v_j^n \left.\frac{\partial a}{\partial z}\right|_j^{n+1} + a_j^{n+1} \left.\frac{\partial v}{\partial z}\right|_j^n \right).$$

Here the velocity component is evaluated explicitly at the current time step t_n, whereas the cross-sectional area is evaluated implicitly at the next time step t_{n+1}. On a uniform mesh, the usual forward-time, central-space difference approximations can be applied such that

$$\frac{a_j^{n+1} - a_j^n}{dt} = -\left(v_j^n \frac{a_{j+1}^{n+1} - a_{j-1}^{n+1}}{2dz} + a_j^{n+1} \frac{v_{j+1}^n - v_{j-1}^n}{2dz} \right) + O(dt, dz^2),$$

for mesh size dz and time step dt, which gives first-order temporal accuracy and second-order spatial accuracy. For non-uniform mesh structures the appropriate difference approximations are applied in order to achieve second-order accuracy in space. This leads to a tridiagonal system of equations for a semi-implicit calculation of the jet area. For example, for a parent-parent mesh structure, the system is given by

$$-v_j^n \frac{dt}{2dz} a_{j-1}^{n+1} + \left(1 + \frac{dt}{2dz}(v_{j+1}^n - v_{j-1}^n) \right) a_j^{n+1} + v_j^n \frac{dt}{2dz} a_{j+1}^{n+1} = a_j^n + O(dt, dz^2).$$

A tridiagonal matrix system can be solved via a simple algorithm consisting of a simplified form of Gaussian elimination [108]. Furthermore, to achieve second-order accuracy in time [108] the average of the explicit and implicit schemes are taken such that

$$\left.\frac{\partial a}{\partial t}\right|_j^n = -\frac{1}{2}\left[\left(v_j^n \left.\frac{\partial a}{\partial z}\right|_j^{n+1} + a_j^{n+1} \left.\frac{\partial v}{\partial z}\right|_j^n \right) + \left(v_j^n \left.\frac{\partial a}{\partial z}\right|_j^n + a_j^n \left.\frac{\partial v}{\partial z}\right|_j^n \right) \right].$$

Similarly, conservation of momentum can be solved; the equation takes the same general form with the addition of a source term on the right-hand side:

$$\left.\frac{\partial F}{\partial t}\right|_j^n = -\left(v_j^n \left.\frac{\partial F}{\partial z}\right|_j^{n+1} + F_j^{n+1} \left.\frac{\partial v}{\partial z}\right|_j^n \right) + S_j^n.$$

For the Newtonian slender-jet equations, $F = h^2 v$ and the source term is defined as

$$S_j^n = \left.\frac{\partial}{\partial z}(h^2 K)\right|_j^{n+1} + 3Oh \left.\frac{\partial}{\partial z}\left(h^2 \frac{\partial v}{\partial z} \right)\right|_j^n,$$

where the first term corresponds to curvature and is known implicitly from the solution of conservation of mass and the second term corresponds to viscosity and is solved explicitly. Again, the appropriate finite-difference approximations are applied according to the local mesh structure and second-order temporal accuracy is achieved by averaging.

5.3.3 An Adaptive-Mesh Example

In this section, we use the adaptive mesh technique alongside our one-dimensional model to simulate the capillary break-up of a liquid bridge, as described in Chapter 3. The Ohnesorge number is set to $Oh = 0.2$, as a typical parameter for CIJ inks, and the Newtonian slender-jet equations (3.1) are solved via the semi-implicit numerical scheme described

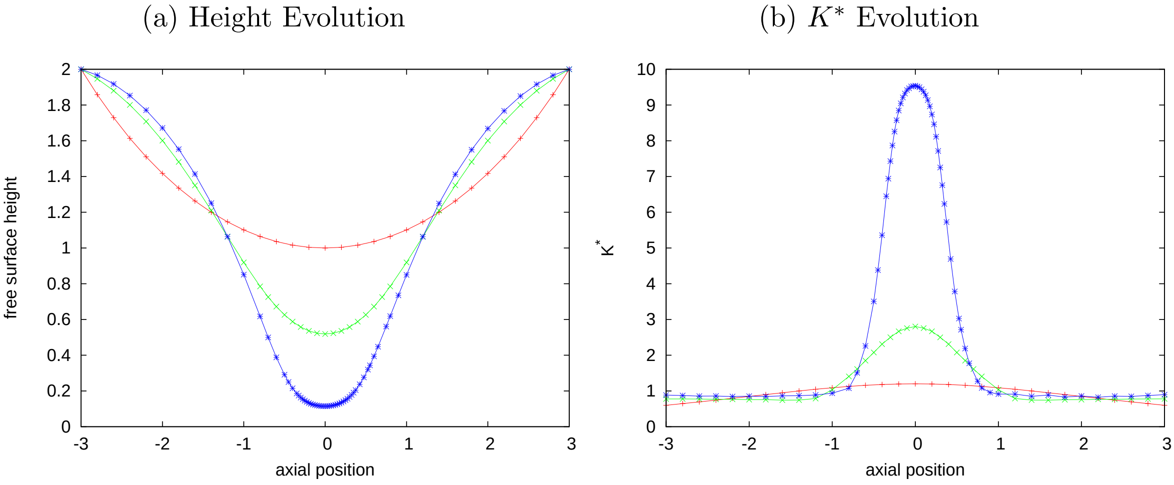
(a) Height Evolution

(b) K^* Evolution

Figure 5.6: (a) Free-surface evolution of the liquid bridge for three time profiles calculated via relative criterion (5.6); (b) corresponding K^* given by equation (5.5). Points indicate the distribution of mesh nodes for $m = 4$ levels of adaption. The Ohnesorge number is $Oh = 0.2$ and the time step is $dt = 10^{-6}$.

above. We assume Dirichlet boundary conditions to simulate a capillary-thinning rheometer; the free surface h is fixed and there is zero axial velocity v at the end-plates.

We select an initial mesh size $dz = 0.2$ and implement $m = 4$ levels of adaption, so that the coarse mesh is refined to $dz = 0.0125$ via the coarse-to-fine refinement process. After adaption, the mesh is smoothed using the algorithm described in section 5.2.2 and coarsened to remove higher-level nodes that are not required. The time step is set to $dt = 10^{-6}$, which proved to be stable in the uniform case for the finest mesh size implemented during adaption.

We choose to refine according to the sum of the absolute magnitude of the components of the curvature term in equation (3.1), that is

$$K^* = \left|\frac{1}{h(1+h_z^2)^{1/2}}\right| + \left|\frac{h_{zz}}{(1+h_z^2)^{3/2}}\right|. \tag{5.5}$$

Since our scheme is second-order spatially accurate, the error incurred calculating K^* at node z_j is of the order $O(dz_j^2)$, where dz_j is the local mesh size. Thus, a suitable adaption criterion is the ‘relative’ condition

$$K^* dz_j \geq \delta_1, \tag{5.6}$$

for some limit δ_1. We find that the choice $\delta_1 = 0.2$ is sufficiently large that the slow dynamics in the end drops are computed on the coarsest mesh size, yet small enough to provide adequate resolution as the bridge thins, as shown in Figure 5.6.

Figure 5.6 shows the evolution of the liquid bridge for three time profiles, with the points indicating the distribution of mesh nodes, alongside the corresponding evolution of K^* given by equation (5.5). Initially, the mesh nodes are seen to be evenly distributed along the bridge with uniform mesh spacing of the largest size $dz = 0.2$. As time progresses,

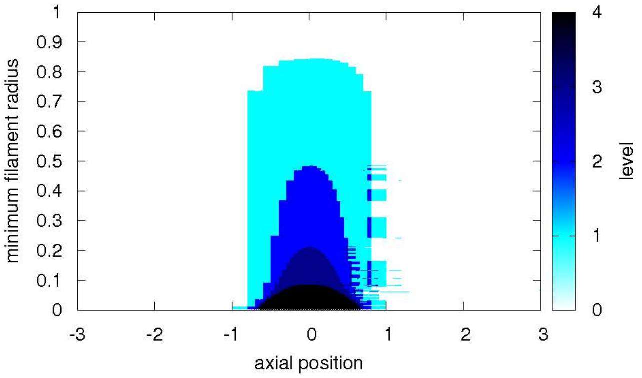

Figure 5.7: Level structure created by adaption criterion (5.6).

surface tension drives the liquid bridge to evolve into a thin filament. Although the curvature remains $O(1)$ in the end drops, K^* increases in the region where the filament radius decays. Consequently, when criterion (5.6) is satisfied, new nodes need to be added to the mesh, so that the mesh spacing becomes smaller in the thin-filament region and a new distribution of nodes can be seen.

The mesh structure becomes highly non-uniform with nodes concentrated in the filament region where the curvature is large. Thus, the resolution is improved in precisely those areas where the dynamics are most complicated. In contrast, the nodes are sparsely distributed in the end-drop regions, where the dynamics are relatively slow and hence where lower resolution is sufficient. Figure 5.7 illustrates how the level distribution of the adaption technique evolves as the minimum filament radius decreases. Light regions indicate the coarsest level of adaption and therefore the largest mesh size, whereas dark areas correspond to higher levels of adaption and consequently smaller mesh sizes. A range of mesh sizes are used as the filament radius decays and a fully resolved mesh is implemented

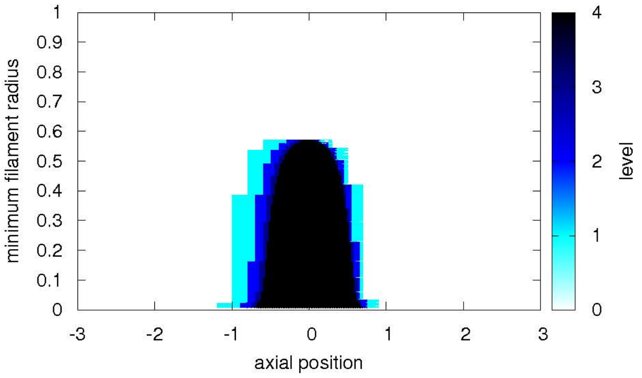

Figure 5.8: Level structure created by adaption criterion (5.7).

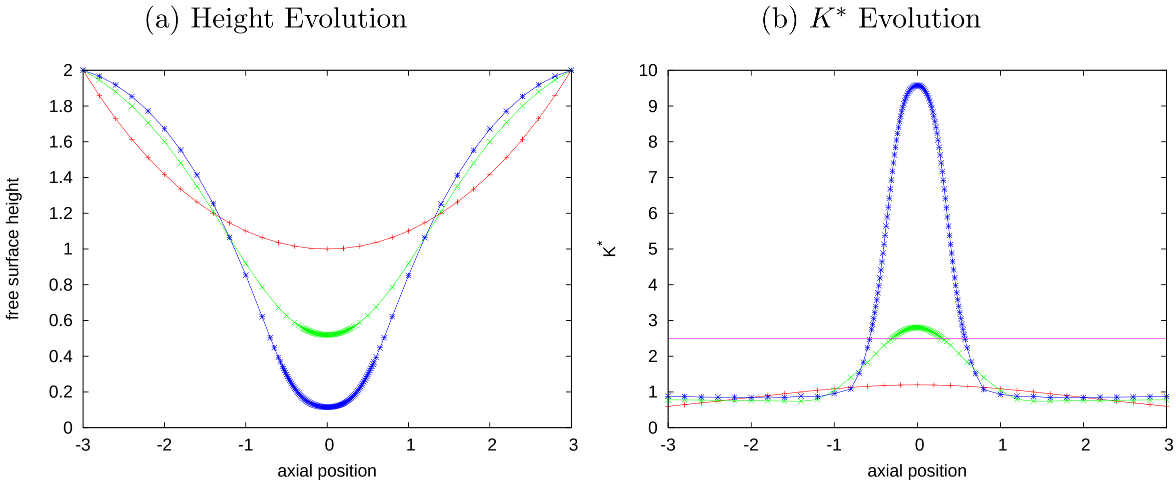

Figure 5.9: (a) Free-surface evolution of the liquid bridge for three time profiles calculated via absolute criterion (5.7); (b) corresponding K^* given by equation (5.5). Points indicate the distribution of mesh nodes for $m = 4$ levels of adaption. The Ohnesorge number is $Oh = 0.2$ and the time step is $dt = 10^{-6}$.

in the filament region for $h_{min} \leq 0.1$. Thus, the mesh adapts to the solution providing high resolution only in the thin-filament region where it is required to capture the fastest dynamics.

An alternative to adaption criterion (5.6) is the 'absolute' condition

$$K^* \geq \delta_2, \tag{5.7}$$

for K^* given by equation (5.5) and some δ_2, for which we find $\delta_2 = 2.5$ is a suitable limit. In this way, a fully resolved mesh is implemented when the criterion (5.7) is satisfied and buffered into a coarser mesh, via the smoothing algorithm, where high resolution is not required. For example, Figure 5.8 illustrates this absolute level structure, in comparison with Figure 5.7 for the relative criterion (5.6). In this case, the darkest shading indicates that a fully resolved mesh is implemented at the larger minimum radius $h_{min} \leq 0.6$.

The solution computed via criterion (5.7) is equivalent to that calculated using the first method (5.6); Figure 5.9 shows the evolution of the liquid bridge alongside the corresponding adaption criterion K^* for comparison with Figure 5.6. However, the advantage of using the absolute criterion (5.7) is that higher resolution is provided in the neck regions during the thinning process, as can be seen in Figure 5.10. Having high resolution in this area is beneficial in the CIJ problem, where break-up of the jet into drops is considered. As a result, the absolute criterion (5.7) is used is preference to the relative criterion (5.6) in ensuing computations.

In Figure 5.11, we compare the free-surface profile at the point of break-up, computed on three different meshes; a coarse uniform mesh ($dz = 0.2$), a fine uniform mesh ($dz = 0.0125$) and the $m = 4$ adaptive mesh described above for adaption criterion (5.7). The time step is $dt = 10^{-6}$ for all cases. The solution computed using our adaptive scheme is

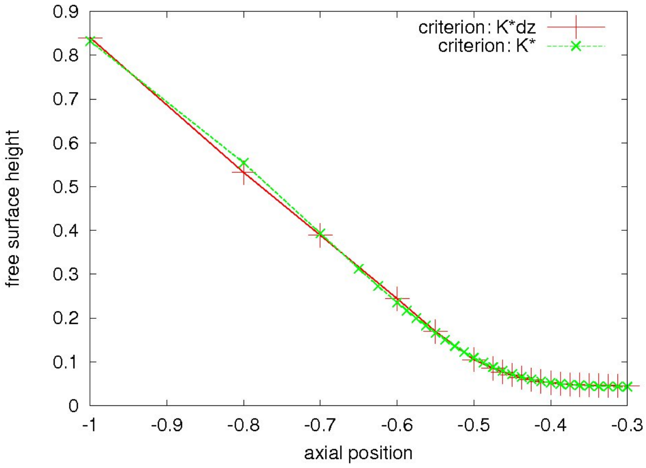

Figure 5.10: The computed neck region for two different adaption criterion (5.6) and (5.7), with points indicating node distribution. The absolute criterion (5.7) provides higher resolution than relative criterion (5.6) in the neck region, which is beneficial in the prediction of satellite drop formation.

in agreement with the uniform solution computed on the high-resolution grid, as shown in Figure 5.11.

In contrast, the uniform mesh with the coarse node spacing does not provide sufficient resolution to compute an accurate solution; Figure 5.11 shows that the absolute difference from the fine-mesh solution is of the order $O(10^{-1})$. By employing the adaptive technique, which uses the larger mesh size for an initial grid and refines to the smaller spacing when required, the error is reduced by the order $O(10^2)$ in the thin-filament region. Note that

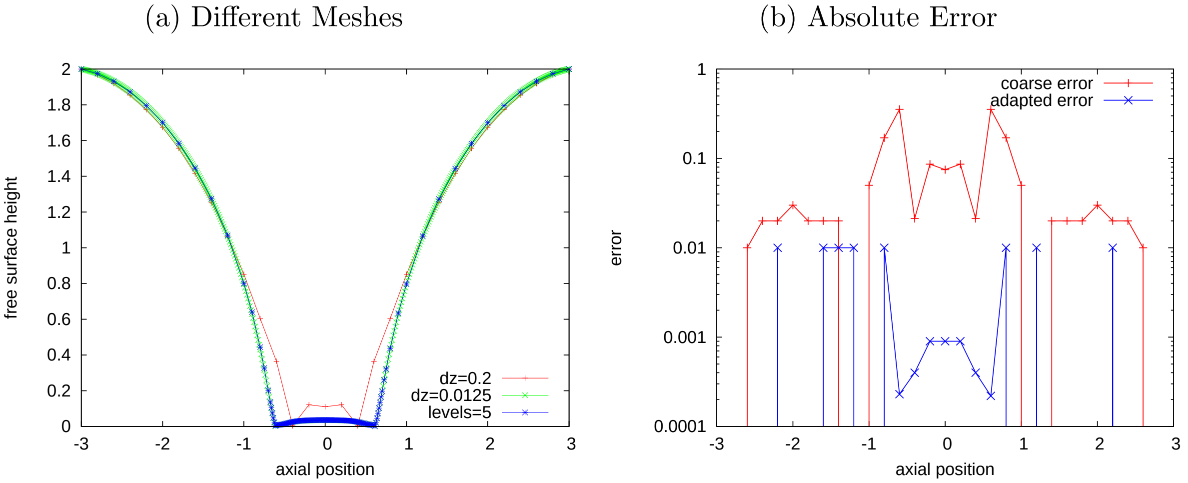

Figure 5.11: (a) The free-surface profile at the point of break-up computed on a coarse uniform mesh ($dz = 0.2$), a fine uniform mesh ($dz = 0.0125$) and an adaptive mesh with $m = 4$ levels of adaption; (b) the absolute error from the fine mesh solution. The Ohnesorge number is $Oh = 0.2$ and time step $dt = 10^{-6}$.

	Coarse	**Fine**	**Adapted**
Mesh size	0.2	0.0125	4 levels
CPU Time (min)	1.13	13.92	2.51
Number of nodes	30	480	141

Table 5.2: Computation time and number of nodes required for a coarse ($dz = 0.2$) and fine ($dz = 0.0125$) uniform mesh compared to the adaptive case using $m = 4$ levels of adaption. Computations were performed on a Dell workstation with 2.40GHz processor, and the time step is $dt = 10^{-6}$ for each case.

the error incurred using this non-uniform mesh is not necessarily symmetric due to the nature of the adaptive technique, because nodes are added ahead of an existing node.

Table 5.2 compares the computation time taken to simulate this liquid bridge problem for the three different meshes described above on a Dell workstation with a 2.40Ghz processor. The increase in computation time from a coarse to fine uniform mesh is approximately linear in the number of points required, which is what one would expect for a tridiagonal solver. However, the computation time can be optimised by using the adaptive mesh scheme; for this problem, the time taken to compute the solution is reduced by a factor of five compared with the fine-mesh solution.

5.4 Modelling a Continuous Inkjet

5.4.1 A Simple Jetting Model

We now consider the dynamics of a continuous inkjet of Newtonian fluid using our adaptive, one-dimensional model. Recall that the slender-jet equations (3.1) are given by

$$\frac{\partial h^2}{\partial t} + \frac{\partial}{\partial z}(h^2 v) = 0,$$
$$\frac{\partial}{\partial t}(h^2 v) + \frac{\partial}{\partial z}(h^2 v^2) = \frac{\partial}{\partial z}\left(h^2\left(K + 3Oh\frac{\partial v}{\partial z}\right)\right),$$

where the curvature term is defined as

$$K \equiv \frac{1}{h(1+h_z^2)^{1/2}} + \frac{h_{zz}}{(1+h_z^2)^{3/2}}, \tag{5.8}$$

and the Ohnesorge number is

$$Oh = \frac{\mu}{\sqrt{\rho\gamma R}}$$

for initial jet radius R. Here jet velocity $v(z,t)$ has been non-dimensionalised with respect to the nozzle radius R and the Rayleigh capillary time T so that the initial dimensionless jet velocity is defined by the Weber number

$$We = \frac{\rho U^2 R}{\gamma},$$

for mean jet velocity U.

The governing equations are solved via the above-described semi-implicit numerical scheme on an adaptive mesh. The mesh refinement is based on the sum of the absolute magnitude of the components of curvature, given by equation (5.5), according to the absolute adaption criterion (5.7), so that new nodes are added if $K^* \geq 2.0$. Since the CIJ problem takes into account break-up of the jet into drops, this adaption limit is chosen to be less than that used for the liquid-bridge problem in section 5.3.3, to implement a larger area of high resolution in the neck regions. The mesh is then smoothed and coarsened.

In the framework of our simplified one-dimensional model, the details of the nozzle are neglected and we consider dynamics at the nozzle exit only. In order to drive the jetting, two different methods are employed. First, the height profile is varied at the nozzle exit such that

$$h_{noz}(t) = (1 + \epsilon \sin(2\pi f t)), \tag{5.9}$$

for some time t. The modulation amplitude is denoted ϵ and the the jetting frequency is defined as

$$f = \frac{\sqrt{We}}{\lambda^*},$$

for the most unstable wavelength $\lambda^* = 9$. In this way, the fastest growing disturbance dominates the flow, since inks generally have low viscosity and are dominated by inertial effects. Modulations in the height mimic thermal fluctuations in the nozzle and we assume constant velocity at the nozzle exit

$$v_{noz}(t) = \sqrt{We}.$$

A similar approach is used by van Hoeve *et al.* [134]. For small amplitudes ($\epsilon \leq 0.01$), a Rayleigh-type instability wave is propagated downstream from the nozzle exit. Although these waves are closely related to Rayleigh waves, they grow with spatial distance from the nozzle, rather than time. However, Keller *et al.* [77] find that the temporal and spatial growth rates agree in the large-Weber-number limit.

More realistically, inkjets are driven by a pressure modulation that translates to a variation in the velocity profile. Thus, the second driving method is to impose a time-dependent velocity perturbation at the nozzle exit such that

$$v_{noz}(t) = \sqrt{We}(1 + \epsilon \sin(2\pi f t)), \tag{5.10}$$

with the jet radius fixed as

$$h_{noz}(t) = 1.$$

Modulations in the velocity profile do not necessarily translate to a sinusoidal variation in the free-surface height and so the instability is not necessarily related to a typical Rayleigh wave. Furthermore, for industrial applications, although the Weber number is typically large ($We \sim 400$), large modulation amplitudes ($\epsilon > 0.01$) are applied, meaning that non-linear interactions become important and Rayleigh theory is no longer valid.

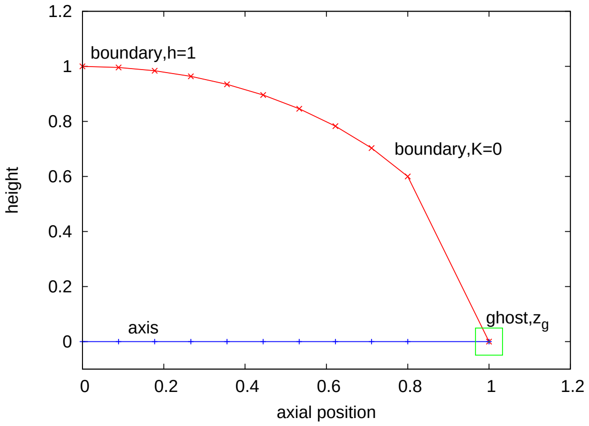

Figure 5.12: The initial condition prescribed for our one-dimensional model as given by the spherical cap equation (5.11).

One-dimensional modelling in this way assumes a plug-flow profile where the velocity is constant across the jet radius. However, in real inkjets, flow through the nozzle generates a Poiseuille flow, which creates a parabolic velocity profile; shear at the nozzle wall slows down fluid located at the free surface, so that the central section of the jet moves faster. Nonetheless, it has been shown that, for a sufficient distance downstream of the nozzle exit, the velocity profile relaxes to plug flow [22]. Hence, a one-dimensional model is expected to be sufficient to model the downstream dynamics of a continuous inkjet.

We assume that the initial shape of the jet takes the form of a spherical cap,

$$h_0(z) = \sqrt{1 - z^2}, \tag{5.11}$$

where z is the nodal position on the axis, as shown in Figure 5.12. We assume that the jet advances from the nozzle in the axial direction, maintaining this prescribed spherical shape at the right-hand boundary. The first and second derivative of a spherical-cap free surface are found analytically to be

$$\frac{\partial h_0}{\partial z} = -\frac{z}{h_0} \quad \text{and} \quad \frac{\partial^2 h_0}{\partial z^2} = -\frac{1}{h_0} - \frac{z^2}{h_0^3},$$

respectively. Consequently, the curvature term given by equation (5.8) in this spherical cap region reduces to

$$K = -1 + 1 = 0. \tag{5.12}$$

Thus, at the leading boundary we impose zero curvature in order to model an advancing spherical cap.

We employ a Eulerian mesh such that the nodes z_j are fixed in the frame of the nozzle. Since the material flows through the mesh, nodes must be ‘switched on’ as the jet advances from the nozzle. In order to switch on new nodes in this manner, we specify a ‘ghost’ node z_g, which corresponds to the axial position at which the jet free surface h is zero. This

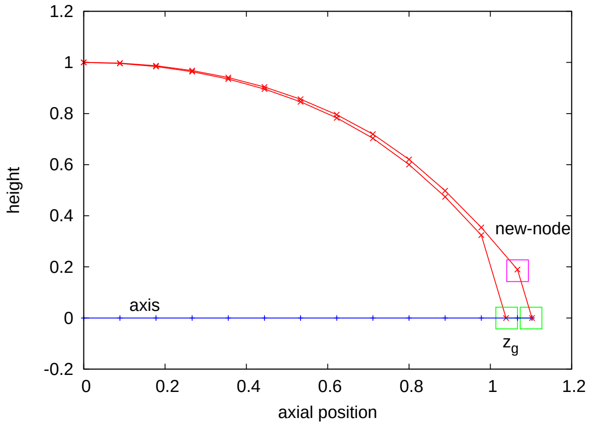

Figure 5.13: Switching on nodes for an advancing jet on an Eulerian mesh.

ghost node is calculated by quadratic Lagrange interpolation of the existing data points. For example, Figure 5.12 shows the initial spherical-cap shape defined at mesh nodes z_j; the ghost node z_g is found by interpolating these prescribed data points.

Over a small time step dt, the jet advances from the nozzle in the axial direction. Thus, at the right-hand boundary node z_J, the height of the jet increases and the ghost node z_g moves along the axis in the direction of the jet, as shown in Figure 5.13. If the ghost nodes exceeds the location of the next node such that

$$z_{\text{ghost}} \geq z_J + dz,$$

then the next node z_{J+1} is switched on. The fluid parameters at the new node, namely height h_{J+1} and velocity v_{J+1}, are calculated by quadratic extrapolation. We assume that the time step is sufficiently small for these new nodes to be located within the spherical-cap region of the advancing jet. Thus, we impose the first and second derivative analytically so that the zero-curvature boundary condition, $K = 0$ in equation (5.12), at the front of the jet is maintained.

We define a break-up criterion when h becomes less than a cut-off radius h_c, which we typically set as 1% of the nozzle radius to ensure $h \gg O(dz^2)$. When $h = h_c$, the fluid ahead of the break-up point is separated from the remaining jet. After separation, the separated fluid evolves to form a droplet. However, since the slender-jet approximation ceases to be valid, the shape of the droplet is not well described and separated drops are removed from the simulation. The distance from the nozzle outlet to this point of break-up is defined to be the break-up length of the jet.

5.4.2 Error Analysis for Simple Jetting

For typical CIJ parameters, $We = 338$ and $Oh = 0.122$, we have tested the accuracy of our adaptive one-dimensional model by considering the variation in jet break-up length for

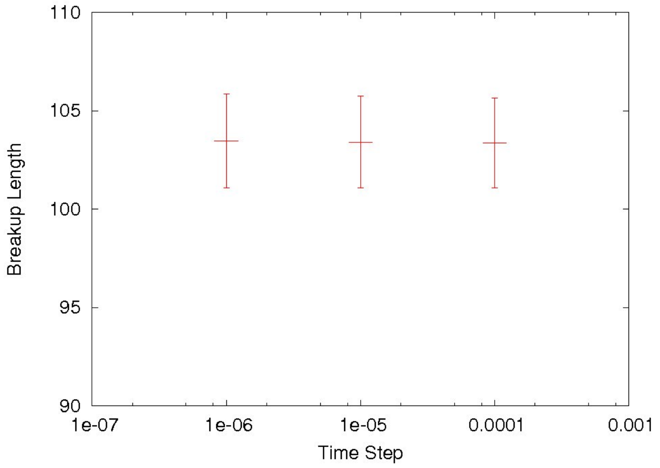

Figure 5.14: Break-up length calculated for a range of time steps dt on a uniform mesh $dz = 0.025$. Error bars indicate standard deviations from the mean; they remain within one wavelength, $\lambda^* = 9$.

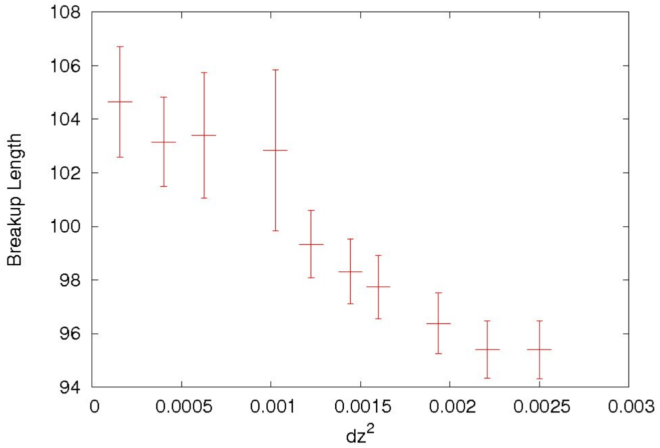

Figure 5.15: Break-up length calculated for a range of uniform mesh sizes dz. Error bars indicate standard deviations from the mean they remain within one wavelength, $\lambda^* = 9$.

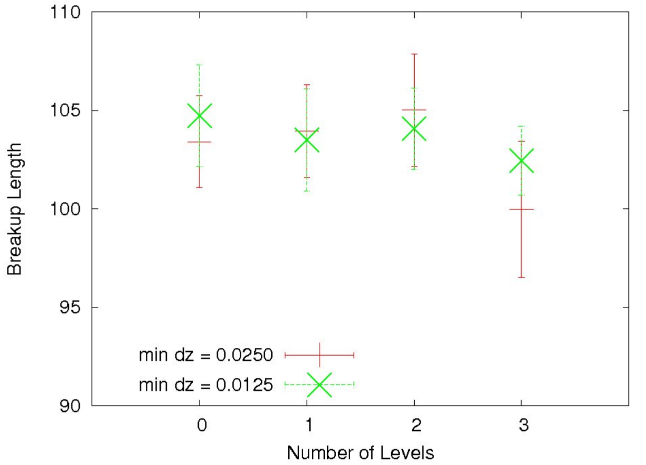

Figure 5.16: Break-up length calculated for a range of levels of adaption m with minimum mesh sizes $dz = 0.0125$ and $dz = 0.025$. Uniform mesh case corresponds to $m = 0$. Error bars indicate standard deviations from the mean; they remain within one wavelength, $\lambda^* = 9$.

various time steps dt, mesh sizes dz and levels of adaption m, where $m = 0$ corresponds to a uniform mesh. In this case, we consider a velocity perturbation, as given by equation (5.10) for $\epsilon = 0.1$ and wavelength $\lambda^* = 9$, and plot in Figures 5.14, 5.15 and 5.16 the mean break-up length calculated over ten drops, with standard deviations indicated by the error bars.

Figure 5.14 shows the break-up length calculated for a range of time steps dt, on a uniform mesh with spacing $dz = 0.025$. We find that the variation in the break-up length is small compared to the wavelength of the jet for each of the time steps $dt = 10^{-5}, 10^{-6}$ and 10^{-7}. Furthermore, the error is approximately constant (≈ 2.3) for decreasing time step, despite the numerical scheme admitting second-order temporal accuracy. We therefore conclude that deviations from the mean length originate from the mesh resolution.

Figure 5.15 shows the break-up length calculated for a range of uniform mesh sizes dz. We see that for decreasing mesh size, the mean length converges to approximately ≈ 104 and the standard deviation from the mean length remains within one wavelength. However, as mesh size is increased, the calculation of the mean break-up length becomes less accurate, with Figure 5.15 showing the mean length decreasing linearly with dz^2 due to the second-order spatial accuracy of the implicit scheme. Somewhat counter-intuitively, the size of the error bar is reduced for coarser mesh sizes. Whereas fine meshes capture all features of break-up, low resolution does not capture the appearance of smaller satellite drops, which cause variation in the break-up length. Thus, since only break-up of the main drops is accounted for, there is a smaller deviation from the mean for larger mesh sizes.

Figure 5.16 shows the break-up length calculated for a number of adaption levels m for minimum mesh sizes $dz = 0.025$ and $dz = 0.0125$. For the uniform cases $m = 0$, we find that decreasing the fully refined mesh size from $dz = 0.025$ to $dz = 0.0125$ does not have a significant effect on the mean break-up length or standard deviation. For increasing levels of adaption m, the standard deviation is found to increase and the calculation of the mean becomes less accurate, departing from the converged value ≈ 104. However, the

Levels	**3**	**2**	**1**	**0**
Coarse Mesh Size	0.2	0.1	0.05	0.025
CPU Time (min)	52.65	65.63	82.4	102.86
Number of nodes	1709	2314	2866	4172

Table 5.3: Computation time and number of nodes required for increasing levels of adaption m with minimum mesh size $dz = 0.025$ on a Dell workstation with 2.40GHz processor for a fixed simulation time. The time step is $dt = 10^{-4}$ for each case. The reduction of resource requirements from a uniform mesh ($m = 0$) is clear in the adaptive cases ($m > 0$).

calculated lengths are within the same wavelength for all m and the size of the variation remains less than the wavelength.

Although the error from the converged mean length is increased for additional levels m, the compromise is small considering the significant reduction in computation time summarised in Table 5.3. By using three levels of adaption to provide fine-mesh resolution $dz = 0.025$ in high-curvature areas, the computation time for the simulation is almost halved compared with the fully-resolved case. Furthermore, we see that the adaption scheme is efficient, since the increase in computation time is approximately linear in the number of nodes used. In the following, we choose $m = 3$ with finest mesh size $dz = 0.025$ and time step $dt = 10^{-5}$.

5.4.3 Rayleigh Behaviour at Moderate Weber Number

We now compare the results of this Newtonian CIJ model with Rayleigh's linear stability theory detailed in Chapter 2. The Weber number is initially chosen as $We = 81$ with Ohnesorge number $Oh = 0.122$. First, we impose a sinusoidal height perturbation at the nozzle exit, as given by equation (5.9) for small amplitude $\epsilon = 0.01$. The most unstable wavelength $\lambda^* = 9$ corresponds to Rayleigh frequency $f^* = 0.91$ at this particular jet velocity.

Figure 5.17 shows the sinusoidal free-surface profile predicted by our one-dimensional model. Due to the uniform jet speed and the relatively small perturbation of the free-surface height, the jet becomes extremely long (approximately $20\lambda^*$) before the capillary instability becomes apparent. Far downstream of the nozzle exit, surface-tension-driven thinning causes the jet to evolve into a series of spherical main drops connected by thinner filaments. The distance between the main drops of fluid is seen to be ~ 9, corresponding to the wavelength imposed at the Rayleigh frequency. In this case, the thinnest part of the jet is downstream of the connecting filament, so that the first pinching event occurs behind the main drop of fluid. At break-up, these filaments contract to form a series of smaller satellite drops interspersed between the main drops. This contraction of the filament after detachment from the main drop has recently been investigated by Eggers [51].

Typical CIJ practices impose a controlled disturbance on the jet velocity, rather than the free-surface height. Thus, for the same fluid parameters $We = 81$ and $Oh = 0.122$, we can instead impose a velocity perturbation at the nozzle exit, as described by equation (5.10), with equivalent Rayleigh frequency $f^* = 0.91$ and small amplitude $\epsilon = 0.01$. At this slow speed and small perturbation size, Figure 5.18 shows that perturbing the driving velocity profile induces a sinusoidal-like variation in the free-surface height and the profile is similar to the perturbed-height case shown in Figure 5.17. Again, we observe the same asymmetry, where pinching occurs downstream of the connecting filament. However, compared to Figure 5.17 for the same amplitude of perturbation, the varied velocity profile gives a significantly shorter jet length; the jet length is nearly halved by changing the driving method.

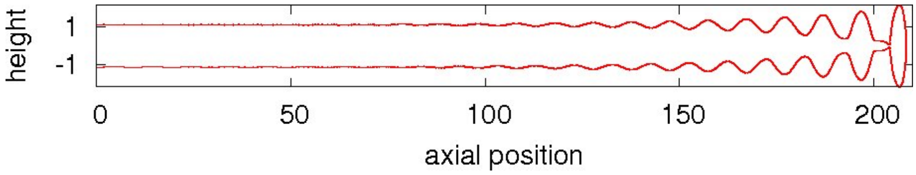
(a) Perturbed Height at Nozzle

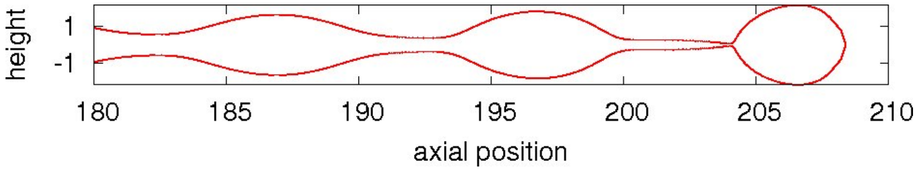
(b) Close-up of Pinch off

Figure 5.17: (a) Free-surface profile predicted by our one-dimensional model for $We = 81, Oh = 0.122$ and $\lambda^* = 9$ with perturbation amplitude $\epsilon = 0.01$ of the height profile at the nozzle given by equation (5.9); (b) a close-up for axial positions in the interval $[180 : 210]$ is also shown.

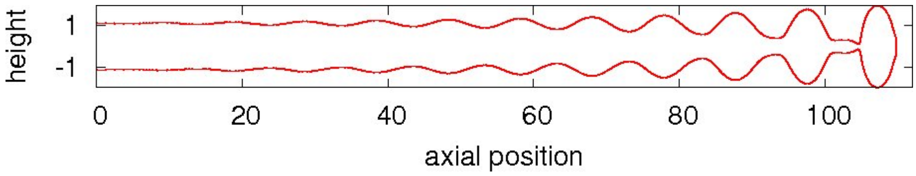
(a) Perturbed Driving Velocity

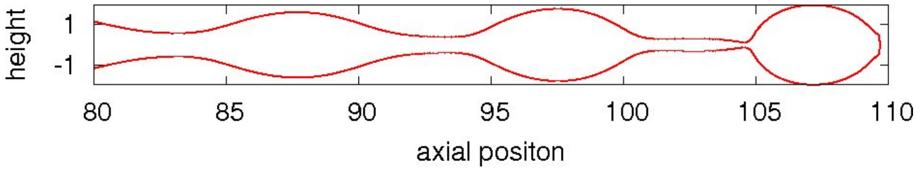
(b) Close-up of Pinch off

Figure 5.18: (a) Free-surface profile predicted by our one-dimensional model for $We = 81, Oh = 0.122$ and $\lambda^* = 9$ with perturbation amplitude $\epsilon = 0.01$ of the driving velocity profile given by equation (5.10); (b) a close-up for axial positions in the interval $[80 : 110]$ is also shown.

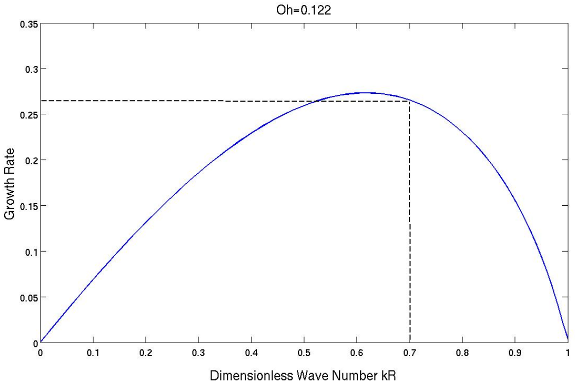

Figure 5.19: The Rayleigh dispersion relation (5.13) for $Oh = 0.122$. The dashed lines are discussed in the main text.

We now explore the effects of varying Weber number and jet wavelength λ and compare our results to the theoretical predictions of Rayleigh's linear stability analysis. Recall that, in the long-wavelength approximation, the dispersion relation for a Newtonian fluid is given by

$$\alpha^2 + \frac{3\mu k^2}{\rho}\alpha - \frac{\gamma k^2}{2\rho R}(1 - k^2R^2) = 0, \tag{5.13}$$

for growth rate α and wave number k. The dispersion relation is plotted in Figure 5.19 for $Oh = 0.122$ and the fastest growing mode is found to have wavelength $\lambda = 9.8$, when taking into account the fluid viscosity. Since the Ohnesorge number is small, the dynamics are dominated by inertia and the Rayleigh mode ($\lambda^* = 9$) is approximately equal to the fastest growing mode. The inverse of the dispersion relation (5.13) gives a break-up curve to predict the ultimate break-up length of the jet for a particular wavelength. For comparison with experimental data, this break-up curve is multiplied by an arbitrary constant that accounts for the initial disturbance. Furthermore, for Weber number We, the break-up length L of the fastest growing mode is predicted to be

$$\frac{L}{R} = C\sqrt{We}(2\sqrt{2} + 6Oh), \tag{5.14}$$

in which C is an arbitrary constant that accounts for the initial disturbance.

Figure 5.20 shows the break-up lengths predicted by the one-dimensional model for driving methods (5.9) and (5.10) with $\epsilon = 0.01$, for a range of Weber numbers. Each simulation is run until ten drops are produced. The average break-up length is then calculated over the number of drops produced during the simulation and the standard deviation from the mean is indicated by the error bar. The error remains within one jet wavelength (in this case it is small ~ 1.5 compared to the axis scale) and originates from the mesh resolution, as discussed earlier. The increase in break-up length with Weber number predicted by our model is in agreement with Rayleigh's theory, given by equation (5.14), which is also plotted in Figure 5.20. However, we observe small discrepancies when driving the velocity component since an exact sinusoidal height profile is not achieved.

Additionally, Figure 5.21 shows the break-up lengths predicted by our one-dimensional

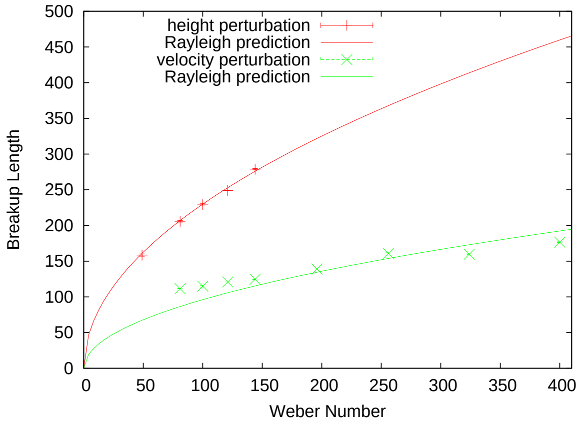

Figure 5.20: Break-up length predicted by our one-dimensional model with small-amplitude perturbation $\epsilon = 0.01$ applied to both driving methods (5.9) and (5.10), compared to equation (5.14) for a range of Weber numbers with $\lambda^* = 9$ and $Oh = 0.122$.

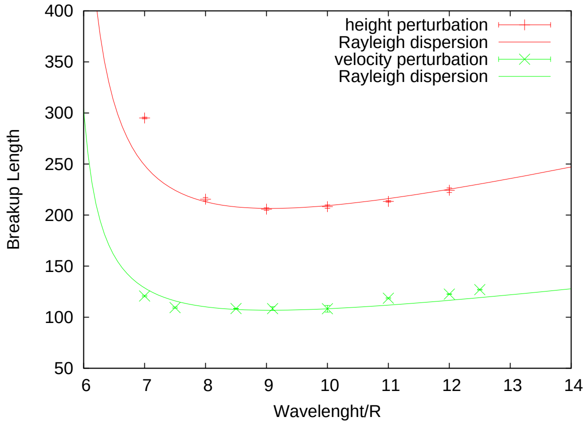

Figure 5.21: Break-up length predicted by our one-dimensional model with small-amplitude perturbation $\epsilon = 0.01$ applied to both driving method (5.9) and (5.10), compared to the inverse of equation (5.13) for a range of wavelengths with $We = 81$ and $Oh = 0.122$

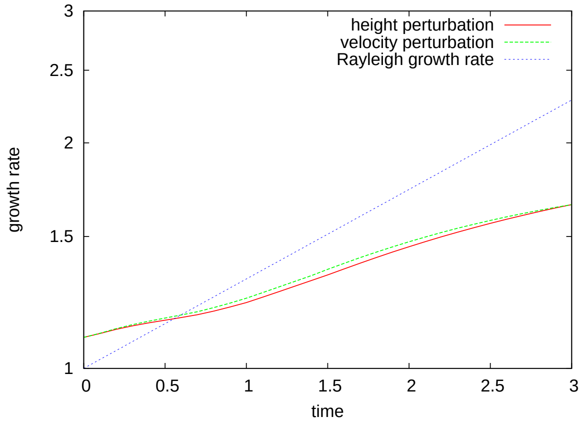

Figure 5.22: Exponential growth of the disturbance wave $\lambda^* = 9$ predicted by our one-dimensional model for small-amplitude perturbation $\epsilon = 0.01$ applied to both driving methods (5.9) and (5.10), compared to the predicted growth rate $\alpha^* = 0.27$ for $We = 81$ and $Oh = 0.122$.

model for a range of wavelengths, again with $\epsilon = 0.01$ for driving methods (5.9) and (5.10). We observe that the shortest jets are generated by the most unstable wavelength $\lambda = 9.8$, and that longer jets can be generated by imposing a different frequency due to the increased stability of the disturbance wave. The results are in agreement with Rayleigh's dispersion relation (5.13), the inverse of which is also plotted in Figure 5.21; again there is some discrepancy for the perturbed-velocity case.

Figure 5.22 shows that, for an $\epsilon = 0.01$ perturbation of each driving method, the disturbance wave initially grows exponentially with time, indicating a linear instability. However, the rate of growth is slower than the $\alpha^* = 0.27$ predicted by Rayleigh's theory shown in Figure 5.19. This discrepancy is due to the nature of the disturbance wave produced by a continuous jet.

5.4.4 Spatially Growing Waves

The linear stability theory of Rayleigh treats a jet as an infinite parallel flow and determines whether the flow becomes unstable to spatially periodic disturbances that grow in time. However, experimentally it is more natural to approach this problem by imposing controlled-time harmonic disturbances on the flow at the nozzle exit. These waves are closely related to Rayleigh waves; however, the waves grow with distance from the nozzle rather than time.

Keller *at al.* [77] analyse spatially amplifying capillary waves by transforming Rayleigh's dispersion relation to a moving jet. In contrast to the Rayleigh analysis, the wave number k is allowed to be complex so that the waves grow only with distance from the nozzle and not with time. Keller *et al.* find that the temporal and spatial growth rates agree only in the infinite-Weber-number limit. One-dimensional theories by Pimbley [105] and Bogy

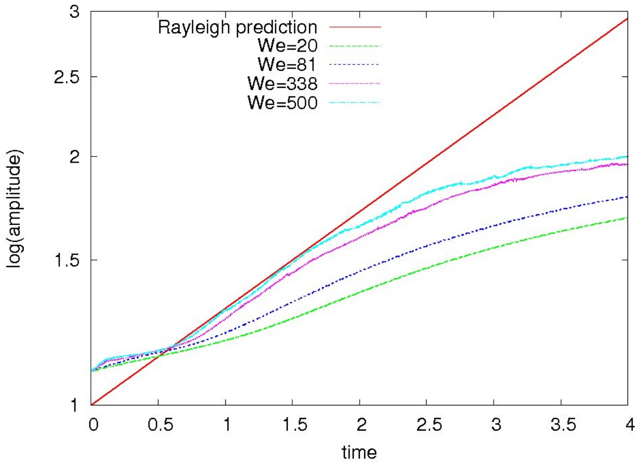

Figure 5.23: Rayleigh's prediction of disturbance growth rate $\alpha^* = 0.27$ found from the dispersion relation (5.13), compared to the growth rate of the disturbance wave predicted by our one-dimensional model for jet velocities $We = 20, 81, 338$ and 500 with $Oh = 0.122$, $\lambda^* = 9$ and $\epsilon = 0.001$.

(a) Modulated Height at Nozzle

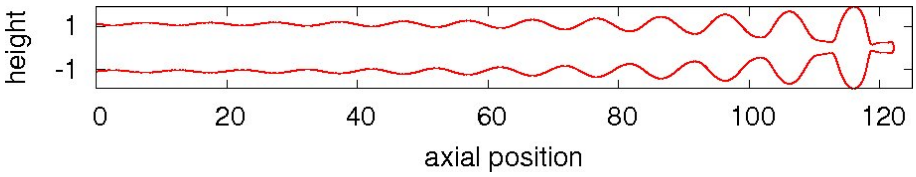

(b) Modulated Driving Velocity

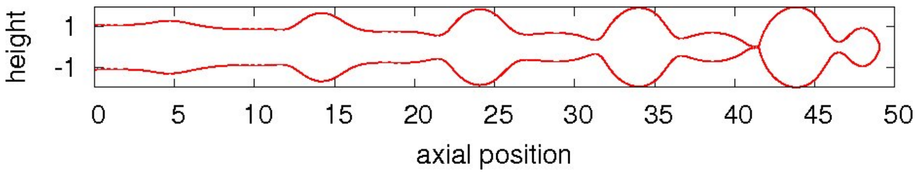

Figure 5.24: Free-surface profiles predicted by our one-dimensional model. (a) $\epsilon = 0.1$ modulation of the height profile given by equation (5.9); (b) $\epsilon = 0.1$ modulation of the driving velocity profile given by equation (5.10). The parameters are $We = 81, Oh = 0.122$ and $\lambda^* = 9$.

[13] find identical results to those of Keller *et al.*.

To test this theory, we simulate a continuous jet of Newtonian fluid having Ohnesorge number $Oh = 0.122$ and varying Weber numbers; the jet is modulated at the Rayleigh frequency f^* for modulation amplitude $\epsilon = 0.001$. Figure 5.23 shows the growth rate of the disturbance wave for a range of jet velocities with Weber numbers $We = 20, 81, 338$ and 500. For comparison, we have plotted the theoretical growth rate $\alpha^* = 0.27$ predicted by the dispersion relation shown in Figure 5.19. As predicted by Keller *et al.*, the growth rate of the instability increases with Weber number and approaches the Rayleigh prediction in the large-Weber-number limit, since the spatial structure of disturbances growing along the jet is almost periodic at large Weber number.

Since CIJ jets operate in the high-Weber-number limit, Rayleigh's temporal theory is considered to be valid for describing the linear dynamics during the jetting process. However, for industrial applications, it is also typical to modulate the jet at much higher amplitudes, around $\sim 10\%$ of the mean jet velocity, to control break-up. Thus, a linear analysis is not sufficient to explain typical features of CIJ jetting.

For example, for parameters $We = 81$, $Oh = 0.122$, $\lambda^* = 9$ and large modulation amplitude $\epsilon = 0.1$, Figure 5.24 shows the free-surface profile predicted by our one-dimensional model for each driving method; that is a height modulation at the nozzle exit, given by equation (5.9), and a modulation of the driving velocity, given by equation (5.10). We observe the same break-up behaviour, where pinching first occurs downstream of the satellite drop, for both driving methods. However, the jet length is significantly reduced in comparison to the small-amplitude cases shown in Figures 5.17 and 5.18. This reduction in jet length is induced by the size of the initial perturbation and is not necessarily accounted for by Rayleigh's linear theory, as we now discuss.

5.5 Characteristics of CIJ Break-up

5.5.1 Modulated High-Weber-Number Jetting

Here we increase the Weber number to $We = 338$, while the Ohnesorge number remains fixed at $Oh = 0.122$, and we consider driving the velocity profile at the nozzle described by equation (5.10). These parameters are used for comparison with the large-scale CIJ experiments detailed in Casterjon-Pita *et al.* [23]. We explore the effects of increasing the modulation amplitude ϵ and varying the jetting frequency f by changing the wavelength λ. Recall that the Rayleigh wavelength is $\lambda^* = 9$, which gives a frequency $f^* = 1.86$ for this particular jet velocity.

Figure 5.25 shows the effect that increasing the amplitude ϵ of the velocity modulation has on the ultimate break-up length of the jet. We consider two different wavelengths, $\lambda^* = 9$ and $\lambda = 7$, which have linear growth rates $\alpha^* = 0.27$ and $\alpha = 0.17$, respectively. As expected, increasing the amplitude of the velocity modulation reduces the break-up length of the jet for both wavelengths. For small amplitudes $\epsilon \leq 0.01$, we see that the Rayleigh mode λ^* generates a shorter jet length than $\lambda = 7$, in line with the relative values of the linear growth rates.

However, as ϵ is increased to a range nearer to that observed CIJ printing, we observe

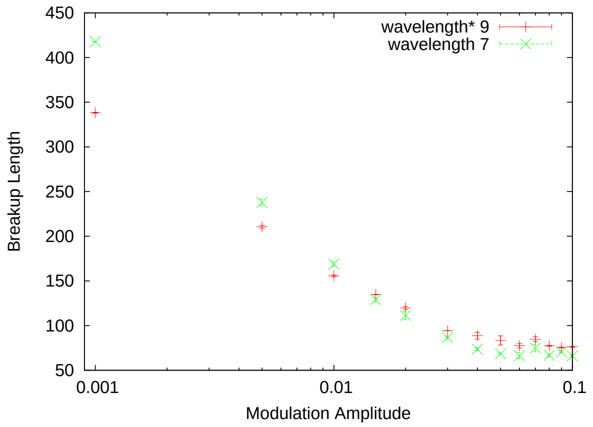

Figure 5.25: Break-up length compared to modulation amplitude ϵ predicted by the one-dimensional model for $We = 338$, $Oh = 0.122$ and two different imposed wavelengths $\lambda = 7$ and $\lambda^* = 9$.

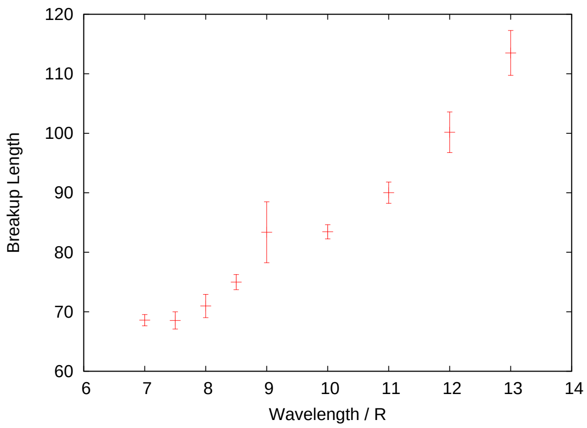

Figure 5.26: Break-up length compared to wavelength λ predicted by the one-dimensional model for $We = 338$, $Oh = 0.122$ and modulation amplitude $\epsilon = 0.05$.

a change from this linear behaviour. In particular, for $\epsilon > 0.01$, Figure 5.25 shows that $\lambda = 7$ generates a shorter jet than the Rayleigh mode, despite the linear theory predicting a slower growth rate. This transition is a result of non-linearity; for amplitudes greater than $\epsilon = 0.01$, non-linear effects become increasingly important and the break-up length can no longer be described by Rayleigh's linear theory. To highlight this non-linear phenomenon, Figure 5.26 shows how the break-up length of the jet increases with increasing disturbance wavelength for fixed modulation amplitude $\epsilon = 0.05$, which effect has also been observed

(a) Modulated Height at Nozzle

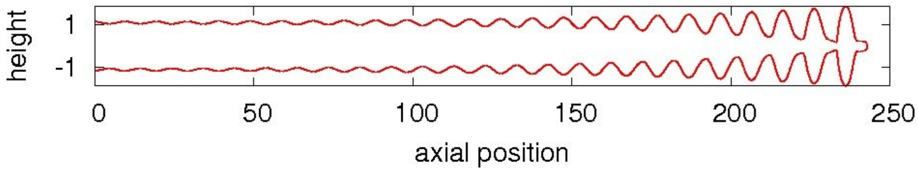

(b) Modulated Driving Velocity

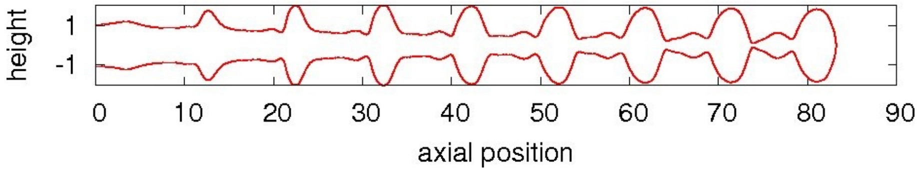

Figure 5.27: Free-surface profiles predicted by our one-dimensional model. (a) $\epsilon = 0.1$ height modulation at the nozzle given by equation (5.9); (b) $\epsilon = 0.1$ modulation of the driving velocity given by equation (5.10). The parameters are $We = 338, Oh = 0.122$ and $\lambda^* = 9$.

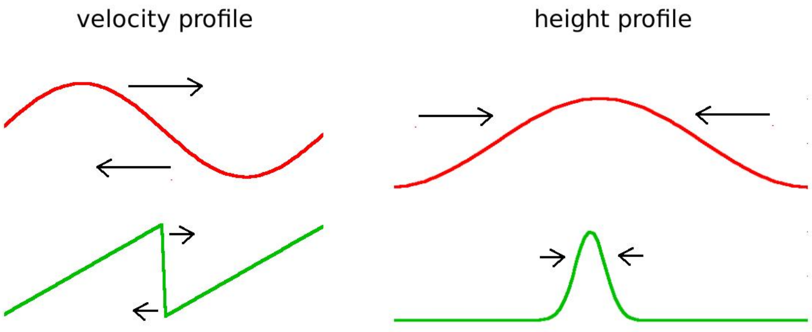

Figure 5.28: Schematic figure showing how the velocity profile evolves into a sawtooth wave causing isolated bulges to form on the uniform thread.

experimentally by Meier *et al.* [95].

We now consider the break-up behaviour of these large-amplitude, high-Weber-number jets for the Rayleigh wavelength $\lambda^* = 9$ and compare both driving methods given by equations (5.9) and (5.10) for $\epsilon = 0.1$. In particular, Figure 5.27 shows the free-surface profile predicted by our one-dimensional model for a $\epsilon = 0.1$ height modulation at the nozzle exit compared to a $\epsilon = 0.1$ modulation of the driving velocity profile. Although using a height modulation to drive the jetting demonstrates the same asymmetric break-up, with pinching occurring downstream, that we have seen for smaller Weber numbers, at this amplitude $\epsilon = 0.1$ (see Figure 5.24) and smaller amplitude $\epsilon = 0.01$ (see Figures 5.17 and 5.18), we observe a dramatic change in behaviour when modulating the driving velocity component at this high Weber number.

The free-surface variation produced by modulated velocity is no longer similar to a sinusoidal wave, as we have seen previously. For this large amplitude and high Weber number, the jet velocity is distorted due to the non-linear advection term appearing in conservation on momentum:

$$\left(v - \frac{6Oh}{h}\frac{\partial h}{\partial z}\right)\frac{\partial v}{\partial z}.$$

Due to this non-linearity, the peak of the velocity profile travels faster than the trough, so that the pulse becomes accumulatively more like a sawtooth wave and generates a shock in the velocity profile, as sketched in Figure 5.28. Consequently, fluid upstream of the shock moves faster than the fluid downstream causing steep bulges to form on the uniform thread, also sketched in Figure 5.28. Due to this distortion, other frequency components are introduced, which we investigate later via a Fourier analysis.

Furthermore, in this case we observe that the pinching position is switched to the opposite end of the connecting filament, causing pinch-off to occur upstream, rather than downstream. We call this phenomenon ‘inverted’ pinching. A transition from downstream to upstream pinching in this way has previously been studied by Pimbley & Lee [106] and Chaudhary & Maxwell [26], and an overview of their results is described in Chapter 2, section 2.3.2. It is evident that this behaviour must originate from the distortion of the velocity profile and, compared to Figure 5.24, occurs only for sufficiently large Weber numbers.

5.5.2 Inversion of Break-up Behaviour

Existing theories of drop formation do not offer a full explanation of satellite formation, or this inverted break-up behaviour we observe in Figure 5.27. Whereas the linear theories of Rayleigh [109], [110], Weber [138] and Keller *et al.* [77] do not account for satellite drops, non-linear theories based on a temporal instability on an infinite jet by Yeun [145] and Lee [86] predict that satellites are always generated, with break-up occurring simultaneously either side of the droplet due to the symmetry of the flow. Although a transition in the break-up behaviour from downstream to upstream pinching is described via a non-linear spatial stability analysis, as in the work of Pimbley & Lee [106], a quantitative agreement with experiments is lacking.

In Chapter 2, we detail how the elimination of satellites depends on whether the first pinching event occurs downstream or upstream. A schematic of these two pinching behaviours is shown in Figure 5.29. If pinching first occurs on the downstream side of the connecting filament, then the front side of the filament separates from the main drop first. On the other hand, if pinching first occurs upstream, the back side of the filament is separated from the main drop first and we observe the inversion phenomenon. The time that exists between the front and back separations is known as the 'satellite interaction time' [106]. During this time, a change in momentum occurs causing the satellite to slow down or speed up relative to the velocity of the main drops. Thus, for the correct parameter space, satellites can either forward-merge with the leading drop or rear-merge with the preceding drop.

Figure 5.30 shows the free-surface profiles predicted by our one-dimensional model for a range of modulation amplitudes $\epsilon = 0.05, 0.1$ and 0.15, with $We = 338$, $Oh = 0.122$ and $\lambda^* = 9$. In general, the jets form a series of main drops connected by thinner filaments, which ultimately contract to form satellite drops at break-up. As predicted by the theory

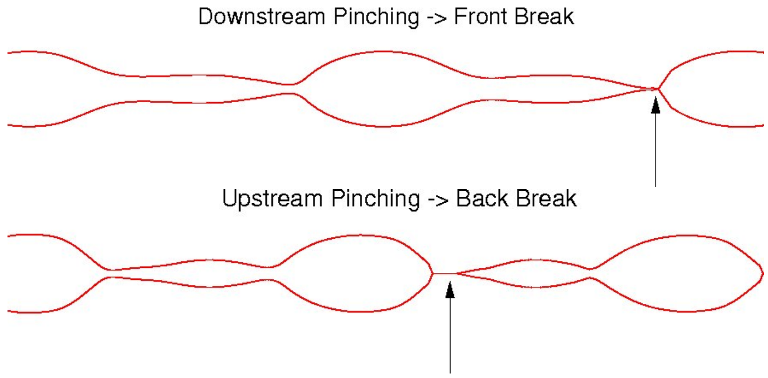

Figure 5.29: Schematic figure showing the difference between downstream and upstream pinching. Upstream pinching produces inverted break-up.

(a) 5%

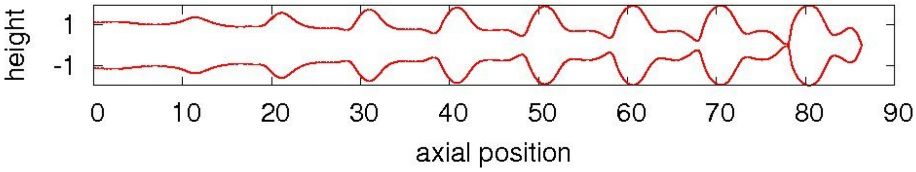

(b) 10%

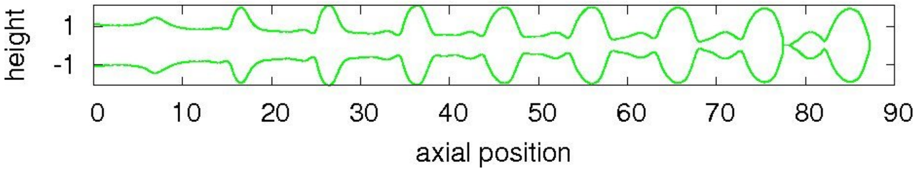

(c) 15%

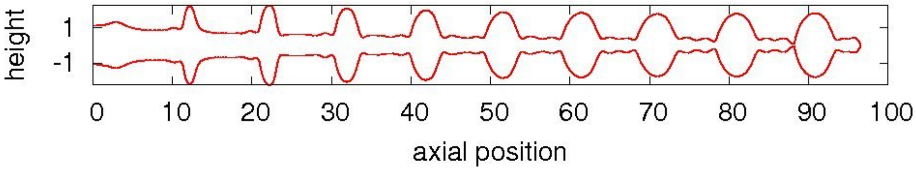

Figure 5.30: Free surface profile predicted by our one-dimensional model. (a) $\epsilon = 0.05$; (b) $\epsilon = 0.1$; (c) $\epsilon = 0.15$. The parameters are $We = 338, Oh = 0.122$ and $\lambda^* = 9$.

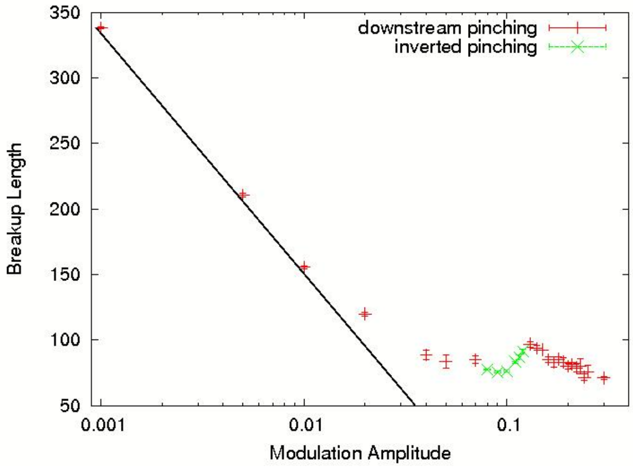

Figure 5.31: The effect of changing amplitude ϵ on the break-up length for $We = 338$, $Oh = 0.122$ and $\lambda^* = 9$. Inverted break-up behaviour is indicated in green.

of Pimbley & Lee [106], we observe that the position of the first pinch-off event is dependent on the modulation amplitude.

Figure 5.30 shows that, for $\epsilon = 0.1$, pinching first occurs upstream, with the back side of the filament detaching from the main drop before the front side. For this inverted case, a complete wavelength of fluid detaches from the jet as a single unit of fluid. Moreover, if this detached unit proceeds to break into a main drop and a satellite drop, then the satellite produced is relatively fast moving due to the positive change in momentum. Thus, the satellite will tend to merge with the leading drop. This inverted break-up behaviour has been observed in both experimental and industrial applications [26],[95], [75], [23] and is considered preferable for eliminating satellites.

In contrast, Figure 5.30 shows that, for $\epsilon = 0.05$ and 0.15, pinching first occurs downstream, with the break position located at the front side of the filament. This type of pinching is less desirable, although the formation of satellites can be managed by rear-merging. Similar break-up behaviour has been observed experimentally and compared to a one-dimensional model by van Hoeve *et al.* [134].

Figure 5.31 shows the effect that increasing the amplitude ϵ of the velocity modulation has on the ultimate break-up length of the jet. The inverted break-up region is indicated in green. For small amplitudes $\epsilon \leq 0.01$, we observe an exponential decay in the break-up length with increasing amplitude, as would be expected for a linear instability. In this region, break-up first occurs downstream, as indicated by the red data. However, when the amplitude exceeds 0.01, non-linear interactions become important and the jet stability deviates from exponential decay. Furthermore, as the amplitude is increased to ~ 0.1, a small increase in break-up length is found; it is in this region, where break-up length increases with amplitude, that we observe inverted pinching. The behaviour then reverts back to downstream pinching and the break-up length decreases with amplitude. The position of the critical window in modulation amplitude for which inverted pinching occurs is sensitive to a number of parameters, as detailed below.

Figure 5.32 shows the position of the critical inversion window for two different wavelengths, the Rayleigh mode $\lambda^* = 9$ and $\lambda = 7$. The Weber number is $We = 338$ and the Ohnesorge number is $Oh = 0.122$. For the Rayleigh mode λ^*, our model predicts that inverted break-up is restricted to the modulation range $0.08 \leq \epsilon \leq 0.12$. However, as found by Pimbley & Lee [106], the transition in behaviour depends on the wavelength of the initial disturbance wave. In particular, Figure 5.32 shows that the critical amplitude at which inversion occurs increases for the shorter wavelength disturbance $\lambda = 7$; inversion is shifted to the larger range $0.12 \leq \epsilon \leq 0.17$.

Furthermore, the critical modulation window for inverted break-up is affected by changing the Weber number and Ohnesorge number, an effect that is not considered by Pimbley & Lee [106]. Figure 5.32 shows that, for a fixed Weber number $We = 338$, increasing viscosity shifts the inverted break-up behaviour to a higher modulation range. This is because viscosity is a resistive force that makes it more difficult to drive the jet forward. Thus,

(a) Changing Wavelength

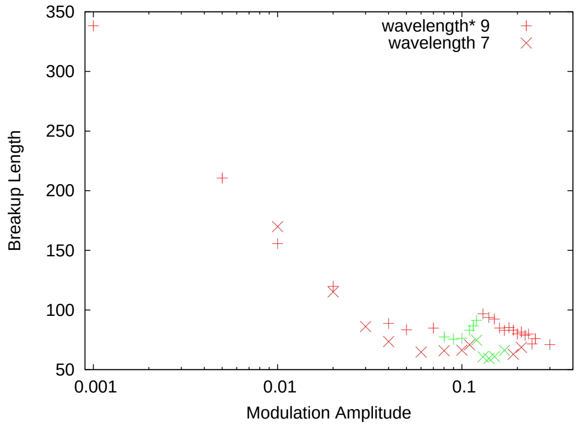

(b) Changing Ohnesorge Number

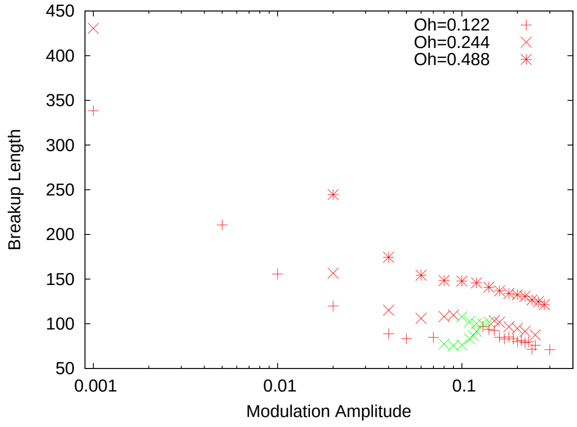

(c) Changing Weber Number

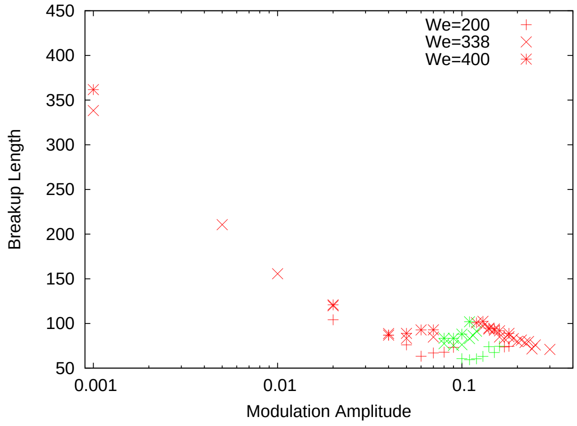

Figure 5.32: Relationship between break-up length and modulation amplitude ϵ for varying physical parameters. (a) The effect of changing wavelength λ with $We = 338$ and $Oh = 0.122$; (b) The effect of changing Ohnesorge number with $We = 338$ and $\lambda^* = 9$; (c) The effect of changing Weber number with $Oh = 0.122$ and $\lambda^* = 9$. Inverted break-up behaviour is indicated in green in all three plots.

a greater velocity is required to achieve the desired break-up behaviour. For sufficiently large viscosity ($Oh = 0.488$), we do not observe inverted behaviour at all. Similarly, Figure 5.32 shows that, for a fixed Ohnesorge number $Oh = 0.122$, increasing the jet inertia make it easier to drive the jet forward and so the inverted break-up regime occurs at a lower velocity modulation. For small Weber numbers ($We = 81$), we do not observe inverted behaviour at all.

5.5.3 A Secondary Instability Wave

As first suggested by Pimbley & Lee [106], large modulations in the driving velocity induce non-linear interactions that generate a secondary instability wave. Indeed, if a component with a shorter wavelength has the chance to grow sufficiently with respect to the fundamental, it will produce an additional growth of surface perturbations across the connecting filament and cause inverted pinching, as suggested in reference [50].

This idea has previously been tested by Eggers [50] within a one-dimensional model. For small amplitudes, the connecting filament region is found to develop symmetrically, causing simultaneous front and back pinching either side of the filament. However, the break-up behaviour remains almost identical for increasing modulation amplitude. Furthermore, the amplitude of the harmonics generated by non-linear interactions are found to remain small, and so do not affect break-up. We suspect that the reason for this is that the viscosity used in Eggers' calculations is large, corresponding to an Ohnesorge number $Oh = 0.396$. In Figure 5.32, inverted pinching is not observed at high Ohnesorge numbers.

To understand this secondary instability wave, we decompose a number of free-surface profiles into their Fourier components. In this way, the jet is divided into a series of simpler functions and we are able to identify whether a second harmonic component is responsible for inverted pinching as previously suggested [106]. Figure 5.33 shows one

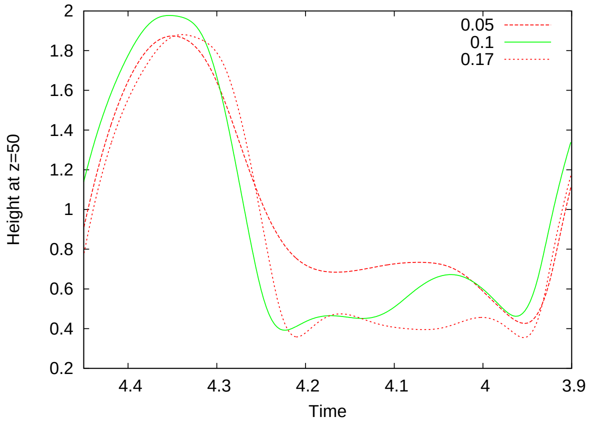

Figure 5.33: One period of the height-time data taken at $z = 50$ for a range of modulation amplitudes $\epsilon = 0.05, 0.1, 0.17$, with $We = 338$, $Oh = 0.122$ and $\lambda^* = 9$.

period of the height-time profile taken at downstream position $z = 50$ for a jet modulated at three different amplitudes ($\epsilon = 0.05, 0.1, 0.15$), with the wavelength set to the Rayleigh mode $\lambda^* = 9$. The fluid parameters are $We = 338$ and $Oh = 0.122$. These amplitudes span the different types of break-up behaviour, as seen from the single-period profiles in Figure 5.33.

The time-dependent height at the point $z = 50$ is fitted to a Fourier series of the form

$$h_{50}(t) = a_0 + \sum_{i=1}^{n} a_i \cos(2\pi i f t) + b_i \sin(2\pi i f t), \tag{5.15}$$

where $f = f^*$ is the Rayleigh frequency. In Figure 5.34 we plot equation (5.15) for $n = 1, 2$ and 3, in the case that $\epsilon = 0.05$. The first harmonic, or the fundamental mode, is the Rayleigh instability and determines the size of the main drops and the inter-drop spacing. The addition of the second harmonic determines the asymmetry between the minima at the front and back of the connecting filament and consequently the pinching behaviour. The third harmonic, when superimposed with the first two harmonics, determines the discrimination between the main drop and the filament.

In order to quantify the magnitude of the secondary harmonic, in Figure 5.35 we plot

$$c_i = \sqrt{a_i^2 + b_i^2}, \quad i = 1, \dots 6,$$

at $z = 50$ for a range of modulation amplitudes. Figure 5.35 shows that the first four Fourier components are the most important, as suggested by the second-order, non-linear analysis of Chaudhary & Redekopp [27]. The fundamental mode, corresponding to the main drops, is clearly the largest and increases as jet modulation is increased. The second harmonic is the second-largest component, although the relative size depends on the modulation amplitude. The third harmonic remains small and the fourth harmonic is also small but grows with increasing amplitude. The Fourier transform

$$F[h_{50}(t)](\omega) = \int_{-\infty}^{\infty} h_{50}(t) e^{-2\pi i t \omega} dt, \tag{5.16}$$

for frequency ω, shown in Figure 5.36, highlights the relative magnitude of the first four Fourier components for the three individual amplitudes $\epsilon = 0.05, 0.1$ and 0.17 that span the break-up behaviour at $z = 50$.

Figure 5.35 shows that, for the region of inverted break-up, $0.08 \leq \epsilon \leq 0.12$, the magnitude of the second harmonic is significantly larger than in the regions of downstream pinching. This change in the second harmonic can also be seen in the Fourier transform shown in Figure 5.36; the second peak is approximately 30% larger for the inverted case $\epsilon = 0.1$, than the downstream pinching cases $\epsilon = 0.05$ and 0.17. This Fourier analysis suggests the existence of a secondary instability wave, which becomes sufficiently large for a limited range of modulation amplitudes corresponding to the region of inverted break-up. The way in which this secondary instability wave interacts with the fundamental solution is key to understanding the break-up behaviour [106], [27].

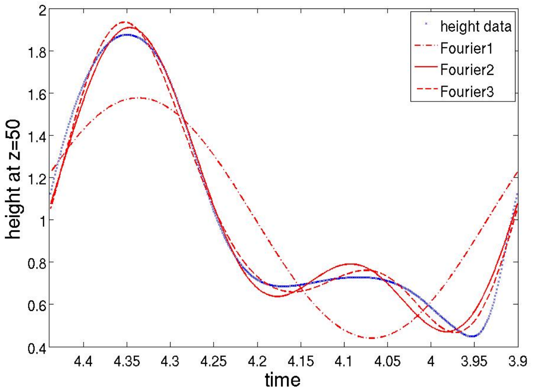

Figure 5.34: Height-time data, h_{50}, for $\epsilon = 0.05$ taken and $z = 50$ alongside reconstruction of the data for one, two and three Fourier modes.

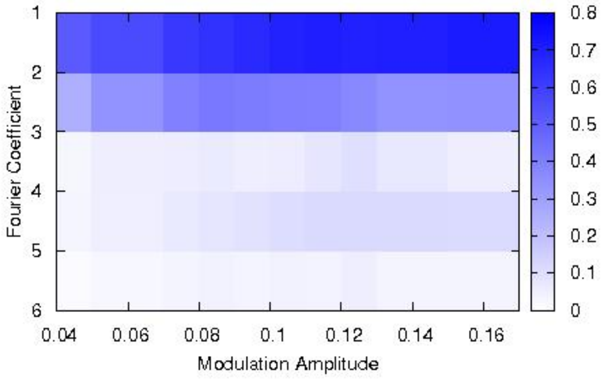

Figure 5.35: Magnitude of Fourier coefficients c_i at $z = 50$ plotted as a function modulation amplitude ϵ.

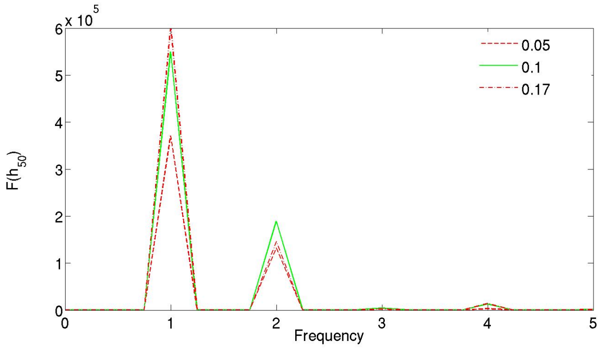

Figure 5.36: Spectrum of frequencies ω identified by the Fourier transform $F(h_{50})$ given by equation (5.16) of the height-time data h_{50} at $z = 50$ for $\epsilon = 0.05, 0.1$ and 0.17. The frequency is normalised so that the fundamental mode occurs at $\omega = 1$.

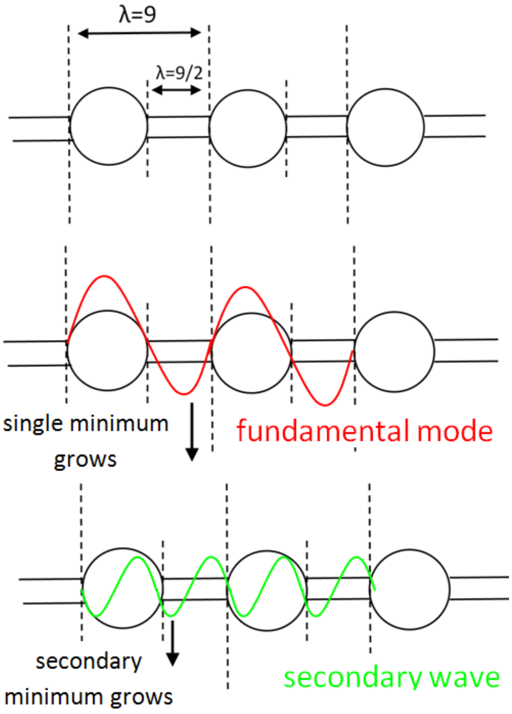

Figure 5.37: Schematic figure showing how a secondary instability grows on the connecting filament generating a second minimum for comparison with the results of our one-dimensional model shown in Figure 5.38.

The fundamental jet consists of a series of main drops connected by filaments. Due to the imposed Rayleigh frequency, the length of the filament is approximately 9/2, as shown by the sketch in Figure 5.37, and does not depend on the amplitude of the disturbance. At small amplitudes, non-linear interactions are small and the fundamental mode dominates. In this case a single minimum in the free-surface height is generated downstream of the connecting filament, as shown in Figure 5.38 for $\epsilon = 0.04$. This single minimum grows undisturbed and eventually causes downstream break-up of the jet.

However, for sufficiently large amplitudes of the driving velocity, the growth of non-linear interactions induce the secondary instability wave. Since this secondary instability wave has twice the Rayleigh frequency, the wavelength is half that of the fundamental mode and so is the same length as the connecting filament, as sketched in Figure 5.37. Hence, for sufficiently large modulation amplitudes, the secondary instability wave is able to grow on the filament region. This secondary instability generates a second minimum in the free-surface height, as shown in Figure 5.38 for $\epsilon = 0.1$. This new minimum is located upstream of the connecting filament and grows faster than the minimum located downstream causing inverted pinching.

As the amplitude is increased further, the filament region becomes ‘frustrated’, a term used by Pimbley & Lee [106] to describe the reduction in growth rate at higher amplitudes. This behaviour is due to the growth of higher-order harmonics, which are stable to the Rayleigh instability, for which $k_i h_f > 1$, where k_i is the wave number of the ith-order

(a) 4%

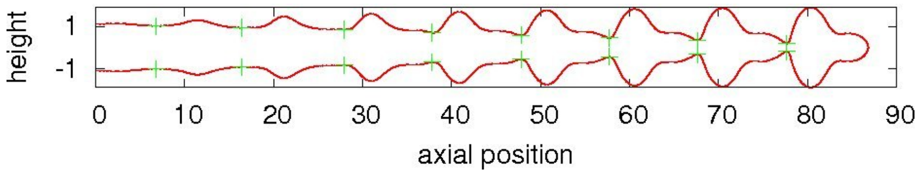

(b) 10%

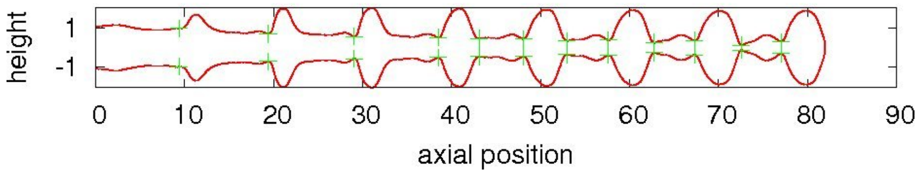

(c) 15%

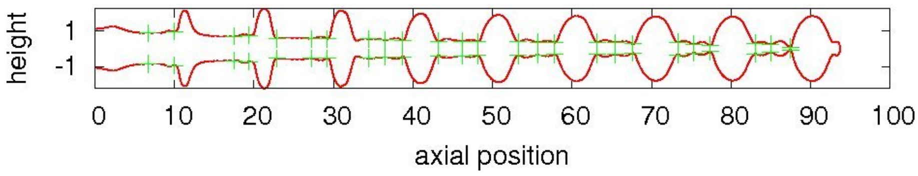

Figure 5.38: Free surface profile predicted by our one-dimensional model. (a) $\epsilon = 0.04$; (b) $\epsilon = 0.1$; (c) $\epsilon = 0.15$. The parameters are $We = 338$, $Oh = 0.122$ and $\lambda^* = 9$. Green points indicate positions of minimum height.

harmonic and h_f is the filament radius. In particular, Figure 5.35 shows how the magnitude of the fourth-order harmonic ($k_4 = 2.8$) increases with modulation amplitude and so is particularly large for $\epsilon = 0.15$. Moreover, at this amplitude, the free surface develops multiple minima, at which point the filament radius is $h_f \approx 0.5$, as shown in Figure 5.38. Thus, the stability criterion $k_4 h_f > 1$ is satisfied. Due to the stability of the higher-order harmonics, break-up reverts back to downstream pinching.

5.5.4 Addition of a Second Harmonic

The addition of harmonics to the initial velocity profile can have a significant effect on the break-up behaviour of a continuous inkjet. In particular, Chaudhary & Redekopp [27] have shown theoretically that the formation of satellites can be controlled by forcing the jet with a suitable harmonic added to the fundamental.

As an example, we examine the effect of adding a secondary harmonic to the velocity profile such that

$$v_{noz}(t) = \sqrt{We}\left(1 + \epsilon \sin(2\pi f_1 t) + \epsilon \sin(2\pi f_2 t + \theta)\right). \tag{5.17}$$

where $f_1 = f^*$ is the Rayleigh frequency and we set $f_2 = 2f_1$. The phase of this second harmonic is given by θ and its amplitude is equal to that of the fundamental ϵ. Eggers

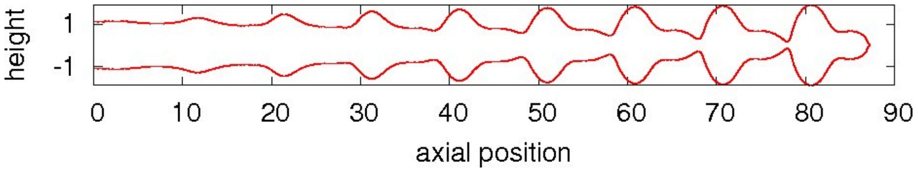
(a) Original Case

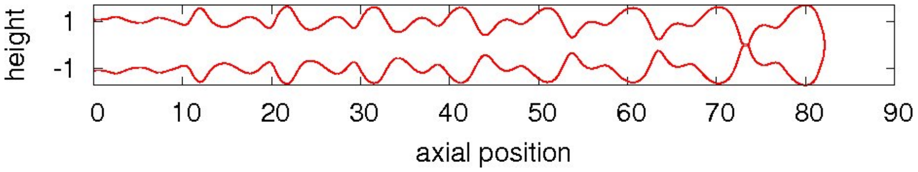
(b) Added Harmonic

Figure 5.39: Free-surface profile predicted by our one-dimensional model. (a) original $\epsilon = 0.04$ case; (b) $\epsilon = 0.4$ case for an added second harmonic component as in equation (5.17) for $\theta = \pi/4$. The parameters are $We = 338$, $Oh = 0.122$, $\lambda^* = 9$.

[50] has previously analysed the effect of adding a second harmonic in his one-dimensional model but he did not find inverted break-up behaviour. In his study, the ratio of the amplitudes of the secondary and the fundamental harmonic is 1/10 and the effect of a phase shift θ is not considered. However, the work of Chaudhary & Redekopp [27] suggests that the magnitude of the two harmonics should be of the same order to affect the break-up behaviour, and that the phase of the various wave components should change with time.

Figure 5.39 shows the effect that the addition of a second harmonic in the form (5.17) has on the free-surface profile predicted by our one-dimensional model for modulation amplitude $\epsilon = 0.04$ and phase shift $\theta = \pi/4$. We observe a distinct change from the

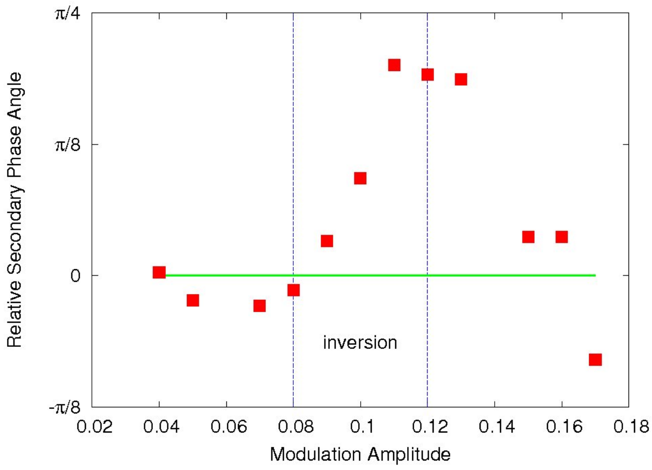

Figure 5.40: Phase angle θ_2 of the second harmonic component relative to the fundamental solution for a range of modulation amplitudes ϵ. The critical modulation window for inversion is indicated by the vertical lines.

usual downstream pinching to inverted break-up behaviour for driving signal (5.17). The addition of a second harmonic to the velocity profile artificially induces a large secondary wave that has half the wavelength of the Rayleigh mode. Since this wave is able to grow on the connecting filament, break-up occurs at the back side of the filament, generating inverted pinching. However, this growth can occur only if the secondary wave has the correct phase θ in relation to the fundamental solution.

In Figure 5.40, we plot the phase angle of the second harmonic component

$$\theta_2 = \tan^{-1}\left(-\frac{b_2}{a_2}\right),$$

for a range of modulation amplitudes, relative to the phase of the fundamental solution, where a_2 and b_2 are the Fourier coefficients in equation (5.15). We see that the relative phase angle of the second harmonic is dependent of the modulation amplitude ϵ. At the lower limit of inversion ($\epsilon = 0.08$), the phase angle becomes positive, increasing with amplitude, but remains in the range $\theta_2 \in (0, \pi/4)$. On the other hand, at the amplitude that the filament becomes frustrated ($\epsilon = 0.12$), the phase angle decreases with amplitude. For our example, we find that imposing a phase shift of $\theta = \pi/4$ or $\pi/8$ generates inverted pinching at $\epsilon = 0.04$; however, phase shifts $\theta = 0$ and $\pi/2$ do not.

5.6 Axisymmetric Simulations with Nozzle Geometry

5.6.1 A Qualitative Comparison

In Figures 5.41 and 5.42, we show a qualitative comparison of the free-surface profile predicted by our one-dimensional model and the full axisymmetric simulation detailed in Chapter 1. A quantitative comparison is given later. The Ohnesorge number and Weber number are $Oh = 0.122$ and $We = 338$, respectively, with $\lambda^* = 9$. The nozzle aspect ratio in the full simulation, defined by

$$\Gamma = \frac{L_{noz}}{R}, \tag{5.18}$$

for nozzle length L_{noz}, is set to $\Gamma = 1$.

The one-dimensional model is in qualitative agreement with the full simulation, with both models demonstrating the two distinct break-up behaviours described in the previous section. However, the free-surface profiles of the full axisymmetric simulation appear to be more elongated than those predicted by the one-dimensional model, particularly near to the nozzle exit.

This effect is due to variations in the velocity over the cross-section generated by flow through a nozzle; the nozzle geometry included in the full simulation generates a Poiseuille flow near to the nozzle exit and the parabolic velocity profile can be seen in Figure 5.43. On the other hand, the one-dimensional model neglects the nozzle dynamics so that the velocity is assumed to have a uniform plug-flow profile.

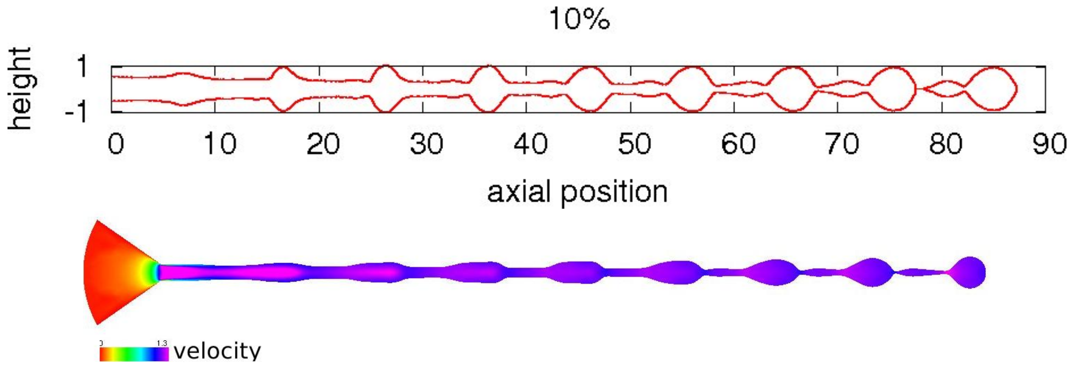

Figure 5.41: *(Top:)* Free-surface profile predicted by the one-dimensional CIJ model; *(Bottom:)* the full axisymmetric simulation with nozzle aspect ratio $\Gamma = 1$. The parameters are $We = 338$, $Oh = 0.122$, $\epsilon = 0.1$ and $\lambda^* = 9$. Colour bar: red-to-pink indicates minimum-to-maximum jet velocity.

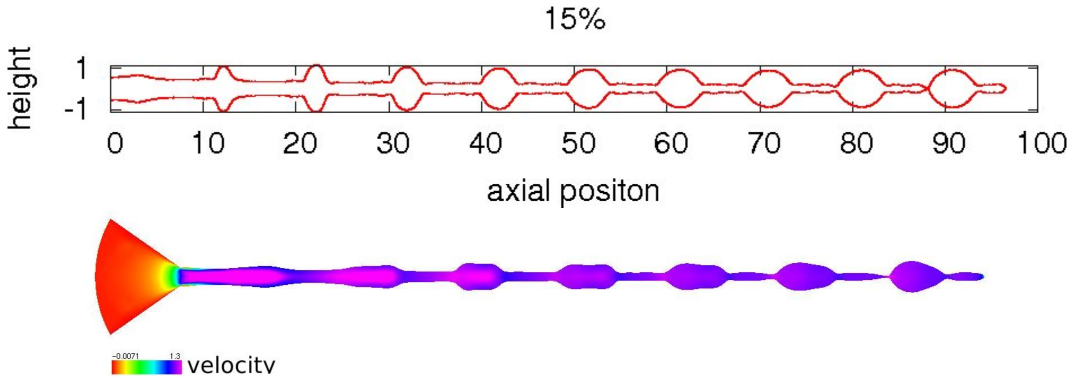

Figure 5.42: *(Top:)* Free-surface profile predicted by the one-dimensional CIJ model; *(Bottom:)* the full axisymmetric simulation for nozzle aspect ratio $\Gamma = 1$. The parameters are $We = 338$, $Oh = 0.122$, $\epsilon = 0.15$ and $\lambda^* = 9$. Colour bar: red-to-pink indicates minimum-to-maximum jet velocity.

5.6.2 The Effect of Poiseuille Flow on Break-up Length

For a sufficient distance downstream of the nozzle exit, the mean flow of the axisymmetric simulation relaxes to a plug-flow profile [22], which is evident in Figure 5.43. However, in the case of a non-uniform velocity profile, the form of the disturbance wave is altered. In fact, the maximum growth rate of a uniform plug-flow profile is found to be four times larger than that of a Poiseuille profile [88].

On the basis of measurements of the centre-line stagnation pressure in jets initially in fully developed laminar flow, Rupe [116] suggests that the jet length required for the velocity profile to relax to a uniform state is comparable with the entry length for laminar flow in a pipe. This has been found to agree well with theoretical results [14], [48] and the relaxation length L_R for which a fully relaxed plug-flow profile is achieved is given by

$$\frac{L_R}{2R} \propto \frac{\sqrt{We}}{Oh},$$

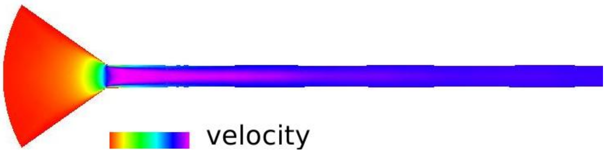

Figure 5.43: Poiseuille flow generated by flow through the nozzle in the axisymmetric simulation for $\epsilon = 0.01$, $Oh = 0.122$, $We = 338$, $\lambda^* = 9$ and nozzle aspect ratio $\Gamma = 1$. Colour bar: red-to-pink indicates minimum-to-maximum jet velocity.

for nozzle radius R, as in Sterling & Slicer [122].

Figure 5.44 compares the break-up length predicted by our one-dimensional model to the full axisymmetric simulation with nozzle aspect ratio 1 for increasing velocity modulation amplitude, ϵ. Again, the average break-up length is calculated over the number of drops produced in the simulation and the standard deviation from the mean is indicated by the error bar. The two models agree for very small perturbations $\epsilon \sim 0.001$, where the length of the jet is extremely long and the initial growth rate is given by linear instability, and for large perturbations $\epsilon > 0.1$, where the break-up length approaches a plateau.

However, for $0.01 < \epsilon < 0.1$, we observe a significant difference between the two models; the axisymmetric simulation predicts a much longer break-up length than our one-dimensional model. We attribute this discrepancy to the effect of unrelaxed Poiseuille flow for this range of modulation amplitudes. In our case, the relaxation length is $L_R = 330$, which is equivalent to the break-up length for the smallest amplitude $\epsilon = 0.001$. However, we find that for amplitudes $\epsilon > 0.001$, the break-up length is shorter than L_R. Thus, once the amplitude exceeds $\epsilon = 0.001$, the stability of the jet is affected by an unrelaxed Poiseuille flow. Hence, for modulation range $0.01 < \epsilon < 0.1$, our one-dimensional model

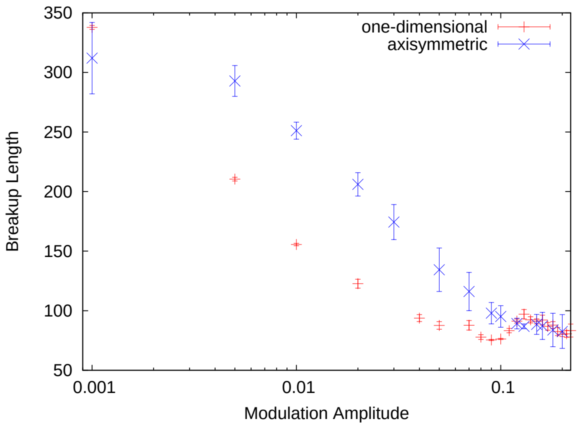

Figure 5.44: Break-up length compared to modulation amplitude ϵ predicted by the one-dimensional CIJ model *(red)* for $We = 338$, $Oh = 0.122$, $\lambda^* = 9$ and full axisymmetric simulations *(blue)* for nozzle aspect ratio $\Gamma = 1$.

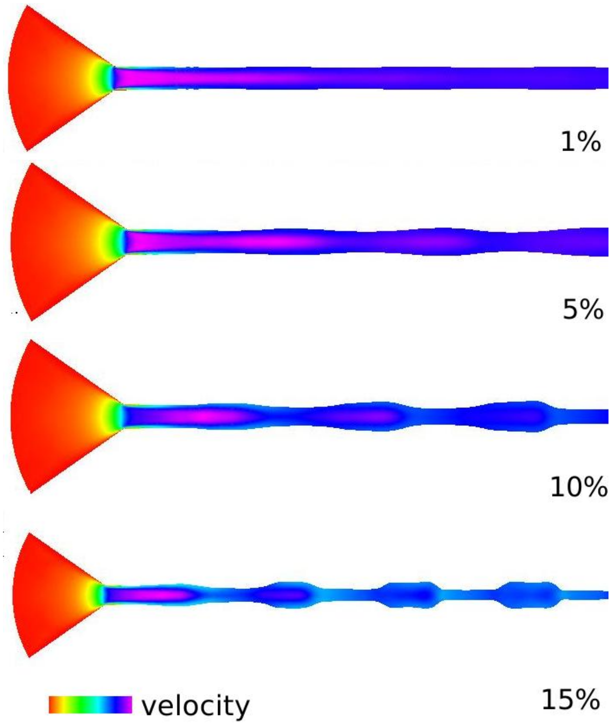

Figure 5.45: Axisymmetric simulations for increasing amplitude $\epsilon = 0.01, 0.05, 0.1$ and 0.15 with $We = 338$, $Oh = 0.122$, $\lambda^* = 9$ and nozzle aspect ratio $\Gamma = 1$. Colour bar: red-to-pink indicates minimum-to-maximum jet velocity.

predicts shorter break-up lengths than the axisymmetric model due to the larger growth rate of the plug-flow velocity profile.

Recall equation (5.14), which shows that the break-up length of a Newtonian jet scales as

$$\frac{L}{R} \propto \sqrt{We}(2\sqrt{2} + 6Oh),$$

due to the Rayleigh instability. From this linear analysis, we can estimate the ratio of L_R/L, as in [122], to be

$$\frac{L_R}{L} \propto \frac{1}{Oh + 3Oh^2}. \tag{5.19}$$

Thus, for large Ohnesorge numbers, the relaxation length is small compared to the break-up length and the effects due to the nozzle flow are small. Conversely, for low viscosity fluids, such as those used in continuous inkjetting, this ratio is small and the non-uniformity of the velocity-profile significantly affects the break-up. It should be noted that this argument assumes that the flow profile is fully developed in the nozzle. However, the nozzle lengths used in CIJ are not long enough for the flow to become fully developed. Furthermore, non-linear interactions due to the size of the initial modulation are not considered in the estimation (5.19).

Figure 5.45 shows how the parabolic velocity profile near to the nozzle is affected by increasing modulation amplitude. For $\epsilon = 0.1$, the bulges in the free surface due to non-linear effects become prominent in the region of the parabolic profile and appear to smooth out the Poiseuille flow; the length of the undisturbed high-velocity region, indicated by

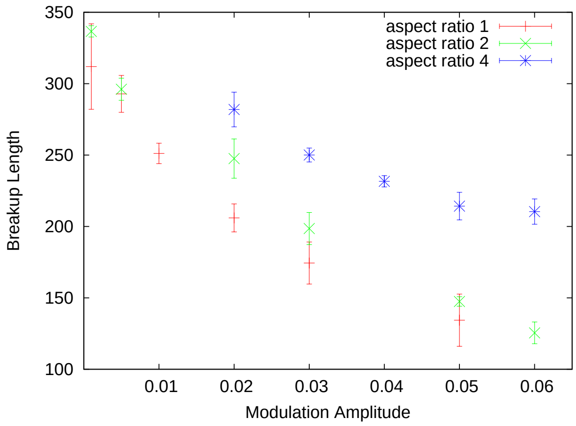

Figure 5.46: Break-up length compared to modulation amplitude ϵ predicted by the axisymmetric CIJ model for $We = 338$, $Oh = 0.122$, $\lambda^* = 9$ with nozzle aspect ratios $\Gamma = 1, 2$ and 4.

the pink shading, is decreased for $\epsilon = 0.1$ compared to the $\epsilon = 0.01$ case. Furthermore, although some variation in first couple of bulges remains, for $\epsilon = 0.1$, the velocity across the filament region is uniform considerably close to the nozzle. Thus, due to the effect of non-linear bulges smoothing the Poiseuille flow in this way, we conclude that nozzle effects do not affect the break-up for amplitudes $\epsilon \geq 0.1$. Hence, the axisymmetric model and the one-dimensional model are in agreement for sufficiently large modulation amplitudes, thereby explaining the results shown in Figure 5.44.

Figure 5.46 shows the effect that changing the nozzle aspect ratio, as given by equation (5.18), has on the break-up length of the jet predicted by the full axisymmetric simulation. By increasing the length of the nozzle, the stabilising effect of the Poiseuille flow is amplified. Thus, as expected, longer nozzle lengths give rise to longer break-up lengths.

5.6.3 Incorporating Nozzle Effects into the One-Dimensional Model

It has previously been recognised and measured that the driving force generated by real industrial nozzles contain high-harmonic components [26]. Such components are produced by non-linearities of the piezoelectric actuator and, due to the non-constant velocity profile being approximately parabolic, depend on the length of the nozzle. This non-linearity translates into non-sinusoidal modulations of the jet. Using the full axisymmetric simulation, we examine this behaviour by conducting a harmonic analysis on the velocity data near to the nozzle and studying the magnitude of the Fourier coefficients.

As used in previous computations, we choose parameters $We = 338$, $Oh = 0.122$, $\lambda^* = 9$ and $\epsilon = 0.1$, and consider a number of nozzle aspect ratios Γ, as defined by equation (5.18). We choose fixed position $z = 20$ downstream of the nozzle exit and, due to the axisymmetry of the simulation, take the average velocity over the cross-sectional

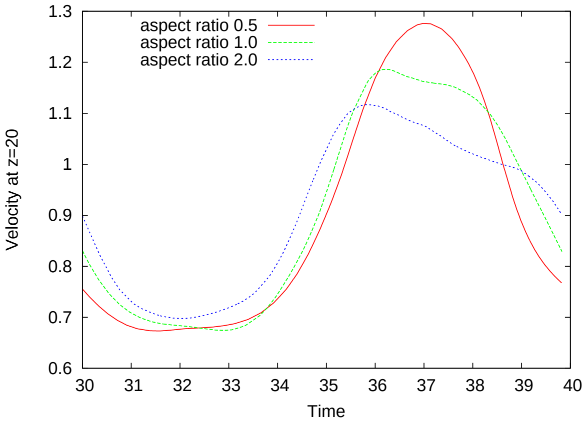

Figure 5.47: Averaged cross-sectional velocity data calculated by the axisymmetric simulation at $z = 20$ for modulation amplitude $\epsilon = 0.1$ with $We = 338$, $Oh = 0.122$ and $\lambda^* = 9$.

area. One cycle of this velocity flux is plotted in Figure 5.47 for nozzle aspect ratios $\Gamma = 0.5, 1$ and 2; the length of the nozzle is varied, whilst the nozzle radius is kept fixed.

We see that the velocity perturbation becomes increasingly non-sinusoidal and lower in amplitude as the aspect ratio increases. To examine the harmonic components of this signal, we fit a Fourier series of the form

$$v_{20}(t) = a_0 + \sum_{i=1}^{3} a_i \cos(2\pi i f t) + b_i \sin(2\pi i f t), \tag{5.20}$$

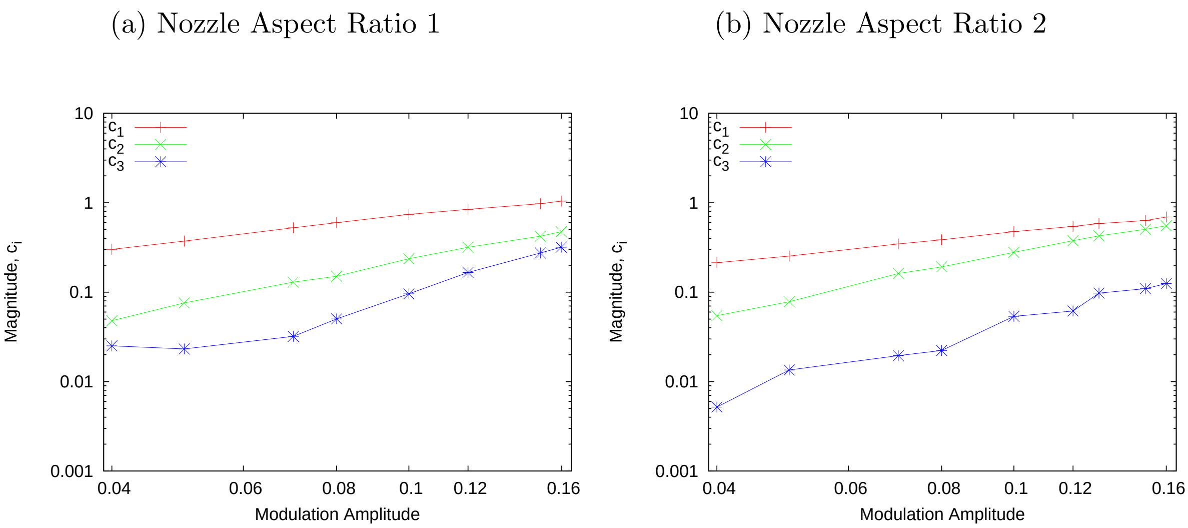
(a) Nozzle Aspect Ratio 1

(b) Nozzle Aspect Ratio 2

Figure 5.48: Magnitude of Fourier coefficients c_i plotted for increasing modulation amplitude ϵ. (a) $\Gamma = 1$; (b) $\Gamma = 2$. The parameters are $We = 338$, $Oh = 0.122$ and $\lambda^* = 9$

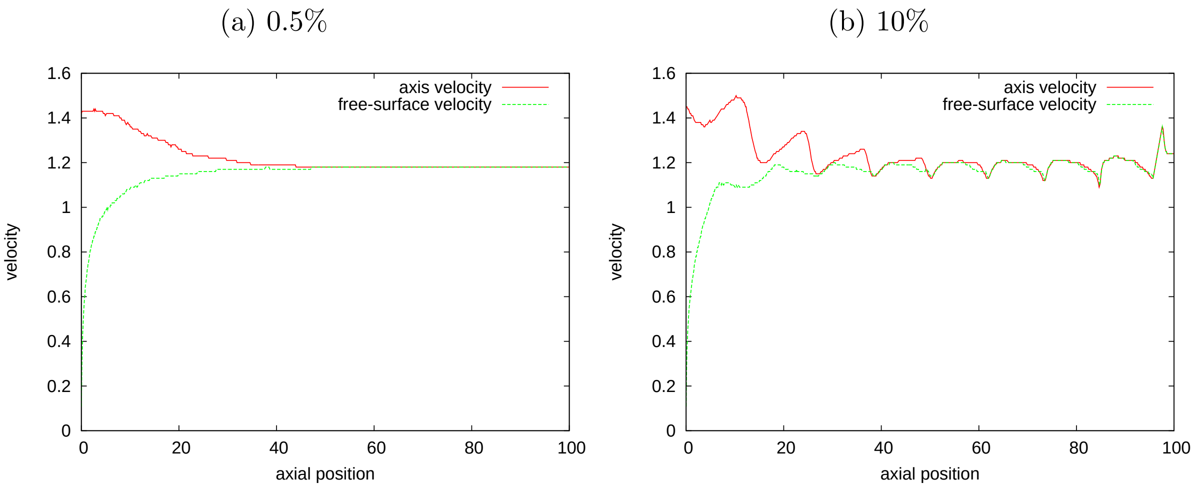

Figure 5.49: Velocity measured from the full axisymmetric model at the axis of symmetry and at the free surface. (a) $\epsilon = 0.005$; (b) $\epsilon = 0.1$. The parameters are $We = 338$, $Oh = 0.122$, $\lambda^* = 9$ and $\Gamma = 2$.

to the velocity flux at $z = 20$. Figure 5.48 shows the magnitude of the Fourier coefficients

$$c_i = \sqrt{a_i^2 + b_i^2}, \quad i = 1, \ldots 3,$$

for a range of modulation amplitudes and nozzle aspect ratios $\Gamma = 1$ and 2. We see that the higher (second and third) harmonic components both increase with amplitude. In contrast, growth of the third harmonic is not observed in the one-dimensional model. We also see that the relative magnitude of the second harmonic compared to the fundamental mode is larger for the longer nozzle length.

Since this full axisymmetric simulation is computationally expensive, it is highly desirable to develop a simpler model that includes these nozzle effects. Thus, we incorporate the initial driving signal created by the axisymmetric simulation into our one-dimensional model. We will call this combined model the one-dimensional splice. As an example, we choose nozzle aspect ratio 2 and the parameters remain the same as previous calculations ($We = 338$, $Oh = 0.122$, $\lambda^* = 9$ and $\epsilon = 0.1$). Since dynamics near to the nozzle are now important, we require a fully resolved mesh upstream, as well as downstream, and so the adaptive scheme is not needed in this case.

To generate the input data, both the radius and cross-section-averaged velocity data are calculated at some fixed point downstream of the nozzle for one time period. We call this point the splice position with notation z_s. The position of the splice is chosen so that the cross-sectional velocity profile is sufficiently relaxed. In Figure 5.49, we plot the axial velocity calculated from the full axisymmetric simulation at the axis of symmetry and at the free surface for modulation amplitudes $\epsilon = 0.005$ and $\epsilon = 0.1$. We see that the velocity along the symmetry axis approaches a constant and eventually equals the velocity at the free surface. This relaxation is seen to occur closer to the nozzle for the smaller-amplitude

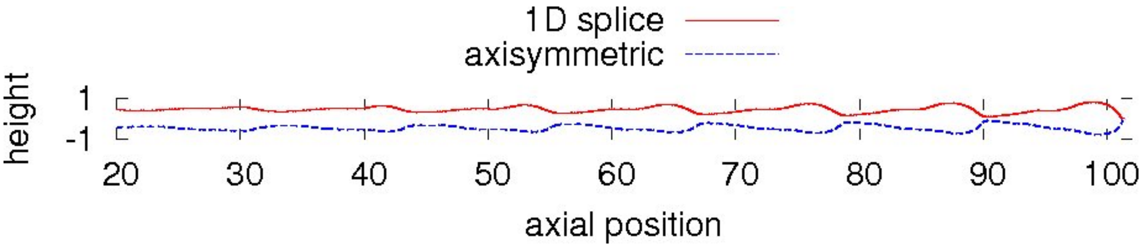

Figure 5.50: Free-surface profile predicted by the one-dimensional splice compared to the full axisymmetric simulation for $\epsilon = 0.1$, $We = 338$, $Oh = 0.122$ and $\lambda^* = 9$. The nozzle aspect ratio is $\Gamma = 2$.

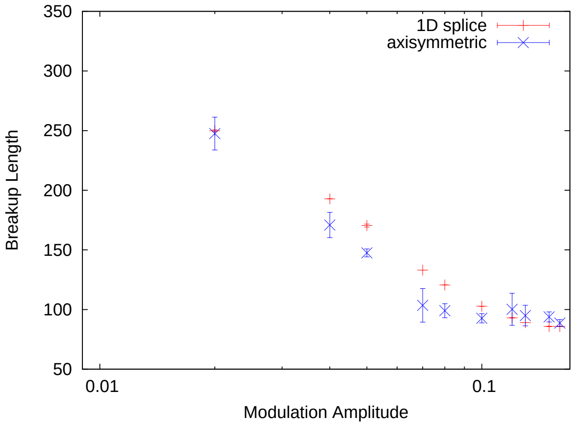

Figure 5.51: Break-up length predicted by the one-dimensional splice compared to the axisymmetric simulations for a range of modulation amplitudes ϵ with $We = 338$, $Oh = 0.122$ and $\lambda^* = 9$. The nozzle aspect ratio is $\Gamma = 2$.

	Hours	Minutes	Seconds
One-Dimensional Splice	**2**	**31**	**20**
axisymmetric input	1	48	55
one-dimensional model	0	42	25
Full Axisymmetric Model	**55**	**08**	**12**

Table 5.4: Computation time taken for the full axisymmetric model compared to the one-dimensional splice model on a Dell workstation with 2.40GHz processor for a fixed simulation time, for parameters used in Figure 5.50.

case; however, as we have seen previously (see Figure 5.45), at $\epsilon = 0.1$ the free surface forms bulges and the velocity of the filament regions relaxes before that of the bulges.

We find that splice position $z_s = 20$ is a suitable choice; at this point the velocity at the axis of symmetric is within 10% of the velocity at the free surface. On the other hand, at $z_s = 10$ the cross-sectional velocity profile is non-uniform and the data does not capture the fully elongated shape of the free surface. Further downstream at $z_s = 30$ gives an equivalent result but for a longer computation time.

The radius and cross-section-averaged velocity at $z_s = 20$ is smoothed by fitting a Fourier series containing three harmonic components, as in equation (5.20). The axisymmetric driving signal is then employed at the nozzle boundary condition of our one-dimensional model such that

$$v_{noz}(t) = a_0 + \sum_{i=1}^{3} a_i \cos(2\pi i f t) + b_i \sin(2\pi i f t),$$
$$h_{noz}(t) = \tilde{a}_0 + \sum_{i=1}^{3} \tilde{a}_i \cos(2\pi i f t) + \tilde{b}_i \sin(2\pi i f t).$$

This creates both a height and velocity perturbation at the inlet of the one-dimensional model that mimic the effects of flow through a nozzle.

Figure 5.50 compares the free-surface profiles predicted by the full axisymmetric simulation and our one-dimensional splice model. We are now able to reproduce, qualitatively and quantitatively, the elongated droplet shape caused by the nozzle geometry in agreement with the axisymmetric simulation. This is in contrast to the differences observed in Figure 5.41. Furthermore, Figure 5.51 shows that the one-dimensional splice is able to predict the longer break-up lengths generated when full nozzle geometry is incorporated. Thus, we are able to mimic the reduced growth rate of the Poiseuille flow caused by flow through the nozzle, which consequently stabilises the jet.

Table 5.4 summarises the computation time used by the one-dimensional splice and the full axisymmetric simulation. For the one-dimensional splice, the computation time is broken down into the time taken to generate the input data via the axisymmetric simulation and the time taken to run the one-dimensional model. Evidently, the computation time is significantly reduced by using this splice model; for the same simulation time, the full axisymmetric simulation is approximately 52 hours longer. Thus, by combining the form of the perturbation at $z_s = 20$ from the full simulation into the boundary condition of our one-dimensional model, we are able to incorporate nozzle effects in a simpler form, for a greatly reduced computation time.

5.7 Concluding Remarks

In this chapter, we have developed a bespoke adaptive numerical procedure for solving the Newtonian slender-jet equations, in order to simulate CIJ printing conditions. By using this adaptive procedure, we have been able to significantly reduce – by comparison with existing regular-mesh methods – the computational resources required to simulate complex CIJ phenomena.

Although Rayleigh's theory asserts that $\lambda^* = 9$ is the fastest growing wavelength, due to large finite-amplitude modulations in the driving velocity profile, we have identified a non-linear regime for which the most unstable jets are generated at frequencies that are larger than the classic Rayleigh mode. In this non-linear regime, our one-dimensional model has exhibited a switch from downstream to upstream (inverted) break-up behaviour, which is considered to be desirable for the elimination of satellite drops. Additionally, we have discovered that this preferable upstream break-up is restricted to a small window in the driving-velocity amplitude. Because of the significant reduction in computational resources offered by our adaptive procedure, we have been able to extend the parameter space considered in previous studies, by which extension we have been able to show that inverted pinching is sensitive to frequency, driving speed and viscosity. Moreover, our Fourier analysis has revealed that this switch from downstream to upstream break-up originates from the growth of a second-harmonic component, which arises due to the increase of non-linear interactions at sufficiently large amplitudes. Consequently, we have demonstrated that the addition of a second-harmonic component to the driving signal can artificially induce inverted pinching, in jets which are modulated at small amplitudes, outside the original window for inversion.

Finally, by comparing our results with those of full axisymmetric simulations, we have been able to explore the effects of nozzle geometry on jet stability. We have been able to incorporate these nozzle effects with demonstrable success (see Figure 5.50), by developing a hybrid 'spliced' model that inputs into our one-dimensional model a driving signal delivered by the full simulation. In this way, the computation time has effectively been reduced (see Table 5.4) from the 55.1 hours required by the axisymmetric simulation to the 2.5 hours taken by our 'spliced' algorithm, which therefore offers a speed-up factor of approximately 22. That is, using less that 5% of the original CPU resources, we have been able to reproduce, both qualitatively and quantitatively, the free-surface profile and break-up length predicted by the full axisymmetric simulation.

Chapter 6

Conclusions and Future Work

6.1 A Concluding Overview

Can inkjet technology revolutionise manufacturing processes as we know them?

Advancing inkjet technology requires understanding the formation of small liquid droplets, particularly from jets containing complex additives. Thus, in the quest to broaden our knowledge of complex inkjets, in this thesis we have discussed the following problems:

- the effect that particles have on established Newtonian break-up regimes;
- the effects of viscoelasticity in DoD jetting, including the maximum polymer concentration that can be jetted at the desired print speed and the possibility of polymer degradation due to flow-induced scission;
- the effects of non-linear driving in Newtonian CIJ printing and the generation of a secondary instability wave that induces 'inverted' break-up.

Using a combination of one-dimensional modelling and full axisymmetric simulations, we have been able to explore these problems and, in some cases, validate our results against experimental data. Here we summarise our findings.

Experimentally, the presence of particles in a Newtonian solvent has previously been observed to accelerate break-up in comparison to the corresponding Newtonian fluid with the same zero-shear-rate viscosity. In order to identify the mechanism for this acceleration, we have developed a one-dimensional model to describe the surface-tension-driven thinning of a liquid bridge, where the viscosity is determined by the local particle density via the well-known Krieger-Dougherty relation. Our model has demonstrated three distinct thinning regimes for particulate suspensions. Initially, we observe continuum dynamics dominate and this Newtonian behaviour is described by Papageorgiou's thinning law for the bulk viscosity. This initial thinning process amplifies fluctuations in the initially uniform particle-density distribution, which are mirrored in the viscosity profile. The development of low-viscosity regions allows the fluid to thin more easily and the thinning therefore enters an accelerated regime, with a thinning rate faster than that of the bulk fluid and the solvent. Eventually, regions develop that contain no particles at all and the thinning enters a solvent regime, which can be described by Papageorgiou's law for the solvent viscosity. We have shown that our model results are in quantitative agreement with experimental data measured using a capillary-thinning rheometer.

On the other hand, the presence of viscoelasticity in a fluid retards the thinning process and polymeric filaments are seen to decay exponentially at an inverse rate that is three times the relaxation time. In DoD printing, although the addition of polymers can be used to eliminate unwanted satellite drops, resistive forces can significantly compromise jetting speed. Three DoD jetting regimes have previously been described, defined by the dominant mechanisms that limit the jet speed; regime 1 is restricted by zero-shear-rate viscosity, regime 2 by viscoelasticity and regime 3 by high-strain-rate extensional viscosity. In order to test these predictions, we have developed a simple jetting model to predict the maximum jettable polymer concentration, such that the desired print speed is achieved, for two polystyrene-solvent systems. For a low-viscosity solvent and slow jetting speed, our model is able to identify the three asymptotic regimes and our results are in quantitative agreement with the experimental data. However, for a high-viscosity solvent and fast jetting speed, we have observed a new behaviour where regime 2 does not fully develop. In this case, we found a significant discrepancy from the experimental data, which we have attributed to three factors. First, the Zimm model under-predicts the relaxation time at concentrations close to ϕ^*. Second, we have identified a pre-stretch mechanism induced by an abrupt contraction in the nozzle geometry. When this effect is included, the model predictions are in better agreement with full axisymmetric simulations and the experimental data. Third, we found that polymers may undergo flow-induced scission due to high strain rates at the nozzle exit.

In CIJ printing, the inks used are predominantly Newtonian and satellite drops are eliminated by exploiting finite-amplitude modulations in the driving velocity profile. However, due to the non-linear nature of the driving profile, complex wave patterns are observed. To explore this non-linear behaviour, we have developed an adaptive mesh technique alongside a one-dimensional model to simulate CIJ jet break-up more computationally efficiently than a full Navier-Stokes simulation. We have found that, for sufficiently large modulations in the velocity profile, jet instability can no longer be described by linear stability analysis and the most unstable jets are generated by driving frequencies that are larger than the Rayleigh mode. Furthermore, different types of break-up behaviour are observed, depending on the driving profile and fluid properties. Our model is able to identify the desired 'inverted' pinching, where break-up occurs upstream of connecting filaments, which prevents satellite drop formation. We have found that the optimum operation window for inverted break-up is restricted to a small range of driving amplitudes and is sensitive to frequency, driving speed and viscosity. A harmonic analysis has revealed that the mechanism for inversion is the growth of a secondary instability wave, and consequently, the addition of a second harmonic component to the driving signal can artificially induce inverted pinching outside the optimum window. We compared our results to full axisymmetric simulations in order to incorporate nozzle effects into the one-dimensional model.

In this thesis, we have made progress in creating a numerical toolbox for simulating complex inkjets under both DoD and CIJ conditions. Pushing the boundaries of print speed and material diversity is key to transforming inkjet into a mainstream process and these simple tools provide a method to test jettability for a wide range of fluid and jetting parameters. The revolution of inkjet technology may be drawing near, however, numerous open questions remain. In this final chapter, we consider some future problems for which our simple models would provide an ideal foundation.

6.2 Future Problem: Star Polymers in DoD Printing

6.2.1 Problem Outline

The behaviour of star polymers in drop-on-demand jetting conditions is considerably different from that of linear chains, even in a dilute non-entangled regime. In particular, de Gans *et al.* [43] investigate the influence of polymer architecture on the jettability of a solution by comparing dilute linear and 6-arm star polymers at comparable concentrations and molecular weights. The jettability of the solution is determined by the behaviour of the ligament produced during the DoD jetting process.

As we know from Chapter 4, for high-molecular-weight polymers, it is the formation of a very long, sustained ligament that significantly limits the jetting speed in DoD printing. However, de Gans *et al.* find that the life-time of the ligament is significantly reduced when the polymer configuration is branched rather than linear. Thus, for an equivalent molecular weight, higher concentrations of star polymers may be jetted at the optimum print speed, compared to the linear case. Hence, if a high-molecular-weight component is required, star polymers may be a valuable additive to inkjet inks. However, there is very little known about branched polymer behaviour during the jetting process.

6.2.2 A Simple Jetting Model[1]

In Chapter 4, we establish the maximum possible concentration that can be jetted at a desired print speed for two linear polystyrene solutions. We use a simple single-mode FENE model, where the parameters are chosen to fit Zimm theory. In this way, the jettable concentration can easily be related to molecular weight. To extend our simple jetting model to explore the effects that a star configuration has on DoD jetting behaviour, we need a description of how the relaxation time and extensibility of a star polymer vary with molecular weight and concentration.

---

[1] Thanks to Laurence Hawke, University of Leeds for helpful discussions deriving this model.

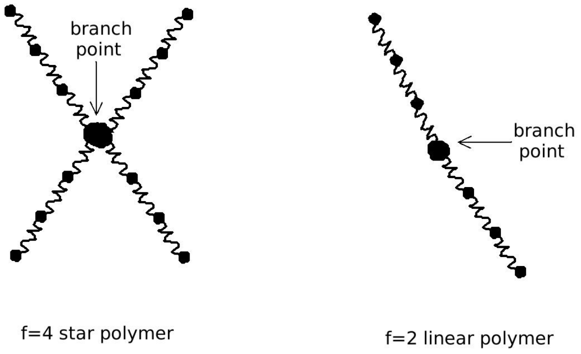

Figure 6.1: Schematic figure showing a $f = 4$ arm star polymer compared to a $f = 2$ arm linear polymer.

For unentangled polymers, the effects of different branching topologies on the rheology can be determined from Rouse theory, in which the polymer is subdivided into sections that are sufficiently long to demonstrate elastic properties [46], as described in Chapter 1. Each section is represented by a spherical bead with friction coefficient ξ and connected by a linear spring with spring constant k_BT/b^2, appropriate for a Gaussian subsection of size b^2.

Rouse Relaxation Time of a Star Polymer

A star polymer consists of a single branch point from which multiple arms stem. We assume that a star has f identical arms stemming from the branch point, with N_a monomers on each, so that the total number of monomers is $N = N_a f$. A schematic of a star polymer with four arms and a linear polymer ($f = 2$) is shown in Figure 6.1. Each arm is similar to a linear chain such that each section of the arm may relax at a different rate. Furthermore, an individual arm may relax at a different rate from other arms. Consequently, the relaxation time of a star polymer is defined by a modal spectrum [7].

Taking an average over all the modes yields the relaxation time of the entire star polymer

$$\tau_R^{\text{star}} \approx \frac{\xi N^2 b^2}{k_B T}\left(\frac{3f-2}{f^2}\right).$$

For $f = 2$, this reduces to the Rouse time for a linear polymer

$$\tau_R^{\text{linear}} \approx \frac{\xi N^2 b^2}{k_B T},$$

derived in Chapter 1. We write the relaxation time in terms of molecular weight by substituting

$$N = \left(\frac{j \sin(\theta/2)^2 M_w}{C_\infty M_u}\right),$$

where M_u is the monomer molecular weight, θ is the carbon-carbon bond angle and j is the number of bonds. Thus, the longest Rouse relaxation time of a star polymer is given by

$$\tau_R^{\text{star}} \approx \frac{\xi b^2}{k_B T}\left(\frac{j\sin(\theta/2)^2 M_w}{C_\infty M_u}\right)^2\left(\frac{3f-2}{f^2}\right).$$

Extensibility of a Star Polymer

The maximum end-to-end length and equilibrium length of a linear polymer are defined to be

$$L_{max}^2 = N^2 b^2 \quad \text{and} \quad R_g^2 = \frac{1}{6}Nb^2,$$

respectively, and so the extensibility is given by the ratio

$$(L^2)^{\text{linear}} = \frac{L_{max}^2}{2R_g^2} = 3N.$$

For a star polymer, on the other hand, the equivalent maximum end-to-end distance is the length of the number of monomers spanning two arms so that

$$L_{max}^2 = (2N_a)^2 b^2,$$

and the radius of gyration is defined to be

$$R_g^2 = CN_a f^{1/2},$$

for some constant C. Thus, the extensibility of a star polymer is given by

$$(L^2)^{\text{star}} = \frac{L_{max}^2}{R_g^2} = 6\sqrt{2}Nf^{-3/2}.$$

where $f = 2$ reduces to the linear case. Thus, in terms of molecular weight, the finite extensibility of a star polymer is given by

$$(L^2)^{\text{star}} = 6\sqrt{2}\left(\frac{j\sin(\theta/2)^2 M_w}{C_\infty M_u}\right)f^{-3/2}.$$

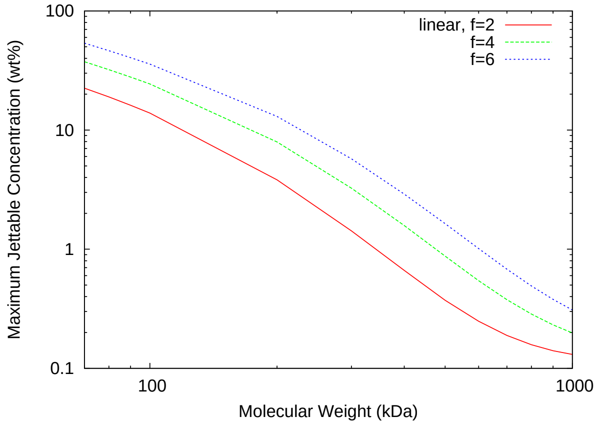

Figure 6.2: Maximum jettable polymer concentration (wt%) against molecular weight M_w for different numbers of arms f in a star polymer. The linear case corresponds to $f = 2$.

In theory, our simple jetting model described in Chapter 4 can be modified to account for the architecture of a star polymer by modifying the relaxation time and extensibility as above to account for number of arms f. Figure 6.2 shows the maximum jettable polymer concentration predicted by our simple model for an increasing number of arms, with parameters equivalent to the polystyrene in ATP case jetted from a micropipette described in Chapter 4. As observed by de Gans *et al.*, we see qualitatively that increasing the number of arms allows more polymer to be ejected at the desired print speed . However, there are a number of limitations to this simple strategy that must be considered further in order to obtain quantitative results.

6.2.3 Further Considerations

First, the Rouse model described above does not account for hydrodynamic interactions or the excluded volume effect included in the Zimm model for dilute solutions. These extra interactions can further restrict the amount of polymer that can be ejected from a nozzle.

Second, in our simple jetting model described in Chapter 4, we use the Mark-Houwink relation for the intrinsic viscosity given by

$$[\mu] = KM_w^a,$$

where K is a constant that depends upon the polymer system and $a = 3\nu - 1$ for a linear polymer in a good solvent. The Mark-Houwink parameters are well described for polystyrene in a number of different solvents [136]. For the case of star polymers, it has been suggested by Zimm & Kilb [146] that, since branched polymers are more dense at any given molecular weight, the intrinsic viscosity will be lowered such that

$$[\mu] = K'M_w^{a-1/4}.$$

where $K' < K$. However, the value of K' for star polymers is not well documented in the literature.

Third, we currently employ a single-mode FENE model, which calculates only the longest Zimm time to describe the relaxation of the polymer. Although it is thought that the behaviour of a star-arm should be equivalent to that of a linear chain, it has been shown experimentally [137] that the relaxation mode distribution is a lot broader for star chains than it is for linear chains. Furthermore, each arm may relax at different rates meaning that the configuration of the molecule will change during the relaxation process. A multiple-mode relaxation model may be required in order to capture these dynamics.

6.3 Future Problem: The Reversal Phenomenon in CIJ

6.3.1 Problem Outline

As we have seen in Chapter 5, the behaviour of even Newtonian fluids during continuous inkjetting is far from simple. Due to the fast jetting speeds and highly modulated velocity

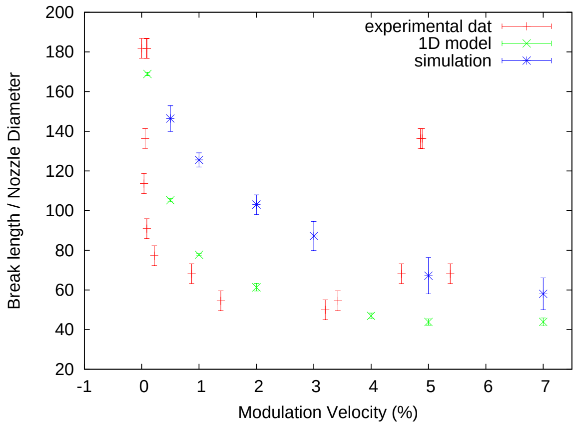

Figure 6.3: Breakup length/nozzle diameter (mm) compared to modulation amplitude ϵ (%) predicted by experiments, the one-dimensional CIJ model and the axisymmetric simulations for $We = 338$, $Oh = 0.122$, $\lambda^* = 9$ and nozzle aspect ratio is $\Gamma = 1$.

profiles, the flow is dominated by non-linearity making it difficult to predict the inverted break-up behaviour we have observed. Moreover, large-scale experiments,[2] exploring the characteristics of CIJ printing, observe a further phenomenon that we are currently unable to explain with either our one-dimensional model or full axisymmetric simulation.

Figure 6.3 compares the normalised break-up length predicted by these experiments to the results of our one-dimensional model and full axisymmetric simulations for increasing velocity-modulation amplitude ϵ. In this case, the Weber number is $We = 338$, the Ohnesorge number is $Oh = 0.122$, the wavelength is $\lambda^* = 9$ and the nozzle aspect ratio is set to $\Gamma = 1$. As we have discussed in Chapter 5, the discrepancy between the one-dimensional model and the axisymmetric simulations is attributed to the Poiseuille flow generated by flow through the nozzle. However, despite including these nozzle effects, the axisymmetric simulations significantly overestimate the break-up length measured experimentally. Furthermore, at $\epsilon \approx 5\%$ the experimental data demonstrates a sharp increase in the break-up length, contrary to the plateau we observe numerically, where the jet length appears to 'reverse' to that of a smaller-amplitude perturbation; we call this phenomenon 'reversal' of the break-up behaviour. This behaviour has also been observed experimentally, but not commented on, by Kalaaji *et al.* [75].

It has been suggested that this behaviour is in fact cyclic and repeats at higher modulations during industrial practice [129], however, repeated reversal has not been observed in the large-scale experiments of Castrejon-Pita. Nevertheless, jet length dependence that repeats cyclically is reminiscent of a Hopf-type bifurcation and limit-cycle stability. To understand this phenomenon, it is necessary to consider further factors, not yet included in the full axisymmetric simulations, that may affect jet stability. The most obvious negation

---

[2] Not yet published. Thanks to Rafa Castrejon-Pita, University of Cambridge.

is the effect of an ambient atmosphere.

6.3.2 Aerodynamic Effects

There are two existing theories that are relevant for describing aerodynamic effects. First, Weber [138] examined the capillary stability of a Newtonian jet ejected into an inviscid atmosphere, so that only the effect of a density gradient is considered. It is found that, for large jet velocities, the aerodynamic interaction between the jet and the surrounding medium leads to an enhanced growth rate of the disturbance wave. This instability at the interface between two horizontal parallel streams of different velocities and densities is usually called the Kelvin-Helmholtz instability. Although large density gradients are a stabilising influence, the flow is always unstable for sufficiently fast jets, as discussed below.

Second, there is the effect of an ambient fluid viscosity. Tomotika [128] examined the stability of a stationary jet surrounded by a second viscous liquid, however, this study did not account for the effect of viscous drag. The viscous drag effect was properly treated by Sterling & Slicer [122], who found that the aerodynamic effects discussed in Weber's analysis are over-estimated by the exclusion of viscosity due to the presence of a protective boundary layer. Their analysis yields a semi-empirical modification to Weber's theory, which is in excellent agreement with experimental results. Nevertheless, the thickness of this boundary layer depends on the jet speed and length, as discussed below.

The Kelvin-Helmholtz Instability

Here we consider the jetting conditions under which a Kelvin-Helmholtz instability is possible. We assume that the Reynolds' number is sufficiently large so that an inviscid analysis is applicable. Thus, Euler's equation for an inviscid fluid with speed $\mathbf{u}$ is given by

$$\rho\left(\frac{\partial \mathbf{u}}{\partial t}+(\mathbf{u}\cdot\nabla)\mathbf{u}\right)=-\nabla p,$$

where ρ is the fluid density and p is pressure. Rather than analyse an axisymmetric jet, we consider a jet confined to the $x-z$ plane, since this is analytically easier and the mechanism is similar.

Let U_1 and ρ_1 be the velocity and density in the upper layer, corresponding to the surrounding air. Similarly, let U_2 and ρ_2 be the velocity and density in the lower layer, corresponding to the jet. A schematic of this planar set-up is shown in Figure 6.4. For small perturbations of the form

$$\tilde{u}(x,z,t)=u'\exp(ik(x-ct)),$$

with wave number k and wave speed c, which may be complex, a linear stability analysis readily yields the dispersion relation

$$c=\frac{\rho_2U_2+\rho_1U_1}{\rho_2+\rho_1}\pm\left(-k\rho_1\rho_2\frac{(U_1-U_2)^2}{\rho_2+\rho_1}+k^2\gamma\right)^{1/2}.$$

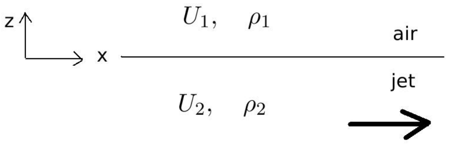

Figure 6.4: Schematic figure illustrating the planar $x - z$ set-up.

For instability, we require $\mathbb{I}m(c) > 0$. Thus, if

$$k\rho_1\rho_2(U_1 - U_2)^2 > k^2\gamma(\rho_2 + \rho_1),$$

then the flow is unstable, with surface tension γ resisting the Kelvin-Helmholtz instability.

Assuming $\rho_2 \gg \rho_1$, we can find the minimum jet speed U_2 required to drive Kelvin-Helmholtz waves at the fluid-air interface. When the surrounding air is at rest, $U_1 = 0$ and for instability we require

$$k\gamma\rho_2 < \rho_1\rho_2U_2^2.$$

Thus, for a jet driven at the Rayleigh wave number $k^* = 2\pi/9R$ and density ratio $\rho = 10^3\rho_g$, we require

$$We > \frac{2\pi}{9}\frac{\rho}{\rho_g} \sim 700,$$

in order to drive the Kelvin-Helmholtz instability, which corresponds to jet speeds much faster than printing speeds. Thus, we conclude that continuous inkjets are not affected by Kelvin-Helmholtz waves.

The Effect of Viscous Drag

Ambient viscosity creates a viscous boundary layer between the liquid jet and the surrounding atmosphere due to the non-slip boundary condition at the liquid-air interface. This exerts a drag force on the jet reducing the jet velocity, but also generates a wake that reduces aerodynamic effects. Here we consider the size of the force corresponding to this viscous drag and the effect of the boundary layer thickness.

The drag equation is given by

$$F_D = \frac{1}{2}\rho_g U^2 C_F R^2,$$

where ρ_g denotes the air density, U is the relative jet velocity and R is the jet radius. The skin friction coefficient C_F is determined by

$$C_F = \frac{\sigma}{\frac{1}{2}\rho_g U^2},$$

where σ is the shear stress. During jetting, the shear stress imparted due to the surrounding air is given by

$$\sigma = 2\mu_g\frac{U}{H},$$

where μ_g is the viscosity of the air and H denotes the thickness of the boundary layer. Thus, the viscous drag force can be written as

$$F_D = 2\mu_g h^2 \frac{U}{H},$$

for free surface height $h(z,t)$ and is clearly small for sufficiently large boundary layers.

The thickness of the boundary layer for some time t can be determined by

$$H = \sqrt{\nu_g t},$$

where ν_g is the dynamic viscosity of the surrounding air. Thus, for time $t = (L - z)/U$, the boundary layer is

$$H = \sqrt{\frac{\mu_g}{\rho_g}\frac{(L-z)}{U}},$$

where L is the break-up length of the jet and z is the axial position measured from the nozzle. Clearly, at the end of the jet $z = L$ there is no boundary layer, whereas upstream the thickness increases due to the shielding effect of the front drop.

However, the boundary layer decreases for shorter jet lengths L, as well as faster jet speeds U. Thus, slow velocities and small-amplitude perturbations that create long jets are more stable to aerodynamic effects due to the protective boundary layer. In contrast, modulated high-Weber number jets, such as those found in CIJ, are more susceptible to the destabilising influence of aerodynamics.

6.3.3 Further Considerations

As discussed earlier, the predictions of break-up length arising from Weber's original theory fail to agree with experimental data, for example see Fenn & Middleman [56]. The discrepancy between Weber's theory and experiments is not only a result of the ambient viscosity, but is also due to the interaction of a Poiseuille flow induced by long nozzle length [122]. This poses the question:

> Does the reversal phenomenon result from an interaction between aerodynamics and the Poiseuille flow generated by the nozzle geometry?

As we have seen in Chapter 5, there exists a critical relaxation length L_R beyond which the nozzle geometry does not affect jet stability. Also, we have seen that increasing the modulation amplitude decreases break-up length, so that the jet length becomes less than the relaxation length; when $L < L_R$, the effects of Poiseuille flow are considered important. However, we find that the scaling law

$$\frac{L_R}{2R} = \frac{\sqrt{We}}{Oh},$$

overpredicts the relaxation length of the velocity profile in our axisymmetric simulations (see Figure 5.41 where $L_R = 330$) because the nozzle length is too short for Poiseuille flow to fully develop. Since this length is shorter than L_R, we shall denote it be z^*.

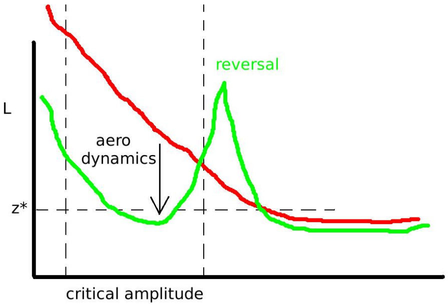

Figure 6.5: Schematic figure to show how aerodynamic effects may be required to generate $L = z^*$ within the range of critical amplitudes where a non-uniform velocity profile is important.

Nonetheless, decreasing jet length by increasing the driving amplitude causes break-up to occur closer to the nozzle, so that, if $L = z^*$, then break-up will occur in the region where the velocity profile has not yet relaxed. This behaviour could cause a reversal in the jet length due to the increased stability caused by a non-uniform velocity profile.

Yet, we must note that z^* is dependent on the modulation amplitude. In particular, for large amplitudes, we observe that the velocity profile is smoothed out by variations in the height profile caused by non-linear bulging (see Figure 5.45). Thus, there exists only a small range of modulation amplitudes for which the relaxation length z^* can affect the jet stability. Hence, reversal can only occur if $L = z^*$ within the critical modulation range where a non-uniform velocity profile affects the dynamics. In order to achieve this critical jet length, within the critical modulation range, we propose that the destabilising effect of aerodynamics is required. Figure 6.5 schematically illustrates this idea.

For example, consider Figure 6.3 and suppose that $z^* = 40$. From the experimental data we have $L = z^*$ at $\epsilon = 5\%$ and reversal is observed. At this modulation amplitude, the parabolic velocity profile is not restricted by the non-linear bulging instability (see Figure 5.45). In contrast, the axisymmetric simulation predicts $L = z^*$ at a much larger amplitude, $\epsilon = 12\%$, where we have observed smoothed velocity profiles (see Figure 5.45). Thus, $L = z^*$ does not occur within the critical modulation range where a non-uniform velocity affects the dynamics. We attribute the difference between the axisymmetric simulation and experimental data to the destabilising effect of aerodynamics, which is not incorporated in the simulation.

To summarise, we propose that aerodynamic effects are required to produce the critical jet length $L = z^*$ within the critical modulation range where a non-uniform velocity profile is important. In the future, we hope to add both nozzle effects and aerodynamics to our one-dimensional model in order to explain this reversal phenomenon. Experimentally, it would be interesting to study break-up lengths of jets ejected into a vacuum.

6.4 Future Problem: Using Jets as Rheometers

6.4.1 Problem Outline

Filament-stretching rheometers have proved unsuccessful in predicting inkjet printing behaviour [70], because they are unable to access the high extension rates found in inkjet printing. Thus, inkjet fluid assessment methods need to provide a full characterisation including both linear and non-linear properties at the high frequencies and shear rates found in inkjet printing. A possible way to achieve this is to use either a DoD jet or a CIJ jet as a rheometrical device.

Since a thin filament is produced via both techniques, in principle the relaxation time τ can be extracted from the minimum-filament-thinning data via the well-known exponential law

$$h_{min}(t) \sim \exp\left(-\frac{t}{3\tau}\right)$$

However, recent experiments[3] have suggested that this thinning law is not achieved under Rayleigh jetting conditions. Figure 6.6 shows that there is a significant difference from the 3τ-decay rate measured in a capillary-thinning rheometer (CaBER) compared to the decay rate measured in a free jet without a forced disturbance. Instead of thinning with a characteristic time of 3τ, the decay rate appears to follow a 2τ time scale.

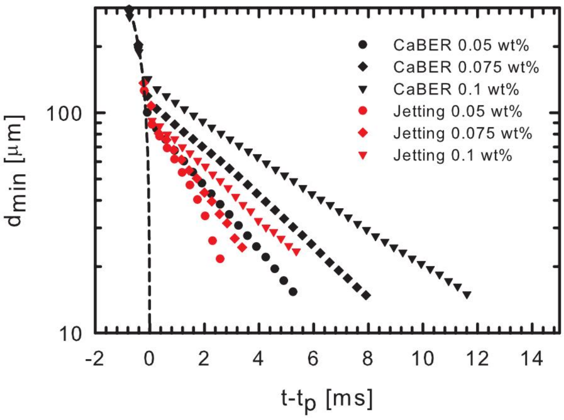

Figure 6.6: Comparing the thinning data of a range of PEO solution measured in a capillary-thinning rheometer (CaBER) and a free jet.

A viscoelastic filament will thin with a 2τ-thinning rate if the force on the filament is a constant. The viscoelastic force F is given by the stress across the cross-sectional area such that

$$F = \pi h^2(\sigma_{zz} - \sigma_{rr}).$$

For the Oldroyd-B model, the axial stress is given by $\sigma_{zz} = G(A_{zz} - 1)$, for elastic modulus G, and the axial conformation satisfies

$$\frac{dA_{zz}}{dt} = 2\dot{\epsilon}A_{zz} - \frac{1}{\tau}(A_{zz} - 1),$$

---

[3] Not yet published. Thanks to Christian Clasen and Wouter Matteus, University of Leuven.

for strain rate $\dot{\epsilon} = -\frac{2}{h}\frac{dh}{dt}$. Thus assuming $A_{zz} \gg 1$, integrating gives

$$A_{zz} = \left(\frac{h_0}{h}\right)^4 \exp\left(-\frac{t}{\tau}\right),$$

for some constant h_0 and, for $\sigma_{rr} \ll 1$, the force across the filament is

$$F \sim \frac{1}{h^2} \exp\left(-\frac{t}{\tau}\right).$$

Hence, if $h \sim \exp(-t/3\tau)$, then the force decays exponentially. But, if $h \sim \exp(-t/2\tau)$, then the force is constant. We have conducted some preliminary simulations using both our one-dimensional model and the full axisymmetric model to test if such a scenario can arise.

6.4.2 Preliminary Simulations

We have simulated both the capillary-thinning technique and the infinite-jet case using our one-dimensional viscoelastic model developed in Chapter 3 and compared our results with full axisymmetric simulations for the Oldroyd-B constitutive model. The non-dimensional fluid parameters are: Ohnesorge number $Oh = 0.15$, Deborah number $De = 4.94$ and concentration $c = 0.5$. For capillary-thinning conditions, the one-dimensional model and axisymmetric simulation are in agreement, with both models demonstrating the 3τ-thinning law, as expected.

For the infinite-jet case, we have tested a range of wavelengths λ, including the Rayleigh wavelength $\lambda^* = 9$ that is achieved during the free-jet experiments. Our one-dimensional model demonstrates 3τ-thinning for all wavelengths, including λ^*, suggesting that the elasto-capillary balance is always established. The axisymmetric simulations are in agreement with the one-dimensional approximation for small wavelengths $\lambda < \lambda^*$, as we have seen in Chapter 3. However, we do observe differences for the longer-wavelength cases.

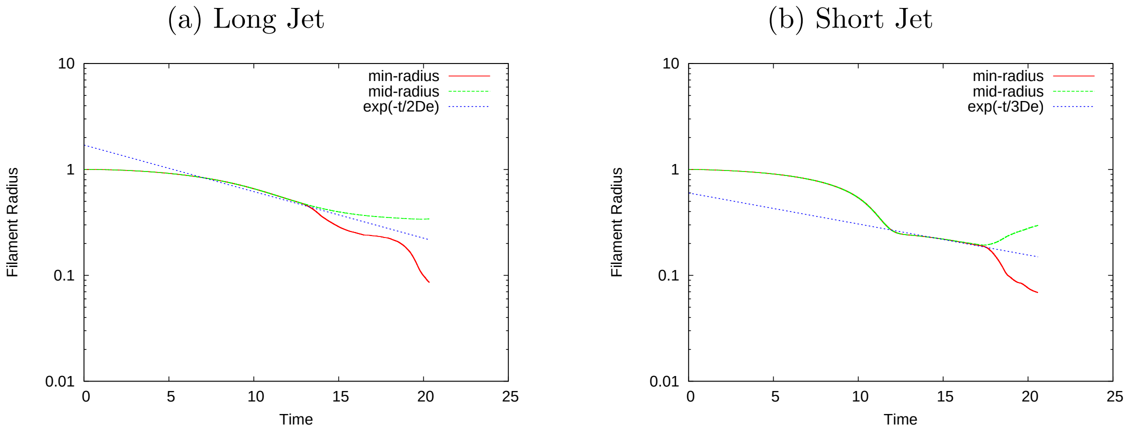

Figure 6.7: Axisymmetric infinite-jet results for (a) $\lambda = 15$; (b) $\lambda = 7.5$. The fluid parameters are $Oh = 0.15$, $De = 4.94$ and $c = 0.5$.

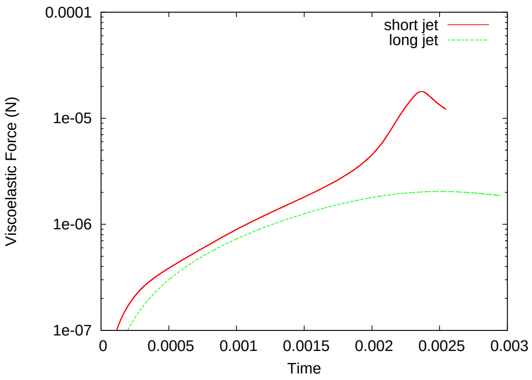

Figure 6.8: Viscoelastic force predicted by the axisymmetric infinite jet for a short ($\lambda = 7.5$) and long ($\lambda = 15$) wavelength for fluid parameters $Oh = 0.15$, $De = 4.94$ and $c = 0.5$.

For $\lambda \geq \lambda^*$, including the Rayleigh wavelength λ^*, the axisymmetric simulation demonstrates a necking instability, where the jet pinches in near to the end drops, before a fully developed exponential thinning regime can be achieved. Figure 6.7 shows how this necking instability is characterised by a divergence in the mid and minimum filament radii. Although 2τ-thinning can be fitted in the region of this necking instability, the rate is found to increase with wavelength and is not equal to 2τ at λ^*, as observed in the free-jet experiments. This behaviour is in contrast to the short-wavelength case, also shown in Figure 6.7, which shows fully developed 3τ-thinning, before the onset of necking.

It is notable that the the free-surface profiles for small wavelengths $\lambda < \lambda^*$ are found to be self-similar, as predicted by the elasto-capillary balance, whereas the profiles are not self-similar for the long-wavelength cases. Furthermore, the viscoelastic force on the

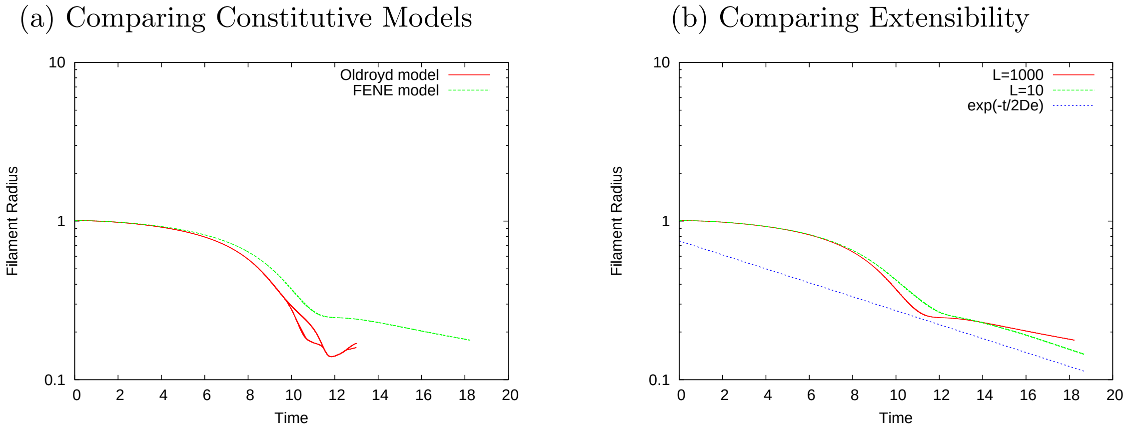
(a) Comparing Constitutive Models
(b) Comparing Extensibility

Figure 6.9: (a) Axisymmetric infinite-jet results for the Oldroyd and FENE ($L = 1000$) constitutive models; (b) the FENE model with extensibility $L = 1000$ and $L = 10$. The fluid parameters $Oh = 0.15$, $De = 4.94$ and $c = 0.5$ and the wavelength is $\lambda = \lambda^*$.

filament is found to depend on the jet wavelength. For example, Figure 6.8 shows the viscoelastic force measured for short wavelength $\lambda = 7.5$ and long wavelength $\lambda = 15$. In the short case, we observe a sharp increase in the force when the elasto-capillary balance is established. On the other hand, we do not observe a significant growth in the force for the long-wavelength case. However, it does not appear to be constant, as suggested by the theoretical analysis.

At the Rayleigh wavelength $\lambda = \lambda^*$, we find that the necking instability can be eliminated by choosing the FENE constitutive model, which incorporates finite extensibility L of the polymer. Somewhat surprisingly, Figure 6.9 demonstrates how the FENE solution for $L = 1000$ does not neck and the exponential thinning regime becomes fully developed, in contrast with the Oldroyd-B solution. However, the 2τ time scale seen in the free-jet experiments is only observed for polymers with small extension length $L = 10$, as shown in Figure 6.9. This result does not agree with the experimental data, where the extensibility is significantly larger ($L = 114$).

The thinning dynamics observed in these preliminary simulations are clearly complex and are sensitive to a number of parameters including wavelength, finite extensibility and the addition of multiple modes. Further work is required to identify the parameter range for which 2τ-thinning is observed.

6.4.3 Further Considerations

The effects of nozzle geometry should also be considered. Indeed, in Chapter 5 we have seen that the interaction of Poiseuille flow can influence the break-up length of a simple Newtonian jet. Furthermore, we have also established that the deformation rates produced at the nozzle in DoD jetting can deform polymers prior to ejection. However, the effect of pre-stretch on the exponential thinning regime is not well understood [4]. In order to explore the possibility of pre-stretch in continuous inkjetting, as well as the effects that this mechanism has on the thinning dynamics, the hybrid model discussed in Chapter 5, with the addition of viscoelasticity, would be ideal.

6.5 Future Problem: Printing Biological Materials

Extending the range of fluids containing functional materials, which can be jetted using inkjet technology, is one key aspect for transforming inkjet into a mainstream process. Here we briefly discuss the printability of cellular material and high-molecular-weight polymers.

Bioprinting is an aspiring technology with the goal of building tissues in the laboratory; one ultimate application is implantable organs, such as the heart or liver. As well as cellular material having highly non-Newtonian properties that affect jetting, one important issue is what happens to cells as they pass through the inkjet nozzle. As we have seen, high strain rates at the nozzle exit are able to pre-stretch and fracture simple polystyrene molecules. Thus, cell damage due to shear and extension during the drop ejection process is a concern for the inkjet printing of cellular material. Consequently, the development of simple models to assess critical strain rates for cell rupture compared to inkjet conditions would be beneficial.

Often biological materials, in particular proteins, contain high-molecular-weight polymers. In Chapter 4 we discuss the printability of long-chain polystyrene and find that the maximum jettable concentration is dramatically restricted by the effects of viscoelasticity. Hence, a method for eliminating the transition between jetting regimes 1 and 2 is highly desirable for a number of biological applications. It has recently been observed that this effect can be achieved by encasing a polymer molecule within an emulsion drop [37]. Strain rates produced by DoD jetting are not sufficient to distort an emulsion drop, thus the encased polymers remain coiled in their equilibrium state. As a result, the jetting problems associated with non-linear rheology can be eradicated by the extension of jetting regime 1. Consequently, it is possible to jet higher concentrations of high-molecular-weight polymer than predicted by both viscoelasticity and finite extensibility.

6.6 Inkjet Status for Digital Fabrication

Inkjet technology has key advantages for digital fabrication, including being flexible and non-contact. A review of current technology and emerging trends can be found in Hutchings & Martin [74]. The ongoing direction in inkjet graphics printing is to focus on achieving high resolution and high reliability, both of which are desirable attributes to the digital fabrication industry. However, in summary, there are three major improvements required to transform inkjet into a mainstream process:

- Range of fluids. Although such flexibility is not required in graphics printing, there will be a greater market uptake for digital fabrication when inkjet is capable of handling a wider variety of fluids.
- Drop Size. A further breakthrough will occur when smaller drop sizes are possible, particularly in the manufacture of conductive tracks.
- Cost. Although the costs of inkjet may be small compared to an overall production system, the technology needs to become more accessible.

Most importantly, digital fabrication industries require technology specifically designed for the manufacturing processes, so that the focus can be on the application of inkjet rather than the development of existing systems.

Appendix: Elastic Effects in Non-Axisymmetric Flow Down a Fibre

A.1 Problem Outline[4]

Coatings are frequently required to provide functional, protective or decorative surfaces, and many fibre-coating processes demand coatings that exhibit viscoelastic properties, e.g. in the industrially widespread polymer coating of both power cables and fibre-optic communication cables. Being able to control the thickness and uniformity of thin-film coatings is important, as variations can affect properties, and therefore performance, of the final product. Hence, effective coating requires an understanding of how non-Newtonian properties affect the structure of the flow, the appearance of instabilities and the morphology of forming patterns.

The Rayleigh-Plateau instability describes the surface-tension-driven thinning and break-up of a liquid cylinder into droplets. For a liquid film coating a fibre, this break-up mechanism is restricted: rather than break up, the liquid film forms bulges along the fibre. In the case of vertical geometry, gravity causes these bulges to propagate downwards and for Newtonian fluids, the dynamics of these bulges is well-modelled [76].

Polymeric additives have a profound effect on surface-tension driven instabilities. Since the fibre-coating flow is dominated by shear, it is a combination of shear thinning and normal stresses present that affect the flow dynamics and therefore the free-surface evolution of viscoelastic coatings. In particular, in the absence of normal stresses, the front profile of the falling bulges is notably steeper [16]. In this chapter, we are interested in axially unsymmetric conformations observed experimentally by Boulogne *et al.* [17], where non-symmetrical drops form on one side of the fibre. We propose that this instability is driven by the existence of a second normal stress difference.

Instabilities driven by second normal stresses have been previously studied. In par-

---

[4] Research undertaken during the David Crighton Fellowship 2014, University of Cambridge under the supervision of Prof. John Hinch

ticular, Hinch *et al.* [69] describe the instability mechanism for two elastic liquids being co-extruded and find that, although the second normal stress difference is usually small, it may drive a stronger non-axisymmetric instability than the first normal stress difference. Details of the mechanism depend on the specific flow and the nature of the complex fluid and have been demonstrated for Couette flow [19], [112], [58], shear-banded micro-channel flow [98] and falling film flows [19].

In this chapter, we consider the flow of a thin viscoelastic film coating a vertical fibre. A linear stability analysis shows that, for materials possessing a second normal stress, there exists an azimuthal mode that is unconditionally unstable to small perturbations in the vorticity direction. In other words, a viscoelastic coating is unstable if it is aligned non-concentrically with the fibre. This instability drives the fluid to flow around the fibre, so that the coating shifts sideways about the fibre. Consequently, the coating becomes much thicker on one side than the other. This shifting mechanism can be described analytically by decomposing the solution into a series of harmonics and initially describes the numerical solution. However, as the thickness tends to zero on the the thinly-coated side, we propose that a draining mechanism prevails, causing a deceleration of the initial shifting instability.

A.2 Newtonian Flow Down a Fibre

Consider a solid vertical fibre of radius R coated by a thin film of viscous liquid of thickness $h(\theta, z, t)$ such that $h \ll R$ and variations in both the z and θ directions are small. Note that we assume the positive z-direction is 'up'. Thus, under a thin-film approximation, the radial coordinate is written as $r = R + y$ for small parameter y such that $0 \leq y \leq h$. Consequently, for fluid velocity $\mathbf{u} = (u_r, u_\theta, u_z)$ and gravity $\mathbf{g} = (0, 0, -g)$ conservation of mass reduces to

$$\frac{\partial u_r}{\partial y} + \frac{1}{R}\frac{\partial u_\theta}{\partial \theta} + \frac{\partial u_z}{\partial z} = 0, \tag{A.1}$$

and for $u_r \ll 1$, Stokes' equations for viscous flow yield

$$\begin{aligned} \frac{\partial p}{\partial y} &= 0, \\ \frac{1}{R}\frac{\partial p}{\partial \theta} &= \mu\frac{\partial^2 u_\theta}{\partial y^2}, \\ \frac{\partial p}{\partial z} &= \mu\frac{\partial^2 u_z}{\partial y^2} - \rho g, \end{aligned} \tag{A.2}$$

for density ρ and dynamic viscosity μ. In this way the pressure p is assumed to be constant across the film thickness and is equal to the Laplace pressure

$$p = \chi\left(\frac{1}{R} - \frac{h + h_{\theta\theta}}{R^2} - h_{zz}\right),$$

for surface tension χ. Assuming no-slip on the fibre and zero stress at the free surface, integrating (A.2) with respect to y finds velocities

$$\begin{aligned} u_\theta &= -\frac{1}{2\mu R} y(2h-y)\frac{\partial p}{\partial \theta}. \\ u_z &= -\frac{1}{2\mu} y(2h-y)\left(\frac{\partial p}{\partial z} + \rho g\right). \end{aligned} \tag{A.3}$$

Finally, integrating conservation of mass (A.1) between $y = 0$ and $y = h$ gives the evolution equation for the film height

$$\frac{\partial h}{\partial t} = \frac{2}{3\mu}\left[\frac{1}{R^2}\frac{\partial}{\partial \theta}\left(h^3 \frac{\partial p}{\partial \theta}\right) + \frac{\partial}{\partial z}\left(h^3\left(\frac{\partial p}{\partial z} + \rho g\right)\right)\right]. \tag{A.4}$$

Consider perturbing the initial film thickness h_0 such that $h = h_0 + \tilde{h}(\theta, z, t)$, where the perturbation takes the form

$$\tilde{h} = \epsilon \exp(i(kz + m\theta) + \alpha t).$$

The amplitude of the perturbation is denoted ϵ, k is the longitudinal wavelength and m is the azimuthal mode. The growth rate of the disturbance wave is denoted α. Hence, substituting the perturbed state into equation (A.4) and linearising yields the dispersion relation

$$\alpha = 2i\frac{gh_0^2}{\mu}k + \frac{2\chi h_0^3}{3\mu}\left(\frac{m^2}{R^4} + \frac{k^2}{R^2} - \frac{m^4}{R^4} - \frac{2m^2k^2}{R^2} - k^4\right).$$

The imaginary part of α corresponds to the downward propagation of the wave due to gravity. For axisymmetric disturbances, $m = 0$, we have

$$\mathbb{R}\mathrm{e}(\alpha) = \frac{2\chi h_0^3}{3\mu}\frac{k^2}{R^2}(1 - k^2R^2). \tag{A.5}$$

Thus, we recover the surface-tension driven instability, first proposed by Rayleigh [110], where growth of the disturbance wave requires long wave lengths such that $kR < 1$.

We are interested in the $m = 1$ mode, which corresponds to perturbing the coating so that it remains cylindrical in shape, but is aligned non-concentrically with the fibre. In this case, we have

$$\mathbb{R}\mathrm{e}(\alpha) = -\frac{2\chi h_0^3}{3\mu}\frac{k^2}{R^2}(1 + k^2R^2) < 0, \tag{A.6}$$

indicating a decaying disturbance and thus stability for all wavelengths. However, if the fluid is uniform in the z-direction so that $k = 0$, then $\mathbb{R}\mathrm{e}(\alpha) = 0$ and the disturbance does not decay. Since there is no contribution to the curvature for this 'shifted' deformation, the cylindrical coating remains in its perturbed state, aligned non-concentrically with the fibre.

A.3 A Second-Order Fluid

For a second-order fluid, the flow is considered to be split into a Newtonian part plus a perturbation so that the pressure, velocity and stress can be written as

$$P = p + \tilde{p} \quad ; \quad \mathbf{U} = \mathbf{u} + \tilde{\mathbf{u}} \quad ; \quad \boldsymbol{\Sigma} = \boldsymbol{\sigma} + \tilde{\boldsymbol{\sigma}},$$

respectively, where the ‘tilde’ denotes the non-Newtonian contribution. In particular, the stress is defined by the constitutive model

$$\boldsymbol{\Sigma} = -(p + \tilde{p})\mathbf{I} + 2\mu\mathbf{E} - 2\Psi_1\overset{\triangledown}{\mathbf{E}} + \Psi_2\mathbf{E}\cdot\mathbf{E},$$

where Ψ_1 and Ψ_2 are the first and second normal stress coefficients, the strain-rate tensor is

$$\mathbf{E} = \frac{1}{2}(\mathbf{K} + \mathbf{K}^T), \text{ where } \mathbf{K} = \frac{\partial\mathbf{u}}{\partial\mathbf{x}}$$

and the upper-convective derivative is

$$\overset{\triangledown}{\mathbf{E}} = -\mathbf{K}\cdot\mathbf{E} - \mathbf{E}\cdot\mathbf{K}^T.$$

In this way, the non-Newtonian stress is simply

$$\tilde{\boldsymbol{\sigma}} = -2\Psi_1\overset{\triangledown}{\mathbf{E}} + \Psi_2\mathbf{E}\cdot\mathbf{E}. \tag{A.7}$$

For a thin-film approximation, conservation of mass for a second-order fluid is given by

$$\frac{\partial}{\partial y}(u_r + \tilde{u}_r) + \frac{1}{R}\frac{\partial}{\partial\theta}(u_\theta + \tilde{u}_\theta) + \frac{\partial}{\partial z}(u_z + \tilde{u}_z) = 0, \tag{A.8}$$

and Stokes’ equations for the non-Newtonian flow are

$$\begin{aligned} \tilde{p} &= \tilde{\sigma}_{rr}, \\ \mu\frac{\partial^2\tilde{u}_\theta}{\partial y^2} &= \frac{1}{R}\frac{\partial N_2}{\partial\theta}, \\ \mu\frac{\partial^2\tilde{u}_z}{\partial y^2} &= -\frac{\partial N_1}{\partial z}, \end{aligned} \tag{A.9}$$

for first $N_1 = \tilde{\sigma}_{zz} - \tilde{\sigma}_{rr}$ and second $N_2 = \tilde{\sigma}_{rr} - \tilde{\sigma}_{\theta\theta}$ normal stresses. The diagonal stress components are found from equation (A.7) to be

$$\begin{aligned} \tilde{\sigma}_{rr} &= \frac{\Psi_2}{4}\left(\left(\frac{\partial u_\theta}{\partial y}\right)^2 + \left(\frac{\partial u_z}{\partial y}\right)^2\right), \\ \tilde{\sigma}_{\theta\theta} &= \left(2\Psi_1 + \frac{\Psi_2}{4}\right)\left(\frac{\partial u_\theta}{\partial y}\right)^2, \\ \tilde{\sigma}_{zz} &= \left(2\Psi_1 + \frac{\Psi_2}{4}\right)\left(\frac{\partial u_z}{\partial y}\right)^2, \end{aligned}$$

where u_θ and u_z are the Newtonian velocities given by equation (A.3). As in the Newtonian case, integrating Stokes’ equations (A.9) subject to no-slip and zero stress at the free surface finds velocities $\tilde{u}_\theta$ and $\tilde{u}_z$ and integrating conservation of mass (A.8) between $y = 0$ and $y = h$ gives the evolution equation

$$\begin{aligned} \frac{\partial h}{\partial t} &= \frac{2}{3\mu}\left[\frac{1}{R^2}\frac{\partial}{\partial\theta}\left(h^3\frac{\partial p}{\partial\theta}\right) + \frac{\partial}{\partial z}\left(h^3\left(\frac{\partial p}{\partial z} + \rho g\right)\right)\right] \\ &\quad - \frac{1}{15\mu^3}\left[\frac{1}{R^2}\frac{\partial^2}{\partial\theta^2}\left(h^5\left(\frac{2\Psi_1}{R^2}\left(\frac{\partial p}{\partial\theta}\right)^2 - \frac{\Psi_2}{4}\left(\frac{\partial p}{\partial z} + \rho g\right)^2\right)\right)\right] \\ &\quad - \frac{1}{15\mu^3}\left[\frac{\partial^2}{\partial z^2}\left(h^5\left(2\Psi_1\left(\frac{\partial p}{\partial z} + \rho g\right)^2 - \frac{\Psi_2}{4R^2}\left(\frac{\partial p}{\partial\theta}\right)^2\right)\right)\right]. \end{aligned} \tag{A.10}$$

The Newtonian case (A.4) is recovered by setting $\Psi_1 = \Psi_2 = 0$.

Recall that the dispersion relation describing the Newtonian flow is given by

$$\mathbb{R}\mathrm{e}(\alpha^N) = \frac{2\chi h_0^3}{3\mu}\left(\frac{m^2}{R^4} + \frac{k^2}{R^2} - \frac{m^4}{R^4} - \frac{2m^2k^2}{R^2} - k^4\right),$$

where α^N denotes the Newtonian growth rate. A similar linear stability analysis shows that the non-Newtonian contribution to evolution equation yields the dispersion relation

$$\mathbb{R}\mathrm{e}(\tilde{\alpha}) = \frac{(\rho g)^2 h_0^4}{3\mu^3}\left(2\Psi_1 k^2 - \frac{\Psi_2 m^2}{4R^2}\right),$$

for non-Newtonian growth rate $\tilde{\alpha}$. Thus, the full dispersion relation for a second-order fluid is given by

$$\mathbb{R}\mathrm{e}(\alpha) = \mathbb{R}\mathrm{e}(\alpha^N + \tilde{\alpha}).$$

For the axisymmetric mode, $m = 0$, the disturbance wave is unstable provided that

$$\mathbb{R}\mathrm{e}(\alpha) = \frac{2\chi h_0^3}{3\mu}\frac{k^2}{R^2}(1 - k^2R^2) + \frac{2(\rho g)^2 h_0^4}{3\mu^3}\Psi_1 k^2 > 0,$$

indicating that the first normal stress coefficient $\Psi_1 > 0$ is a destabilising influence compared the Newtonian axisymmetric case (A.5).

For $m = 1$, the dispersion relation reduces to

$$\mathbb{R}\mathrm{e}(\alpha) = -\frac{2\chi h_0^3}{3\mu}\frac{k^2}{R^2}(1 + k^2R^2) + \frac{(\rho g)^2 h_0^4}{3\mu^3}\left(2\Psi_1 k^2 - \frac{\Psi_2}{4R^2}\right).$$

Since we assume $\Psi_2 < 0$, both the first and second normal stresses are destabilising factors in this case. Moreover, if the fluid coating is uniform in the z-direction so that $k = 0$, then we have growth of the disturbance wave provided that

$$\mathbb{R}\mathrm{e}(\alpha) = -\frac{(\rho g)^2 h_0^4}{12R^2\mu^3}\Psi_2 > 0.$$

Thus, the flow is always unstable when there exists a second normal stress. Furthermore, this non-axisymmetric mode grows more rapidly than the symmetric instability, which is unconditionally stable for $k = 0$. Similar behaviour has been observed in co-extrusion due to elastic stratification [69].

The origin of this instability is the stress gradient imposed by the initially non-uniform coating; the thickly-coated side has a larger second normal stress, which generates velocity in the vorticity direction. Consequently, the fluid flows around the fibre, causing the thickness of the coating to decrease on the thinly-coated side, and therefore increase on the other, so that the coating becomes progressively non-uniform in the vorticity direction. This is in contrast to the Newtonian case (A.6) where shifting the fluid coating about the fibre is unconditionally stable.

A.4 A One-Dimensional Approximation

For azimuthal disturbances such that $\frac{\partial}{\partial z} = 0$, we assume tension in the vorticity lines only so that Ψ_1 can be neglected. Thus, the evolution equation (A.10) reduces to the

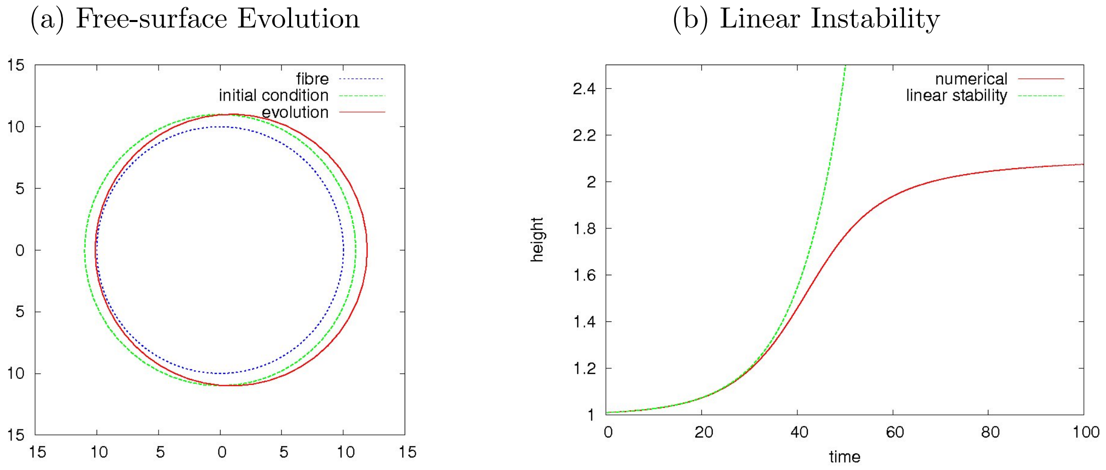

Figure A.1: (a) Evolution of $m = 1$ perturbation for $h_0 = 1$ and $R = 10$; (b) $h(2\pi, t)$ compared to linear stability solution given by equation (A.13) for $C_1 = 1, C_2 = -0.02$.

one-dimensional form

$$\frac{\partial h}{\partial t} = -C_1 \frac{\partial}{\partial \theta}\left(h^3 \frac{\partial}{\partial \theta}(h + h_{\theta\theta})\right) + C_2 \frac{\partial^2}{\partial \theta^2}(h^5), \tag{A.11}$$

where we have the coefficients

$$C_1 = \frac{2\chi}{3\mu R^2} \quad ; \quad C_2 = \frac{\Psi_2(\rho g)^2}{60\mu^3 R^2}.$$

The ratio $C1/|C_2|$ sets the time scale of the flow. We assume that the second normal stress coefficient is small so that $C_1 \gg |C_2|$ and for $C_2 = 0$, the evolution equation reduces to the one-dimensional Newtonian case. This governing equation can be solved via the Lax-Wendroff finite-difference scheme.

Consider a thin coating with initial thickness $h_0 = 1$ and $m = 1$ perturbation of the form

$$h(\theta, 0) = h_0(1 + a_0 \cos\theta), \tag{A.12}$$

for $a_0 = 0.01$. For fluid parameters $C_1 = 1, C_2 = -0.02$, Figure A.1 demonstrates how the perturbed free surface shifts sideways, creating a non-uniform coating that is much thicker on one side of the fibre.

The addition of an axial perturbation deforms the free surface in the z-direction also. Thus, a series of droplets is expected to form along one side of the fibre and propagate downwards due to gravity. This morphology of non-axisymmetrical droplets has been observed experimentally by Boulogne *et al.* [17] in the study of polymer solutions coating a fibre.

According to linear stability, the evolution of the $m = 1, k = 0$ instability is described by

$$h(\theta, t) = h_0 + a_0 \exp(-5C_2 h_0^4), \tag{A.13}$$

and Figure A.1 shows that our numerical solution $h(2\pi, t)$ is in agreement at early times $0 \leq t \leq 30$. However, the deformation begins to depart from the linear solution when non-linear terms become important.

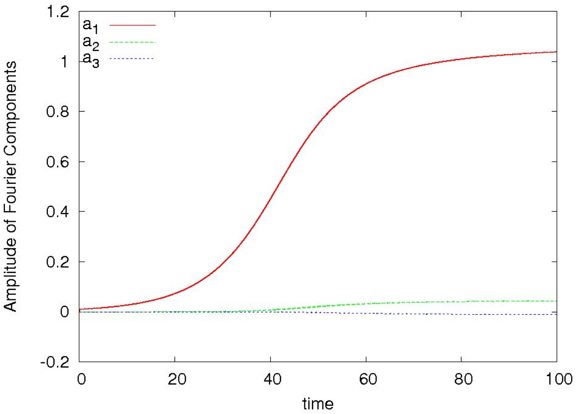

Figure A.2: Fourier decomposition of numerical solution for $C_1 = 1$ and $C_2 = -0.02$.

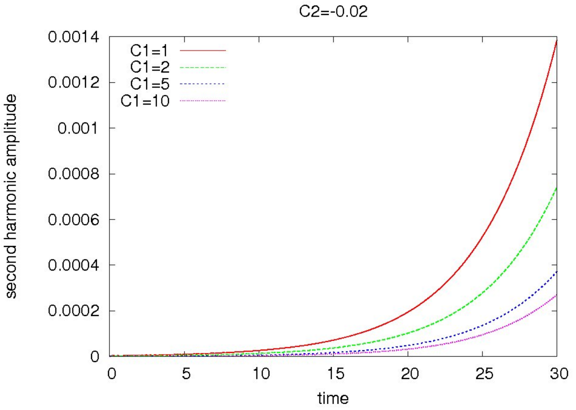

Figure A.3: Second harmonic amplitude a_2 for a range of surface tension parameter C_1 with $C_2 = -0.02$

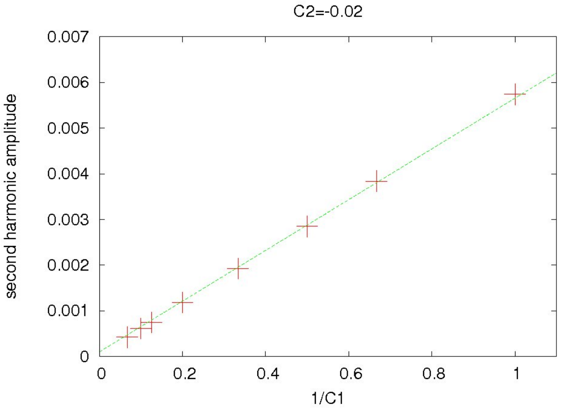

Figure A.4: Scaling of second harmonic amplitude a_2 with $1/C_1$ taken at sample time $a_1 = 0.4$ with $C_2 = -0.02$

To understand this free surface deformation, we decompose our solution into Fourier components such that

$$h(\theta, t) = \frac{a_0}{2} + \sum_i a_i \cos(i\theta),$$

where the Fourier coefficients are defined as

$$a_i(t) = \frac{1}{\pi} \int_0^{2\pi} h(\theta) \cos(i\theta).d\theta.$$

As shown in Figure A.2, the amplitude a_1 is the largest and bounded such that $0 \leq a_1 \leq 1$, as prescribed by the initial condition (A.12). This first harmonic component corresponds to the dominant shifting mechanism demonstrated in Figure A.1.

Although the thick side of the coating tends to remain cylindrical in shape due to surface tension, the pressure becomes large in the thin layer, which can deform the coating from a circle. Thus, higher-order harmonics $i > 1$ correspond to localised deformations in the free surface and are much smaller, increasing as $h \to 0$. The second and third harmonic amplitude, a_2 and a_3, respectively, are shown in Figure A.2.

Local deformations are of course dampened by surface tension, which acts to maintain the cylindrical profile. Figure A.3 shows how the amplitude of the second harmonic a_2 is reduced for increasing values of the surface tension parameter C_1. In fact, we find that the amplitude of the second harmonic a_2 is directly proportional to $1/C_1$, as shown in Figure A.4 for sample time $a_1 = 0.4$

In light of our numerical results, we write the free-surface evolution as

$$h(\theta, t) = h_0(1 + a(t)\cos\theta) + \frac{1}{C_1} f(\theta, t), \tag{A.14}$$

where $a(t)$ represents the dominant shifting mechanism determined numerically by a_1 and $f(\theta, t)$ represents the higher-order harmonics $a_2, a_3, \ldots$, etc, which are assumed to be small $O(C_2)$. Without loss of generality we set $h_0 = 1$ and seek an analytic representation of $a(t)$ and $f(\theta, t)$.

A.5 The Shifting Mechanism

First, we seek an analytic solution to the first-harmonic component $a(t)$ by neglecting the higher-order harmonics from equation (A.14). Thus, substituting

$$h(\theta, t) = 1 + a(t)\cos\theta,$$

into the evolution equation (A.11) and integrating with respect to θ twice yields

$$C_1(h + h_{\theta\theta}) = -\frac{\dot{a}}{2a(1 + a\cos\ \theta)^2} + \frac{5}{2}C_2(1 + \cos\theta)^2,$$

where $\dot{a} = \frac{da}{dt}$. Since $h + h_{\theta\theta} = g(\theta)$ is periodic on $[0, 2\pi]$ for know function $g(\theta)$, we require

$$\int_0^{2\pi} g(\theta) \cos\theta.d\theta = 0,$$

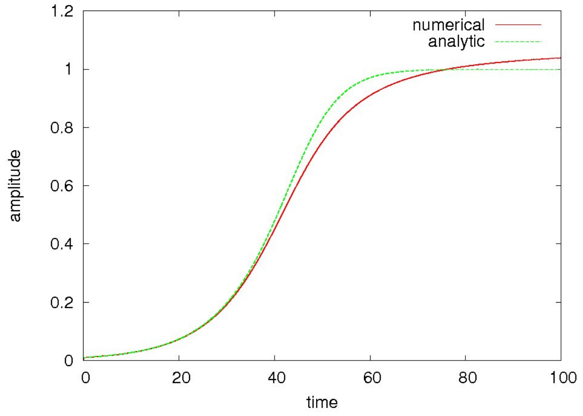

Figure A.5: Amplitude of first harmonic $a_1(t)$ compared to analytic solution $a(t)$ from equation (A.15) for $C_1 = 1, C_2 = -0.02$.

which is solved to yield the evolution equation

$$\dot{a}(t) = -5C_2 a(1-a^2)^{3/2}. \tag{A.15}$$

The amplitude $a(t)$ of the disturbance can be found by finite differencing. Comparing the amplitude of the first harmonic $a_1(t)$ to our prediction found from equation (A.15), Figure A.5 shows excellent agreement for time $0 \leq t \leq 40$. This behaviour is independent of C_1 provided $C_1 \gg |C_2|$.

We now include the higher-order harmonics denoted by $f(\theta, t)$. Assuming $1/C_1 \ll 1$, substituting equation (A.14) into the evolution equation (A.11) and integrating twice yields

$$f + f_{\theta\theta} \approx -\frac{\dot{a}}{2a(1+a\cos\theta)^2} + \frac{5}{4}C_2 a^2 \cos 2\theta.$$

By binomial expansion, this can be solved to give

$$f \approx -\frac{\dot{a}}{2a}\left(-\frac{a^2}{2}\cos 2\theta + \frac{a^3}{8}\cos 3\theta + \dots\right) - \frac{5}{12}C_2 a^2 \cos 2\theta, \tag{A.16}$$

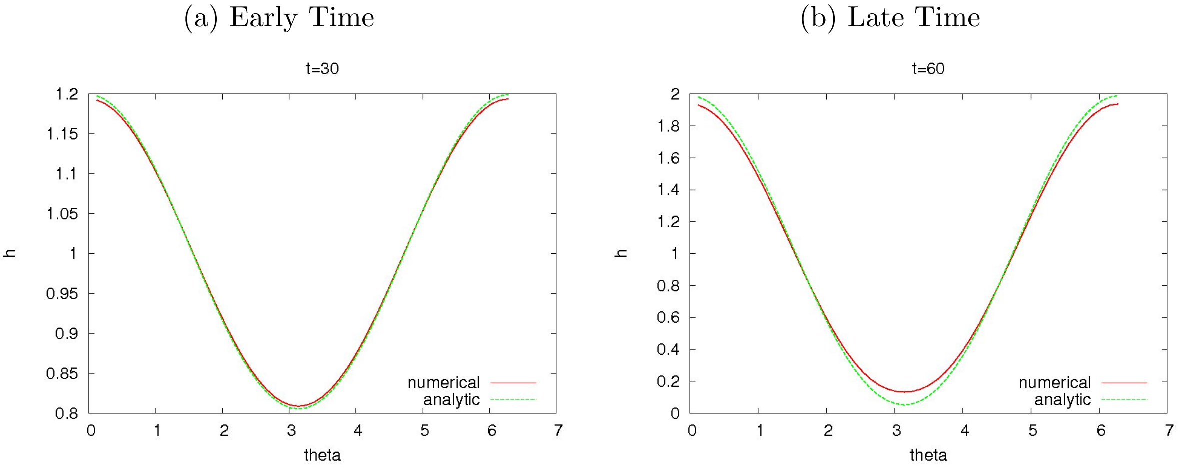
(a) Early Time

(b) Late Time

Figure A.6: Numerical solution compared to analytic solution (A.14) at times (a) $t = 30$; (b) $t = 60$ for $C_1 = 1, C_2 = -0.02$.

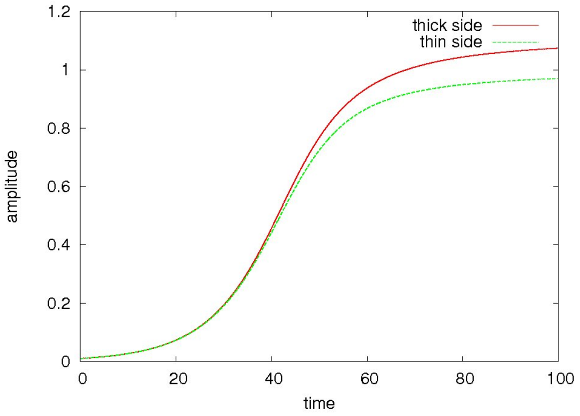

Figure A.7: Amplitude of the growth on the thin side ($\theta = \pi$) and the thick side ($\theta = 2\pi$) for $C_1 = 1, C_2 = -0.02$.

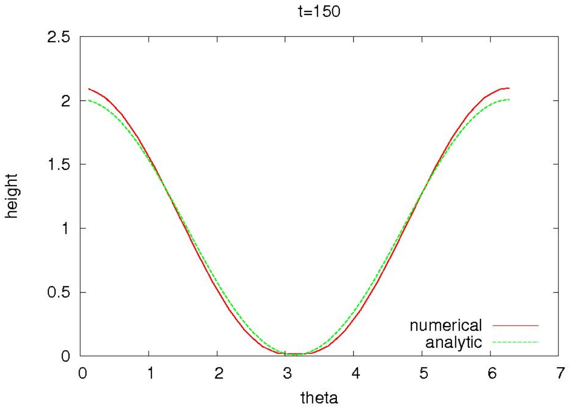

Figure A.8: Numerical solution (A.11) at time $t = 150$ compared to analytic solution (A.14) for $C_1 = 1, C_2 = -0.02$.

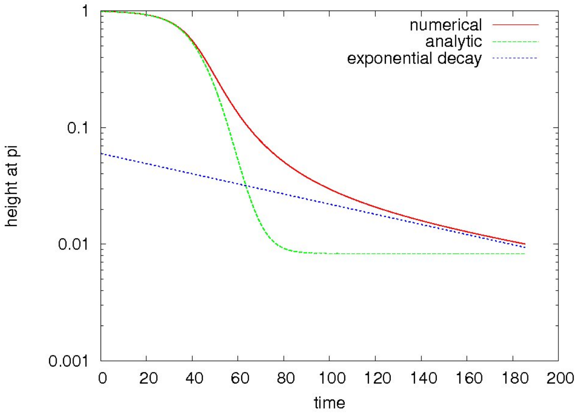

Figure A.9: Exponential decay at $h(\pi, t)$ compared to analytic solution (A.14) for $C_1 = 1, C_2 = -0.02$.

where $\dot{a}$ is given by equation (A.15). When the binomial expansion is taken to order $O(a^6)$, Figure A.6 shows that the finite-difference solution is in excellent agreement with the full analytic solution (A.14) for time $t = 30$.

However, we see significantly different behaviour at time $t = 60$ due to $a(t)$ not describing the numerical solution well at late times, as shown in Figure A.5. This discrepancy is due to the analytic solution not taking into account the curvature of the free-surface as $h \to 0$. As the pressure becomes large in the thinly coated region, higher-order harmonics, although remain small, become comparable to $1 - a_1$ at around $t \approx 60$.

A.6 The Draining Mechanism

Although the second normal stress always drives the flow around the fibre, as the coating becomes increasingly thin it becomes more difficult to squeeze the fluid out of the confined layer. Consequently, the dynamics evolve into a much slower draining flow governed by the pressure in the thinly-coated region. To illustrate this mechanism, Figure A.7 shows the amplitude of the growth on the thin side of the coating ($\theta = \pi$) compared to the thick side of the coating ($\theta = 2\pi$). It is clear that the evolution of the thinly-coated side is decelerated first due to the reduced flow. The growth of the thick side is then restricted as a result.

At later time $t = 150$, Figure A.8 shows that the numerical solution is much flatter in the thin region than the profile predicted by equation (A.14), suggesting that the fluid slowly wraps around the fibre. Furthermore, the free-surface height $h(\pi, t)$ is seen to enter an exponentially thinning regime at this late time, as shown in Figure A.9. This is in contrast to the analytic solution, which reaches a steady state comparatively the early. Similar thinning behaviour has been observed for a thin film of polymer solution separating an approaching bubble from bulk air [44] and is typical of polymer solutions in extensional flow [54], [35].

A.7 Concluding Remarks

In the case of a viscoelastic fluid coating a vertical fibre, we have established a non-axisymmetric instability driven by a second normal stress. For small perturbations in the vorticity direction, the flow is unconditionally unstable so that the thickness of the coating becomes progressively non-uniform. The formation of thinly-coated regions leads to weaknesses in the coating, which is highly undesirable for industrial applications. Yet, this instability can easily be induced through uneven wetting of the fibre during the coating process.

Initially, the growth of the instability can be explained by a shifting mechanism that describes the overall flow of the fluid around the fibre, along with localised deformations in the free-surface that are dampened by surface tension. However, the flow dynamics at late times appear more complicated than we originally thought; the growth of the instability is found to be significantly slower than that predicted by a simple Fourier decomposition. We attribute this discrepancy to a more complex draining flow decelerating the instability.

Bibliography

[1] K. A-Alamry, K. Nixon, R. Hindely, J. A. Odell, and S. G. Yeates, *Flow-induced polymer degredation during inkjet printing*, Macromol. Rapid Commun. **32** (2011), 316–320.

[2] C. Ainsley, N. Reis, and B. Derby, *Freeform fabrication by controlled droplet deposition of powder filled melts*, J. Mat. Sci. **37** (2002), 3155–3161.

[3] B. Ambravaneswaran, E. D. Wilkes, and O. A. Basaran, *Drop formation from a capillary tube: Comparison of one-dimensional and two-dimensional analysis and occurence of satellite drops*, Phys. Fluids **14** (2002), 2606–2621.

[4] S. L. Anna, *Filament stretching rheometry of model elastic solutions*, Ph.D. thesis, Harvard University, 2000.

[5] S. L. Anna and G. H. McKinley, *Elasto-capillary thinning and breakup of model elastic liquids*, J. Rheol. **45** (2001), 115–138.

[6] A. M. Ardekani, V. Sharma, and G. H. McKinley, *Dynamics of bead formation, filament thinning and breakup in weakly viscoelastic jets*, J. Fluid Mech. **665** (2010), 46–56.

[7] P. Bacova, L. G. D. Hawke, D. J. Read, and A. J. Moreno, *Dynamics of branched polymers: A combined study by molecular dynamics simulations and tube theory*, Macromolecules **46** (2013), 4633–4650.

[8] O. A. Basaran, G. Haijing, and P. P. Bhatt, *Nonstandard inkjets*, Annu. Rev. Fluid Mech. **45** (2013), 85–113.

[9] A. D. Basilevskii, J. D. Meyer, and A. N. Rohzkov, *Dynamics and breakup of pulse microjets of polymeric fluids*, Fluid Dyn. **29** (2005), 381–432.

[10] A. V. Basilevskii, V. M. Entov, M. M. Lerner, and A. N. Rozhkov, *Failure of polymer solution filaments*, Polym. Sci. **39** (1997), 316–324.

[11] P.P. Bhatt, S. Appathurai, M. T. Harris, M. Pasquali, G. H. McKinley, and O. A. Basaran, *Formation of beads-on-a-string structures during breakup of viscoelastic filaments*, Nature Phys. **6** (2010), 625–631.

[12] P.P. Bhatt, O. A. Basaran, and M. Pasquali, *Dynamics of viscoelastic liquid filaments: Low capillary number flows*, J. Non-Newt. Fluid Mech **150** (2008), 211–225.

[13] D. B. Bogy, *Use of one-dimensional Cosserat theroy to study instability in a viscous liquid jet*, Phys. Fluids **21** (1978), 190–197.

[14] N. Bohr, *Determination of the surface tension of water by the method of jet*, Phil. Trans. **209** (1909), no. 281-317.

[15] C. Bonnoit, E. Clement, and A. Lindner, *Accelerated drop detachment in dense granular suspensions*, Phys. Fluids **24** (2012), no. 043304.

[16] F. Boulogne, L. Pauchard, and F. Giorgiutti-Dauphine, *Instability and morphology of polymer solutions coating a fibre*, J. Fluid Mech. **704** (2012), 232–250.

[17] F. Boulogne, L. Pauchard, and F. Giorgiutti-Dauphine, *private communication*, 2012.

[18] D. W. Bousfield, R. Keunings, and G. Marrucci anf M. M. Denn, *Nonlinear analysis of the surface tendion driven breakup of viscoelastic filaments*, J. Non-Newt. Fluid Mech. **21** (1986), 79–97.

[19] J. Brady and I. C. Carpen, *Second normal stress jump instability in Non-Newtonian fluids*, J. Non-Newt. Fluid Mech. **102** (2002), 219–232.

[20] G. Brenn, Z. Liu, and F. Durst, *Linear analysis of the temporal stability of axisymmetrical non-Newtonian liquid jets*, Int J. Multiphase Flow **26** (2000), 1621–1644.

[21] L. Campo-Deano and C. Clasen, *The slow retraction method (SRM) for the determination of ultra-short relaxation times in capillary break-up extensional rheometry experiments*, J. Non-Newt. Fluid Mech. **165** (2010), 1688–1699.

[22] J. R. Castrejon-Pita, S. D. Hoath, and I. M. Hutchings, *Velocity profiles in a cylindrical liquid jet by reconstructed velocimetry*, ASME J. Fluids Engineering **134** (2012), no. 011201-1.

[23] J. R. Castrejon-Pita, N. F. Morrison, O. G. Harlen, G. D. Martin, and I. M. Hutchings, *Experiments and Lagrangian simulations on the formation of droplets in continuous mode*, Phys. Rev. E **83** (2011), no. 016301.

[24] J. R. Castrejon-Pita, N. F. Morrison, O. G. Harlen, G. D. Martin, and I. M. Hutchings, *Experiments and Lagrangian simulations on the formation of droplets in drop-on-demand mode*, Phys. Rev. E **83** (2011), no. 036306.

[25] H. C. Chang, E. A. Demekhin, and E. Kalaidin, *Iterated stretching of viscoelastic jets*, Phys. Fluids **11** (1999), 1717–1737.

[26] K. C. Chaudhary and T. Maxworthy, *The non-linear capillary instability of a liquid jet. Part 2. Experiments on jet behaviour before droplet formation*, J. Fluid Mech. **96** (1980), 275–286.

[27] K. C. Chaudhary and L. G. Redekopp, *The non-linear capillary instability of a liquid jet. Part 1. Theory*, J. Fluid Mech. **96** (1980), 257–274.

[28] M. Chellamuthu, E. M. Arndt, and J. P. Rothstein, *Extensional rheology of shear thickening nano-particle suspensions*, Soft Matter **5** (2009), 2117–2124.

[29] A. U. Chen, P. K. Notz, and O. A. Basaran, *A new method for significantly reducing drop radius without reducing nozzle radius in drop-on-demand drop production*, Phys. Fluids **14** (2002), 1–4.

[30] Y. Chen, Y. Huang, C. Kuo, and S. Chang, *Investigation of design parameters for droplet generators driven by piezoelectric actuators*, In. J. Mech. Sci **49** (2007), 733–740.

[31] M. D. Chilcott and J. M. Rallison, *Creeping flow of dilute polymer solutions past cylinders and spheres*, J. Non-Newt. Fluid Mech. **29** (1988), 381–432.

[32] Y. Christanti and L. Walker, *Surface-tension-driven jet breakup of strain-hardening polymer solutions*, J. Non-Newt. Fluid Mech. **100** (2001), 9–26.

[33] C. Clanet and J. C. Lasheras, *Transition from jetting to dripping*, J. Fluid Mech. **383** (1999), 307–326.

[34] C. Clasen, J. Bico, V. Entov, and G. H. McKinley, *'Gobbling drops': the jetting/dripping transition in flows of polymer solutions*, J. Fluid Mech. **636** (2009), 5–40.

[35] C. Clasen, J. Eggers, M. A. Fontelos, J. Li, and G. H. McKinley, *The beads-on-string structure of viscoelastic threads*, J. Fluid Mech. **556** (2006), 283–308.

[36] C. Clasen, J. P. Plog, W. M. Kulicke, M. Owens, C. Macosko, L. E. Scriven, M. Verani, and G. H. McKinley, *How dilute are dilute solutions in extensional flows?*, J. Rheol. **50** (2006), 849–881.

[37] University of Durham Colin Bain, *private communication*, 2014.

[38] A. Crosby and J. R. Lister, *Falling plumes of point particles in viscous fluid*, Phys. Fluids **24** (2012), no. 123101.

[39] L. da Vinci, *Codex Leicester*, Christies London, 1980.

[40] R. F. Day, E. J. Hinch, and J. R. Lister, *Self-similar capillary pinch-off of an inviscid fluid*, Phys. Rev. Lett. **80** (1998), no. 4, 704–707.

[41] B. J. de Gans, P. C. Duineveldl, and U. S. Schubert, *Inkjet printing of polymers: State of the art and future developments*, Adv. Matter **16** (2004), no. 3.

[42] B. J. de Gans, E. Kazancioglu, W. Meyer, and U. S. Schubert, *Inkjet printing of polymers and polymer libraries using micropippettes*, Macromol. Rapid Commun. **25** (2004), 292–296.

[43] B. J. de Gans, L. Xue, U. S. Agarwal, and U. S. Schubert, *Inkjet printing of linear and star polymers*, Macromolecular **26** (2005), 310–314.

[44] G. Debregeas, P. G. de Gennes, and F. Brochard-Wyart, *The life and death of 'bare' viscous bubbles*, Science **279** (1998), 1704–1707.

[45] B. Derby, *Inkjet printing of functional and structural materials: Fluid property requirements, feature stability and resolution*, Annu. Rev. Mater. Res. **40** (2010), 395–414.

[46] M. Doi and S. F. Edwards, *The theroy of polymer dynamics*, Oxford University Press, 1986.

[47] H. Dong, W. W. Carr, and J. F. Morris, *An experiemental study of drop-on-demand formation*, Phys. Fluids **18** (2006), no. 072102.

[48] J. L. Duda and J. L. Vrentas, *Fluid mechanics of laminar liquid jets*, Chem. Eng. Sci. **22** (1967), 855.

[49] J. Eggers, *Universal pinching of 3D axisymmetric free-surface flow*, Phys. Rev. Lett. **71** (1993), no. 21, 3458–3460.

[50] J. Eggers, *Nonlinear dynamics and breakup of free surface flows*, Rev. Mod. Phys. **69** (1997), no. 3.

[51] J. Eggers, *Post-breakup solution of Navier-Stokes and Stokes threads*, Phys. Fluids **26** (2014), no. 072104.

[52] J. Eggers and T. F. Dupont, *Drop formation in a one-dimensional approximation of the Navier-Stokes equation*, J. Fluid Mech. **262** (1994), 205–221.

[53] J. Eggers and E. Villermaux, *Physics of liquid jets*, Rep. Prog. Phys. **71** (2008), no. 036601.

[54] V. M. Entov and E. J. Hinch, *Effect of a spectrum of relaxation times on the capillary thinning of a filament of elastic liquid*, J. Non-Newt. Fluid Mech. **72** (1997), 31–53.

[55] V. M. Entov and A. L. Yarin, *Influence of elastic stress on the capillary break-up of dilute polymer solutions*, Fluid Dyn. **19** (1984), 21–29.

[56] R. W. Fenn and S. Middleman, *Newtonian jet stability: The role of air resistance*, AIChe J. **15** (1969), 379–383.

[57] J. D. Ferry, *Viscoelastic properties of polymers*, 3 ed., John Wiley and Sons, 1980.

[58] S. Fielding, *Viscoelastic Taylor-Couette instability of shear-banded flow*, Phys. Rev. Lett. **104** (2010), no. 198303.

[59] M. G. Forest and Q. Wang, *Change-of-type behaviour in viscoelastic slender jet models*, J. Theor. Comput. Fluid Dyn. **2** (1990), no. 1-25.

[60] R. J. Furbank and J. R. Morris, *An experimental study of particle effects on drop formation*, Phys. Fluids **16** (2004), 1777–1790.

[61] R. J. Furbank and J. R. Morris, *Pendant drop thread dynamics of particle-laden liquids*, Int. J. Multiphase Flow **66** (2007), 448–468.

[62] M. Goldin, J. Yerushalmi, R. Pfeffer, and R. Shinnar, *Breakup of a laminar capillary jet of a viscoelastic fluid*, J. Fluid Mech. **38** (1968), 689–711.

[63] S. L. Goren and M. Gottlieb, *Surface tension driven breakup of viscoelastic liquid threads*, J. Fluid Mech. **120** (1982), 245–266.

[64] R. P. Grant and S. Middleman, *Newtonian jet stability*, AIChE J. **12** (1966), 669–678.

[65] M. Hameed and J. F. Morris, *Break-up of a liquid jet containing solid particles: A singularity approach*, SIAM J. Applied Math. **70** (2009), 885–900.

[66] O. G. Harlen and N. Morrison, *Viscoelasticity in inkjet printing*, Rheol. Acta **49** (2010), 619–632.

[67] O. G. Harlen, J. M. Rallison, and P. Szabo, *A split Langrangian-Eulerian method for simulating transient viscoelastic flows*, J. Non-Newt. Fluid Mech. **60** (1995), 81–104.

[68] J. H. Hilbing and S. D. Heister, *Droplet size control in liquid jet break-up*, Phys. Fluids **8** (1996), no. 1574.

[69] E. J. Hinch, O. J. Harris, and J. M. Rallison, *The instability mechanism for two liquids being co-extruded*, J. Non-Newt Fluid Mech. **43** (1992), 311–324.

[70] S. D. Hoath, , D. C. Vadillo, O. G. Harlen, C. McIlrot, N. F. Morrison, W. K. Hsiao, T. R. Tuladhar, S. Jung, G. D. Martin, and I. M. Hutchings, *Inkjet printing weakly elastic polymer solutions*, J. Non-Newt. Fluid Mech. **205** (2014), 1–10.

[71] S. D. Hoath, O. G. Harlen, and I. M. Hutchings, *Jetting behaviour of polymer solutions in drop-on-demand inkjet printing], volume = 56, year = 2012,*, J. Rheol, no. 1109.

[72] S. D. Hoath, W. Hsiao, S. Jung, G. D. Martin, and I. M. Hutchings, *Dependence of drop speed on nozzle diameter, viscosity and drive amplitude in drop-on-demand inkjet printing*, Proc NIP27 (2011), 62–65.

[73] S. D. Hoath, G. D. Martin, and J. R. Casrejon-Pita I. M. Hutchings, *Satellite formation in drop-on-demand printing of polymer solutions*, Society for Imaging Science and Technology **23** (2007), no. 331-335.

[74] I. M. Hutchings and G. D. Martin, *Inkjet technology for digital fabrication*, John Wiley and Sons Ltd, 2013.

[75] A. Kalaaji, B. Lopez, P. Attane, and A. Soucemarianadin, *Break-up length of forced liquid jets*, Phys. Fluids **15** (2003), no. 2469.

[76] S. Kalliadas and H-C. Chang, *Drop formation during coating vertical fibres*, J. Fluid Mech. **261** (1994), 135–168.

[77] J. B. Keller, S. I. Rubinow, and Y. O. Tu, *Spatial instability of a jet*, Phys. Fluids **16** (1973), no. 12.

[78] M. A. Kelmanson, *MATH 3475/5475 Modern Numerical Methods*, http://www1.maths.leeds.ac.uk/ mark/MATH3475/downloads.html.

[79] M. A. Kelmanson, *Dynamically adaptive rectangular meshes*, Defence Research Agency Working Paper **D/ER1/9/4/2062/142/RARDE/3** (1991), 29.

[80] M. A. Kelmanson, *Implementation details of a 2D Eulerian mesh preprocessor*, Defence Research Agency Working Paper **D/ER1/9/4/2062/142/RARDE/5** (1992), 48.

[81] M. A. Kelmanson, *Error analysis of a ”D Eulerian impact code*, Defence Research Agency Working Paper **D/ER1/9/4/2062/142/RARDE/6** (1993), 65.

[82] M. A. Kelmanson, *Unstructured rectangular adpative-mesh generation for 2D conservative schemes*, Appl. Math. Lett. **6** (1993), 17–22.

[83] I. M. Krieger and T. J. Dougherty, *A mechanism for non-Newtonian flow in suspension of rigid spheres*, Trans. Soc. Rheology **3** (1959), 137–152.

[84] P. S. Laplace, *Mechanique celeste supplement aux libre*, Courier: Paris, 1805.

[85] P. D. Lax, *Hyperbolic systems of conservation laws*, Commun. Pure Applied Math. **10** (1957), 537–566.

[86] H. C. Lee, *Drop formation in a liquid jet*, IBM J. Res. Develop. **18** (1974), 364–369.

[87] T. M. Lee, T. G. Kang, and J. S. Yang, *Drop-on-demand solder droplet jetting system for fabricating microstructure*, IEEE Transactions on Electronics Packaging Manufacture **31** (2008), 202–210.

[88] S. J. Leib and M. E. Goldstein, *The generation of capillary instabilities on a liquid jet*, J. Fluid Mech. **168** (1986), 479–500.

[89] R. N. Leyden, J. S. Thayer, and B. J. L Bedal, *Selective deposition modelling method and apparatus for forming three-dimensional objects and supports*, Patent WO 1997/011837 (1997).

[90] J. Li and M. A. Fontelos, *Drop dynamics on the beads-on-string structure for viscoelastic jets: A numerical study*, Phys. Fluids **15** (2003), 922–937.

[91] G. D. Martin, S. D. Hoath, and I. M. Hutchings, *Inkjet printing - the physics of manipulating liquid jets and drops*, J. Phys. Conf. Ser. **105** (2008), no. 012001.

[92] W. Matheus and C. Clasen, *private communication*, 2013.

[93] G. H McKinley, *Visco-elasto-capillary thinning and break-up of complex fluids*, Rheol. Revs. (2005), no. 1-48.

[94] G. H McKinley and M. Renardy, *Wolfgang von Ohnesorge*, Phys. Fluids **23** (2011), no. 127101.

[95] G. E. A. Meier, A. Klopper, and G. Grabitz, *The influence of kinematic waves on jet break down*, Experiments in Fluids **12** (1992), 173–180.

[96] S. Middleman, *Stability of a viscoelastic jet*, Chem. Eng. Sci. **20** (1965), no. 1037-1040.

[97] A. J. Muller, J. A. Odell, and A. Keller, *Polymer degradation in extensional flow*, Poly. Commun **30** (1989), 298–301.

[98] P. Nghe, S. Fielding, P. Tabeling, and A. Ajdari, *Interfacially driven instability in the microchannel flow of a shear banding fluid*, Phys. Rev. Lett. **104** (2010), no. 248303.

[99] J. A. Odell and A. Keller, *Flow-induced chain fracture of isolated linear macromolecules in solution*, J. Polym. Sci. Part B: poly. Phys. **24** (1986), 1889–1916.

[100] B. K. Oksendal, *Stochastic differential equations: An introduction with applications*, Springer, Berlin, 2003.

[101] M. S. N Oliveira and G. H. McKinley, *Iterated stretching and multiple beads-on-string phenomena in dilute solutions of high extensible flexible polymers*, Phys. Fluids **17** (2005), no. 071704.

[102] M. S. N Oliveira, R. Yeh, and G. H. McKinley, *Iterated stretching, extensional rheology and formation of beads-on-string structures in polymer solutins*, J. Non-Newt. Fluid Mech. **137** (2006), 137–148.

[103] D. T. Papageorgiou, *On the break-up of viscous liquid threads*, Phys. Fluids **7** (1995), 1529–1544.

[104] D. H. Peregrine, G. Shoker, and A. Symon, *The bifurcation of liquid bridges*, J. Fluid Mech. **212** (1990), 25–39.

[105] W. T. Pimbley, *Drop formation from a liquid jet: A linear one-dimensional analysis considered as a boundary value problem*, IBM J. Res. Develop. (1976), 148–156.

[106] W. T. Pimbley and H. C. Lee, *Satellite drop formation in a liquid jet*, IBM J. Res. Develop. (1977), 21–30.

[107] J. A. F. Plateau, *On the recent theories of the constitution of jets of liquid issuing from circular orifices*, Philosophical Magazine **12** (1856), 286.

[108] W. H. Press, S. A. Tekolsky, W. T. Vetterling, and B. P. Flannery, *Numerical recipes in Fortran 77*, 2 ed., Cambridge University Press, 1992.

[109] Lord Rayleigh, *On the instability of jets*, Proc. of London Math. soc. **10** (1878), 4–13.

[110] Lord Rayleigh, *On the instability of a cylinder of viscous liquid under capillary force*, Phil. Mag. **34** (1892), 145–154.

[111] M. Renardy, *Some comments on the surface-tension driven break-up (or lack of it) of viscoelastic jets*, J. Non-Newt. Fluid Mech. **51** (1994), 97–107.

[112] Y. Y. Renardy and M. Renardy, *Instability due to second normal stress jump in two-layer shear flow of the Giesekus fluid*, J. Non-Newt. Fluid Mech. **81** (1999), 215–234.

[113] M. D. Rintoul and S. Torquato, *Computer simulations of dense hard-sphere systems*, J. Chem. Phys. **105** (1996), 9258–9265.

[114] M. Roche and H. Kellay anf H. A. Stone, *Heterogeneity and the role of normal stresses during the extensional thinning of non-Brownian shear-thickening fluids*, Phys. Rev. Lett. **107** (2011), no. 134503.

[115] E. A. Roth, T. Xu, M. Das, C. Gregory, J. J. Hickman, and T. Boland, *Inkjet printing for high-throughput cell patterning*, Biomaterials **25**, 3707–3715.

[116] J. H. Rupe, *On the dynamic characterisation of free liquid jets and partial correlation with orifice geometry*, Jet. Prop. Lab., Cal. Inst. Tech. **Tech. Rep.** (1962), 32–207.

[117] R. Sattler, S. Gier, J. Eggers, and C. Wagner, *The final stages of capillary break-up of polymer solutions*, Phys. Fluid **24** (2012), no. 023101.

[118] R. Savart, *Memoire sur la constitution des veines liquides lancees par orifices circulaires en mince parol*, Ann. Chim. **53** (1833), no. 337.

[119] P. Schummer and K. Tebel, *A new elongational rheometer for polymer solutions*, J. Non-Newt. Fluid Mech. **12** (1983), 331–347.

[120] H. J. Shore and G. M. Harrison, *The effect of added polymer on the formation of drops ejected from a nozzle*, Phys. Fluids **17** (2005), no. 033104.

[121] M. I. Smith, R. Besseling, M. E. Cates, and V. Bertola, *Dilatancy in the flow and fracture of stretched colloidal suspensions*, Nature Commun. **1119** (2010).

[122] A. M. Sterling and C. A. Sleicher, *The instabilities of capillary jets*, J. Fluid Mech. **68** (1975), 477–495.

[123] R. G. Sweet, *Fluid droplet recorder*, U.S. Patent No. 3,596,275 (1971).

[124] P. Szabo, G. H. McKinley, and C. Clasen, *Constant force extensional rheometry of polymer solutions*, J. Non-Newt. Fluid Mech. (2012), 26–41.

[125] E. Tekin, P. J. Smith, and U. S. Schubert, *Inkjet printing as a deposition and patterning tool for polymers and inorganic particles*, Soft Matter **4** (2008), 703–713.

[126] M. Tembely, D. Vadillo, and M. R. Mackley, *The matching of a 'one-dimensional' numerical simulation and experimental results for low viscosity Newtonian and non-Newtonian fluids during fast filament stretching and subsequent break-up*, J. Rheol. **56** (2012), 159–183.

[127] L. Ting and J. B. Keller, *Slender jets and thin sheets with surface tension*, SIAM J. Appl. Math, **50** (1990), 1533.

[128] S. Tomotika, *Unknown Title*, Proc. Roy Soc. London **A150** (1935), 322.

[129] Domino UK, *private communication*, 2014.

[130] D. C. Vadillo, W. Matthues, and C. Clasen, *Microsecond relaxation processes in shear and extensional flows of weakly viscoelastic polymer solutions*, Rheol. Acta. **51** (2012), 755–769.

[131] D. C. Vadillo, M. Tembley, N. F. Morrison, O. G. Harlen, M. R. Mackley, and A. Soucemarianadin, *The matching of polymer solution fast filament stretching, relaxation and breakup experimental results with 1D and 2D numerical viscoelastic simulation*, J. Rheology **56** (2012), no. 1491.

[132] D. C. Vadillo, T. R. Tuladhar, A. Mulji, and M. R. McKinley, *Evaluation of the inkjet fluid's performance using the 'Cambridge Trimaster' filament stretch and break-up device*, J. Rheol. **54** (2010), 261–282.

[133] M. S. van Deem, T. Bertrand, N. Vu, D. Quere, E. Clement, and A. Lindner, *Particles accelerate the detatchment of viscous fluids*, Rheol. Acta. **52** (2013), 403–412.

[134] W. van Hoeve, S. Gekle, J. H. Snoeijer, M. Versluis, M. P. Brenner, and D. Lohse, *Break-up of diminutive Rayleigh jets*, Phys. Fluids **22** (2010), no. 122003.

[135] P. Vassallo and N. Ashgriz, *Satellite formation and merging liquid jet break-up*, Proc. Royal Soc. London Ser. A **433** (1991), 269–286.

[136] H. L. Wagner, *The Mark-Houwink-Sakurada equation for the viscosity of atactic polystyrene*, J. Phys. Chem. Ref. Data **14** (1985), 1101–1106.

[137] H. Watanabe, H. Yoshida, and T. Kotake, *Model calculation for viscoelastic and dielectric relaxation functions of non-entangled star chains with arm length distribution*, Polymer Journal **22** (1990), 153–161.

[138] C. Weber, *Unknown Title*, Z. angew. Math. Mech. **11** (1931), 136.

[139] H. Westborg and O. Hassager, *Creeping motion of long bubbles and drops in capillary tubes*, J. Colloidal and Interface Science **133** (1989), 135–147.

[140] E. E. Bischoff White, M. Chellamuthu, and J. P. Rothstein, *Extensional rheology of shear thickening cornstarch and water suspension*, Rheol. Acta. **49** (2010), no. 119-129.

[141] D. Xu, V. Sanchez-Romaguera, S. Barbosa, W. Travis, J. de Wit, P. Swan, and S. G. Yeates, *Inkjet printing of polymer solutions and the role of chain entanglement*, J. Mater. Chem. **17** (2007), 4902–4907.

[142] Q. Xu and O. A. Basaran, *Computational analysis of drop-on-demand drop formulation*, Phys. Fluids **19** (2007), no. 012111.

[143] M. Yao and G. H. McKinley, *Numerical simulations of extensional deformations of viscoelastic bridges in filament stretching devices*, J. Non-Newt. Fluid Mech **74** (1998), 47–88.

[144] T. Young, *An essay on the cohesion of fluids*, Phil. Trans. R. Soc. London **95** (1805).

[145] M. C. Yuen, *Non-linear capillary instability of a liquid jet*, J. Fluid Mech **33** (1968), 151–163.

[146] B. H. Zimm and R. W. Kilb, *Dynamics of branched polmyer molecules in dilute solution*, J. Polym Sci. **37** (1959), 19–42.

[147] P. J. Zimoch and G. H. McKinley, *Capillary break-up of discontinuously rate-thickening suspensions*, Phys. Rev. Lett. **111** (2013), no. 036001.